

الجمهورية الجزائرية الديمقراطية الشعبية
DEMOCRATIC AND POPULAR REPUBLIC OF ALGERIA
MINISTRY OF HIGHER EDUCATION AND SCIENTIFIC RESEARCH



SETIF 1 UNIVERSITY-FERHAT ABBAS

FACULTY OF TECHNOLOGY

THESIS

Submitted to the Process Engineering Department for a

DOCTORATE DEGREE

Option : Environnement Engineering

BY

MADI Kamilia

TITLE OF THE THESIS

**Synthesis of New Hybrid Materials Incorporated into Photocatalytic
Semiconductors, Application in Urban and Industrial Wastewater
Treatment**

Defended on 24/04/ 2025 in front of the Jury

KAABI Ilhem	MCA	Univ. Sétif 1	Chairman
CHEBLI Derradji	Professor	Univ. Sétif 1	Supervisor
AIT YUCEF Hakima	MCA	Univ. Sétif 1	Co- Supervisor
NASRALLAH Noredine	Professor	USTHB	Reviewer
BOUALLOUCHE SAADI Rachida	MCA	USTHB	Reviewer
EL KOLLI Hayet	MCA	Univ. Sétif 1	Reviewer
BOUGUETTOUCHA Abdallah	Professor	Univ. Sétif 1	Guest

الجمهورية الجزائرية الديمقراطية الشعبية

République Algérienne Démocratique et Populaire

Ministère de L'Enseignement Supérieur et de la Recherche Scientifique



UNIVERSITÉ SETIF1 FERHAT ABBAS

FACULTÉ DE TECHNOLOGIE

THESE

Présentée au Département de Génie Des Procédés

Pour l'obtention du diplôme de

DOCTORAT

Option : Génie de l'environnement

Par

MADI Kamilia

THÈME

**Synthèse de nouveaux matériaux hybrides incorporés dans des
semiconducteurs photocatalytiques ; application dans le traitement des
eaux usées urbaines et industriels**

Soutenue le 24/04/ 2025 devant le Jury :

KAABI Ilhem	MCA	Univ. Sétif 1	Présidente
CHEBLI Derradji	Professeur	Univ. Sétif 1	Directeur de Thèse
AIT YUCEF Hakima	MCA	Univ. Sétif 1	Co-Directeur de Thèse
NASRALLAH Noredine	Professeur	USTHB	Examineur
BOUALLOUCHE née SAADI Rachida	MCA	USTHB	Examinatrice
EL KOLLI Hayet	MCA	Univ. Sétif 1	Examinatrice
BOUGUETTOUCHA Abdallah	Professeur	Univ. Sétif 1	Invité

Scientific publications

K. Madi, D. Chebli, H. Ait Youcef, H. Tahraoui, A. Bouguettoucha, M. Kebir, J. Zhang, A. Amrane, Green Fabrication of ZnO Nanoparticles and ZnO/rGO Nanocomposites from Algerian Date Syrup Extract: Synthesis, Characterization, and Augmented Photocatalytic Efficiency in Methylene Blue Degradation, Catalysts 14 (2024) 62. <https://doi.org/10.3390/catal14010062> .

National Communications

Kamilia Madi, Benkouachi Oumnia Rayen, Hichem Tahraoui, Derradji Chebli. Facile synthesis and characterization of new hybrid nanocomposite Polyaniline/(Fe-Cu) co-Doped CeO₂ with Enhanced Photocatalytic Degradation of Methylene Blue under Visible Light, National Conference on Process Engineering, Safety and Environment NCPSE 2024. University of Medea Algeria.

Kamilia Madi, CHEBLI Derradji, Photodeposition synthesis of Ag/ZnO nanocomposites for photodegradation of methylene blue, 1^{er} Webinaire National sur la Chimie Verte dans la Protection de l'Environnement et le Développement Durable (WCVPEDD 23), university of Amar Telidji-Laghouat– Algeria.

Kamilia Madi, CHEBLI Derradji, Photocatalytic degradation of methylene blue with ZnO/rGO synthesized by the green method, The first national symposium first circular water, health and environment 2023 impact of climate change. University of Abbas Leghrour de Khenchela Algeria.

International Communications

Kamilia Madi, BENKOUACHI OUMNIA, TAHRAOUI Hichem, CHEBLI Derradji and AIT YOUCEF Hakima., Enhanced Photocatalytic Degradation of Organic Dyes Using Polyaniline-Modified Fe and Cu Co-Doped Cerium Oxide Nanocomposites. 1st International Conference on Technological Applications of Materials (ICTAM& 24), 30- 31 October 2024, FARHAT Abbas university Setif 1 Algeria.

Kamilia Madi, CHEBLI derradji, Synthesis of Ta₂O₅/ZnO Coupled Semiconductor Oxide with High Photocatalytic Activity, 1st international conference on applied chemistry and renewable energies 2022, Larbi tebessi -Tebessa university, Algeria.

Kamilia Madi, BENKOUACHI OUMNIA, TAHRAOUI Hichem, CHEBLI Derradji and Bouguettocha Abdallah, influence of parameters and scavengers on the UV-light induced degradation of methylene blue in ZnO/rGO nanocomposite, international conference on materials of renewable energy ICMRE 2023 Setif 1 university, Algeria.

Acknowledgements

I would like to thank above all Allah, who granted me the strength, patience, and guidance to successfully carry out this research work. Without His mercy and blessings, none of these accomplishments would have been possible.

*I would like to express my profound gratitude to my thesis advisor, **Prof. CHEBLI Derradji**, for his constant support and insightful advice, which have been crucial at every stage of this research. His benevolent supervision and expertise have greatly contributed to the completion of this thesis.*

*I would also like to thank my co-supervisor, **Ms. AIT YOUSSEF Hakima**, for her kindness and insightful advice, which have facilitated the progress of my work.*

*A special thanks goes to my colleague, **Dr. TAHRAOUI Hichem**, whose invaluable support, both scientifically and personally, has been immensely helpful. His presence and commitment have allowed me to overcome many challenges.*

*I would like to express my sincere gratitude to **Ms. KAABI Ilham**, who has kindly agreed to serve as the president of my thesis defense jury. I am deeply honored by her acceptance and appreciate the valuable time she dedicates to reviewing my work.*

*I also extend my heartfelt thanks to each member of the jury: **Prof. NASRALLAH Noredine**, **Ms. BOUALLOUCHE Rachida**, and **Ms. KOLLI Hayat**. Your expertise, critical insights, and observations will undoubtedly enhance the quality of this research, and I am truly grateful for your participation in this pivotal moment of my academic journey.*

I am grateful to the entire team at the Chemical Process Engineering Laboratory (LGPC) of the University of Sétif 1 for their collaboration and technical support, which greatly facilitated the completion of my experiments.

*A big thank you to my teachers, colleagues, and friends, especially **LATOUI Mourad**, **BENKOUACHI Oumnia**, and **REDJILI Selma**, for their moral support and encouragement, which helped me stay motivated and determined throughout this journey.*

*I wish to express my deep gratitude to my parents, **Djamel** and **Souad**, for their unwavering support and encouragement. Their love and sacrifices have been essential to the realization of my dreams.*

*I also thank my sisters, **Abir** and **Samar**, as well as my brother, **Mohammed**, for their comforting presence and constant encouragement, which have been a source of motivation.*

*Finally, my gratitude goes to my grandmother, **Farida**, whose affection and wise advice have always inspired and encouraged me.*

I also want to acknowledge my family, friends, and colleagues, whose unwavering support and trust in me have been crucial to my success. Each of you has contributed to making this project a reality, and I sincerely thank you.

Thank you to all

Dedication

إلى جدي محمد عرعار

إلى الروح التي فارقتني

أهديك كل إنجاز، وكل تعب، وكل سهر، وكل نجاح تحقق، فقد كنت السند والمعين لي في كل خطوة
كم تمنيت أن تكون حاضرًا في يوم تخرجي، لتشهد ثمرة دعمك التي لولاها لما وصلت إلى ما أنا عليه اليوم.
رحمك الله وأسكنك فسيح جناته، ودمت في القلب حاضرًا بكل ما غمرتنا به من حب وعطاء.

À mon cher grand-père,

Ta sagesse et ta bienveillance ont été des lumières qui ont guidé ma vie. Bien que tu ne sois plus avec nous, ton esprit continue de m'inspirer chaque jour. Je dédie cette réussite à toi, car tu as cru en moi lorsque j'en avais le plus besoin. Merci pour ton amour, tes histoires et les leçons que tu as partagées. Tu auras toujours une place spéciale dans mon coeur.

To my dear grandfather,

Your strength and love have shaped the person I am today. You taught me the importance of perseverance and kindness, and your stories have always inspired me to dream bigger. Although you are no longer here, your spirit lives on in my heart. This achievement is for you, as a tribute to the incredible legacy you have left behind. Thank you for everything you will always miss and cherish.

List of figures

Chapter I. Bibliographic review

Figure I.1. Classification of dyes.....	10
Figure I.2. Molecular structure of the Biebrich Scarlet.....	12
Figure I.3. Molecular structure of the Methylene blue.....	13
Figure I.4: Energy band diagram of a conductor, semiconductor, and Insulator.....	17
Figure I.5. Photocatalysis mechanism.....	22

Chapter II: Synthesis and Characterization Methods of materials: Theoretical approach

Figure II.1: Batch photocatalytic reactor for Dye degradation.....	46
---	----

Chapter III. Green Fabrication of ZnO Nanoparticles and ZnO/rGO Nanocomposites from Algerian Date Syrup Extract: Synthesis, Characterization, and Augmented Photocatalytic Efficiency in Methylene Blue Degradation

Figure III.1. The precursors used for green synthesis.....	55
Figure III.2. Algerian Date Syrup (Molasses) extract preparation.....	57
Figure III.3. Schematic presentation of ZnO green synthesis.....	59
Figure III.4. Schematic diagram for preparing the ZnO/rGO _x nanocomposites.....	60
Figure III.5. XRD patterns of pure ZnO and ZnO-rGO _x	61
Figure III.6. FT-IR spectra of ZnO and ZnO/rGO _x nanocomposite.....	63
Figure III.7. SEM images of (a) Pure ZnO, (b) ZnO/rGO _{10%}	65
Figure III.8. Band gap energies and UV-vis diffuse reflectance spectra of ZnO at different calcination temperatures and ZnO/rGO _{10%}	66
Figure III.9. Effect of calcination temperature on the photocatalytic activity of ZnO for the photocatalytic degradation of MB (Neutral pH, catalyst 1g/L, [MB] = 10 mg/L).....	67

Figure III.10 Photodegradation of MB dye by ZnO/rGO _x (x= 5, 10 and 15 %) (Neutral pH, catalyst 1g/L, [MB] = 10 mg/L).....	69
Figure III.11 Effect of catalyst dose on photodegradation of MB by ZnO/rGO _{10%} (Neutral pH, [MB] = 10 mg/L).....	71
Figure III.12 Effect of reaction pH on photodegradation of MB by ZnO/rGO _{10%} (Catalyst 1g/L, [MB] = 10 mg/L).....	73
Figure III.13 Comparative performance of reused ZnO/rGO photocatalyst.....	75
Figure III.14. Effect of scavengers on the photocatalytic activity of ZnO (a) and ZnO/rGO (b) (Neutral pH, catalyst 1g/L, [MB] = 10 mg/L).....	77
Figure III.15. Pseudo-first order apparent constant values for the different initial concentrations of MB.....	78
Figure III.16. Langmuir-Hinshelwood kinetic plot for the photocatalytic decolorization of methyl blue.....	79
Figure III.17. The photodegradation mechanism of methylene blue.....	81

Chapter IV. First-Time Green Synthesis, Characterization, and Photocatalytic Activity of Bi₁₂ZnO₂₀, Bi₂O₃ and Bi₁₂ZnO₂₀/Bi₂O₃

Figure IV.1. FTIR spectra of Bi ₁₂ ZnO ₂₀ , Bi ₂ O ₃ and Bi ₁₂ ZnO ₂₀ / Bi ₂ O ₃	94
Figure IV.2. XRD patterns of Bi ₁₂ ZnO ₂₀ , Bi ₂ O ₃ , and the composite Bi ₁₂ ZnO ₂₀ /Bi ₂ O ₃	96
Figure IV.3. MEB image of (a) Bi ₁₂ ZnO ₂₀ , (b) Bi ₂ O ₃ and (c) Bi ₁₂ ZnO ₂₀ /Bi ₂ O ₃	99
Figure IV.4. Band Gap Energy for Various Samples.....	100
Figure IV.5. Influence of Calcination Temperature on Bi ₁₂ ZnO ₂₀ 's Photocatalytic Efficiency for BS Degradation under Neutral pH Conditions (1 g/L Catalyst, 20 mg/L MB).	101
Figure IV.6. Photocatalytic degradation of BS dye by Bi ₁₂ ZnO ₂₀ /Bi ₂ O ₃ (X/Y) (neutral pH, [BS] = 20mg/L, catalyst dose = 1g/L).....	103

Figure IV.7. Catalyst dose effect on the degradation of BS (neutral pH, [BS] = 20mg/L , catalyst dose = 1g/L).....	104
Figure IV.8. Effect of reaction pH on BS degradation (Catalyst dose = 1g/L, [BS] = 20mg/L).....	106
Figure IV.9. Influence of the initial concentration of BS dye on photodegradation reaction (neutral pH, catalyst dose = 1g/L).	107
Figure IV.10. Six recycling runs of photocatalytic degradation of BS with Bi ₁₂ ZnO ₂₀ /Bi ₂ O ₃ (Neutral pH, 1 g/L Catalyst, and 20 mg/L MB).....	108
Figure IV.11. Effects of different scavengers on BS degradation with Bi ₁₂ ZnO ₂₀ /Bi ₂ O ₃	109
Figure IV.12. representation of Langmuir-Hinshelwood equation for photocatalytic removal of BS by Bi ₁₂ ZnO ₂₀ /Bi ₂ O ₃	110
Figure IV.13. Photocatalytic degradation mechanism of BS over Bi ₁₂ ZnO ₂₀ /Bi ₂ O ₃	111

Chapter V. Streamlined Synthesis of P-g-C₃N₄@Ti-g-C₃N₄ Composite: A Simple Approach to High-Efficiency Photocatalysts

Figure V.1. Synthesis Scheme of P-g-C ₃ N ₄ , Ti- g-C ₃ N ₄ , and Ti- g-C ₃ N ₄ @P- g-C ₃ N ₄	121
Figure V.2. FTIR spectra of g-C ₃ N ₄ , P- g-C ₃ N ₄ , Ti- g-C ₃ N ₄ , and the P-g-C ₃ N ₄ @ Ti-g-C ₃ N ₄	122
Figure V.3. XRD patterns of pure g-C ₃ N ₄ , P- g-C ₃ N ₄ , Ti- g-C ₃ N ₄ , and the P-g-C ₃ N ₄ @ Ti-g-C ₃ N ₄	123
Figure V.4. The Scanning electron microscopy (SEM), elemental mapping, and Energy-dispersive X-ray (EDX) spectroscopy analyses of the (a) g-C ₃ N ₄ , (b) P-g-C ₃ N ₄ , (c) Ti-g- C ₃ N ₄ , and (d) P-g- C ₃ N ₄ @Ti-g- C ₃ N ₄	127
Figure V.5. TEM images of different samples g-C ₃ N ₄ (a) and (b), P- g-C ₃ N ₄ (c) and (d), Ti- g-C ₃ N ₄ (e) and (f).....	128
Figure V.6. Band gap energies and UV-vis diffuse reflectance spectra of pure g-C ₃ N ₄ , P- g-C ₃ N ₄ , Ti- g-C ₃ N ₄ , and the P-g-C ₃ N ₄ @ Ti-g-C ₃ N ₄	129

Figure V.7. Photoluminescence spectra pure g-C ₃ N ₄ , P- g-C ₃ N ₄ , Ti- g-C ₃ N ₄ , and the P-g-C ₃ N ₄ @ Ti-g-C ₃ N ₄	130
Figure V.8. Photodegradation behaviors of BS on pure and Ti-doped g-C ₃ N ₄ under visible light irradiation. (neutral pH, catalyst 1 g/L, [BS] = 30 mg/L).....	133
Figure V.9. Photodegradation behaviors of BS on pure and P-doped g-C ₃ N ₄ under visible light irradiation. (neutral pH, catalyst 1 g/L, [BS] = 30 mg/L).....	135
Figure V.10. Photodegradation of BS dye P-C ₃ N ₄ @ Ti-C ₃ N ₄ (x/y) (x = 25, 50 and 75%) (y = 75, 50 and 25%) (neutral pH, catalyst 1 g/L, [BS] = 30 mg/L).....	137
Figure V.11. The effects of operational parameters on photocatalytic degradation of BS Where (a) dose effect, (b) pH effect, (c) initial concentration effect.....	139
Figure V.12. The normalized intensities of the absorption bands for BS.....	141
Figure V.13. The cycling degradation curves of BS using P-g-C ₃ N ₄ @Ti-g-C ₃ N ₄ composite photocatalyst (a); XRD patterns of the fresh and the used catalysts after 4 recycling runs (b).....	142
Figure V.14. The degradation rates of BS using P-g-C ₃ N ₄ @Ti-g-C ₃ N ₄ photocatalyst when adding different scavengers.....	144
Figure V.15. The photodegradation mechanism of BS.....	146

List of Tables

Chapter I. Bibliographic review

Table I.1: Conventional Dye Treatment Methods: Advantages and Disadvantages.....	14
---	----

Chapter II: Synthesis and Characterization Methods of materials: Theoretical approach

Table II.1: Overview of Synthesis Methods: Advantages, Disadvantages, and Typical Application.....	36
---	----

Table II.2. Advantages and Disadvantages of Green Nanomaterial Synthesis.....	40
--	----

Chapter III. Green Fabrication of ZnO Nanoparticles and ZnO/rGO Nanocomposites from Algerian Date Syrup Extract: Synthesis, Characterization, and Augmented Photocatalytic Efficiency in Methylene Blue Degradation

Table III.1. The crystallite size of the different samples.....	62
--	----

Table III.2 The rate constant 'k' of MB degradation with ZnO calcined at different temperatures.....	67
---	----

Table III.3. The rate constant 'k' of MB with ZnO/rGO _x	68
---	----

Table III.4. Rate constant K of degradation of MB with different dosages of ZnO/rGO.....	71
---	----

Table III.5. Rate constant K of degradation of MB with ZnO/rGO in different pH.....	73
--	----

Table III.6. Comparison of the photocatalytic efficacy of commercial TiO ₂ P25 and ZnO nanoparticles.....	82
---	----

Chapter IV. First-Time Green Synthesis, Characterization, and Photocatalytic Activity of Bi₁₂ZnO₂₀, Bi₂O₃ and Bi₁₂ZnO₂₀/Bi₂O₃

Table IV.1. The average crystallizes size and lattice parameter of Bi ₁₂ ZnO ₂₀ , Bi ₂ O ₃ and Bi ₁₂ ZnO ₂₀ / Bi ₂ O ₃	96
---	----

Table IV.2. Photocatalytic performances of various Bi ₁₂ ZnO ₂₀ based materials in the degradation of different pollutants.....	112
--	-----

Chapter V. Streamlined Synthesis of P-g-C₃N₄@Ti-g-C₃N₄ Composite: A Simple Approach to High-Efficiency Photocatalysts

Table V.1. Photocatalytic Efficiency of g-C ₃ N ₄ -Based Composites in the Degradation of Various Organic Dyes.....	147
--	-----

List of abbreviations

AOPs	Advanced Oxidation Process
BS	Biebrich Scarlet
C	Concentration (mg/L or ppm)
C₀	Initial concentration (mg/L or ppm)
°C	Degree Celsius
CB	Conduction band
D	Crystal size (nm)
e⁻	electron
E_{bg}	Bandgap energy (eV)
VB	Valence band
FTIR	Fourier transform infrared
FWHM	full width half maximum
h⁺	hole
k	Rate constant (mg/L/min)
k_r	Intrinsic reaction rate constant (mg/L/min)
K_{app}	Pseudo-first-order constant(1/s)
MB	Methylene Blue
PL	Photoluminescence
rGO	reduced Graphene Oxide.
SEM	Scanning electron microscopy

t	Time (s or min)
TEM	Transmission electron microscopy
UV/vis-DRS	UV/visible-Diffuse Reflectance Spectroscopy
XPS	X-ray Photoelectron Spectroscopy
XRD	X-ray diffraction
EDX	Energy Dispersive X-ray Spectroscopy
θ	Angular coordinate
λ	Light intensity (nm)

Table of Contents

List of figures.....	i
List of tables.....	v
List of abbreviations.....	vi
General introduction.....	1

Chapter I. Bibliographic review

I.1. Introduction.....	7
I.2. Context of Water Pollution	7
I.3. Synthetic Organic Dyes in Water	8
I.3.1. Classification of Dyes	9
I.3.2. Toxicity of Synthetic Dyes.....	10
I.3.3. Presentation of Model Dyes.....	11
Biebrich Scarlet (BS).....	11
Methylene Blue.....	12
I.4. Conventional Methods for Treating Organic Dyes	13
I.4.1. Physical Methods	13
I.4.2. Chemical Methods	14
I.4.3. Biological Methods.....	14
I.5. Advanced Oxidation Processes (AOPs).....	15
I.6. Technology Used	16
I.7. Photocatalytically Active Semiconductors	16
I.7.1. Metal Oxides	18
I.7.2. Bismuth-Based Oxide Semiconductors	19
I.7.3. Sillenite-Type Materials.....	20
I.7.4. Chalcogenides: Beyond Oxides	20
I.7.5. Organic Semiconductors.....	21
I.8. Principle of Photocatalysis.....	21
I.9. Parameters Influencing Photocatalysis	22
I.10. Kinetics of Photocatalytic Reactions	23

Chapter II. Synthesis and Characterization Methods of materials: Theoretical approach

II.1.	Introduction.....	35
II.2.	Traditional Synthesis Methods for Nanomaterials.....	35
II.2.1.	Sol-Gel Synthesis.....	35
II.2.2.	Chemical Vapor Deposition (CVD).....	35
II.2.3.	Hydrothermal Synthesis.....	36
II.2.4.	Sonochemical Synthesis.....	36
II.2.5.	Laser Ablation.....	36
II.2.6.	Flame Spray Pyrolysis (FSP).....	36
II.3.	Green synthesis	37
II.3.1.	Biological Sources for the Green Synthesis of Nanoparticles	37
a.	Bacteria-Mediated Nanoparticle Generation	38
b.	Fungi-Mediated Nanoparticle Generation	38
c.	Yeast-Mediated Nanoparticle Generation	39
d.	Algae-Mediated Nanoparticle Generation	39
e.	Plant-Mediated Nanoparticle Generation	39
II.3.2.	Benefits and limitations of green synthesis	39
II.4.	Characterization techniques	40
II.4.1.	Fourier Transform Infrared (FTIR).....	40
II.4.2.	X-Ray Diffraction (XRD).....	41
II.4.3.	Scanning Electron Microscopy (SEM).....	42
II.4.4.	Transmission Electron Microscopy (TEM)	43
II.4.5.	Energy Dispersive X-ray Spectroscopy (EDX)	43
II.4.6.	Elemental Mapping.....	43
II.4.7.	UV-Visible (UV-Vis).....	44
II.4.8.	The photoluminescence (PL)	44
II.5.	Protocol for Photocatalytic Degradation Experiments in a Batch Reactor.....	45
II.6.	Determining the Role of Reactive Species in Photocatalytic Degradation through Scavenger Trapping Experiments.....	46

Chapter III. Green fabrication of zno nanoparticles and ZnO/rGo nanocomposites from algerian date syrup extract: synthesis, characterization, and augmented photocatalytic efficiency in methylene blue degradation

III.1. Introduction	53
III.2. Experiment	57
III.2.1. Algerian Date Syrup (Molasses) extract preparation.....	57
III.2.2. Synthesis of ZnO NPs.....	58
III.2.3. Preparation of ZnO/rGOx photocatalysts	59
IV. Results.....	61
IV.1.1. Characterization	61
IV.1.1.1. X-Ray diffraction	61
IV.1.1.2. Fourier-transform infrared spectroscopy.....	62
IV.1.1.3. Scanning electron microscopy images	64
IV.1.1.4. UV-visible diffuse reflectance spectroscopy	65
IV.1.2. Photocatalytic results	66
IV.1.2.1. Effect of calcination temperature on the photocatalytic activity of ZnO NPs	66
IV.1.2.2. Photocatalytic activity of ZnO/rGO _x	68
IV.1.2.3. Effect of catalyst dosage	69
IV.1.2.4. Effect of reaction pH	71
IV.1.2.5. Cycling test of the photocatalytic degradation of methylene blue under UV light	74
IV.1.2.6. Effect of Scavengers.....	75
IV.1.2.7. Degradation kinetic modeling	77
IV.1.2.8. Proposed photodegradation mechanism.....	79
IV.2. Comparison of the photocatalytic efficacy of commercial TiO ₂ P25 and ZnO nanoparticles synthesized by deferent methods.....	81

Chapter IV. First-Time Green Synthesis, Characterization, and Photocatalytic Activity of Bi₁₂ZnO₂₀, Bi₂O₃ and Bi₁₂ZnO₂₀/Bi₂O₃

IV.1. Introduction.....	90
IV.2. Experiment.....	91
IV.2.1. Prickly pear peel extract preparation	91
IV.2.2. Synthesis of Bi ₁₂ ZnO ₂₀ and Bi ₂ O ₃	92

IV.3.	Characterization Results	93
IV.3.1.	FTIR.....	93
IV.3.2.	The X-ray diffraction XRD.....	94
IV.3.3.	Scanning electron microscopy images (SEM).....	97
IV.3.4.	The bandgap energies	99
IV.4.	Photocatalytic results	100
IV.4.1.	Effect of calcination temperature on the photocatalytic activity of Bi ₁₂ ZnO ₂₀ ...	100
IV.4.2.	Photocatalytic activity of Bi ₁₂ ZnO ₂₀ /Bi ₂ O ₃ (X/Y)	101
IV.4.3.	Catalyst dosage effect	103
IV.4.4.	Initial concentration effect	106
IV.4.5.	Recycling test of Bi ₁₂ ZnO ₂₀ /Bi ₂ O ₃ for BS degradation	107
IV.4.6.	Scavengers effect	109
IV.4.7.	Degradation kinetic modeling.....	110
IV.4.8.	Proposed photodegradation mechanism	111
IV.5.	Comparative Performance of Bi ₁₂ ZnO ₂₀ -Based Photocatalysts for Pollutant photocatalytic Degradation	112

Chapter V. Streamlined Synthesis of P-g-C₃N₄@Ti-g-C₃N₄ Composite: A Simple Approach to High-Efficiency Photocatalysts

V.1.	Introduction	117
V.2.	Experiment	119
V.2.1.	Preparation of P-g-C ₃ N ₄ @Ti-g-C ₃ N ₄	119
V.2.1.1.	g-C ₃ N ₄ preparation	119
V.2.1.2.	Phosphorus-Doped g-C ₃ N ₄ synthesis.....	120
V.2.1.3.	Titanium-doped g-C ₃ N ₄ synthesis	120
V.2.1.4.	The P-g-C ₃ N ₄ @Ti-g-C ₃ N ₄ preparation.....	120
V.3.	Results	121
V.3.1.	Characterization	121
V.3.1.1.	The Fourier transform infrared (FTIR)	121
V.3.1.2.	X ray Diffraction	122
V.3.1.3.	SEM, Elemental mapping, and EDX spectroscopy.....	124
V.3.1.4.	Transmission Electron Microscopy (TEM).....	127

V.3.1.5. UV-Visible Diffuse Reflectance Spectroscopy (UV-DRS)	129
V.3.1.6. Fluorescence spectra (PL)	130
V.3.2. Photocatalytic results	132
V.3.2.1. Titanium- g-C ₃ N ₄ doped.....	132
V.3.2.2. Phosphorus-g-C ₃ N ₄ doped.....	134
V.3.2.3. P-C ₃ N ₄ @ Ti-C ₃ N ₄ (x/y) Composite	136
V.3.2.4. The effects of operational parameters on photocatalytic degradation of biebrich scarlet	138
V.3.2.5. Normalized intensities of absorption bands	139
V.3.2.6. Systematic Evaluation of Photostability and Reusability of P-g-C ₃ N ₄ @Ti-g-C ₃ N ₄ Composite	142
V.3.2.7. Scavengers effect.....	143
V.3.3. The plausible photodegradation mechanism.....	144
V.4. Comparison of the Photocatalytic Efficacy of various g- C ₃ N ₄ -based composites in degrading different organic dyes	147
Conclusions and Outlook.....	154



General introduction

General introduction

The preservation of the environment and the resolution of ecological problems are essential issues for sustainably improving the quality of life and ensuring sustainable development [1]. Water plays a fundamental role in various human activities, such as domestic, agricultural, and industrial uses. Globally, agriculture consumes about 70% of water resources, while 11% is allocated for urban needs and 19% for industry [2]. Faced with the rapid increase in the global population and the intensification of agricultural and industrial activities, the demand for freshwater continues to grow [3]. Thus, the preservation of natural water resources and innovation in water and wastewater treatment technologies have emerged as major environmental priorities of the 21st century [4].

The pollution of water resources is largely due to the presence of toxic substances of chemical and biological origin, resulting from various human activities such as industry, agriculture, and domestic uses [5]. Among these pollutants, organic dyes hold a significant place. Massively used in industries such as textiles, leather, and cosmetics [6] these compounds are particularly resistant to natural degradation processes, which contribute to their persistence in aquatic environments [7]. In addition to their low biodegradability, dyes can affect water quality by disrupting light transmission, which harms photosynthetic processes and disrupts aquatic ecosystems.

Despite significant efforts for wastewater treatment, only 60% of polluted water is treated, while the rest is discharged directly into nature [8]. This leads to an accumulation of recalcitrant substances which are difficult to biodegrade, exacerbated by the inefficiency of current treatment systems to reduce the concentration of toxins [9]. This poor treatment of wastewater contributes to the degradation of water resources, thereby impacting on the quality of drinking water which is already insufficient in many countries.

Conventional wastewater treatment methods, whether physical, chemical, or biological, have a major drawback [10,11], they often transfer pollutants from one phase to another rather than completely eliminating them [12]. In practice, these processes transfer contaminants from water to by-products such as concentrated sludge resulting in the accumulation of secondary waste. This transfer does not truly solve the environmental problem but rather shifts it while requiring

additional solutions to manage these residues, which are often difficult and costly to treat [13]. These constraints highlight the urgency of designing more innovative and sustainable depollution solutions, capable not only of effectively eliminating contaminants from wastewater but also of minimizing the production of secondary waste and reducing the overall environmental impact of treatment processes.

The most recent advances in the field of water treatment have been made in the oxidation of "biologically recalcitrant" organic compounds that are highly present in textile effluent discharges [14,15]. These methods rely on the formation of highly reactive chemical entities that will decompose the most recalcitrant molecules into biologically degradable molecules [16] or mineral compounds such as CO_2 and H_2O these are the Advanced Oxidation Processes (POA) [17]. Among these, we can mention: ozonation, photolysis, sonolysis, Fenton, photo-Fenton, and photocatalysis [18]. Particularly, photocatalysis is a light-induced catalytic process that oxidizes or reduces organic molecules through reactions occurring on the surface of semiconductors under light irradiation [19]. During the process, free radicals ($\bullet\text{OH}$, $\text{O}_2\bullet^-$) are generated which will react with the pollutants, leading to their degradation and mineralization [20].

The creation of effective catalysts that satisfy crucial requirements is the main goal of current catalytic materials research. They must have strong catalytic activity to effectively speed up chemical reactions and be stable over time to retain their efficacy without deteriorating. Since the catalyst must maximize the production of the target molecule while reducing unwanted byproducts, selectivity is also essential. Reproducible performances are also crucial since they guarantee consistent outcomes every time they are used. Furthermore, two essential elements to guarantee practical use are the catalyst's regeneration capability and ease of application.

The search for new, effective, and suitable materials for the photocatalytic degradation of existing organic pollutants in water remains an important issue. In this study, we focused on the synthesis of hybrid nanomaterials for the degradation of two pollutants: methylene blue and Biebrich scarlet.

This research aims to achieve the following objectives:

- ✓ Develop innovative photocatalysts based on zinc and bismuth, followed by an in-depth characterization to evaluate their effectiveness in degrading specific dyes under UV irradiation.
- ✓ Optimize the photocatalytic properties of g-C₃N₄ by doping with two elements, with the aim of improving its efficiency under visible irradiation.
- ✓ Implement eco-friendly approaches for the synthesis of photocatalysts, prioritizing the use of plant extracts and physical methods to minimize the environmental impact associated with conventional chemicals.

Manuscript structure

This thesis is divided into five chapters structured as follows:

The first chapter provides a general overview of water pollution: the sources of water pollution, the main pollutants, we are interested in pollution caused by dyes as well as the different treatment processes, advanced oxidation processes (AOPs) in particular heterogeneous photocatalysis.

The second chapter groups the experimental techniques used. The methods for synthesizing photocatalysts, the different physico-chemical characterization methods (XRD, FTIR, UV-vis DRS, SEM-EDX, and TEM), and the reactor used during the photocatalytic application.

The third chapter focuses on a green approach for the synthesis of ZnO nanoparticles and ZnO/rGO nanocomposites, using Algerian date syrup extract as a reducing agent. The detailed characterization of the physical and chemical properties of the synthesized materials is followed by an in-depth evaluation of their photocatalytic efficiency, particularly in the degradation of methylene blue.

In the fourth, it discusses the first green synthesis of bismuth-based compounds, notably Bi₁₂ZnO₂₀ and Bi₂O₃, as well as their composite Bi₁₂ZnO₂₀/Bi₂O₃. These materials are then characterized to evaluate their structural and morphological properties. The chapter also explores their photocatalytic activity, particularly in the context of the degradation of organic pollutants.

The fifth chapter presents a simplified synthesis method for the production of P-g-C₃N₄ e@Ti-g-C₃N₄ composites, recognized for their potential as high-performance photocatalysts. The

described approach is both simple and effective, offering a pathway to the design of promising photocatalysts. The chapter focuses on optimizing the photocatalytic properties of the obtained materials, highlighting the synergies between the two materials to improve light capture and the mechanisms of pollutant degradation.

References

- [1] K.E. Portney, Taking sustainable cities seriously: Economic development, the environment, and quality of life in American cities, MIT Press, 2013. <https://books.google.com/books?hl=fr&lr=&id=fLofEAAAQBAJ&oi=fnd&pg=PR7&dq=The+preservation+of+the+environment+and+the+resolution+of+ecological+problems+are+essential+issues+for+sustainably+improving+the+quality+of+life+and+ensuring+sustainable+development&ots=trJcJOocpx&sig=fONVKeiugQ3YH9Xxy8df8d39zvA> (accessed October 21, 2024).
- [2] M. Flörke, E. Kynast, I. Bärlund, S. Eisner, F. Wimmer, J. Alcamo, Domestic and industrial water uses of the past 60 years as a mirror of socio-economic development: A global simulation study, *Global Environmental Change* 23 (2013) 144–156.
- [3] R.K. Mishra, Fresh water availability and its global challenge, *British Journal of Multidisciplinary and Advanced Studies* 4 (2023) 1–78.
- [4] G. Ssekyanzi, M.J. Ahmad, K.-S. Choi, Sustainable Solutions for Mitigating Water Scarcity in Developing Countries: A Comprehensive Review of Innovative Rainwater Storage Systems, *Water* 16 (2024) 2394.
- [5] J. Singh, P. Yadav, A.K. Pal, V. Mishra, Water Pollutants: Origin and Status, in: D. Pooja, P. Kumar, P. Singh, S. Patil (Eds.), *Sensors in Water Pollutants Monitoring: Role of Material*, Springer Singapore, Singapore, 2020: pp. 5–20. https://doi.org/10.1007/978-981-15-0671-0_2.
- [6] M. Behera, J. Nayak, S. Banerjee, S. Chakraborty, S.K. Tripathy, A review on the treatment of textile industry waste effluents towards the development of efficient mitigation strategy: An integrated system design approach, *Journal of Environmental Chemical Engineering* 9 (2021) 105277.
- [7] A.K. Alsukaibi, Various approaches for the detoxification of toxic dyes in wastewater, *Processes* 10 (2022) 1968.
- [8] H. Trabelsi, Etude de la dégradabilité et de la toxicité des colorants par ozonation et photocatalyse, PhD Thesis, Yahia Fares University of Medea Medea, Algeria, 2014.
- [9] A. Saravanan, P.S. Kumar, S. Jeevanantham, S. Karishma, B. Tajsabreen, P.R. Yaashikaa, B. Reshma, Effective water/wastewater treatment methodologies for toxic pollutants removal: Processes and applications towards sustainable development, *Chemosphere* 280 (2021) 130595.
- [10] N. Sharma, A. Singh, N. Batra, Modern and Emerging Methods of Wastewater Treatment, in: V. Achal, A. Mukherjee (Eds.), *Ecological Wisdom Inspired Restoration Engineering*, Springer Singapore, Singapore, 2019: pp. 223–247. https://doi.org/10.1007/978-981-13-0149-0_13.

- [11] C. Grandclément, I. Seyssiecq, A. Píram, P. Wong-Wah-Chung, G. Vanot, N. Tiliacos, N. Roche, P. Doumenq, From the conventional biological wastewater treatment to hybrid processes, the evaluation of organic micropollutant removal: a review, *Water Research* 111 (2017) 297–317.
- [12] I.A. Saleh, N. Zouari, M.A. Al-Ghouti, Removal of pesticides from water and wastewater: Chemical, physical and biological treatment approaches, *Environmental Technology & Innovation* 19 (2020) 101026.
- [13] S.M. Jiménez, M.M. Micó, M. Arnaldos, F. Medina, S. Contreras, State of the art of produced water treatment, *Chemosphere* 192 (2018) 186–208.
- [14] J.O. Tijani, O.O. Fatoba, G. Madzivire, L.F. Petrik, A Review of Combined Advanced Oxidation Technologies for the Removal of Organic Pollutants from Water, *Water Air Soil Pollut* 225 (2014) 2102. <https://doi.org/10.1007/s11270-014-2102-y>.
- [15] D. Mantzavinos, E. Psillakis, Enhancement of biodegradability of industrial wastewaters by chemical oxidation pre-treatment, *J of Chemical Tech & Biotech* 79 (2004) 431–454. <https://doi.org/10.1002/jctb.1020>.
- [16] F. Audino, Advanced oxidation process models for optimisation and decision making support in water management, (2019). <https://upcommons.upc.edu/handle/2117/327399> (accessed October 23, 2024).
- [17] M. Coha, G. Farinelli, A. Tiraferri, M. Minella, D. Vione, Advanced oxidation processes in the removal of organic substances from produced water: Potential, configurations, and research needs, *Chemical Engineering Journal* 414 (2021) 128668.
- [18] S. Bognár, D. Jovanović, V. Despotović, N. Finčur, P. Putnik, D. Šojić Merkulov, Advancing Wastewater Treatment: A Comparative Study of Photocatalysis, Sonophotolysis, and Sonophotocatalysis for Organics Removal, *Processes* 12 (2024) 1256.
- [19] P. Riente, T. Noël, Application of metal oxide semiconductors in light-driven organic transformations, *Catalysis Science & Technology* 9 (2019) 5186–5232.
- [20] J. Zhang, G. Zhang, H. Lan, M. Sun, H. Liu, J. Qu, Synergetic Oxidation of the Hydroxyl Radical and Superoxide Anion Lowers the Benzoquinone Intermediate Conversion Barrier and Potentiates Effective Aromatic Pollutant Mineralization, *Environ. Sci. Technol.* 57 (2023) 12117–12126. <https://doi.org/10.1021/acs.est.3c03406>.



Chapter I

Bibliographic review

Chapter I. Bibliographic review

I.1. Introduction

This chapter aims to provide a comprehensive overview of various aspects addressed in this thesis before delving into the experimental sections and results. We will begin with an in-depth discussion on water pollution caused by synthetic organic dyes, clarifying the environmental challenges and impacts on human health. The chapter will cover the different classifications of dyes and their toxicity, focusing on model dyes such as Biebrich Scarlet (BS) and Methylene Blue. We will then evaluate the conventional methods for treating organic dyes, examining the available techniques and their limitations. Specifically, we will focus on advanced oxidation processes (AOPs), with a particular emphasis on photocatalysis. This process utilizes semiconductor materials to generate free radicals capable of degrading organic pollutants into simple mineral products. A summary table of process parameters, optimal conditions, used photocatalysts, and their removal efficiencies will be provided to illustrate advancements in this field. The chapter will further explore photocatalytically active semiconductors, including metal oxides, bismuth-based oxides, sillenite-type materials, and chalcogenides. Organic semiconductors will also be discussed for their photocatalytic potential. The chapter will detail the principles of photocatalysis, the parameters influencing the process, and the kinetics of photocatalytic reactions.

I.2. Context of Water Pollution

In the context of rapid economic growth and population expansion, the preservation of water resources has become an essential priority. [1]. The growing demand for water, exacerbated by rapid urbanization and industrialization, is placing considerable pressure on available resources. [2]. Every day, approximately 2 million tons of pollutants from various industrial, agricultural, and domestic sources are discharged into water reserves [3]. These uncontrolled discharges include toxic chemicals, organic waste[4], heavy metals [5] and other contaminants that severely compromise water quality. This degradation of drinking water leads to disastrous consequences for human health, with waterborne diseases causing thousands of deaths daily, primarily in the most vulnerable regions of the world. [6]. The situation is particularly alarming in developing

countries, where water treatment infrastructure is often insufficient to handle the growing pollution. However, developed countries are not exempt; intensive industrial and agricultural practices also contribute to the contamination of both groundwater and surface water. [7]. In response to this reality, it is urgent to revise and strengthen water resource management policies, with an emphasis on pollution prevention, wastewater treatment, and the protection of aquatic ecosystems. These policies must be comprehensive and integrated, involving not only governments but also industries, local communities, and international organizations. Among the numerous sources of water pollution, organic dyes [8] used in the textile industry and other manufacturing processes pose a particularly insidious threat. These dyes, often non-biodegradable, persist in the environment for extended periods [9], altering the color of water bodies and obstructing sunlight penetration essential for aquatic photosynthetic processes[10]. Their presence in water can also be toxic to aquatic wildlife, disrupting ecosystems and allowing dangerous substances to accumulate within the food chain [11]. Organic dyes may contain carcinogenic and mutagenic compounds, thereby increasing health risks for humans when they contaminate drinking water. Managing this form of pollution requires advanced treatment technologies, along with stringent regulations on the use and discharge of these substances into the environment.

I.3. Synthetic Organic Dyes in Water

Despite being present in low concentrations, synthetic organic dyes are ubiquitous due to large-scale production and diverse applications [12]. The first synthetic organic dye, mauveine, was discovered by William Perkin in 1865 [13], parking a revolution in the dye industry. Today, the major producers of dyes are China and India [14], which also dominate global textile production [15]. Synthetic organic dyes represent the largest group of coloring substances, with over 100,000 dyes commercially available and global production exceeding one million tons annually [16,17]. These dyes are widely used in the textile [18], tanning, printing [19], paper, pharmaceutical, cosmetic, and food industries[20]. The massive production of these dyes and their varied uses generate significant volumes of colored wastewater and post-production waste. The textile industry is a major source of dye pollution in aquatic environments, with up to 50% of dyes being lost during dyeing processes [21]. Furthermore, some synthetic organic dyes are poorly biodegradable or non-biodegradable, making their treatment in wastewater plants more complex [22]. Studies have confirmed the toxic properties of certain dyes, including

carcinogenic, allergic, and dermatological effects, highlighting the risks associated with their production and use[23,24]. Recently, several reports have been published on the presence of synthetic organic dyes in water [25], sediments, and wild fish, confirming their environmental impact. Although their full effect on aquatic ecosystems is not yet fully assessed, monitoring their presence in the environment is essential.

I.3.1. Classification of Dyes

Synthetic dyes are artificial colorants produced through chemical processes and are widely used in various industries [26], such as textiles, cosmetics, and food. They are often distinguished by their superior brightness and stability compared to natural dyes. Synthetic dyes are classified into ionic and non-ionic compounds based on their chemical properties and application method [27].

Ionic dyes contain charged ions, which can be either positively charged (cationic) [28] or negatively charged (anionic) [29]. Cationic dyes, which carry a positive charge, are commonly used to color materials with negatively charged surfaces, such as acrylic fibers and certain types of paper [30]. They establish electrostatic attractions with the negatively charged groups on the substrate, leading to strong binding. These dyes interact with the substrate through ionic interactions, forming strong bonds with materials having opposite charges [31]. Anionic dyes, which carry a negative charge, are often employed to color materials with positively charged surfaces, such as natural fibers like cotton and wool. They form bonds with positively charged groups on the substrate through electrostatic interactions [32].

In contrast, non-ionic dyes do not possess a net charge on their molecules [33]. They rely on weaker forces, such as Van der Waals forces, hydrogen bonds, and hydrophobic interactions, to adhere to the substrate [34]. Non-ionic dyes are frequently used to dye materials with neutral surfaces or surfaces that do not interact easily with charged molecules. They offer significant versatility in terms of compatibility with various substrates and can be used across a wide range of materials [35].

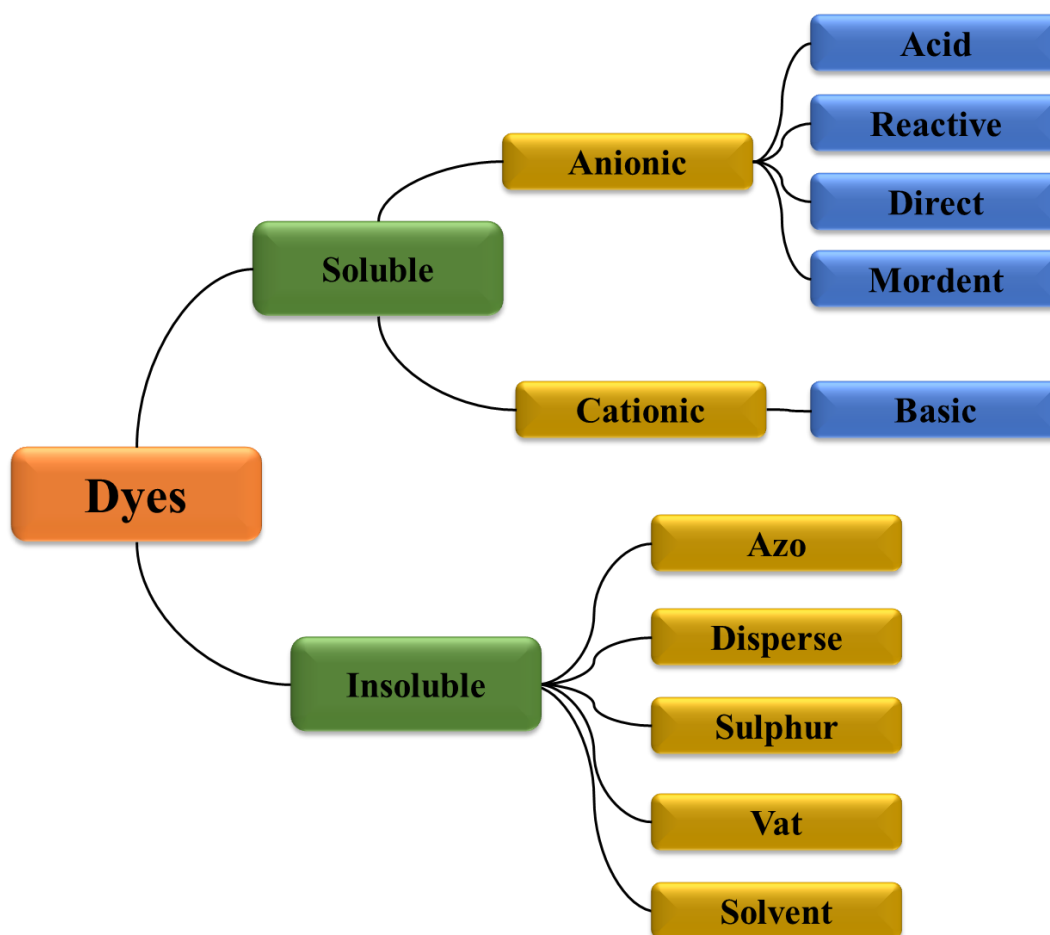


Figure I.1. Classification of dyes.

I.3.2. Toxicity of Synthetic Dyes

Toxicity is defined as the ability of a substance to cause harmful effects on living organisms [36], including humans, bacteria, plants, or even specific structures within these organisms, such as the liver. Research on approximately 3,000 commercial dyes has revealed that basic dyes are the most toxic to algae [37]. This finding was confirmed by mortality tests on fish, which showed that basic dyes, particularly those belonging to the triphenylmethane family, exhibit high toxicity [38]. Additionally, fish also appear to display significant sensitivity to acidic dyes. The likelihood of human mortality caused by the acute toxicity of dyes is generally considered low [39]. While some dyes may induce allergic or dermatological reactions, these effects are relatively rare. However, the toxicity of aromatic amines is closely related to their molecular structure, especially the position of the amine groups [40]. For example, 2-naphthylamine is recognized as a carcinogen, while 1-naphthylamine exhibits significantly lower toxicity. Similarly, for azo

dyes, toxicity varies depending on the nature and position of substituents on the aromatic ring [41]. The presence of nitro (-NO₂) groups and halogens, particularly chlorine, tends to increase toxicity. Conversely, the introduction of carboxyl or sulfonate groups into the dye structure can reduce their toxicity [42].

Given the harmful effects of dyes, especially azo dyes, it is crucial to prevent their accumulation in the environment. Therefore, it is essential to implement wastewater treatment processes that achieve the complete degradation of these dyes, ensuring their total mineralization and minimizing their environmental impact.

I.3.3. Presentation of Model Dyes

Biebrich Scarlet (BS)

Biebrich Scarlet (BS) is an anionic azo dye widely used across various industries, particularly in textiles and papermaking. This dye is also classified as an acid dye due to its ability to dissolve in acidic solutions. It is known by several names, including Acid Red 66, Ponceau BS, and the sodium salt of Biebrich Scarlet. Its IUPAC name is 2-[(2-hydroxy-1-naphthyl) azo]-5-[(4-sulfophenyl)azo]benzenesulfonic acid disodium salt, with the chemical formula C₂₂H₁₄N₄Na₂O₇S₂. With a molar mass of 556 g/mol, it is characterized by good solubility in water as well as in alcoholic solvents [43].

This dye is identified by the CI number 26905 and exhibits a maximum absorption peak (λ_{max}) at 506 nm, making it particularly effective for producing bright and intense shades. Biebrich Scarlet is primarily used for dyeing natural fibers such as cotton, wool, and silk, as well as paper. It is valued for its ability to produce a vibrant and brilliant hue with a distinctive fluorescent effect [44], making it a popular choice in applications that require vivid and long-lasting colors.

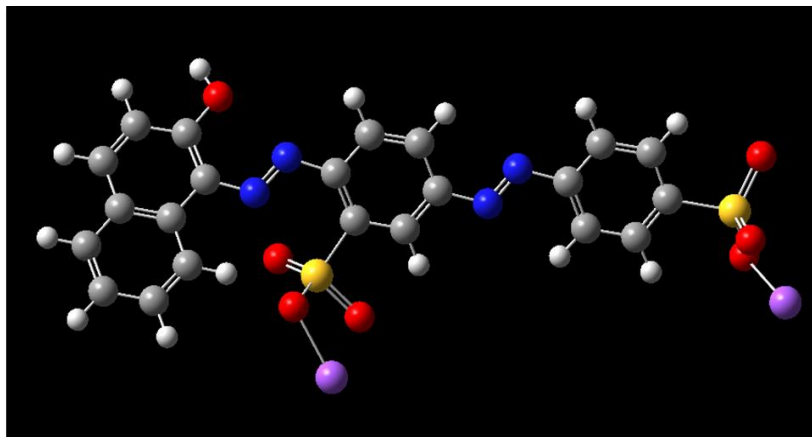


Figure I.2. Molecular structure of the Biebrich Scarlet.

Methylene Blue

Methylene blue is an organic dye from the thiazine class, widely used across various scientific and industrial fields. Its IUPAC name is 3,7-bis(dimethylamino)phenothiazin-5-ium chloride, with the chemical formula $C_{16}H_{18}ClN_3S$ and a molar mass of 319.85 g/mol. This dye is water-soluble, forming a distinctive blue solution, and can also dissolve in certain organic solvents [45]. Methylene blue is primarily used in microbiology for staining tissue samples and cells, aiding in their observation under a microscope. In chemistry and biology, it acts as a redox agent, participating in reduction reactions and oxygen detection. Furthermore, it is used in medicine as an antidote for certain chemical poisonings and in the textile industry to produce bright, durable blue hues [46]. The dye has a maximum absorption peak around 665 nm, corresponding to its intense blue color in solution. Its versatility and distinctive properties make it a valuable tool in numerous scientific and industrial applications [47].

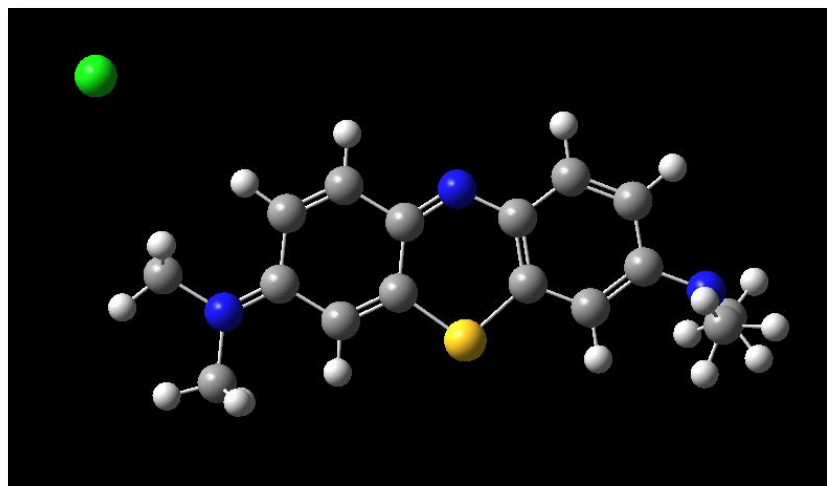


Figure I.3. Molecular structure of the Methylene blue.

I.4. Conventional Methods for Treating Organic Dyes

The treatment of organic dyes in wastewater is a major concern due to their environmental impact. These dyes can be eliminated through various conventional methods, classified into two main categories: physical methods and chemical methods. Each category encompasses different techniques, each with its own mechanisms of action, advantages, and limitations.

I.4.1. Physical Methods

Physical methods rely on physical processes to separate or concentrate dyes without altering their chemical structure. Here are some common examples:

- **Coagulation-Flocculation:** This method involves the addition of coagulants to neutralize the charges of colloidal particles, causing them to precipitate as flocs. These flocs can then be separated by sedimentation or filtration [48].
- **Adsorption:** Adsorption involves binding dye molecules to the surface of an adsorbent, such as activated carbon. This technique is particularly effective in removing dissolved dyes at low concentrations [49].
- **Membrane Filtration (Ultrafiltration, Nanofiltration, Reverse Osmosis):** These techniques use semi-permeable membranes to separate dye molecules from water. Ultrafiltration is effective in removing macromolecules and colloids, while nanofiltration and reverse osmosis are used to retain small molecules, including dyes. Reverse osmosis,

in particular, can remove almost all dissolved particles, including ions and organic molecules [50].

I.4.2. Chemical Methods

Chemical methods involve chemical reactions that transform dyes into other compounds, often less harmful or easier to remove. These methods include:

- **Chemical Oxidation:** This method uses powerful oxidants such as chlorine, ozone, or hydrogen peroxide to break down dyes into simpler compounds. While effective for degrading persistent dyes, it may generate potentially toxic by-products [51].
- **Electrochemical Processes:** Electrochemical processes use the application of an electric current to induce oxidation or reduction reactions that degrade dyes. These processes can be highly effective for the degradation of complex dyes, but they require specialized infrastructure and can be energy-intensive [52].

I.4.3. Biological Methods

Although not purely physical or chemical, biological methods are worth mentioning for their ability to treat organic dyes. These methods use microorganisms to break down dyes into less toxic substances. Biological processes are generally eco-friendly and cost-effective, but they can be limited by the non-biodegradable nature of certain dyes [53].

Table I.1: Conventional Dye Treatment Methods: Advantages and Disadvantages.

<i>Method</i>	<i>Advantages</i>	<i>Disadvantages</i>
<i>Coagulation-Flocculation</i>	Simple to implement, relatively low cost.	Generates secondary sludge, variable effectiveness depending on dyes.
<i>Adsorption</i>	Effective for a wide range of dyes, reusable adsorbents.	High cost of adsorbents, rapid saturation.
<i>Membrane Filtration</i>	Highly effective at removing small molecules and particles.	High installation and maintenance cost, membrane fouling.
<i>Nanofiltration</i>	Retains small molecules, reduces energy needs compared to reverse osmosis.	Less effective for very small molecules, membrane costs.

<i>Reverse Osmosis</i>	Almost complete removal of impurities, highly effective for a wide range of dyes.	High cost and energy consumption, potential membrane fouling.
<i>Chemical Oxidation</i>	Fast, effective for persistent dyes.	High cost of reagents, possible production of toxic by-products.
<i>Electrochemical Processes</i>	Effective for complete dye degradation, minimal chemical residues.	High energy consumption, expensive infrastructure.
<i>Biological Treatment</i>	Eco-friendly, low operational cost.	Long treatment time, limited effectiveness for non-biodegradable dyes.

These conventional methods, while widely used, have limitations that necessitate the exploration of more advanced processes, such as advanced oxidation techniques, for more complete and environmentally friendly degradation of organic dyes.

I.5. Advanced Oxidation Processes (AOPs)

Advanced Oxidation Processes (AOPs) are treatment technologies particularly effective for degrading persistent organic pollutants, including dyes [54]. These processes are distinguished by their ability to generate highly reactive radical species, such as hydroxyl radicals ($\bullet\text{OH}$), which oxidize contaminants by converting them into less harmful substances or mineralizing them into carbon dioxide and water [55]. Among AOPs, photocatalysis is a commonly used method that employs a semiconductor catalyst activated by a light source to produce hydroxyl radicals, enabling the degradation of various organic pollutants [56]. Advanced ozonation, which combines ozone with agents such as hydrogen peroxide or UV light, is also effective at generating radicals and enhancing the degradation of contaminants [57]. Fenton and Photo-Fenton processes exploit the reaction between hydrogen peroxide and ferrous ions to produce hydroxyl radicals, with Photo-Fenton additionally using a light source to enhance the reaction efficiency [58]. Hydrogen peroxide oxidation, often combined with UV light or metallic ions, also generates radicals for treating industrial wastewater (Mukherjee et al., 2023). Advanced electrochemical processes use electricity to generate oxidizing agents in situ or to directly

decompose organic pollutants [59]. Advanced electrochemical processes use electricity to generate oxidizing agents in situ or to directly decompose organic pollutants [60]. Cold plasma, an emerging technique, generates free radicals in a gas through electrical discharges, which then react with pollutants in water [61]. Finally, catalytic wet oxidation combines heat, pressure, and a catalyst to oxidize organic matter present in effluents, offering an effective solution for concentrated organic pollutant streams [62]. These methods, often used in combination, allow for the adaptation of treatment to specific needs based on the nature of the contaminants and treatment conditions.

I.6. Technology Used

Photocatalysis is an advanced oxidation process that facilitates chemical reactions by utilizing electronically excited species generated through the absorption of photons [63]. This process relies on the use of semiconductor materials, which, when exposed to light radiation, produce free radicals such as $\text{OH}\cdot$, $\text{HO}_2\cdot$, and $\text{O}_2\cdot^-$ [64]. These radicals are capable of degrading even the most resistant organic compounds into simple mineral products, such as carbon dioxide (CO_2) and water (H_2O) [65]. Photocatalysis is a clean process, free from excessive energy production and the need for additives, and is characterized by the absence of residues, making it an entirely eco-friendly method [66]. Additionally, photocatalysis operates under normal temperature and humidity conditions, without requiring specific parameters [67].

I.7. Photocatalytically Active Semiconductors

Semiconductors, discovered in the 19th century, began to find practical applications from 1947 onward [68]. These solid materials are primarily used for electrical conduction. A semiconductor exhibits electrical properties intermediate between those of a metal and an insulator [69], characterized by two specific energy bands: the valence band (lower energy level) and the conduction band (higher energy level). These two bands are separated by an energy gap, also known as the bandgap, defined by an energy barrier measured in electron volts [70]. The larger the bandgap (E_g), the greater the energy required to excite electrons from the valence band to the conduction band [71]. This energy gap represents the energy needed for an electron to transition from the valence band to the conduction band. Once in the conduction band, the electron is free to move through the material, no longer bound to a specific atom.

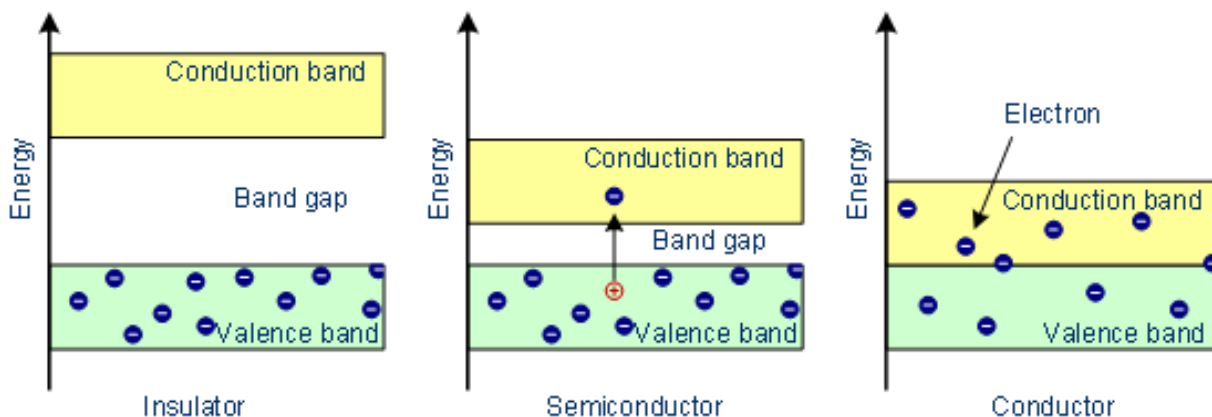


Figure I.4: Energy band diagram of a conductor, semiconductor, and Insulator.

Unlike semiconductors, conductors have overlapping valence and conduction bands, allowing for easy electrical conduction. Metals such as copper, silver, gold, and aluminum are among the best conductors due to this configuration [72]. Insulators, on the other hand, have a valence band completely filled with electrons and an empty conduction band [73]. In semiconductors, although there is an energy gap between the valence band and the conduction band, some valence electrons can be excited into the conduction band under the influence of sufficient energy, whether thermal, magnetic, or light. Once excited, these electrons become charge carriers, enabling conduction.

Semiconductors can be classified into two categories: intrinsic, where the electrical properties are determined solely by the pure material [74], and extrinsic, where impurities are added to modify their conductive properties [75]. In photocatalytic reactions, semiconductors act as catalysts, facilitating the chemical reaction without being consumed in the overall process. These materials are thus referred to as photocatalysts, and their ability to generate free radicals under the influence of light makes them key players in advanced oxidation processes.

To be effective, a catalyst must exhibit several essential characteristics:

- **Photoactivity:** Capable of accelerating targeted reactions, allowing for a reduction in the amount of catalysts needed as activity increases.
- **Response to UV/Visible Radiation:** The catalyst must be activatable by ultraviolet and/or visible light.

- **Selectivity:** It should exclusively catalyze the desired reaction, thereby enhancing selectivity and reducing the need for subsequent purification.
- **Photostability:** The catalyst must resist deactivation during the reaction to ensure long-term efficiency.
- **Cost and Safety:** It should be economically viable and non-toxic to both the environment and human health.

I.7.1. Metal Oxides

Metal oxides (MO) are compounds formed when metal ions establish coordination bonds with oxide ions (O^{2-}), resulting in compact and stable crystalline structures. They are essential semiconductor materials in photocatalysis, thanks to their distinctive properties that make them particularly effective for various environmental and energy applications [76]. These materials are characterized by remarkable chemical stability and a wide bandgap, which allows them to absorb light efficiently. Under light irradiation, MOs generate electron-hole pairs, which initiate chemical reactions on their surface crucial for the degradation of organic pollutants and the conversion of solar energy [77].

Titanium Dioxide (TiO_2) is one of the most extensively studied metal oxides. Its chemical stability and ability to generate highly reactive hydroxyl radicals ($\bullet OH$) under UV irradiation make it an excellent candidate for applications such as self-cleaning coatings, air purifiers, and the degradation of pollutants in water [78].

Iron (III) Oxide (Fe_2O_3), commonly known as hematite, is another example of a metal oxide with a bandgap of approximately 2.1 eV, enabling it to absorb part of the visible spectrum. This property is utilized in water photoelectrolysis, a process where solar energy is employed to split water into oxygen and hydrogen, and in other solar energy conversion applications [79]. It is particularly effective for the degradation of organic compounds under visible light and for hydrogen production, a clean energy carrier.

Molybdenum Trioxide (MoO_3), on the other hand, is applied in advanced oxidation reactions and catalysis for fine chemistry. It is notably used to degrade complex organic compounds and to synthesize high-value chemical products, owing to its unique catalytic properties [80].

Focus on ZnO (Zinc Oxide)

ZnO is a metal oxide semiconductor particularly effective for photocatalytic applications due to its bandgap of approximately 3.37 eV, which allows it to absorb UV light (Bindhu et al., 2020). This property endows ZnO with a high capacity to generate free radicals under UV irradiation, which are capable of decomposing organic pollutants in water and air. However, ZnO is sensitive to photo-corrosion, which limits its prolonged use [81]. To enhance the photocatalytic efficiency of ZnO and address this limitation, the incorporation of reduced graphene oxide (rGO) into ZnO-rGO composites proves to be a promising solution. rGO, with its partially reduced graphene structure, improves the electronic conductivity of the composite, facilitating charge transfer between ZnO and rGO. This enhancement in charge transfer contributes to more efficient separation of the electron-hole pairs generated under UV irradiation, thereby optimizing the production of free radicals.

Moreover, rGO plays a crucial role in reducing the photo-corrosion of ZnO by protecting it from oxidative conditions and increasing its stability. Additionally, rGO can extend the absorption range of the composite into the visible light spectrum, enabling photocatalytic activation under a broader range of light conditions. This combination of ZnO and rGO thus enhances the overall efficiency of the photocatalyst for organic pollutant degradation, offering more effective and sustainable environmental applications [82].

I.7.2. Bismuth-Based Oxide Semiconductors

Bismuth oxides are highly efficient photocatalytic materials under visible light irradiation due to their narrow bandgap, which ranges from 1.6 to 3.1 eV, thereby promoting the absorption of visible light [83]. This property arises from the hybridization of the $6s^2$ orbitals of bismuth with the $2p^6$ orbitals of oxygen, which increases the energy of the valence band and reduces the bandgap width, enhancing hole mobility [84]. In addition to these electronic properties, bismuth oxides, such as Bi_2O_3 , are stable, chemically inert, and non-toxic, making them attractive for industrial applications [85]. Their crystalline structure and small particle size contribute to better charge mobility and reduced electron-hole pair recombination, thereby increasing their efficiency in processes such as the degradation of organic pollutants and water purification under visible light irradiation [86].

Bismuth oxides can be categorized into several families, including simple oxides like Bi_2O_3 , mixed oxides with alkaline earth metals (such as NaBiO_3), transition metals (such as $\text{Bi}_4\text{Ti}_3\text{O}_{12}$ and Bi_2WO_4), and halogens [87]. Among these families, bismuth oxide Bi_2O_3 has been extensively studied for its photocatalytic applications, particularly in the degradation of organic pollutants and water purification under visible light, due to its ability to generate reactive free radicals.

I.7.3. Sillenite-Type Materials

Sillenite-type materials have recently found diverse and innovative applications, ranging from optical data processing and storage to fields such as electro-optics, acoustics, piezoelectricity, optoelectronics, and electronics. Their use also extends to fiber optic sensors, image amplification, real-time and multispectral holographic imaging, metrology, and various photocatalytic applications [88].

Bismuth oxide crystals with a sillenite structure, represented by the general formula $\text{Bi}_{12}[\text{M}]\text{O}_{20}$ (BMO), where M denotes a tetravalent ion from groups II to VIII of the periodic table, exhibit a body-centered cubic structure described by the space group I23. The crystalline structure of the ideal $\text{Bi}_{12}\text{MO}_{20}$ sillenite is characterized by the local arrangement of atoms around the Bi and M sites. Specifically, the BMO structure consists of a bismuth ion (Bi^{3+}) surrounded by eight oxygen atoms, which share their corners with other similar BiO_8 polyhedra. The tetravalent MO_4 ions occupy positions both at the center and corners of the cube, contributing to the stability and uniqueness of the crystalline structure [89].

I.7.4. Chalcogenides: Beyond Oxides

In addition to metal oxides, various chalcogenides have been investigated for their photocatalytic activity. Among them, metal sulfides are particularly noteworthy due to their low bandgap energy, ranging from 1.3 to 2.40 eV, which allows for optimal utilization of solar energy [90]. Semiconductor materials based on sulfides, such as CdS (cadmium sulfide), ZnS (zinc sulfide), Sb_2S_3 (antimony trisulfide), Bi_2S_3 (bismuth trisulfide), and MoS_2 (molybdenum disulfide), exhibit narrow bandgaps suitable for photocatalytic processes [91].

Sulfide-based semiconductors possess valence bands primarily composed of S3p orbitals, which are positioned at a more negative energy compared to the O2p orbitals found in metal oxides.

Despite their ability to respond to visible light, metal sulfides are often prone to photocorrosion, limiting their practical application.

I.7.5. Organic Semiconductors

Photocatalytic organic semiconductors are innovative materials that combine the properties of semiconductors with the advantages of organic compounds, such as flexibility, low production cost, and the ability to efficiently absorb visible light [92]. When exposed to light, these materials generate electron-hole pairs, enabling chemical reactions on their surface. This capability is essential for applications such as the degradation of organic pollutants or hydrogen production.

Polyaniline (PANI) is a key example of an organic semiconductor used in photocatalysis. This conductive polymer, often combined with metal oxides, forms nanocomposites that are highly effective in degrading organic pollutants under visible light. PANI helps in charge separation and extends the catalyst's response to visible light, thereby enhancing the photocatalytic efficiency. Another notable example is poly(3-hexylthiophene) (P3HT), a widely used semiconductor polymer in organic photovoltaic cells, which also holds potential for photocatalytic applications due to its ability to generate charges under light irradiation [93].

Graphitic carbon nitride (g-C₃N₄) is arguably one of the most promising organic semiconductors for photocatalysis. Composed of carbon and nitrogen, this material has a graphite-like structure and a bandgap of approximately 2.7 eV [94], allowing for efficient absorption of visible light. g-C₃N₄ is particularly effective in applications such as organic dye degradation and hydrogen production from water under light irradiation. In addition to its chemical stability and low toxicity, its low cost makes it an ideal candidate for large-scale environmental applications [95]. Moreover, the performance of g-C₃N₄ can be optimized by doping it with non-metallic elements, such as phosphorus or sulfur, to tune its bandgap and enhance its reactivity under visible light. These characteristics position g-C₃N₄ as a material of choice in the field of organic photocatalysis [96].

I.8. Principle of Photocatalysis

Photocatalysis is based on the interaction of light with a semiconductor (SC), where the absorption of light with energy equal to or greater than the bandgap ($h\nu \geq E_g$) induces the excitation of electrons from the valence band (VB) to the conduction band (CB) [97]. This electronic transfer simultaneously generates positive holes in the VB, creating oxidation sites

(hole, h^+) and reduction sites (electron, e^-) on the semiconductor's surface. These electron-hole pairs (e^-/h^+) can either recombine, releasing energy in the form of heat, or interact independently with molecules in the surrounding environment. The holes (h^+) can oxidize electron donors such as water (H_2O), hydroxyl anions (OH^-), or organic compounds adsorbed on the SC surface, thereby producing hydroxyl radicals (OH^\bullet) and organic radicals (R^\bullet). Conversely, the electrons (e^-) are captured by acceptors such as molecular oxygen (O_2), forming superoxide radicals ($O_2^{\bullet-}$) and, potentially, hydrogen peroxide (H_2O_2). These oxidative species play a crucial role in the oxidation of adsorbed molecules, potentially leading to their complete mineralization into carbon dioxide (CO_2) and water (H_2O) [98].

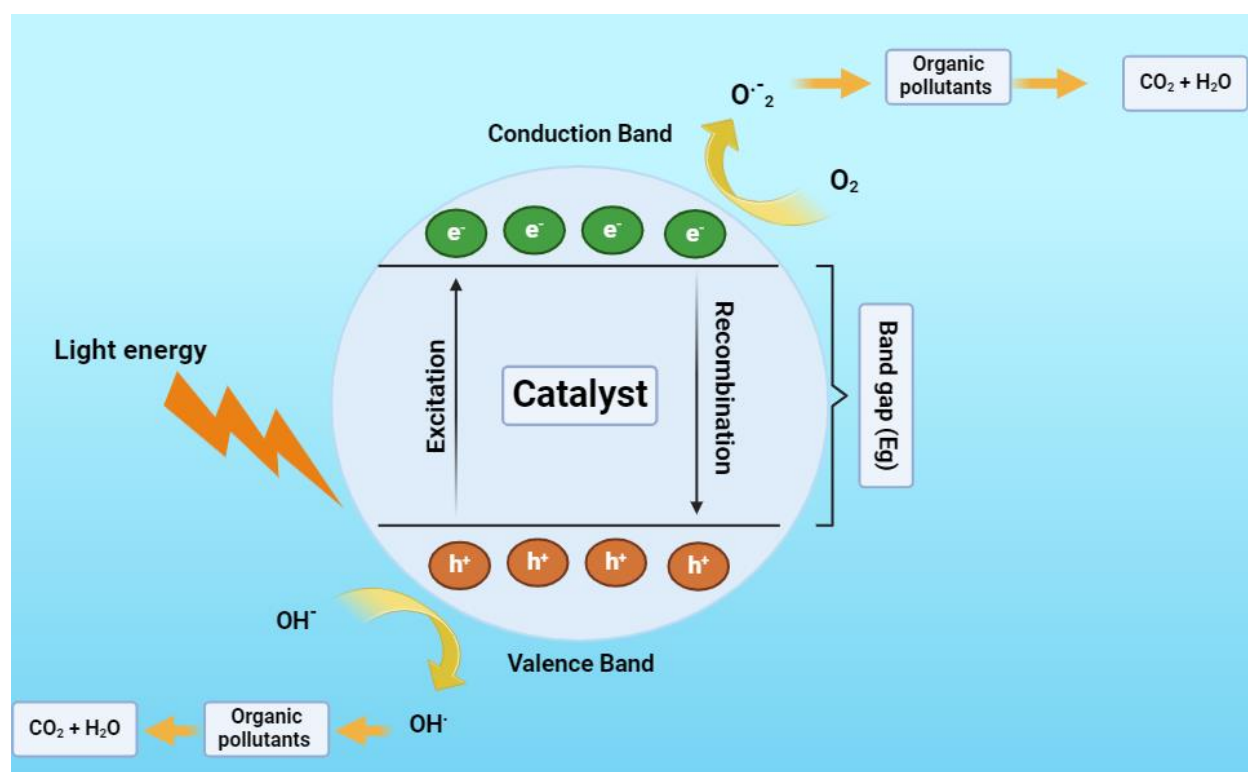


Figure I.5. Photocatalysis mechanism.

I.9. Parameters Influencing Photocatalysis

Several parameters significantly impact the efficiency of heterogeneous photocatalysis. Among these factors, light intensity plays a crucial role, as adequate illumination of the reactor promotes the formation of electron-hole pairs on the catalyst's surface. The rate of the photocatalytic reaction is proportional to the light intensity up to a certain threshold, beyond which the rate becomes proportional to the square root of the intensity [99].

The pH of the aqueous solution is another key parameter, as it affects the surface charge of the catalyst and can lead to particle aggregation when close to the point of zero charge (pHpzc). This phenomenon can reduce photocatalytic efficiency, particularly at neutral pH, where the balance of positive and negative charges on the catalyst surface may cause aggregation [100].

The initial concentration of the pollutant also influences the degradation yield. A high concentration can result in a screening effect, limiting photon penetration to the catalyst surface and reducing reaction efficiency. Additionally, a high concentration of adsorbed pollutants can saturate the catalyst's active sites, thereby decreasing the generation of hydroxyl radicals necessary for pollutant degradation [101].

The reaction temperature, although often overlooked in photocatalytic systems operating at ambient temperature, can also affect efficiency. Lower temperatures enhance pollutant adsorption on the catalyst surface, while excessive temperatures beyond 80°C can inhibit this exothermic adsorption [102].

Finally, the catalyst dose must be optimized according to experimental conditions and the geometry of the photoreactor. An excessively high concentration can render the solution opaque and create a screening effect, reducing light penetration and, consequently, photocatalytic yield [103].

I.10. Kinetics of Photocatalytic Reactions

The kinetics of photocatalytic reactions are often described using the Langmuir-Hinshelwood model, one of the most widely used models in this field due to its ability to capture the underlying mechanisms of adsorption and chemical reaction on catalyst surfaces. This model is based on several fundamental assumptions that make it applicable to a variety of photocatalytic systems [104].

Assumptions of the Langmuir-Hinshelwood Model

- 1. Langmuir-Type Adsorption:** The model assumes that substrate adsorption on the catalyst surface follows a Langmuir isotherm. This means that the catalyst surface has a fixed number of adsorption sites, each capable of adsorbing a single molecule of substrate, and these sites are homogeneous in terms of adsorption energy.

2. **Rate of Adsorption and Desorption:** The adsorption and desorption steps are considered to be rapid compared to the chemical reaction rate itself. This implies that adsorption equilibrium is quickly reached, and the kinetics of the reaction are primarily controlled by the chemical transformation of the adsorbed substrate.
3. **Constant Adsorption Energy:** It is also assumed that the adsorption energy is the same for all adsorption sites and does not vary with the degree of surface coverage. This simplifies the analysis by positing that the probability of absorbing a substrate molecule does not depend on the presence or absence of other nearby adsorbed molecules.
4. **Non-Saturation of Adsorption Sites:** The adsorption sites are not permanently bound to the substrate and can be freed after the reaction, allowing for continuous and renewed adsorption of the substrate.

Equations of the Langmuir-Hinshelwood Model

The Langmuir-Hinshelwood kinetic model is extensively employed to elucidate the kinetics governing the photocatalytic oxidation of organic pollutants. This model provides a framework for quantifying the rate of degradation of an organic pollutant under varying concentrations.

The reaction rate can be mathematically represented as:

$$r_0 = - \frac{dc}{dt} = \frac{kr.KC}{1+KC} \quad (\text{I.1})$$

Where:

- r is the degradation rate of the pollutant (mg/min),
- kr is the reaction rate constant for the chemical transformation (mg/L·min),
- K is the adsorption equilibrium constant of the reactant (L/mg),
- C is the pollutant concentration (mg/L) [105].

The inverse of the equation leads to

$$\frac{1}{r_0} = \frac{1}{kr} + \frac{1}{kr.K} \cdot \frac{1}{C_0} \quad (\text{I.2})$$

References

- [1] W.J. Cosgrove, D.P. Loucks, Water management: Current and future challenges and research directions, *Water Resources Research* 51 (2015) 4823–4839.
- [2] M. Arfanuzzaman, A.A. Rahman, Sustainable water demand management in the face of rapid urbanization and ground water depletion for social–ecological resilience building, *Global Ecology and Conservation* 10 (2017) 9–22.
- [3] H. Kumari, Sonia, Suman, R. Ranga, S. Chahal, S. Devi, S. Sharma, S. Kumar, P. Kumar, S. Kumar, A. Kumar, R. Parmar, A Review on Photocatalysis Used For Wastewater Treatment: Dye Degradation, *Water Air Soil Pollut* 234 (2023) 349. <https://doi.org/10.1007/s11270-023-06359-9>.
- [4] N. Akhtar, M.I. Syakir Ishak, S.A. Bhawani, K. Umar, Various natural and anthropogenic factors responsible for water quality degradation: A review, *Water* 13 (2021) 2660.
- [5] K. Sardar, S. Ali, S. Hameed, S. Afzal, S. Fatima, M.B. Shakoor, S.A. Bharwana, H.M. Tauqueer, Heavy metals contamination and what are the impacts on living organisms, *Greener Journal of Environmental Management and Public Safety* 2 (2013) 172–179.
- [6] K.R. Bhattarai, M. Bhasin, Water pollution is the main problem for human health, *Journal of Algebraic Statistics* 13 (2022) 2812–2817.
- [7] U.S.E.P.A.O. of W. Regulations, U.S.E.P.A.O. of W. Planning, National Water Quality Inventory: Report to Congress, The Office, 1996. [https://books.google.com/books?hl=fr&lr=&id=uy8SAAAYAAJ&oi=fnd&pg=PP31&dq=.+National+Water+Quality+Inventory+Report+to+Congress+\(2009\)+Washington,+D.C.:+United+States+Environmental+Protection+Agency+\(EPA\).+EPA+841-F-08-03.&ots=YZtFiSRgBK&sig=mPW3xiJvJUBRDFVPmC0ycFUAhHM](https://books.google.com/books?hl=fr&lr=&id=uy8SAAAYAAJ&oi=fnd&pg=PP31&dq=.+National+Water+Quality+Inventory+Report+to+Congress+(2009)+Washington,+D.C.:+United+States+Environmental+Protection+Agency+(EPA).+EPA+841-F-08-03.&ots=YZtFiSRgBK&sig=mPW3xiJvJUBRDFVPmC0ycFUAhHM) (accessed August 14, 2024).
- [8] S. Devi, S. Chahal, S. Singh, P. Kumar, S. Kumar, A. Kumar, V. Kumar, Magnetic Fe₂O₃/CNT nanocomposites: characterization and photocatalytic application towards the degradation of Rose Bengal dye, *Ceramics International* 49 (2023) 20071–20079.
- [9] K. Maheshwari, M. Agrawal, A.B. Gupta, Dye Pollution in Water and Wastewater, in: S.S. Muthu, A. Khadir (Eds.), *Novel Materials for Dye-Containing Wastewater Treatment*, Springer Singapore, Singapore, 2021: pp. 1–25. https://doi.org/10.1007/978-981-16-2892-4_1.
- [10] R. Al-Tohamy, S.S. Ali, F. Li, K.M. Okasha, Y.A.-G. Mahmoud, T. Elsamahy, H. Jiao, Y. Fu, J. Sun, A critical review on the treatment of dye-containing wastewater: Ecotoxicological and health concerns of textile dyes and possible remediation approaches for environmental safety, *Ecotoxicology and Environmental Safety* 231 (2022) 113160.

- [11] S. Dutta, S. Adhikary, S. Bhattacharya, D. Roy, S. Chatterjee, A. Chakraborty, D. Banerjee, A. Ganguly, S. Nanda, P. Rajak, Contamination of textile dyes in aquatic environment: Adverse impacts on aquatic ecosystem and human health, and its management using bioremediation, *Journal of Environmental Management* 353 (2024) 120103.
- [12] A. Tkaczyk, K. Mitrowska, A. Posyniak, Synthetic organic dyes as contaminants of the aquatic environment and their implications for ecosystems: A review, *Science of the Total Environment* 717 (2020) 137222.
- [13] A.S. Travis, Perkins Mauve: Ancestor of the Organic Chemical Industry, *Technology and Culture* 31 (1990) 51–82.
- [14] G. Clayton, A. Filarowski, R. Straughan, The increasing price of dyes and pigments-short and long term issues, *Biotechnic & Histochemistry* 89 (2014) 398–399. <https://doi.org/10.3109/10520295.2014.909607>.
- [15] R. Berwal, Global aspect of Indian textile industry and their challenges and opportunities: A review, *International Journal of Home Science* (2020). <https://www.homesciencejournal.com/archives/2020/vol6issue1/PartE/6-1-59-153.pdf> (accessed August 15, 2024).
- [16] K. Singh, S. Arora, Removal of Synthetic Textile Dyes From Wastewaters: A Critical Review on Present Treatment Technologies, *Critical Reviews in Environmental Science and Technology* 41 (2011) 807–878. <https://doi.org/10.1080/10643380903218376>.
- [17] H. Zollinger, Color chemistry: syntheses, properties, and applications of organic dyes and pigments, John Wiley & Sons, 2003. <https://books.google.com/books?hl=fr&lr=&id=0Ynge4E5rqYC&oi=fnd&pg=PA1&dq=Synthetic+organic+dyes+represent+the+largest+group+of+colouring+substances,+with+over+100,000+dye+s+commercially+available+and+a+global+production+exceeding+one+million+tonnes+per+year&ots=pWsuW4lsfp&sig=jYAzufekY1Ag21cuwWHqnCA5uHs> (accessed August 15, 2024).
- [18] M.R. Islam, M.G. Mostafa, Textile dyeing effluents and environment concerns-a review, *Journal of Environmental Science and Natural Resources* 11 (2018) 131–144.
- [19] D. Kumar, H.P. Bhati, S. Kumar, N. Kumari, P. Kumar, BIOSORPTION OF MALACHITE GREEN DYE BY MYCOMASS AND PHYTOMASS INFLUENCE BY INDUSTRIAL EFFLUENT HEAVY METALS, *Invited/Lead Papers* (n.d.). https://www.asthafoundation.in/img/book/GRISAAS-2019%20Conference%20Book_compressed.pdf#page=95 (accessed August 15, 2024).

- [20] H. Ghazal, M. Elshamy, Ecofriendly finishing and Dyeing of textile using bioactive agents derived from plant extracts and waste, *Journal of Textiles, Coloration and Polymer Science* 21 (2024) 569–590.
- [21] R. Kant, Textile dyeing industry an environmental hazard, (2011). https://www.scirp.org/html/4-8301582_17027.htm (accessed August 15, 2024).
- [22] T. Islam, Md.R. Repon, T. Islam, Z. Sarwar, M.M. Rahman, Impact of textile dyes on health and ecosystem: a review of structure, causes, and potential solutions, *Environ Sci Pollut Res* 30 (2022) 9207–9242. <https://doi.org/10.1007/s11356-022-24398-3>.
- [23] E.O. Alegbe, T.O. Uthman, A review of history, properties, classification, applications and challenges of natural and synthetic dyes, *Heliyon* (2024). [https://www.cell.com/heliyon/fulltext/S2405-8440\(24\)09677-4](https://www.cell.com/heliyon/fulltext/S2405-8440(24)09677-4) (accessed August 15, 2024).
- [24] A.P. Periyasamy, Recent advances in the remediation of textile-dye-containing wastewater: prioritizing human health and sustainable wastewater treatment, *Sustainability* 16 (2024) 495.
- [25] D. Tamburini, F. Sabatini, S. Berbers, M.R. van Bommel, I. Degano, An introduction and recent advances in the analytical study of early synthetic dyes and organic pigments in cultural heritage, *Heritage* 7 (2024) 1969–2010.
- [26] H.B. Slama, A. Chenari Bouket, Z. Pourhassan, F.N. Alenezi, A. Silini, H. Cherif-Silini, T. Oszako, L. Luptakova, P. Golińska, L. Belbahri, Diversity of synthetic dyes from textile industries, discharge impacts and treatment methods, *Applied Sciences* 11 (2021) 6255.
- [27] E. Gurr, *Synthetic dyes in biology, medicine and chemistry*, Elsevier, 2012. <https://books.google.com/books?hl=fr&lr=&id=Y-2THuZuhOwC&oi=fnd&pg=PP1&dq=Synthetic+dyes+are+classified+into+ionic+and+non-ionic+compounds+according+to+their+chemical+properties+and+application+method&ots=0Ptza cSL9M&sig=mGT1-APwjnRBohIN8SwnsX8NDCQ> (accessed August 18, 2024).
- [28] M.A.M. Salleh, D.K. Mahmoud, W.A.W.A. Karim, A. Idris, Cationic and anionic dye adsorption by agricultural solid wastes: a comprehensive review, *Desalination* 280 (2011) 1–13.
- [29] M.M. Hassan, C.M. Carr, Biomass-derived porous carbonaceous materials and their composites as adsorbents for cationic and anionic dyes: A review, *Chemosphere* 265 (2021) 129087.
- [30] S.A. Shapovalov, Cation–Anionic Interactions of Dyes in Aqueous Solutions: Bromocresol Purple in the Processes of Dissimilar Association, *Colorants* 1 (2021) 5–19.
- [31] A. Safavi, H. Abdollahi, N. Maleki, S. Zeinali, Interaction of anionic dyes and cationic surfactants with ionic liquid character, *Journal of Colloid and Interface Science* 322 (2008) 274–280.

- [32] R.J. Aguado, A. Mazega, Q. Tarrés, M. Delgado-Aguilar, The role of electrostatic interactions of anionic and cationic cellulose derivatives for industrial applications: A critical review, *Industrial Crops and Products* 201 (2023) 116898.
- [33] Q. Li, Q.-Y. Yue, H.-J. Sun, Y. Su, B.-Y. Gao, A comparative study on the properties, mechanisms and process designs for the adsorption of non-ionic or anionic dyes onto cationic-polymer/bentonite, *Journal of Environmental Management* 91 (2010) 1601–1611.
- [34] M.D. Garcia, A. Sanz-Medel, Dye-surfactant interactions: a review, *Talanta* 33 (1986) 255–264.
- [35] W. Konicki, K. Cendrowski, G. Bazarko, E. Mijowska, Study on efficient removal of anionic, cationic and nonionic dyes from aqueous solutions by means of mesoporous carbon nanospheres with empty cavity, *Chemical Engineering Research and Design* 94 (2015) 242–253.
- [36] A. Bensakhria, Toxicité Aigue, *Toxicologie Générale*, Chapitre II (2018) 21–28.
- [37] R. Majumdar, W.A. Shaikh, S. Chakraborty, S. Chowdhury, A review on microbial potential of toxic azo dyes bioremediation in aquatic system, *Microbial Biodegradation and Bioremediation* (2022) 241–261.
- [38] P.K. Singh, R.L. Singh, Bio-removal of azo dyes: a review, *International Journal of Applied Sciences and Biotechnology* 5 (2017) 108–126.
- [39] R.R. Karri, G. Ravindran, M.H. Dehghani, Wastewater—sources, toxicity, and their consequences to human health, in: *Soft Computing Techniques in Solid Waste and Wastewater Management*, Elsevier, 2021: pp. 3–33.
<https://www.sciencedirect.com/science/article/pii/B9780128244630000001X> (accessed August 18, 2024).
- [40] L. Pereira, P.K. Mondal, M. Alves, Aromatic amines sources, environmental impact and remediation, *Pollutants in Buildings, Water and Living Organisms* (2015) 297–346.
- [41] W. Wu, S. Liang, Y. Chen, L. Shen, H. Zheng, L. Wu, High efficient photocatalytic reduction of 4-nitroaniline to p-phenylenediamine over microcrystalline SrBi₂Nb₂O₉, *Catalysis Communications* 17 (2012) 39–42.
- [42] T. Xian, H. Yang, L. Di, J. Ma, H. Zhang, J. Dai, Photocatalytic reduction synthesis of SrTiO₃-graphene nanocomposites and their enhanced photocatalytic activity, *Nanoscale Research Letters* 9 (2014) 1–9.
- [43] N.H. AL-Shammari, D.E. AL-Mammar, Adsorption of Biebrich Scarlet Dye into Remains Chromium and Vegetable Tanned Leather as Adsorbents, *Iraqi Journal of Science* (2022) 2814–2826.
- [44] D. Chebli, A. Bouguettoucha, A. Reffas, C. Tiar, M. Boutahala, H. Gulyas, A. Amrane, Removal of the anionic dye Biebrich scarlet from water by adsorption to calcined and non-calcined Mg–Al

- layered double hydroxides, *Desalination and Water Treatment* 57 (2016) 22061–22073. <https://doi.org/10.1080/19443994.2015.1128365>.
- [45] M.H. Tareque, Photocatalytic Decomposition of Selected Textile Industrial Effluent on Fe-Ti-Zn Oxide Catalysts, PhD Thesis, University of Rajshahi, 2020. <http://rulrepository.ru.ac.bd/handle/123456789/1062> (accessed August 18, 2024).
- [46] G. Sbati, K. Oukili, M. Loukili, Etude de la dégradation des colorants de textile application sur le Bleu de Méthylène [Study of the degradation of the colouring agents of textile application on the Methylene blue], *International Journal of Innovation and Applied Studies* 16 (2016) 272.
- [47] Z. El Kerdoudi, J. Bensalah, N. Ferraa, A. El Mekkaoui, A. Berisha, Z. Safi, H. Ouaddari, F. Khallouki, M. Dauebait, H.-A. Nafidi, Physicochemical characterization of clay and study of cationic methylene blue dye adsorption, *ACS Omega* 8 (2023) 40848–40863.
- [48] R. Lefa, Optimization of a water treatment process with respect to coagulation and sedimentation process of a conventional water treatment plant., PhD Thesis, Faculty of Engineering and the Built Environment, University of the ..., 2022. <https://wiredspace.wits.ac.za/server/api/core/bitstreams/7e55b10d-1ebe-44e4-8df1-1f2b608ce649/content> (accessed August 18, 2024).
- [49] P.S. Kumar, G.J. Joshiba, C.C. Femina, P. Varshini, S. Priyadharshini, M.A. Karthick, R. Jothirani, A critical review on recent developments in the low-cost adsorption of dyes from wastewater, *Desalin. Water Treat* 172 (2019) 395–416.
- [50] B. Rai, A. Shrivastav, Removal of emerging contaminants in water treatment by nanofiltration and reverse osmosis, in: *Development in Wastewater Treatment Research and Processes*, Elsevier, 2022: pp. 605–628. <https://www.sciencedirect.com/science/article/pii/B9780323855839000260> (accessed August 18, 2024).
- [51] G. Crini, E. Lichtfouse, L.D. Wilson, N. Morin-Crini, Conventional and non-conventional adsorbents for wastewater treatment, *Environmental Chemistry Letters* 17 (2019) 195–213.
- [52] P.V. Nidheesh, M. Zhou, M.A. Oturan, An overview on the removal of synthetic dyes from water by electrochemical advanced oxidation processes, *Chemosphere* 197 (2018) 210–227.
- [53] H.M. Solayman, M.A. Hossen, A. Abd Aziz, N.Y. Yahya, K.H. Leong, L.C. Sim, M.U. Monir, K.-D. Zoh, Performance evaluation of dye wastewater treatment technologies: A review, *Journal of Environmental Chemical Engineering* 11 (2023) 109610.
- [54] V. Vinayagam, K.N. Palani, S. Ganesh, S. Rajesh, V.V. Akula, R. Avoodaiappan, O.S. Kushwaha, A. Pugazhendhi, Recent developments on advanced oxidation processes for degradation of pollutants from wastewater with focus on antibiotics and organic dyes, *Environmental Research* (2023) 117500.

- [55] L. Yang, Z. Chen, Q. Cao, H. Liao, J. Gao, L. Zhang, W. Wei, H. Li, J. Lu, Structural regulation of photocatalyst to optimize hydroxyl radical production pathways for highly efficient photocatalytic oxidation, *Advanced Materials* 36 (2024) 2306758.
- [56] L.G. Devi, R. Kavitha, A review on non metal ion doped titania for the photocatalytic degradation of organic pollutants under UV/solar light: Role of photogenerated charge carrier dynamics in enhancing the activity, *Applied Catalysis B: Environmental* 140 (2013) 559–587.
- [57] A. Tufail, W.E. Price, F.I. Hai, A critical review on advanced oxidation processes for the removal of trace organic contaminants: A voyage from individual to integrated processes, *Chemosphere* 260 (2020) 127460.
- [58] C. Wang, P. Shi, Z. Wang, R. Guo, J. You, H. Zhang, Efficient wastewater disinfection through FeOOH-mediated photo-Fenton reaction: A review, *Journal of Environmental Chemical Engineering* (2023) 111269.
- [59] J. Mukherjee, B.K. Lodh, R. Sharma, N. Mahata, M.P. Shah, S. Mandal, S. Ghanta, B. Bhunia, Advanced oxidation process for the treatment of industrial wastewater: A review on strategies, mechanisms, bottlenecks and prospects, *Chemosphere* (2023) 140473.
- [60] F. Long, D. Ghani, R. Huang, C. Zhao, Versatile electrode materials applied in the electrochemical advanced oxidation processes for wastewater treatment: A systematic review, *Separation and Purification Technology* (2024) 128725.
- [61] G. Tomei, M. Saleem, E. Ceriani, A. Pinton, E. Marotta, C. Paradisi, Cold Plasma for Green Advanced Reduction/Oxidation Processes (AROPs) of Organic Pollutants in Water**, *Chemistry A European J* 29 (2023) e202302090. <https://doi.org/10.1002/chem.202302090>.
- [62] Y. Segura, A.C. Del Álamo, M. Munoz, S. Álvarez-Torrellas, J. García, J.A. Casas, Z.M. De Pedro, F. Martínez, A comparative study among catalytic wet air oxidation, Fenton, and Photo-Fenton technologies for the on-site treatment of hospital wastewater, *Journal of Environmental Management* 290 (2021) 112624.
- [63] S.C. Pillai, N.B. McGuinness, C. Byrne, C. Han, J. Lalley, M. Nadagouda, P. Falaras, A.G. Kontos, M.A. Gracia-Pinilla, K. OShea, Photocatalysis as an effective advanced oxidation process, *Advanced Oxidation Processes for Water Treatment: Fundamentals and Applications* (2017) 333–381.
- [64] F. Mohamadpour, A.M. Amani, Photocatalytic systems: reactions, mechanism, and applications, *RSC Advances* 14 (2024) 20609–20645.
- [65] J. Bhattacharjee, S. Roy, A Review on Photocatalysis and Nanocatalysts for Advanced Organic Synthesis, *Hybrid Advances* (2024) 100268.

- [66] W. Guo, T. Guo, Y. Zhang, L. Yin, Y. Dai, Progress on simultaneous photocatalytic degradation of pollutants and production of clean energy: A review, *Chemosphere* (2023) 139486.
- [67] E. Gauthier, Etude du couplage Adsorption-Photocatalyse au sein d'une même opération unitaire pour la dégradation de Composés Organiques Volatils, PhD Thesis, Université de Grenoble, 2007. <https://theses.hal.science/tel-00965283/> (accessed August 19, 2024).
- [68] J.W. Orton, Semiconductors and the information revolution: magic crystals that made IT happen, Academic Press, 2009. <https://books.google.com/books?hl=fr&lr=&id=6YLL9197NfMC&oi=fnd&pg=PP1&dq=Semiconductors,+discovered+in+the+19th+century,+have+seen+their+practical+applications+emerge+from+1947&ots=1osRZt2KRe&sig=GVgFwk-ZrTD4nihH-MaQgG1Hc70> (accessed August 19, 2024).
- [69] M.J. Deen, F. Pascal, Electrical Characterization of Semiconductor Materials and Devices, in: S. Kasap, P. Capper (Eds.), *Springer Handbook of Electronic and Photonic Materials*, Springer International Publishing, Cham, 2017: pp. 1–1. https://doi.org/10.1007/978-3-319-48933-9_20.
- [70] A. Lathe, A.M. Palve, Types and Properties of Semiconductors, in: *Handbook of Semiconductors*, CRC Press, n.d.: pp. 26–39. <https://www.taylorfrancis.com/chapters/edit/10.1201/9781003450146-3/types-properties-semiconductors-ajay-lathe-anil-palve> (accessed August 19, 2024).
- [71] Y. Xu, M.A.A. Schoonen, The absolute energy positions of conduction and valence bands of selected semiconducting minerals, *American Mineralogist* 85 (2000) 543–556. <https://doi.org/10.2138/am-2000-0416>.
- [72] S. Kasap, C. Koughia, H.E. Ruda, Electrical Conduction in Metals and Semiconductors, in: S. Kasap, P. Capper (Eds.), *Springer Handbook of Electronic and Photonic Materials*, Springer International Publishing, Cham, 2017: pp. 1–1. https://doi.org/10.1007/978-3-319-48933-9_2.
- [73] L. Bergerot, Etude de l'élaboration d'oxyde transparent conducteur de type-p en couches minces pour des applications à l'électronique transparente ou au photovoltaïque, PhD Thesis, Université Grenoble Alpes, 2015. <https://theses.hal.science/tel-01168478/> (accessed August 19, 2024).
- [74] A.D. Terna, E.E. Elemike, J.I. Mbonu, O.E. Osafire, R.O. Ezeani, The future of semiconductor nanoparticles: Synthesis, properties and applications, *Materials Science and Engineering: B* 272 (2021) 115363.
- [75] V. Gurylev, Nanostructured Photocatalyst via Defect Engineering: Basic Knowledge and Recent Advances, Springer International Publishing, Cham, 2021. <https://doi.org/10.1007/978-3-030-81911-8>.

- [76] U. Kumar, J.Z. Hassan, R.A. Bhatti, A. Raza, G. Nazir, W. Nabgan, M. Ikram, Photocatalysis vs adsorption by metal oxide nanoparticles, *Journal of Materials Science & Technology* 131 (2022) 122–166.
- [77] L. Jing, W. Zhou, G. Tian, H. Fu, Surface tuning for oxide-based nanomaterials as efficient photocatalysts, *Chemical Society Reviews* 42 (2013) 9509–9549.
- [78] D. Rosa, N. Abbasova, L. Di Palma, Titanium Dioxide Nanoparticles Doped with Iron for Water Treatment via Photocatalysis: A Review, *Nanomaterials* 14 (2024) 293.
- [79] C.V. Mabaso, First-principles study of Hematite (α -Fe₂O₃) surface structures doped with Copper (Cu), Titanium (Ti), nickel (Ni) and manganese (Mn), PhD Thesis, 2023. <https://univendspace.univen.ac.za/handle/11602/2479> (accessed August 19, 2024).
- [80] M. Zhang, C. Yang, Z. Zhang, W. Tian, B. Hui, J. Zhang, K. Zhang, Tungsten oxide polymorphs and their multifunctional applications, *Advances in Colloid and Interface Science* 300 (2022) 102596.
- [81] M.R. Bindhu, K. Ancy, M. Umadevi, G.A. Esmail, N.A. Al-Dhabi, M.V. Arasu, Synthesis and characterization of zinc oxide nanostructures and its assessment on enhanced bacterial inhibition and photocatalytic degradation, *Journal of Photochemistry and Photobiology B: Biology* 210 (2020) 111965.
- [82] D. Singh, K.M. Batoo, S. Hussain, A. Kumar, Q.H. Aziz, F.S. Sheri, H. Tariq, P. Singh, Enhancement of the photocatalytic activity of rGO/NiO/Ag nanocomposite for degradation of methylene blue dye, *RSC Advances* 14 (2024) 2429–2438.
- [83] M. Ikram, M.A. Bari, Bismuth Oxyhalides: Synthesis and photocatalytic applications, IOP Publishing, 2024. <https://iopscience.iop.org/book/mono/978-0-7503-5934-4> (accessed August 20, 2024).
- [84] V. Thakur, S. Singh, P. Kumar, S. Rawat, V.C. Srivastava, S.-L. Lo, U.L. Štanger, Photocatalytic behaviors of bismuth-based mixed oxides: Types, fabrication techniques and mineralization mechanism of antibiotics, *Chemical Engineering Journal* (2023) 146100.
- [85] Q. Han, H. Ding, Z. Wang, A Comprehensive Review on Non-Trivalent Bismuth-Based Materials: Structure, Synthesis, and Strategies for Improving Photocatalytic Performance, *Solar RRL* 8 (2024) 2300872. <https://doi.org/10.1002/solr.202300872>.
- [86] Z. Wu, H. Tüysüz, F. Besenbacher, Y. Dai, Y. Xiong, Recent developments in lead-free bismuth-based halide perovskite nanomaterials for heterogeneous photocatalysis under visible light, *Nanoscale* 15 (2023) 5598–5622.

- [87] H. Mai, D. Chen, Y. Tachibana, H. Suzuki, R. Abe, R.A. Caruso, Developing sustainable, high-performance perovskites in photocatalysis: design strategies and applications, *Chemical Society Reviews* 50 (2021) 13692–13729.
- [88] W.F. Yao, H. Wang, X.H. Xu, X.N. Yang, Y. Zhang, J.T. Zhou, Y.H. Liu, S.X. Shang, M. Wang, Photocatalytic property of Zn-doped Bi₁₂TiO₂₀, *Journal of Materials Science Letters* 22 (2003). <https://search.ebscohost.com/login.aspx?direct=true&profile=ehost&scope=site&authtype=crawler&jrnl=02618028&asa=N&AN=16693546&h=fhTgeK%2FKIkY8wYbtHzkjq4vxfRcI2e7uK3ObN8hRy9ce3onCvFvTD%2BJpy07KMKzN136x0MiMOd5Oj6vdi3uTpQ%3D%3D&crl=c> (accessed August 20, 2024).
- [89] O. Baaloudj, H. Kenfoud, A.K. Badawi, A.A. Assadi, A. El Jery, A.A. Assadi, A. Amrane, Bismuth sillenite crystals as recent photocatalysts for water treatment and energy generation: A critical review, *Catalysts* 12 (2022) 500.
- [90] A. Rahman, M.M. Khan, Chalcogenides as photocatalysts, *New Journal of Chemistry* 45 (2021) 19622–19635.
- [91] D. Karmakar, S. Karmakar, A. Ghosh, D. Jana, A Comparative Overview of the Recent Progress of Some Novel Metal Oxide and sulfide Nanomaterials-Based Photocatalyst, *Materials Today Communications* (2024) 110115.
- [92] Y.-Z. Chen, W.-H. Li, L. Li, L.-N. Wang, Progress in organic photocatalysts, *Rare Met.* 37 (2018) 1–12. <https://doi.org/10.1007/s12598-017-0953-2>.
- [93] Q. Wang, J. Hui, J. Li, Y. Cai, S. Yin, F. Wang, B. Su, Photodegradation of methyl orange with PANI-modified BiOCl photocatalyst under visible light irradiation, *Applied Surface Science* 283 (2013) 577–583.
- [94] M. Minella, F. Sordello, C. Minero, Graphitic carbon nitride-based metal-free photocatalyst, in: *Materials Science in Photocatalysis*, Elsevier, 2021: pp. 449–484. <https://www.sciencedirect.com/science/article/pii/B9780128218594000258> (accessed August 20, 2024).
- [95] A. Aljuaid, M. Almeahmadi, A.A. Alsaiani, M. Allahyani, O. Abdulaziz, A. Alsharif, J.A. Alsaiani, M. Saih, R.T. Alotaibi, I. Khan, g-C₃N₄ based photocatalyst for the efficient photodegradation of toxic methyl orange dye: Recent modifications and future perspectives, *Molecules* 28 (2023) 3199.
- [96] A. Zheng, S. Xie, K. Li, C. Zhang, H. Shi, Performance and mechanism investigation on the enhanced photocatalytic removal of atrazine on S-doped g-C₃N₄, *Chemosphere* 347 (2024) 140663.

- [97] R. Ameta, S.C. Ameta, Photocatalysis: principles and applications, Crc Press, 2016. <https://www.taylorfrancis.com/books/mono/10.1201/9781315372396/photocatalysis-suresh-ameta-rakshit-ameta> (accessed August 20, 2024).
- [98] B. Rani, A.K. Nayak, N.K. Sahu, Fundamentals principle of photocatalysis, in: Nanostructured Materials for Visible Light Photocatalysis, Elsevier, 2022: pp. 1–22. <https://www.sciencedirect.com/science/article/pii/B9780128230183000099> (accessed August 20, 2024).
- [99] A.G. Variar, M.S. Ramyashree, V.U. Ail, K. Sudhakar, M. Tahir, Influence of various operational parameters in enhancing photocatalytic reduction efficiency of carbon dioxide in a photoreactor: A review, *Journal of Industrial and Engineering Chemistry* 99 (2021) 19–47.
- [100] A.S. Soares, F.P. Araujo, R. França, J.A. Osajima, Y. Guerra, S. Castro-Lopes, E.C. Silva-Filho, F.E. Santos, L.C. Almeida, B.C. Viana, R.R. Peña-Garcia, Effect of pH on the growth and ibuprofen photocatalytic response of $Zn_{1-x}Co_xO$ compound synthesized by the co-precipitation method, *Journal of Materials Research* 38 (2023) 2439–2452. <https://doi.org/10.1557/s43578-023-00980-4>.
- [101] O. Sacco, V. Vaiano, D. Sannino, Main parameters influencing the design of photocatalytic reactors for wastewater treatment: a mini review, *J of Chemical Tech & Biotech* 95 (2020) 2608–2618. <https://doi.org/10.1002/jctb.6488>.
- [102] A. Gnanaprakasam, V.M. Sivakumar, M. Thirumarimurugan, Influencing Parameters in the Photocatalytic Degradation of Organic Effluent via Nanometal Oxide Catalyst: A Review, *Indian Journal of Materials Science* 2015 (2015) 1–16. <https://doi.org/10.1155/2015/601827>.
- [103] M. Salehi, H. Hashemipour, M. Mirzaee, Experimental study of influencing factors and kinetics in catalytic removal of methylene blue with TiO_2 nanopowder, *American Journal of Environmental Engineering* 2 (2012) 1–7.
- [104] Y. Li, S. Sun, M. Ma, Y. Ouyang, W. Yan, Kinetic study and model of the photocatalytic degradation of rhodamine B (RhB) by a TiO_2 -coated activated carbon catalyst: Effects of initial RhB content, light intensity and TiO_2 content in the catalyst, *Chemical Engineering Journal* 142 (2008) 147–155.
- [105] D. Kiani, I.E. Wachs, The Conundrum of “Pair Sites” in Langmuir–Hinshelwood Reaction Kinetics in Heterogeneous Catalysis, *ACS Catalysis* 14 (2024) 10260–10270.



Chapter II

Synthesis and Characterization

Methods of materials: Theoretical approach

Chapter II. Synthesis and Characterization Methods of materials: Theoretical approach

II.1. Introduction

This chapter provides a theoretical overview of the methods for synthesizing and characterizing nanoparticles, which are crucial for their application in various scientific and industrial fields. Nanoparticles are noted for their unique properties, making their understanding essential for optimizing their performance. We will first discuss the main synthesis methods, including Sol-Gel, Chemical Vapor Deposition (CVD), Hydrothermal synthesis, Sonochemical methods, Laser Ablation, and Flame Spray Pyrolysis (FSP), highlighting their advantages, disadvantages, and typical applications. Next, the chapter will explore green synthesis, which uses biological sources to produce nanoparticles, addressing its environmental benefits and limitations. Finally, we will cover characterization techniques necessary for analyzing morphological, crystalline, and optical properties.

Overall, this chapter provides a theoretical foundation for understanding nanoparticle synthesis and characterization methods, setting the stage for practical applications and future research.

II.2. Traditional Synthesis Methods for Nanomaterials

The synthesis of nanomaterials is a continuously evolving field, offering numerous applications in various sectors. Many methods have been developed to produce these materials at the nanoscale, each with its specific advantages and disadvantages. Let's take a closer look at the most common traditional synthesis methods:

II.2.1. Sol-Gel Synthesis

Sol-gel synthesis is a versatile and relatively simple method for producing a wide range of nanomaterials [1]. It involves the formation of a gel from liquid precursors, followed by a drying and calcination process. Nanomaterials produced via this method have applications in areas such as catalysis, biomedicine, and construction materials. Although this method is versatile, it has drawbacks related to the use of organic solvents and may require relatively long drying times [2].

II.2.2. Chemical Vapor Deposition (CVD)

CVD is a powerful technique for producing thin films and high-purity nanostructures. It involves the reaction of gaseous precursors on a heated surface. CVD is widely used for the fabrication of

electronic materials, such as graphene and carbon nanotubes. However, this method requires specialized equipment and can be energy intensive [3].

II.2.3. Hydrothermal Synthesis

Hydrothermal synthesis is a gentle and efficient method for producing crystalline nanomaterials. It involves heating precursors in an autoclave filled with a solvent, usually water. This method is particularly well-suited for the synthesis of porous-structured materials, such as zeolites and microporous materials [4].

II.2.4. Sonochemical Synthesis

Sonochemistry harnesses the energy of ultrasound to induce chemical reactions and form cavitation bubbles. These bubbles, when they collapse, create extreme temperature conditions and pressure, promoting the formation of nanomaterials. This method is fast and simple to implement, but it can be limited by difficulties in controlling particle size and distribution [5].

II.2.5. Laser Ablation

Laser ablation is an advanced technique for producing high-purity nanoparticles with controlled morphology. It involves irradiating a target material with a pulsed laser, which leads to the ablation of material in the form of plasma. This plasma then condenses into nanoparticles. This method is used for the production of metallic nanoparticles and composite materials [6].

II.2.6. Flame Spray Pyrolysis (FSP)

FSP is a high-temperature synthesis method that allows the continuous production of large quantities of nanoparticles. It involves injecting a liquid precursor into a flame, where it decomposes and forms nanoparticles. This method is particularly suitable for producing catalytic materials and pigments [7].

Table II.1: Overview of Synthesis Methods: Advantages, Disadvantages, and Typical Application.

Method	Advantages	Disadvantages	Typical Applications
Sol-Gel	Versatility, low cost	Drying time, use of solvents	Catalysis, biomaterials, construction materials
CVD	High purity, precise control	Specialized equipment, energy-intensive	Electronics, 2D nanomaterials

Hydrothermal	Gentle conditions, porous materials	Autoclaves, reaction times	Porous materials, zeolites
Sonochemical	Fast, simple	Limited particle size control	Catalysis, composite materials
Laser Ablation	High purity, morphology control	High cost, specialized equipment	Metallic nanoparticles, composite materials
FSP	Large-scale production, high temperature	Pollutant emissions	Catalysis, pigments

II.3. Green synthesis

Recent advancements have focused on developing cost-effective, fast, efficient, and environmentally friendly methods for nanoparticle synthesis, using plant extracts, microorganisms (bacteria, fungi, and algae), enzymes, and biomolecules [8]. Green synthesis is an eco-friendly biorreduction process where biological molecules, such as proteins, enzymes, phenolic compounds, amines, and alkaloids, act as reducing and stabilizing agents, facilitating the transformation of metal ions into nanoparticles [9].

To address the limitations of traditional methods, green synthesis approaches are gaining attention in material science and technology research. These methods emphasize minimizing waste, reducing pollution, and utilizing safer, non-toxic solvents and renewable raw materials [10]. The core principles of green synthesis aim to prevent the production of harmful byproducts by promoting sustainable and environmentally responsible procedures.

Among the various green synthesis routes, plant extract-mediated synthesis offers a simple, scalable method for producing metal oxide nanoparticles compared to bacteria or fungi-mediated processes [11]. This approach allows for the large-scale production of biogenic nanoparticles, which are synthesized through natural biological processes and contribute to more sustainable nanomaterial development.

II.3.1. Biological Sources for the Green Synthesis of Nanoparticles

Traditional physical and chemical methods for the synthesis of metallic nanoparticles require high energy consumption and the use of highly toxic reducing and stabilizing agents, which have

harmful effects on humans and marine life. In contrast, green synthesis offers a low-cost, eco-friendly, one-step approach that initiates reactions with low energy input. The biological routes for synthesizing metallic and metal oxide nanoparticles focus on using reducing agents such as bacteria, fungi, yeast, algae, and plant extracts, which are considered biocompatible and suitable for large-scale production.

a. Bacteria-Mediated Nanoparticle Generation

Bacterial species have been extensively studied in commercial biotechnological applications, including bioremediation, bioleaching, and genetic engineering, due to their relatively easy manipulation. It has been found that bacteria are good candidates for preparing metallic and novel nanoparticles [12]. In particular, prokaryotes and actinomycetes have been widely used to synthesize metal and metal oxide nanoparticles. Certain bacteria with specific shapes and sizes, such as *Bacillus cereus*, *Lactobacillus casei*, *Aeromonas species*, *Pseudomonas proteolytica*, *Escherichia coli*, etc., can be used to synthesize silver-based nanomaterials through biological reduction. Additionally, other bacterial agents such as *Shewanella alga*, *Bacillus subtilis* 168, *Plectonema boryanum* UTEX 485, and *Rhodopseudomonas capsulata* have been applied for the synthesis of gold nanoparticles [13].

b. Fungi-Mediated Nanoparticle Generation

Biosynthesis of metallic and metal oxide nanoparticles using fungal species is considered an efficient method for producing monodispersed nanoparticles with appropriate morphologies [14]. Compared to other organisms, fungi are better biological agents for synthesizing nanoparticles (such as silver and gold) due to their intracellular enzymes, proteins, and reducing components on their cell surface. Fungi also have the ability to produce a larger number of nanoparticles compared to bacteria. The mechanism of metal nanoparticle formation can be explained by enzymatic reduction within fungal cells or their cell walls. The use of fungal extracts for nanoparticle synthesis has several advantages over bacterial extracts. They are economically viable, enable large-scale production, are easy to extract, eco-friendly, and possess a large surface area. Moreover, they serve as a good source of metabolites and enzymes that can reduce bulk salts into elemental ions, which are essential for nanoparticle synthesis [15].

c. Yeast-Mediated Nanoparticle Generation

Yeasts are unicellular microorganisms within eukaryotic cells, with only 1,500 species identified so far. Numerous studies have focused on synthesizing nanoparticles and nanostructures using various yeast species, which can produce reducing enzymes intracellularly or extracellularly. For example, gold and silver nanoparticles have been synthesized using a silver-tolerant yeast strain and *Saccharomyces cerevisiae* broth [16].

d. Algae-Mediated Nanoparticle Generation

Algae are rarely used as biofactories for synthesizing metallic nanoparticles. For the first time, extracellular gold nanoparticles with high stability were produced using marine algae (*Sargassum wightii*). Additionally, the green synthesis of palladium and platinum nanoparticles has been reported using their salts containing metal chlorides. The green synthesis of three metal oxide nanoparticles, namely copper oxide, ferric oxide, and zinc oxide has also been investigated using marine algae [17].

e. Plant-Mediated Nanoparticle Generation

Among biological components, plants have attracted significant attention for the synthesis of nanoparticles. Their excellent properties include low cost, stability, simplicity, safety in handling, low energy consumption, reduced use of toxic chemicals, rapid reaction times, and a wide range of biomolecules [18]. Typically, plants have excellent potential to reduce metallic salts into nanoparticles due to certain biomolecules such as carbohydrates, proteins, and coenzymes. Various parts of plants also have the ability to accumulate heavy metals. Additionally, plant extracts can control the synthesis of nanoparticles to obtain well-defined morphologies and sizes in just one step with high yield [19]. As a result, great attention has been given to the biosynthesis of nanoparticles using various plant parts such as leaves, roots, flowers, and fruits as an easy, efficient, cost-effective, and alternative method to traditional production processes [20]. Gold and silver were the first biosynthesized nanoparticles using plant extracts.

II.3.2. Benefits and limitations of green synthesis

The green synthesis of nanoparticles has become a crucial approach in nanotechnology, relying on eco-friendly processes that use biological resources. Below are the benefits and limitations of this method.

Table II.2. Advantages and Disadvantages of Green Nanomaterial Synthesis.

Advantages	Disadvantages
Environmental Benefits	Polydispersity
Reduction of pollution and waste	Variability in the size and shape of nanoparticles produced.
Cost-Effectiveness	Longer Reaction Times
Utilization of readily available natural resources	Synthesis methods may require more time than traditional methods.
Biocompatibility	Limited Control Over Synthesis Parameters
Suitable for medical and pharmaceutical applications.	Difficult to achieve precise control over the size, shape, and crystallinity of nanoparticles.
Simplicity and Efficiency	Raw Material Availability
Processes are often one-step, facilitating production.	Availability of certain biological resources may be limited.
Diverse Applications	Scalability Issues
Utilization in medicine, agriculture, and environmental applications.	Scaling up processes for industrial applications can present challenges.

II.4. Characterization techniques

II.4.1. Fourier Transform Infrared (FTIR)

Fourier Transform Infrared (FTIR) spectroscopy is a technique employed to study the structure and composition of materials. A typical FTIR system consists of two distinct beams originating from the IR source, passing through both the sample and reference chambers. In the optical chopper, the reference and sample channels are combined [21].

To perform an analytical comparison of the transmitted photon beam data, one beam passes through the sample, while the other passes through a specific reference sample. After interaction with the sample, the radiation passes through, and the wavefront is dispersed across the instrument's frequencies using gratings and slits. The slit size influences the system's performance: narrower slits enhance resolution and frequency discrimination, while wider slits allow lighter to reach the detector, thereby increasing the system's sensitivity.

The detector receives an electrical signal emitted by the wavefront, which is subsequently processed by a computer using a mathematical algorithm to generate the final spectrum. An Agilent Technologies Fourier Transform Infrared (FTIR) spectrophotometer was used for recording the infrared spectra, operated by a microcomputer. Spectral data were collected in the range of 4500 to 400 cm^{-1} [22, 23].

II.4.2. X-Ray Diffraction (XRD)

X-ray diffraction (XRD) is employed to identify the crystalline phases present in a solid. Several successive crystal lattices are necessary to form visible diffraction peaks [24]. The analysis is based on Bragg's Law:

$$n \cdot \lambda = 2d \sin \theta \quad (\text{II.1})$$

where:

- n is the diffraction order,
- λ is the wavelength of the X-ray radiation used (1.5418 Å),
- d is the interplanar spacing (Å),
- θ is the diffraction angle.

X-rays are produced when electrons, emitted from a heated cathode and accelerated by an electric field, strike a metal anode (anticathode). The resulting data is presented as diffractograms, which plot the intensity of diffracted photons as a function of 2θ [25]. This method allows the identification of the crystal structure and phase of materials using ASTM (American Society for Testing Materials) tables or JCPDS (Joint Committee on Powder Diffraction Standards) files. It can also provide information on grain size and orientation, with each crystalline phase corresponding to a characteristic set of diffraction peaks [26]. X-ray powder diffraction is further useful for verifying the purity of prepared phases and determining structural characteristics such as dimensionality, disorder, and lattice parameters. The crystallite size, D , can be calculated using the Scherrer equation:

$$D = \frac{K\lambda}{\beta \cos(\theta)} \quad (\text{II.2})$$

where:

- D is the particle size (nm),
- λ is the X-ray wavelength,
- β is the full width at half maximum (FWHM) of the diffraction peak.

This technique provides a comprehensive analysis of crystalline materials, crucial for understanding their structural properties [27].

II.4.3. Scanning Electron Microscopy (SEM)

The mechanism of Scanning Electron Microscopy (SEM) involves directing a primary electron beam onto the surface of a sample for analysis. The SEM technique enables the observation of the microscopic texture of materials by scanning the surface with a focused beam of accelerated electrons. As the electron beam interacts with the sample surface, secondary electrons are emitted and collected by detectors. The data is then transmitted to a cathode-ray screen, where the scan pattern matches that of the incident electron beam, allowing for the visualization of the sample's surface[28].

In solid phases, SEM reveals the presence of voids, as well as variations in shape and size. This technique is particularly useful in the analysis of monophase catalysts, where it helps monitor the consistency of preparation methods and assess the distribution and frequency of various elements [29].

The interaction of electrons within the material forms a so-called "interaction volume" or "pear-shaped region," which generates various signals. These signals can be used to create high-resolution images or to perform quantitative analysis of the sample's composition. Additionally, the electron beam penetrates the crystalline structure depending on the angle of incidence, providing detailed information on different families of crystalline planes [30].

SEM thus plays a crucial role in the morphological analysis and characterization of materials, especially in the field of catalyst study and preparation [31].

II.4.4. Transmission Electron Microscopy (TEM)

Transmission Electron Microscopy (TEM) utilizes a beam of electrons to produce high-resolution images, allowing for the observation of the internal structure of materials at the nanometric scale. Unlike Scanning Electron Microscopy (SEM), where electrons primarily interact with the surface of the sample, TEM enables the electron beam to pass through the sample, providing detailed information about its internal structure [32].

In TEM, a beam of electrons is transmitted through an extremely thin sample (typically on the order of a few nanometers). The electrons that pass through the sample interact with the atoms, experiencing scattering or absorption depending on the density and thickness of the material. The transmitted electrons are then projected onto a fluorescent screen or detector, generating an enlarged image of the sample [33].

II.4.5. Energy Dispersive X-ray Spectroscopy (EDX)

Energy Dispersive X-ray Spectroscopy (EDX) is an analytical technique used for both qualitative and quantitative analysis of materials. Commonly integrated with Scanning Electron Microscopy (SEM) and Transmission Electron Microscopy (TEM), EDX allows for the identification and measurement of the elemental composition of a sample's surface. When the sample is bombarded with a focused beam of electrons, it emits characteristic X-rays from the atoms present, which are detected and analyzed to determine the elements within the material. This method provides valuable insights into the distribution and concentration of elements across the sample, making it a key tool in material science for compositional analysis [34].

II.4.6. Elemental Mapping

Elemental Mapping is an advanced analytical technique used to visualize the spatial distribution of elements across the surface of a material. Often performed in conjunction with Scanning Electron Microscopy (SEM) or Transmission Electron Microscopy (TEM), this method allows for a detailed analysis of the elemental composition at specific locations [35]. By scanning the sample with a focused electron beam, characteristic X-rays emitted from the material are detected and mapped. This produces images that display the concentration and distribution of elements in different regions, providing valuable information on the material's homogeneity, phase distribution, and potential impurities. Elemental Mapping is widely used in material

science, metallurgy, and nanotechnology to study complex systems and improve material design [36].

II.4.7. UV-Visible (UV-Vis)

UV-Visible (UV-Vis) spectrophotometry is a widely used analytical technique to investigate the optical properties of solid materials, particularly semiconductors. It is crucial for determining parameters such as the band gap and the absorption coefficient [37]. The method involves illuminating a sample with monochromatic light, which generates both reflected and diffusely scattered rays [38]. The scattered rays are captured by an integrating sphere and directed unidirectionally to a detector, while the reflected rays are canceled out. The diffuse reflectance theory, developed by Kubelka and Munk in 1931, relates diffuse reflectance to absorption via the following equation [39]:

$$\frac{k}{S} = \frac{(1-R)^2}{2R} \quad (\text{II.3})$$

where k is the absorption coefficient, S is the scattering coefficient, and R is the diffuse reflectance. This approach also allows for the calculation of the band gap energy (E_g) using the relation:

$$(\alpha h\nu)^n = A(h\nu - E_g) \quad (\text{II.4})$$

where h is Planck's constant, ν is the frequency (c/λ), E_g is the band gap energy, and n indicates the nature of the optical transition ($n = 2$ for a direct transition and $n = 1/2$ for an indirect transition). In a UV-Vis spectrophotometer, light typically within the 200–1000 nm range passes through a sample, and the absorption depends on factors such as sample concentration, path length, and the sample's absorption efficiency at a specific wavelength. This absorption phenomenon induces electronic transitions from ground to excited states, making UV-Vis spectroscopy a powerful tool for both qualitative and quantitative chemical analysis, as well as for studying the electronic structure and optical properties of materials [40].

II.4.8. The photoluminescence (PL)

The photoluminescence (PL) characterization technique allows for the analysis of the optical and electronic properties of photocatalysts. It involves the excitation of a material by a light source, typically in the ultraviolet or visible range, causing the migration of electrons from the valence

band to the conduction band. When these electrons recombine with holes in the valence band, the material emits light, a phenomenon known as photoluminescence. By studying PL, one can gain a deeper understanding of the charge carrier recombination mechanisms in photocatalysts [41]. Low-intensity photoluminescence indicates good separation of electrons and holes, which is advantageous for photocatalytic applications, as it implies greater availability of electrons for photocatalytic reactions. Conversely, high-intensity PL suggests rapid electron-hole recombination, which can limit the efficiency of the photocatalyst. Therefore, PL plays a crucial role in evaluating the efficiency of photocatalysts and optimizing their performance for applications such as pollutant degradation and hydrogen production [42].

II.5. Protocol for Photocatalytic Degradation Experiments in a Batch Reactor

Photocatalytic degradation experiments were conducted at room temperature using a batch reactor. The reactor was equipped with two types of lamps, positioned horizontally on either side of the reactor box:

- **UV Lamps:** Philips UV PL-L 24W lamps emitting a peak wavelength at 253.7 nm.
- **Visible Lamps:** 300 W LED visible light lamps.

The lamps were placed 5 cm above a graduated cylinder containing the solution to be treated. The aqueous solution contained a model dye, either Methylene Blue (MB) or the industrial dye BS. Before irradiation, the suspension of the photocatalyst in the solution was stirred in the dark for 40 minutes to achieve adsorption-desorption equilibrium.

Once the equilibrium was reached, the lamps were switched on, and 1 mL of the suspension was sampled every 20 minutes, diluted ($\times 3$), and immediately centrifuged to separate the photocatalyst from the solution. The remaining solution was then analyzed using UV-Vis spectroscopy to determine the residual concentration of the dye.

All experiments were conducted in duplicate to ensure photocatalyst stability and reproducibility. The color removal efficiency was calculated using the following formula:

$$\text{Color removal efficiency (\%)} = \frac{C_0 - C_e}{C_0} \times 100 \quad (\text{II.5})$$

where C_0 is the initial dye concentration and C_e is the residual concentration at time t

The reaction kinetics of photocatalytic degradation were investigated using the Langmuir-Hinshelwood model:

$$-\ln (C/C_0) = kt \quad (\text{II.6})$$

where C_0 is the initial concentration, C is the concentration at time t , and k is the apparent kinetic constant.

The reactor was enclosed in a black box to prevent interference from external light sources, ensuring controlled irradiation conditions.

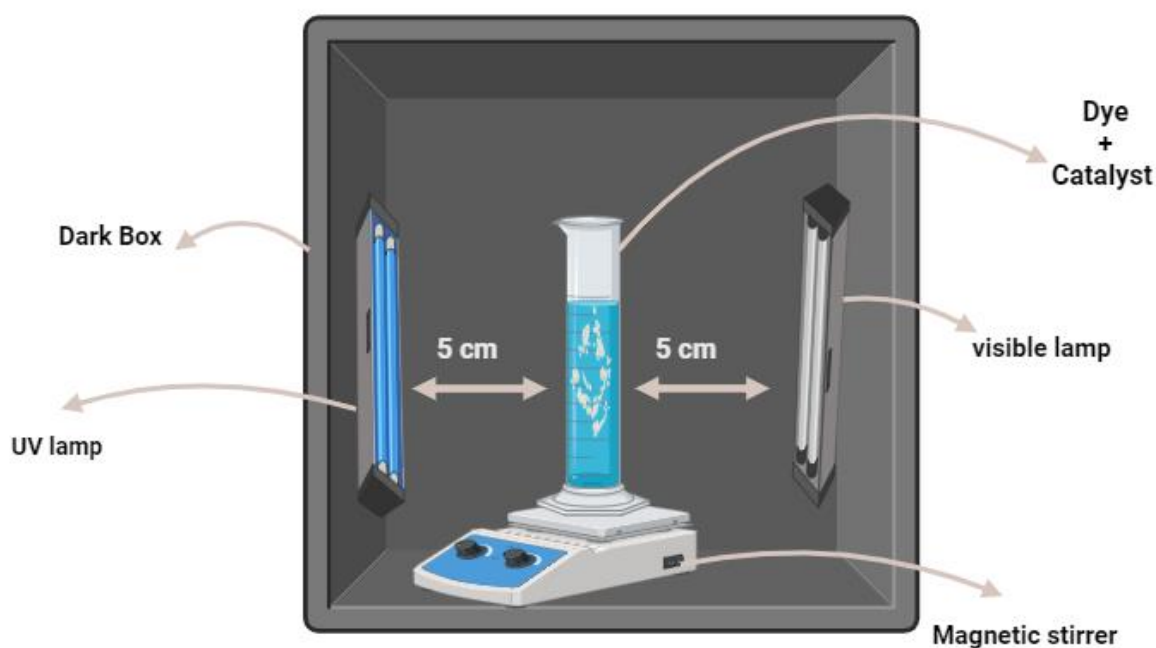


Figure II.1: Batch photocatalytic reactor for Dye degradation.

II.6. Determining the Role of Reactive Species in Photocatalytic Degradation through Scavenger Trapping Experiments

To assess the role of reactive species in photocatalytic degradation, trapping experiments are typically conducted using various scavengers. These scavengers help identify the key reactive

species involved in the degradation process. Hydroxyl radicals (OH) are often targeted using ethanol [43], which effectively neutralizes them, providing insights into their contribution. Electrons (e^-) are captured using potassium dichromate ($K_2Cr_2O_7$) [44], allowing for the determination of their role in the photocatalytic reaction. Disodium ethylenediaminetetraacetate (Na_2 -EDTA) is commonly used to scavenge holes (h^+) [45], revealing the importance of these positively charged species in the degradation mechanism.

References

- [1] D. Navas, S. Fuentes, A. Castro-Alvarez, E. Chavez-Angel, Review on sol-gel synthesis of perovskite and oxide nanomaterials, *Gels* 7 (2021) 275.
- [2] M. Niederberger, Nonaqueous Sol–Gel Routes to Metal Oxide Nanoparticles, *Acc. Chem. Res.* 40 (2007) 793–800. <https://doi.org/10.1021/ar600035e>.
- [3] K. Hachem, M.J. Ansari, R.O. Saleh, H.H. Kzar, M.E. Al-Gazally, U.S. Altimari, S.A. Hussein, H.T. Mohammed, A.T. Hammid, E. Kianfar, Methods of chemical synthesis in the synthesis of nanomaterial and nanoparticles by the chemical deposition method: a review, *BioNanoScience* 12 (2022) 1032–1057.
- [4] Y.X. Gan, A.H. Jayatissa, Z. Yu, X. Chen, M. Li, Hydrothermal synthesis of nanomaterials, *Journal of Nanomaterials* 2020 (2020). <https://search.proquest.com/openview/0b5dac961163c6a8a3841ed8ce470525/1?pq-origsite=gscholar&cbl=237784> (accessed September 6, 2024).
- [5] H. Jiao, Q. Mao, N. Razzaq, R. Ankri, J. Cui, Ultrasound technology assisted colloidal nanocrystal synthesis and biomedical applications, *Ultrasonics Sonochemistry* 103 (2024) 106798.
- [6] M. Kim, S. Osone, T. Kim, H. Higashi, T. Seto, Synthesis of nanoparticles by laser ablation: A review, *KONA Powder and Particle Journal* 34 (2017) 80–90.
- [7] C. Dimitriou, P. Psathas, M. Solakidou, Y. Deligiannakis, Advanced Flame Spray Pyrolysis (FSP) Technologies for Engineering Multifunctional Nanostructures and Nanodevices, *Nanomaterials* 13 (2023) 3006.
- [8] G. Pal, P. Rai, A. Pandey, Green synthesis of nanoparticles: A greener approach for a cleaner future, in: *Green Synthesis, Characterization and Applications of Nanoparticles*, Elsevier, 2019: pp. 1–26. <https://www.sciencedirect.com/science/article/pii/B9780081025796000010> (accessed September 6, 2024).
- [9] P. Bhardwaj, B. Singh, S.P. Behera, Green approaches for nanoparticle synthesis: emerging trends, *Nanomaterials* (2021) 167–193.
- [10] Х.С. Сэмуэль, Э.Э. Этим, У. Нвеке-Мараизу, Ш. Якубу, Advancements in green chemistry: sustainable synthesis and processes, *Журнал Белорусского Государственного Университета. Химия* (2024) 3–16.

- [11] J. Jeevanandam, S.F. Kiew, S. Boakye-Ansah, S.Y. Lau, A. Barhoum, M.K. Danquah, J. Rodrigues, Green approaches for the synthesis of metal and metal oxide nanoparticles using microbial and plant extracts, *Nanoscale* 14 (2022) 2534–2571.
- [12] B. Koul, A.K. Poonia, D. Yadav, J.-O. Jin, Microbe-mediated biosynthesis of nanoparticles: Applications and future prospects, *Biomolecules* 11 (2021) 886.
- [13] S. Agrawal, M. Kuchlan, J. Panwar, M. Sharma, Bacterial synthesis of metallic nanoparticles: current trends and potential applications as soil fertilizer and plant protectants, *Nanoscale Engineering in Agricultural Management* (2019) 30–63.
- [14] R.A. de Jesus, G.C. de Assis, R.J. de Oliveira, J.A.S. Costa, C.M.P. da Silva, H.M. Iqbal, L.F.R. Ferreira, Metal/metal oxide nanoparticles: A revolution in the biosynthesis and medical applications, *Nano-Structures & Nano-Objects* 37 (2024) 101071.
- [15] F. Xu, Y. Li, X. Zhao, G. Liu, B. Pang, N. Liao, H. Li, J. Shi, Diversity of fungus-mediated synthesis of gold nanoparticles: properties, mechanisms, challenges, and solving methods, *Critical Reviews in Biotechnology* 44 (2024) 924–940. <https://doi.org/10.1080/07388551.2023.2225131>.
- [16] S.A. Khan, C.-S. Lee, Green Biological Synthesis of Nanoparticles and Their Biomedical Applications, in: Inamuddin, A.M. Asiri (Eds.), *Applications of Nanotechnology for Green Synthesis*, Springer International Publishing, Cham, 2020: pp. 247–280. https://doi.org/10.1007/978-3-030-44176-0_10.
- [17] A.K. Shukla, A.K. Upadhyay, L. Singh, Algae-Mediated Biological Synthesis of Nanoparticles: Applications and Prospects, in: S.K. Mandotra, A.K. Upadhyay, A.S. Ahluwalia (Eds.), *Algae*, Springer Singapore, Singapore, 2021: pp. 325–338. https://doi.org/10.1007/978-981-15-7518-1_14.
- [18] J.O. Adeyemi, A.O. Oriola, D.C. Onwudiwe, A.O. Oyediji, Plant extracts mediated metal-based nanoparticles: synthesis and biological applications, *Biomolecules* 12 (2022) 627.
- [19] K. Vijayaraghavan, T. Ashokkumar, Plant-mediated biosynthesis of metallic nanoparticles: A review of literature, factors affecting synthesis, characterization techniques and applications, *Journal of Environmental Chemical Engineering* 5 (2017) 4866–4883.
- [20] A.M.E. Shafey, Green synthesis of metal and metal oxide nanoparticles from plant leaf extracts and their applications: A review, *Green Processing and Synthesis* 9 (2020) 304–339. <https://doi.org/10.1515/gps-2020-0031>.

- [21] C. Berthomieu, R. Hienerwadel, Fourier transform infrared (FTIR) spectroscopy, *Photosynth Res* 101 (2009) 157–170. <https://doi.org/10.1007/s11120-009-9439-x>.
- [22] M.A. Mohamed, J. Jaafar, A.F. Ismail, M.H.D. Othman, M.A. Rahman, Fourier transform infrared (FTIR) spectroscopy, in: *Membrane Characterization*, Elsevier, 2017: pp. 3–29. <https://www.sciencedirect.com/science/article/pii/B9780444637765000012> (accessed September 6, 2024).
- [23] C.-P.S. Hsu, Infrared spectroscopy, *Handbook of Instrumental Techniques for Analytical Chemistry* 249 (1997). https://diverdi.colostate.edu/all_courses/handbook%20of%20instrumental%20techniques%20for%20analysis/ch15.pdf (accessed October 15, 2024).
- [24] C.F. Holder, R.E. Schaak, Tutorial on Powder X-ray Diffraction for Characterizing Nanoscale Materials, *ACS Nano* 13 (2019) 7359–7365. <https://doi.org/10.1021/acsnano.9b05157>.
- [25] J. Epp, X-ray diffraction (XRD) techniques for materials characterization, in: *Materials Characterization Using Nondestructive Evaluation (NDE) Methods*, Elsevier, 2016: pp. 81–124. <https://www.sciencedirect.com/science/article/pii/B9780081000403000043> (accessed September 6, 2024).
- [26] W. Wong-Ng, H.F. McMurdie, C.R. Hubbard, A.D. Mighell, JCPDS-ICDD research associateship (cooperative program with NBS/NIST), *Journal of Research of the National Institute of Standards and Technology* 106 (2001) 1013.
- [27] L.S. Zevin, G. Kimmel, *Quantitative X-ray diffractometry*, Springer Science & Business Media, 2012. https://books.google.com/books?hl=fr&lr=&id=0XfrBwAAQBAJ&oi=fnd&pg=PR5&dq=X-Ray+Diffractometry&ots=CIruuN_cJK&sig=5HZqLCquS8TmVLXnCV6olJTSbCE (accessed October 15, 2024).
- [28] K. Akhtar, S.A. Khan, S.B. Khan, A.M. Asiri, *Scanning Electron Microscopy: Principle and Applications in Nanomaterials Characterization*, in: S.K. Sharma (Ed.), *Handbook of Materials Characterization*, Springer International Publishing, Cham, 2018: pp. 113–145. https://doi.org/10.1007/978-3-319-92955-2_4.
- [29] N.G. Yadav, N. Folastre, M. Bolmont, A. Jamali, M. Morcrette, C. Davoisne, Study of failure modes in two sulphide-based solid electrolyte all-solid-state batteries via in situ SEM, *Journal of Materials Chemistry A* 10 (2022) 17142–17155.
- [30] B. Hafner, *Scanning electron microscopy primer*, Characterization Facility, University of Minnesota-Twin Cities (2007) 1–29.

- [31] B.Z. Zondo, Synthesis of Carbon Nanotube/gold/iron Oxide Composite for Lead Removal from Wastewater, PhD Thesis, University of Johannesburg, 2022. https://ujcontent.uj.ac.za/view/pdfCoverPage?instCode=27UOJ_INST&filePid=138429570007691&download=true (accessed October 15, 2024).
- [32] D.J. Smith, Characterization of nanomaterials using transmission electron microscopy, (2015). <https://books.rsc.org/books/edited-volume/1940/chapter/2569325> (accessed September 6, 2024).
- [33] D.B. Williams, C.B. Carter, The Transmission Electron Microscope, in: Transmission Electron Microscopy, Springer US, Boston, MA, 1996: pp. 3–17. https://doi.org/10.1007/978-1-4757-2519-3_1.
- [34] M. Abd Mutalib, M.A. Rahman, M.H.D. Othman, A.F. Ismail, J. Jaafar, Scanning electron microscopy (SEM) and energy-dispersive X-ray (EDX) spectroscopy, in: Membrane Characterization, Elsevier, 2017: pp. 161–179. <https://www.sciencedirect.com/science/article/pii/B9780444637765000097> (accessed September 6, 2024).
- [35] A. Limbeck, L. Brunnbauer, H. Lohninger, P. Pořízka, P. Modlitbová, J. Kaiser, P. Janovszky, A. Kéri, G. Galbács, Methodology and applications of elemental mapping by laser induced breakdown spectroscopy, *Analytica Chimica Acta* 1147 (2021) 72–98.
- [36] J.J. Friel, C.E. Lyman, Tutorial review: X-ray mapping in electron-beam instruments, *Microscopy and Microanalysis* 12 (2006) 2–25.
- [37] M. Picollo, M. Aceto, T. Vitorino, UV-Vis spectroscopy, *Physical Sciences Reviews* 4 (2019) 20180008. <https://doi.org/10.1515/psr-2018-0008>.
- [38] J.Z. Zhang, Optical properties and spectroscopy of nanomaterials, World Scientific, 2009. [https://books.google.com/books?hl=fr&lr=&id=AfLFCgAAQBAJ&oi=fnd&pg=PR7&dq=UV-Visible+\(UV-Vis\)+spectrophotometry+is+a+widely+used+analytical+technique+to+investigate+the+optical+properties+of+solid+materials,+particularly+semiconductors.+It+is+crucial+for+determining+parameters+such+as+the+band+gap+and+the+absorption+coefficient.+&ots=WXIqA1GRz3&sig=OL-bft79ovsVw0GpZKEikwIIFHI](https://books.google.com/books?hl=fr&lr=&id=AfLFCgAAQBAJ&oi=fnd&pg=PR7&dq=UV-Visible+(UV-Vis)+spectrophotometry+is+a+widely+used+analytical+technique+to+investigate+the+optical+properties+of+solid+materials,+particularly+semiconductors.+It+is+crucial+for+determining+parameters+such+as+the+band+gap+and+the+absorption+coefficient.+&ots=WXIqA1GRz3&sig=OL-bft79ovsVw0GpZKEikwIIFHI) (accessed September 6, 2024).
- [39] E.L. Simmons, Diffuse reflectance spectroscopy: a comparison of the theories, *Applied Optics* 14 (1975) 1380–1386.
- [40] H. Förster, UV/vis spectroscopy, *Characterization I: -/-* (2004) 337–426.

- [41] L. Zhang, J. Ran, S.-Z. Qiao, M. Jaroniec, Characterization of semiconductor photocatalysts, *Chemical Society Reviews* 48 (2019) 5184–5206.
- [42] S. Yurdakal, C. Garlisi, L. Özcan, M. Bellardita, G. Palmisano, (Photo) catalyst characterization techniques: adsorption isotherms and BET, SEM, FTIR, UV–Vis, photoluminescence, and electrochemical characterizations, in: *Heterogeneous Photocatalysis*, Elsevier, 2019: pp. 87–152. <https://www.sciencedirect.com/science/article/pii/B9780444640154000043> (accessed September 6, 2024).
- [43] R. Noroozi, M. Gholami, V. Oskoei, M. Hesami Arani, S.A. Mousavifard, B. Nguyen Le, M. Fattahi, Fabrication of new composite NCuTiO₂/CQD for photocatalytic degradation of ciprofloxacin and pharmaceutical wastewater treatment: degradation pathway, toxicity assessment, *Scientific Reports* 13 (2023) 16287.
- [44] N.K. Gupta, Y. Ghaffari, S. Kim, J. Bae, K.S. Kim, M. Saifuddin, Photocatalytic degradation of organic pollutants over MFe₂O₄ (M= Co, Ni, Cu, Zn) nanoparticles at neutral pH, *Scientific Reports* 10 (2020) 4942.
- [45] A. Trenczek-Zajac, M. Synowiec, K. Zakrzewska, K. Zazakowny, K. Kowalski, A. Dziedzic, M. Radecka, Scavenger-Supported Photocatalytic Evidence of an Extended Type I Electronic Structure of the TiO₂@Fe₂O₃ Interface, *ACS Appl. Mater. Interfaces* 14 (2022) 38255–38269. <https://doi.org/10.1021/acsami.2c06404>.



Chapter III

Green Fabrication of ZnO Nanoparticles and ZnO/rGO Nanocomposites from Algerian Date Syrup Extract: Synthesis, Characterization, and Augmented Photocatalytic Efficiency in Methylene Blue Degradation

Chapter III. Green Fabrication of ZnO Nanoparticles and ZnO/rGO Nanocomposites from Algerian Date Syrup Extract: Synthesis, Characterization, and Augmented Photocatalytic Efficiency in Methylene Blue Degradation

III.1. Introduction

The field of photocatalysis research and development has seen substantial growth in recent years as illustrated by the increasing number of publications on this subject matter, mainly due to its potential applications in environmental technologies such as hydrogen production [1], organic synthesis, medicinal chemistry, and water treatment [2].

The emergence of nanotechnology could have a major impact on the field of photocatalysis for the production of new materials, typically semiconductors. One of the most advantages of nanostructures is their ability to exhibit exceptional properties, which can be used to create new photocatalysts or improve existing ones [3]. Furthermore, nanotechnologies enable the development of more efficient and energy-saving photocatalytic systems to address current environmental and energy challenges [4].

It is undoubted that the advancements in nanomaterials synthesis techniques are resulting in the emergence of new materials with desired chemical and physical properties [5]. Nanoparticles can be synthesized using different techniques, which are generally classified into two primary methods. The first approach, known as the bottom-up technique, employs chemical processes such as hydrothermal, co-precipitation, electrochemical, pyrolysis, sonochemical, photochemical, microemulsion, microwave, redox, and sol-gel. These methods involve the combination of individual atoms or molecules to produce nanoparticles [6]. The second method is characterized by a top-down approach, which requires the use of physical techniques, such as laser ablation, inert gas condensation, sonication, electric arc discharge, lithography and the radiofrequency (RF) plasma method. These physical techniques consume a lot of energy and raise the temperature of the surrounding air around the source material since it takes so long for them to achieve thermal stability. Additionally, these methods occupy a large amount of space, especially in the case of furnaces [7]. The chemical processes have undesirable effects on the

environment and are environmentally unfriendly [8] due to the use of harsh reducing agents such as sodium citrate, sodium borohydride, and organic solvents.

Generally, the concept of "Green Synthesis" refers to the application of ecological principles of "green chemistry" such as extract of plants and microorganisms such as fungal, bacteria, and algae to the biosynthesis of nanoparticle oxides, allowing pure and safe nanoparticles to be obtained from different organisms such as fungi, plants, bacteria, and actinomycetes [9]. "Green synthesis" using biomaterials comprises a diverse array of compounds, including proteins, flavonoids and polyphenols, which have the potential to substitute hazardous chemical products as reducing agents, in order to lower the valence state of metal ions. Consequently, it offers many benefits, including biocompatibility, low toxicity, simplified production, improved profitability, and the possibility of regulating the synthesis process [10].

Metallic nanoparticles can be fabricated using extracts from various biological sources, both cellular and cell-free, as illustrated in Figure 1. It is essential to ensure that the nanoparticle synthesis process aligns with the principles of green chemistry [11]. This involves meticulous consideration of factors such as the choice of environmentally friendly solvents, the use of eco-friendly reducing agents, and the selection of non-toxic materials for nanoparticle stabilization. Furthermore, it has been established that compounds like peptides, polyphenolics, sugars, vitamins, and aqueous components derived from plant extracts demonstrate compatibility and efficacy in the synthesis of nanoparticles [12].

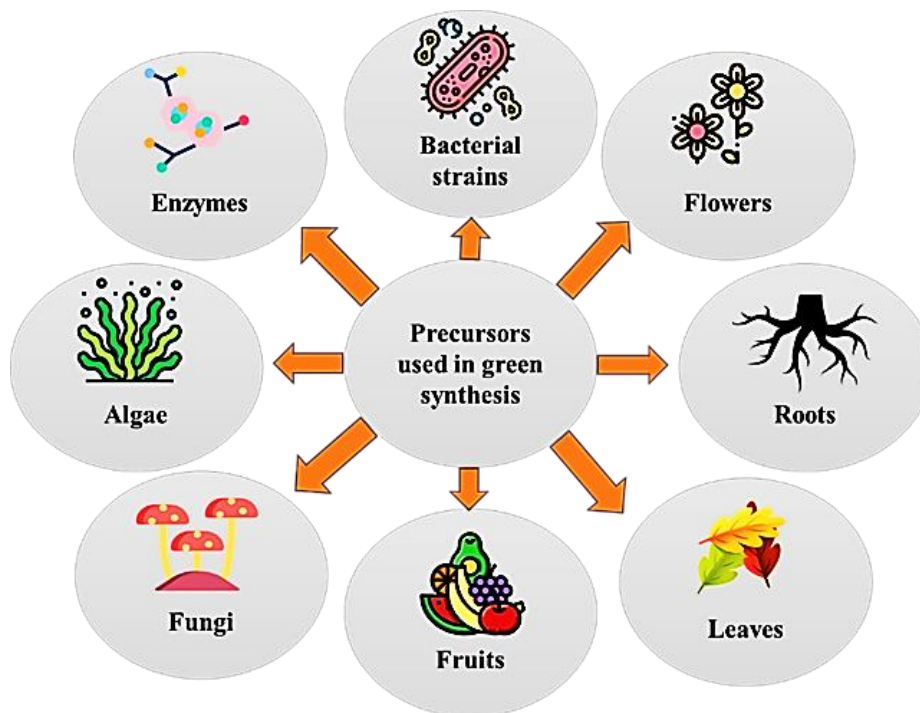


Figure III.1. The precursors used for green synthesis.

Date syrup, also known as date molasses or date honey, is a thick, sweet syrup made from boiled and reduced dates. This substance is a natural source rich in sugars, vitamins, antioxidants, and minerals [13]. Recently, interest in the use of natural products such as date molasses in the "green synthesis" of nanoparticles and other materials has increased significantly. Date molasses contains natural reducing agents, such as sugars (fructose and glucose), alkaloids, terpenoids and polyphenols, which seem to be a prominent solution to reduce easily metal ions and form nanoparticle catalysts [14].

In particular, nanoparticles ZnO have become a very interesting topic due to their ease of preparation, low production cost and safety[15]. Due to its high catalytic activity ZnO is a significant semiconductor photocatalyst. It can effectively destroy organic material when exposed to ultraviolet radiation, making it useful in a variety of environmental applications like the treatment of wastewater and air purification [15].

In previous studies, Graphene oxide (GO), reduced graphene oxide (rGO), and their derivatives have found extensive application in wastewater treatment for the removal and degradation of organic pollutants [16].

This widespread use in many fields is attributed to their exceptional adsorption, oxidation, and catalytic properties, as well as their large pore volume, huge specific surface area, high electrical conductivity, diverse surface chemical composition, and impressive length-to-diameter ratio [17]. It has been reported that the combination of materials boosts the photocatalytic activity, in this context to elaborate, graphene serves a thermodynamic role in crafting heterojunction photocatalysts capable of responding to a wide spectrum of light or in the doping of semiconductors possessing wide bandgaps [18].

Additionally, graphene's kinetic utilization enhances photocatalytic efficiency by capitalizing on its remarkable adsorption capacity for both organic and inorganic contaminants [19]. Given these factors, the integration of graphene with diverse semiconductors has emerged as a promising avenue for advancing research in this field [18].

In this chapter, ZnO/rGOx nanocomposites were manufactured and subjected to comprehensive characterization using various techniques, including X-ray diffraction (XRD), Fourier-transform infrared spectroscopy (FTIR), and scanning electron microscopy (SEM). Additionally, the analysis of the optical properties of these nanocomposites was conducted using UV-Visible spectrophotometry to assess their UV absorption capacity and determine the width of the band gap. Concurrently, the study examined the impact of parameters such as calcination temperature, catalyst dosage, and solution pH on the degradation efficiency of the compounds. Cycling tests were performed to confirm the stability of the ZnO/rGOx nanocomposite, and a degradation mechanism was proposed, based on the generation of electron-hole pairs and the attack of the dye by hydroxyl and superoxide radicals. This research highlights the remarkable potential of ZnO/rGOx nanocomposites in water treatment for the removal of organic pollutants. However, it is essential to note that future research efforts will be needed to adapt these nanocomposites for practical wastewater treatment applications.

This study significantly enriches our understanding of advanced photocatalytic materials and their potential applications in environmental remediation. A primary contribution lies in the innovative use of ZnO/rGOx nanocomposites, a unique combination of ZnO and rGOx, which introduces a fresh perspective on enhancing photocatalytic performance, particularly in the degradation of methylene blue. The research achieves a notable level of depth and sophistication through its comprehensive materials characterization, encompassing crystallographic verification

via XRD, the identification of functional groups using FTIR, and the detailed examination of material morphology through SEM. The most remarkable breakthrough, however, is the compelling evidence of a substantial enhancement in the photocatalytic efficiency of ZnO/rGOx nanocomposites in comparison to pure ZnO. This carries profound implications for water treatment, as it addresses the challenge of organic pollutant removal with unprecedented effectiveness. Moreover, the study goes beyond material synthesis and characterization by systematically exploring the influence of various reaction parameters and underlining the stability of these nanocomposites, reinforcing their potential for practical and sustainable applications in real-world wastewater treatment scenarios. In sum, this research represents a significant enrichment of our knowledge in the field, setting the stage for promising advancements in the quest for improved water quality and the mitigation of environmental pollution.

III.2. Experiment

III.2.1. Algerian Date Syrup (Molasses) extract preparation

for this preparation, industrial date molasses from the SALAMA brand, originating from the Biskra region in the southeast of Algeria, was utilized.

To make the extract, 20 g of date molasses were dispersed in 200 mL of distilled water. The mixture was then heated to 60 °C for 20 min under stirring until all the date molasses was evenly mixed. After heating, the solution was allowed to cool and filtered using Whatman filter paper, and the filtrate was collected. Subsequently, the resulting filtrate was used as a stock solution for the synthesis of ZnO nanoparticles as shown in figure III.1.

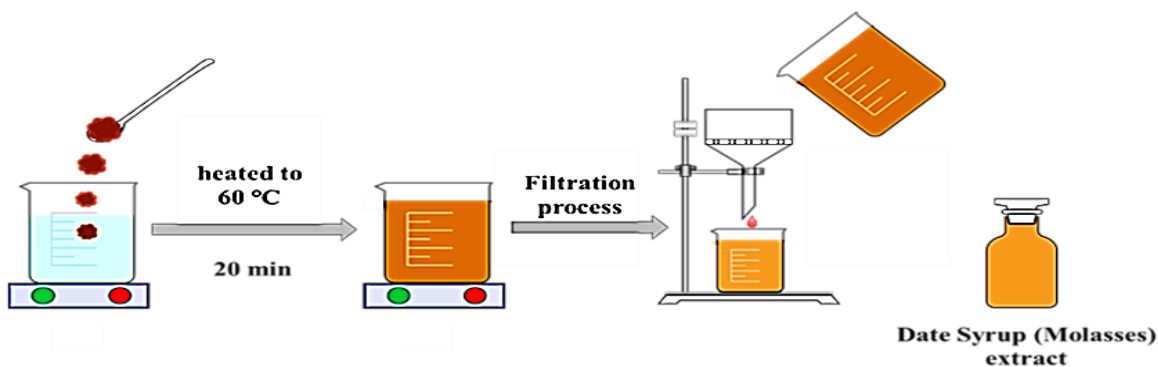


Figure III.2. Algerian Date Syrup (Molasses) extract preparation.

III.2.2. Synthesis of ZnO NPs

The synthesis of ZnO nanoparticles was meticulously initiated by the gradual addition of 20 mL of the extract, into an 80 mL solution of 0.1 M zinc acetate. The reaction vessel was maintained at a precise temperature of 90 °C, and the mixture was subjected to stirring at 700 rpm to ensure homogeneity. Upon achieving the designated temperature, a NaOH solution was delicately introduced dropwise into the reaction mixture. This marked the commencement of a carefully monitored 4-hour aging process, during which a remarkable transformation occurred—the solution's initial brown hue evolved into a pristine white, indicative of the formation of the desired precipitate.

Following this intriguing phase, ultrasonic treatment was meticulously applied for 60 minutes. This step was crucial for further enhancing the homogeneity and structural integrity of the synthesized ZnO nanoparticles. The resulting solution, now rich in well-formed nanoparticles, underwent a precision-controlled centrifugation process at 3600 rpm for 30 minutes. This step was imperative for efficiently collecting the synthesized ZnO nanoparticles, as the centrifugal force facilitated the separation of the nanoparticles from the remaining solution.

To ensure the purity of the synthesized nanoparticles, they were subjected to a meticulous purification process. The collected ZnO NPs were suspended in a carefully crafted mixture of ethanol and distilled water. This purification step aimed to eliminate any impurities or unreacted substances that might have been present in the solution. The suspension was then subjected to controlled conditions, allowing for the removal of solvent through air-drying at 60 °C in a vacuum oven overnight. The resulting dried powder, rich in synthesized ZnO nanoparticles, was delicately collected for further characterization.

In the subsequent phase, the collected sample underwent a thermal treatment process known as calcination. This involved subjecting the sample to varying temperatures, specifically 450 °C, 550 °C, and 600 °C. The selection of these temperatures was based on a comprehensive understanding of the desired structural and chemical properties of the ZnO nanoparticles. The thermal treatment was meticulously illustrated in Figure 16, providing a visual representation of the temperature-dependent transformations and the resultant characteristics of the synthesized nanoparticles.

The incorporation of molasses in our synthesis process holds paramount importance, its richness in diverse compounds offers various possibilities in ZnO synthesis. Natural sugars present, such as glucose, fructose, and sucrose, can act as reducing agents. Phenolic compounds contribute to reducing and stabilizing properties, while natural antioxidants help maintain the stability of nanoparticles. Minerals and trace elements

in date molasses could also influence the growth and properties of ZnO nanoparticles. In the absence of molasses, the reduction process could face impediments, potentially compromising the efficiency of ZnO nanoparticle synthesis. Molasses, with its organic diversity, emerges as an environmentally friendly alternative, offering a sustainable approach that replaces traditional chemical reducing agents with notable advantages in terms of both efficiency and ecological impact. The incorporation of molasses aligns with a green synthesis approach, emphasizing the eco-friendly nature of our methodology.

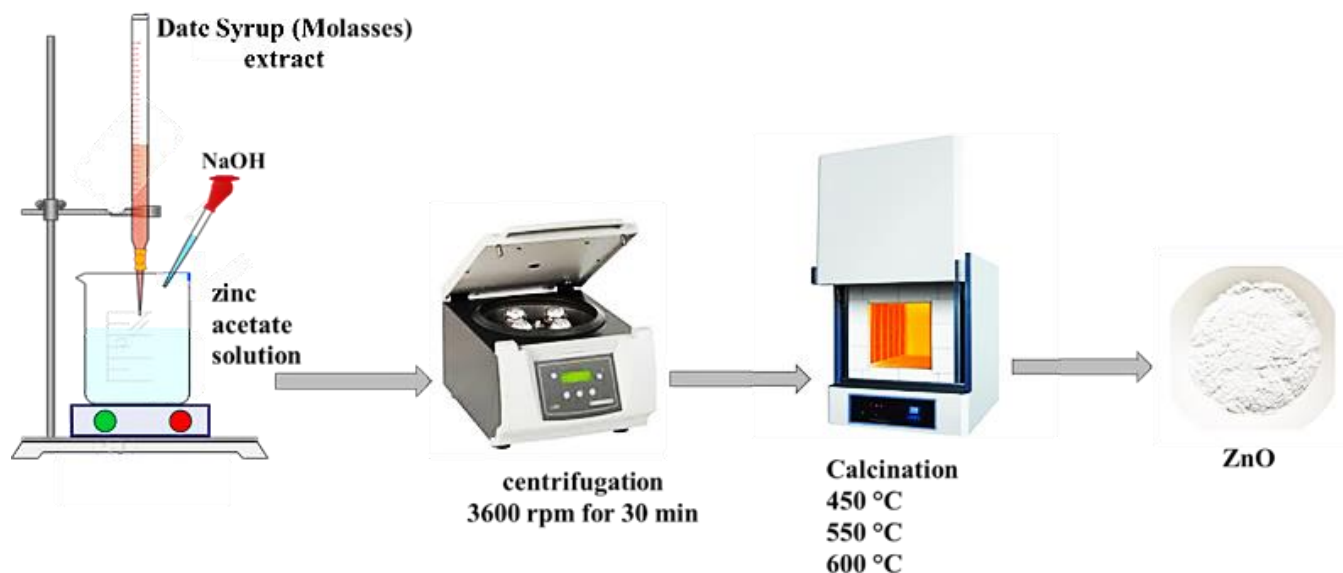


Figure III.3. Schematic presentation of ZnO green synthesis.

III.2.3. Preparation of ZnO/rGOx photocatalysts

ZnO/rGOx photocatalysts were synthesized using a hydrothermal method through varying the weight ratios of rGO to ZnO at 5%, 10%, and 15% by weight of rGO to ZnO. In this process 1 gram of ZnO powder and an appropriate mass percent of Graphene were dispersed in a solution

of double distilled water and ethanol, the obtained mixture was treated for 1 h in an ultrasonic bath and stirred for another 2 h to obtain homogeneous suspension. The resulting suspension was then placed in a Teflon-sealed autoclave and kept for 12 h at 120 °C. The resulting product was washed four times using a combination of distilled water and ethanol using a centrifuge and dried in an oven at 65 °C for 24 h in the manner indicated by the diagram (figure III.3).

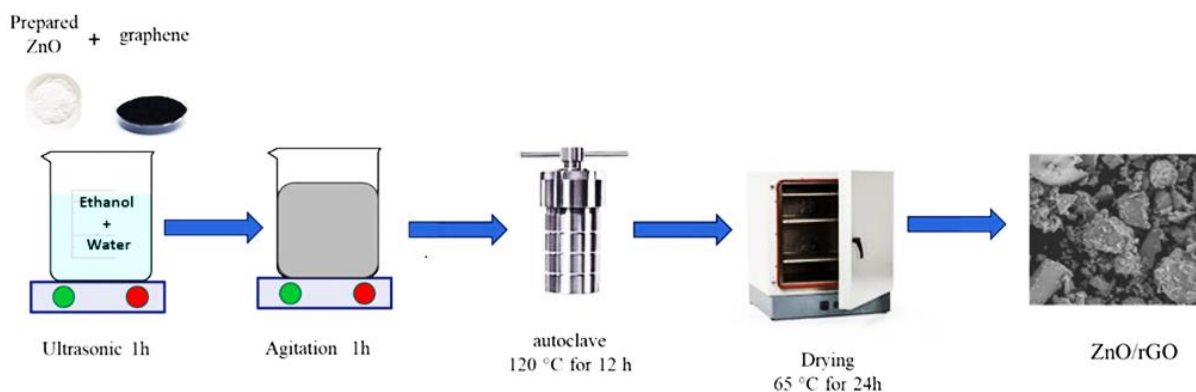


Figure III.4. Schematic diagram for preparing the ZnO/rGO_x nanocomposite

IV. Results

IV.1.1. Characterization

IV.1.1.1. X-Ray diffraction

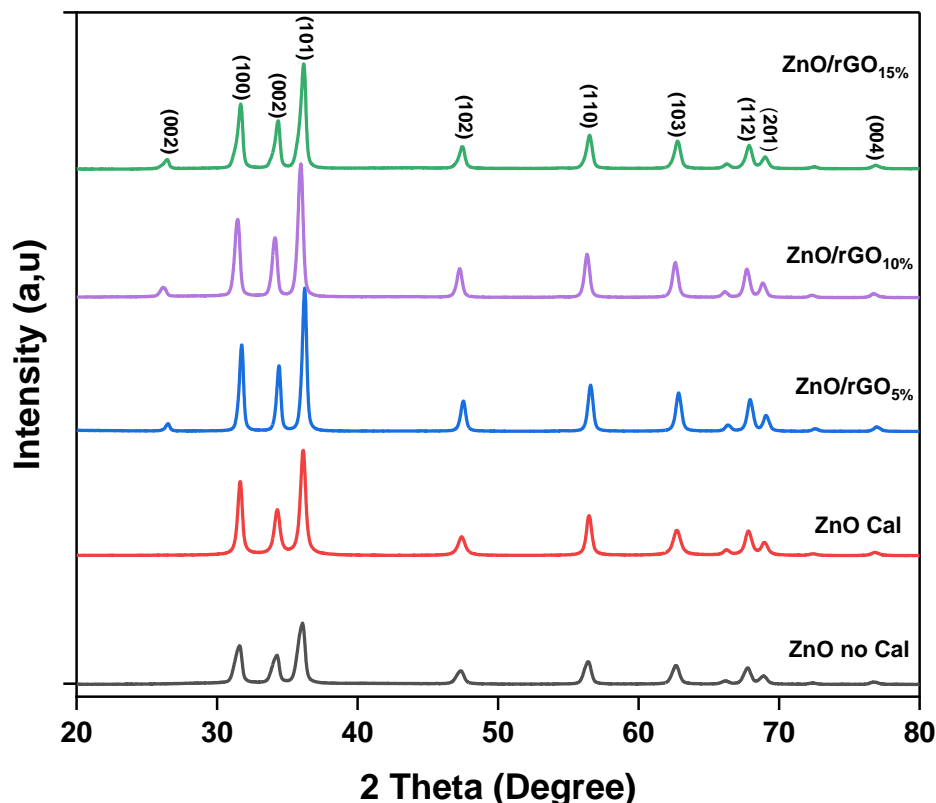


Figure III.5. XRD patterns of pure ZnO and ZnO-rGO_x.

In Figure III.5, the XRD patterns of both pure ZnO and the ZnO/rGO nanohybrid photocatalysts are presented. The observed diffraction peaks in the XRD pattern of the synthesized photocatalysts closely match the characteristic pattern of the hexagonal wurtzite phase of ZnO, as indicated by its reference in the JCPDS database under No. 36-1451 [20]. Specifically, the XRD pattern displays distinct peaks at various 2θ angles, namely 31.6° , 34.28° , 36.11° , 47.4° , 56.5° , 62.5° , 67.8° , 68.9° and 76.8° . These peaks correspond to the 100, 002, 101, 102, 110, 103, 112, 201 and 004 crystalline planes of ZnO [21]. The presence of distinct diffraction peaks at 26.2° (002) for rGO strongly indicates the effective anchoring of ZnO nanoparticles onto the rGO [22]. This alignment of observed peaks with the standard wurtzite phase of ZnO confirms

the crystalline structure of the synthesized photocatalysts and suggests the successful formation of ZnO/rGO nanohybrids. The crystallite sizes were calculated by using the Scherrer formula.

Table III.1. The crystallite size of the different samples.

<i>Samples</i>	Crystallite Size (nm)
ZnO non calcined	13.99
ZnO calcined at 550 °C	14.18
ZnO/rGO 5%	21.42
ZnO/rGO 10%	20.06
ZnO/rGO 15%	17.31

ZnO/rGO nanohybrids were observed to have bigger crystallite sizes when compared to pure ZnO. When ZnO is combined with rGO, the interactions between ZnO nanoparticles and rGO lead to a restructuring of ZnO particles. This particular process promotes the growth of pre-existing crystallites, leading to a subsequent increase in their size dimension. This result shows that larger crystal sizes can be associated with improved photocatalytic activity or enhanced performance in specific applications. However, it is essential to understand the underlying mechanisms to design and optimize nanomaterials, according to the specific requirements of each application [23].

IV.1.1.2. Fourier-transform infrared spectroscopy

The absorption bands in the FTIR spectrum of the ZnO-rGO composite presented in figure II.6 reveal crucial insights. The absorption band in the range of 3600-3200 cm^{-1} corresponds to the stretching vibrations of (OH) groups, either from water or hydroxyl groups linked to the composite's surface from moisture, polyphenols and some N-H of amine overlapping [24], bearing significance for surface chemistry [25]. The band at 2340 cm^{-1} is associated with the absorption of atmospheric carbon dioxide (CO_2), originating from the natural CO_2 content in the air during the analysis, contributing to specific spectral features [26] or aldehyde peak due to C=O stretching vibration [27]. The 1700-1600 cm^{-1} region is associated with the angular

deformation vibration (OH) groups of adsorbed water groups [28], while the range of 1600-1500 cm^{-1} is linked to vibrations of carbonyl groups or other bands (C=C), (–CO) and (C=O) from organic residue of the extract (the phenolic and flavonoids) absorbed on the surface of ZnO [29]. The 1500-1400 cm^{-1} region may be attributed to vibrations involving hydroxyl groups (O-H) or carboxylate of zinc groups [30]. Lastly, the band around 500-400 cm^{-1} is the fingerprint region which represents the bending and deformation vibrations of Zn-O of the crystalline lattice of nanoparticle metal oxide ZnO [31], consistent with previous findings in the literature [32]. The decrease in infrared peak intensity upon adding reduced graphene oxide (rGO) to zinc oxide (ZnO) can be attributed to various factors associated with composite formation. rGO's strong adsorption capacity may lead to the adsorption of ZnO particles onto rGO sheets, reducing ZnO availability for infrared signals. Interactions between rGO and ZnO induce changes in crystal structure, affecting vibrational modes and peak characteristics. The incorporation of rGO into the ZnO matrix forms a composite with unique properties, influencing infrared peak intensities. Additionally, rGO's conductive nature affects electronic properties, altering ZnO's interaction with infrared radiation and contributing to changes in peak intensity. Moreover, the difficulty in distinct between ZnO and ZnO/rGO may be due to the reduction of graphene during the preparation of the process.

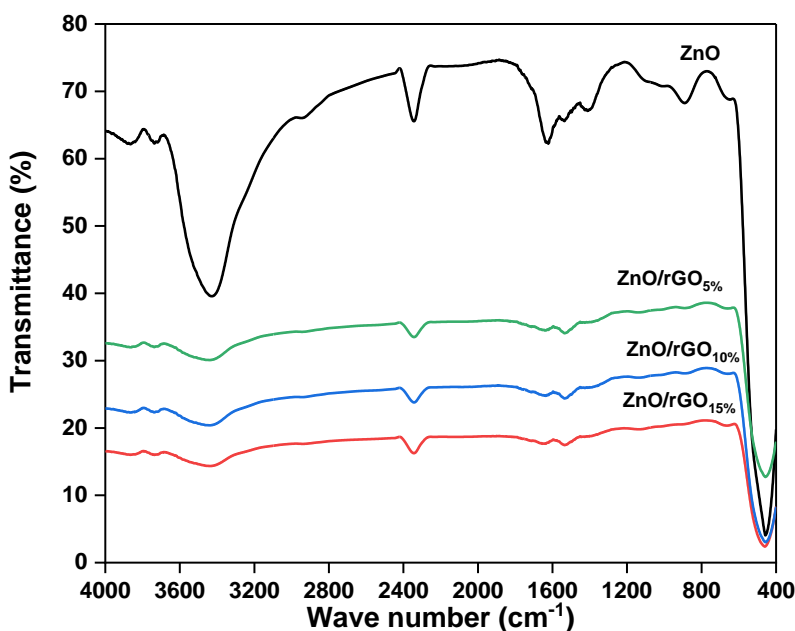
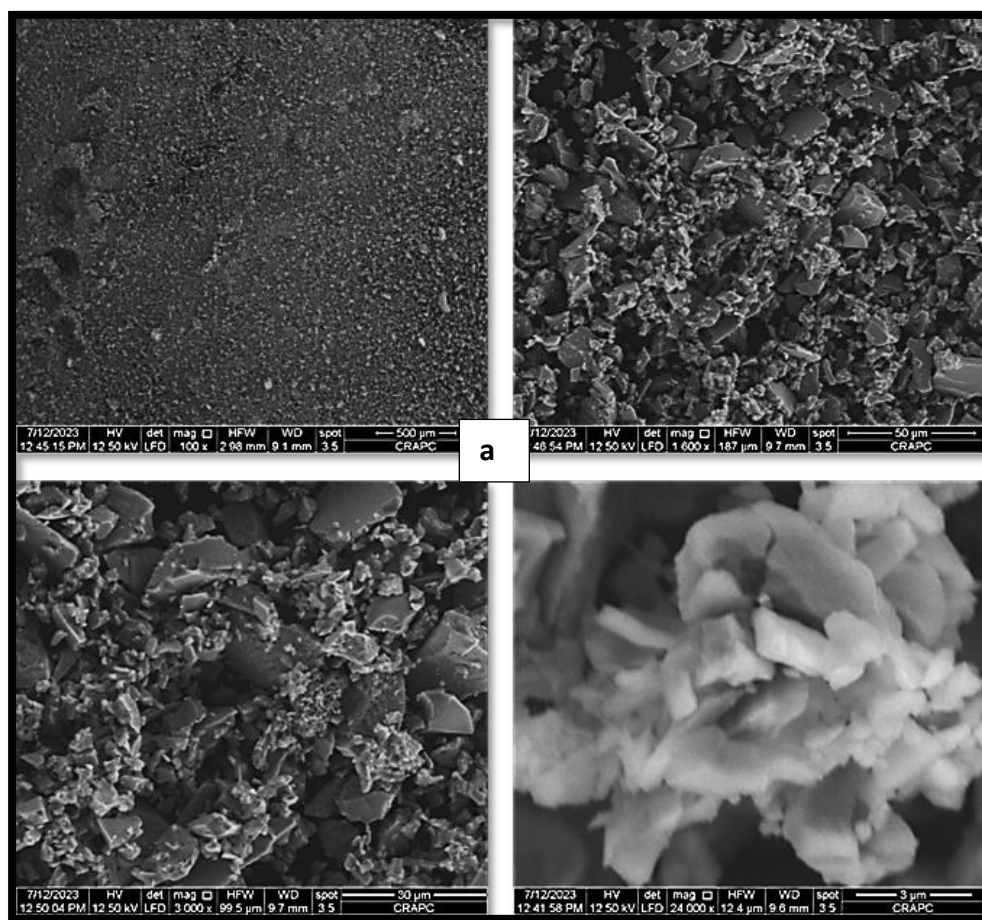


Figure III.6. FT-IR spectra of ZnO and ZnO/rGO_x nanocomposite.

IV.1.1.3. Scanning electron microscopy images

The morphology of ZnO/rGO was assessed using scanning electron microscopy (SEM). In Figure 7.a, it is evident that the ZnO nanoparticles exhibit diverse shapes. This phenomenon can be attributed to the interaction with organic components from the molasses extract. Additionally, Figure.b clearly shows that the ZnO nanocrystals are evenly spread out on the graphene sheets (marked with a red circle). This confirms the formation of the ZnO/rGOx heterojunction [33].



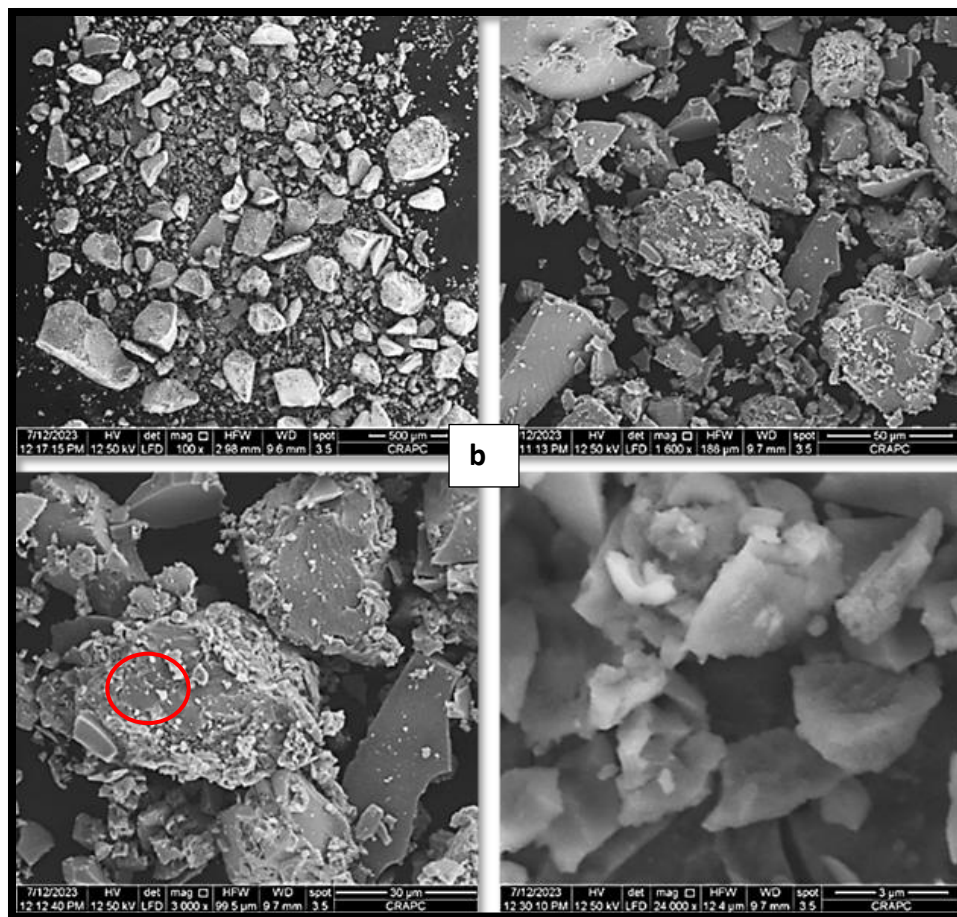


Figure III.7. SEM images of (a) Pure ZnO, (b) ZnO/rGO_{10%}.

IV.1.1.4. UV-visible diffuse reflectance spectroscopy

The optical characteristics of the ZnO and ZnO/rGO samples were assessed via UV-visible diffuse reflectance spectroscopy (DRS). As depicted in Figure 5, the DRS spectra of the ZnO samples demonstrated pronounced light absorption in the ultraviolet region [34]. This absorption phenomenon originates from electron transitions occurring between the valence and conduction bands of ZnO when subjected to UV light irradiation.

The initial band gap value for as-synthesized ZnO nanoparticles is 3.19 eV. However, after undergoing calcination at different temperatures (450°C, 550°C, and 600°C), the band gap decreases to 3.18 eV, 3.17 eV, and 3.15 eV, respectively. This decrease is linked to changes in the crystallite size of the nanoparticles, which tends to increase with higher calcination temperatures. Essentially, as the calcination temperature rises, the nanoparticles grow larger, leading to a smaller band gap [35].

When rGO is added to ZnO, the value of ZnO's bandgap energy decreases from 3.15 to 2.93 eV and this reduction is due to several factors. rGO acts as a dopant, introducing additional charges into the material's structure, which shifts energy levels and reduces the bandgap energy [36]. Additionally, as a good conductor of electricity, rGO can interact with ZnO, causing a redistribution of electronic energy levels and potentially altering the crystalline structure of the composite material [37]. This reduction in the bandgap energy makes the composite material more conductive, which can be advantageous in various applications.

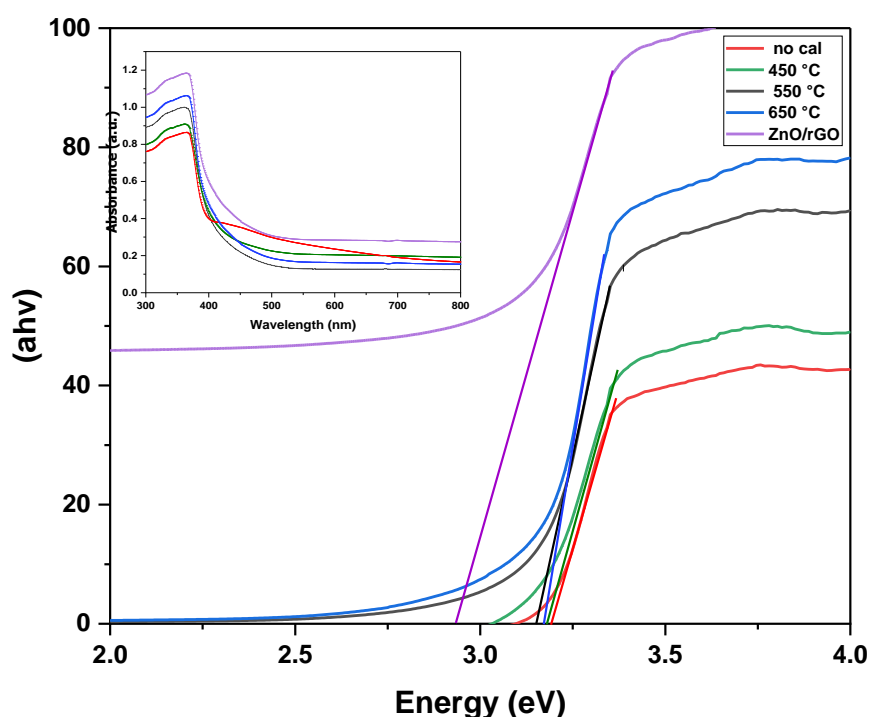


Figure III.8. Band gap energies and UV-vis diffuse reflectance spectra of ZnO at different calcination temperatures and ZnO/rGO 10%.

IV.1.2. Photocatalytic results

IV.1.2.1. Effect of calcination temperature on the photocatalytic activity of ZnO NPs

To investigate the effect of calcination temperature on the photocatalytic activity of the ZnO semiconductor, a series of ZnO samples were prepared by the green method at different calcination temperatures. The photocatalytic activity was examined by the photodegradation of

MB. The photocatalytic performance of calcined ZnO (98% for ZnO calcined at 550°C) significantly increases compared to that of non-calcined ZnO (73.6%). The activity of the ZnO NPs increased when the calcination temperature increased from 450 to 550°C but slightly decreased when the calcination temperature increased to 600 °C. Further, the rate constant “k” value for ZnO calcined at 550 °C is 0.01565 min⁻¹ against 0.00393 min⁻¹ for non-calcined ZnO indicating higher photocatalytic activity for catalyst calcined at 550 °C (Figure III.9). The “k” values are shown in Table 2. The influence of calcination temperature on the photocatalytic activity of ZnO is related to the morphological, optical, and surface properties of the ZnO NPs [38,39].

Table III.2 The rate constant ‘k’ of MB degradation with ZnO calcined at different temperatures.

Samples	No calcined	600°C	550 °C	450 °C
K (min⁻¹)	0.0039	0.0106	0.0156	0.0103
R²	0.94113	0.99285	0.99026	0.99124

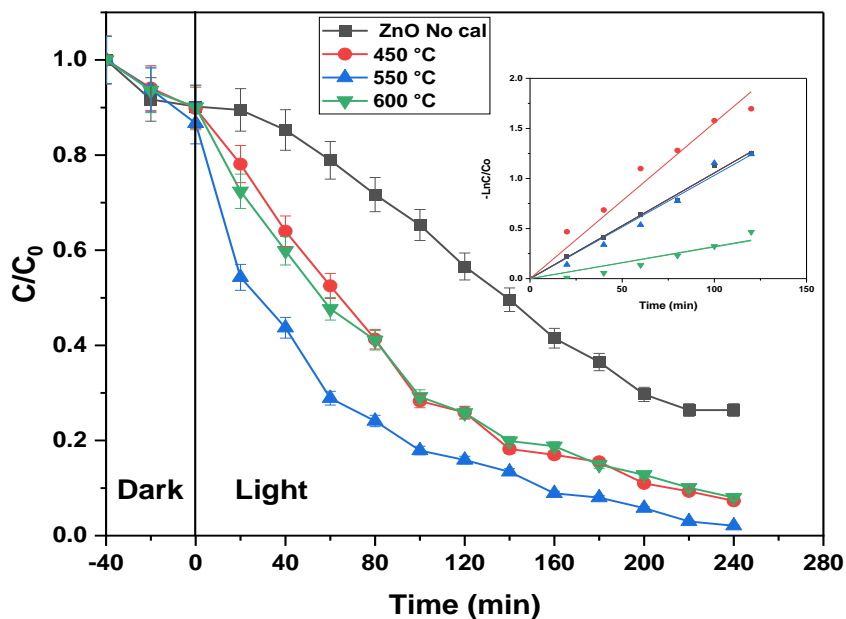


Figure III.9. Effect of calcination temperature on the photocatalytic activity of ZnO for the photocatalytic degradation of MB (Neutral pH, catalyst 1g/L, [MB] = 10 mg/L).

IV.1.2.2. Photocatalytic activity of ZnO/rGO_x

The photocatalytic effectiveness of both ZnO (calcined at 550°C) and ZnO/rGO nanohybrid photocatalysts was assessed through the degradation of MB under UV light irradiation, as illustrated in figure III.10. In comparison, pure ZnO achieved a degradation of only 85.4% for MB after 140 minutes of irradiation. In contrast, the ZnO/rGO nanohybrids exhibited significantly enhanced photocatalytic performance, with degradation efficiencies of 96%, 100%, and 88.6% for ZnO/rGO₅, ZnO/rGO₁₀, and ZnO/rGO₁₅, respectively, after 140 minutes of irradiation. Therefore, the incorporation of rGO resulted in a notable reduction in the time required for the complete degradation of MB, decreasing it from 240 minutes to 140 minutes. Table 3 shows that the reaction rate constant "k" exhibits an ascending trend with values of 0.0156, 0.0106, 0.0272, and 0.0103 for ZnO, ZnO/rGO₅%, ZnO/rGO₁₀%, and ZnO/rGO₁₅%, respectively.

The deliberate selection of ZnO calcined at 550°C as the reference for the entire study, including compounds coupled with rGO, was based on preliminary photodegradation tests at varying calcination temperatures. Notably, the optimal result of 86.6% degradation was consistently achieved at 550°C (ZnO calcined at 550°C without coupling with rGO).

It is crucial to note that rGO acts as an electron trapper, thereby preventing their recombination within the semiconductor material. This characteristic of rGO is pivotal as it promotes a faster and more efficient degradation of the dye. By averting electron recombination, rGO enables the excited electrons to interact with the dye, thus facilitating chemical degradation reactions [40]. Furthermore, rGO possesses a large specific surface area and a two-dimensional sheet-like structure, allowing for increased adsorption of organic pollutants on its surface. This creates more active sites for photocatalytic reactions to occur [41].

Table III.3. The rate constant 'k' of MB with ZnO/rGO_x.

Samples	ZnO	ZnO/rGO ₅ %	ZnO/rGO ₁₀ %	ZnO/rGO ₁₅ %
K (min⁻¹)	0.0156	0.0106	0.0272	0.0103
R²	0.99026	0.99628	0.99944	0.98212

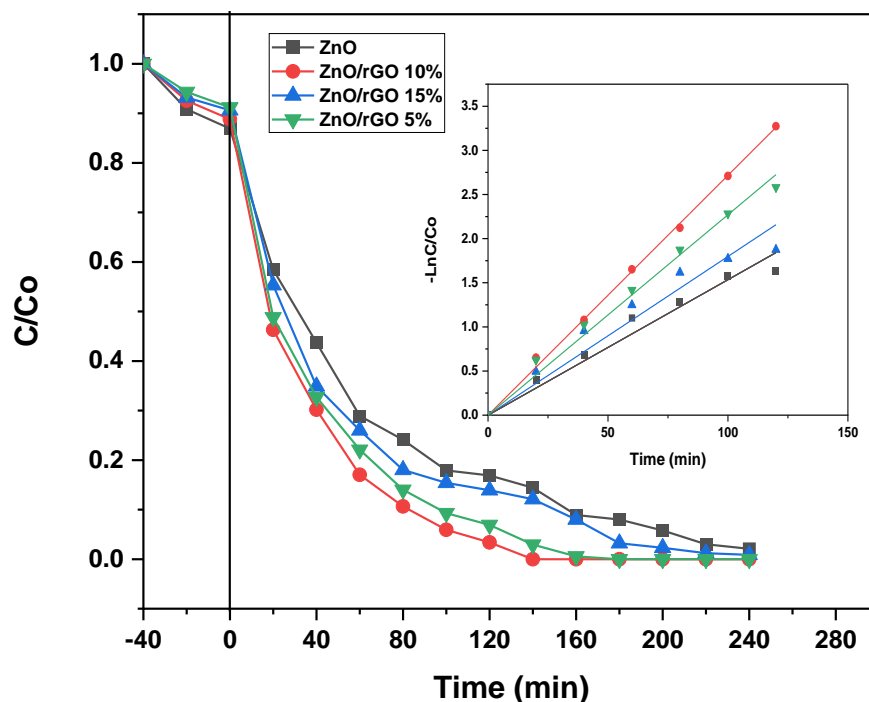


Figure III.10 Photodegradation of MB dye by ZnO/rGO_x (x= 5, 10 and 15 %) (Neutral pH, catalyst 1g/L, [MB] = 10 mg/L).

IV.1.2.3. Effect of catalyst dosage

The quantity of catalysts is a crucial factor in the production of active radicals in photocatalytic degradation reactions. However, an excessive amount of catalyst can impede the penetration of incident light, hence potentially reducing the degradation process. Therefore, the influence of catalyst dosage on the degradation of MB ([MB] = 10 mg/L) was systematically investigated by varying the quantity of ZnO/rGO nanocomposite within the range from 0.25 g/L to 2 g/L, while maintaining neutral pH conditions and subjecting the reaction to 140 minutes of irradiation. As the catalyst dosage was incrementally increased from 0.25 to 1 g/L, the degradation efficiency experienced a corresponding rise, progressing from 62.3% to reach a complete degradation of 100%. However, when the catalyst dosage was further elevated to 2 g/L, the degradation efficiency exhibited a decrease to 67.4% (figure III.11). This observed enhancement in degradation with the initial increase in catalyst dosage, from 0.25 to 1 g/L, can be attributed to the greater available catalyst surface area. This increased surface area facilitated the enhanced

absorption of photons, thus promoting the photocatalytic process through the greater number of (e^- , h^+) pairs resulting in the generation of more active radicals [42]. The reduction in the degradation rate beyond a catalyst dosage of 1 g/L can be attributed to the increasing solution turbidity and the adverse effects associated with surpassing the optimal photocatalyst dose. This finding is supported by the First-order rate constants shown in Table 4, for various catalysts which give trend values of 0.0156, 0.0106, 0.0272, and 0.0103 for ZnO, ZnO/rGO_{5%}, ZnO/rGO_{10%}, and ZnO/rGO_{15%}, respectively.

These effects encompass particle agglomeration, diminished UV light penetration, restricted mobility of reactants, increased recombination of electron-hole pairs, saturation of active surface sites, and the emergence of undesired side reactions. Consequently, precise control of photocatalyst dosage is imperative to mitigate these issues and fine-tune the photocatalytic process for applications [43].

Regarding the evolution of K values, a notable observation was the increase in the kinetic constant only for doses from 0.25 to 1 g/L, followed by a decrease at the 2 g/L dose. The correlation between methylene blue degradation and the kinetic constant derived from linear regression takes on particular significance. It sheds light on the relationship between the efficiency of the degradation process and the speed of that degradation. The kinetic constant, representing the reaction rate in the degradation process, holds central importance. A higher kinetic constant has been indicative of a rapid reaction, signaling increased efficiency in methylene blue degradation. Conversely, a lower kinetic constant may suggest a slower reaction, potentially linked to a decrease in efficiency in the degradation process. This nuanced interpretation underscores the crucial importance of kinetic constant in a comprehensive understanding of the kinetics of methylene blue degradation.

Examining the K values for each dose from Table 4 (0.25 g/L, 0.5 g/L, 1 g/L, 2 g/L) revealed a significant variation. K values increased from 0.0115 to 0.0272 for doses from 0.25 to 1 g/L, suggesting a positive correlation between the substance concentration and the degradation rate. However, the K value then decreased to 0.0082 for the 2 g/L dose. This fluctuation highlights the specific influence of concentration on the degradation kinetics, reinforcing the importance of the kinetic constant in evaluating the efficiency of the methylene blue degradation process.

Table III.4. Rate constant K of degradation of MB with different dosages of ZnO/rGO.

Dosage(g/L)	0.25	0.5	1	2
K (min⁻¹)	0.0115	0.0188	0.0272	0.0082
R²	0.99219	0.99801	0.99944	0.99401

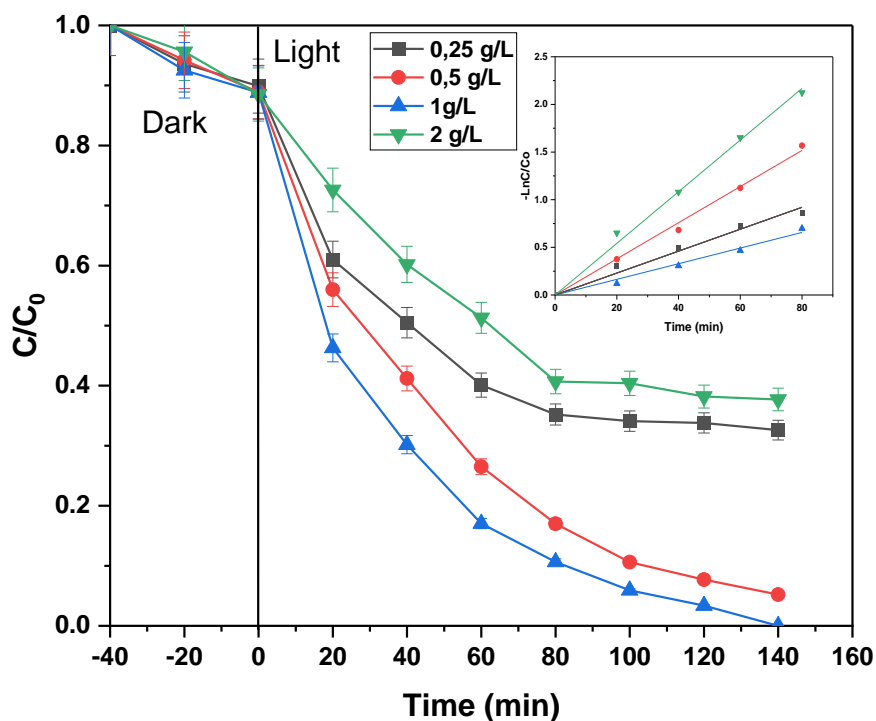


Figure III.11 Effect of catalyst dose on photodegradation of MB by ZnO/rGO_{10%} (Neutral pH, [MB] = 10 mg/L).

IV.1.2.4. Effect of reaction pH

In previous studies, researchers have highlighted the significant effect of the initial pH value in the reaction mixture, emphasizing its substantial influence on the photocatalytic performance [45]. The impact of solution pH on the photocatalytic degradation of MB was investigated at initial pH levels of 4, neutral (approximately 7), 8, and 10. Figure III.12 shows that the decomposition rate of MB with ZnO/rGO_{10%} catalysis is significantly influenced by the pH of the dye solution, with the catalyst exhibiting greater efficiency in a neutral environment. With a

degradation rate of 100% at neutral pH, this value decreases to 75% at pH 4. Subsequently, an increase in the rates is observed, with 90% and 94% corresponding to pH 9 and 10, respectively. The photocatalytic activity of ZnO/rGO_{10%} is typically higher under neutral to slightly basic pH values for several reasons. For the most precise assessment, the kinetic degradation constant for MB has been computed at various pH values, and these values are delineated in Table 5. First, ZnO/rGO_{10%} exhibits greater stability at neutral pH levels, as extremes in acidity or alkalinity can lead to rapid dissolution or corrosion, shortening the material's lifespan [46]. Second, at neutral pH, the recombination of charge carriers (electrons and holes) is generally reduced, allowing photoexcited electrons a better chance to react with other reactive species before recombining, thus enhancing photocatalytic efficiency [11]. Third, the balance between surface protonation and deprotonation at neutral pH creates a surface conducive to photocatalytic reactions by enabling the formation of hydroxyl radicals ($\bullet\text{OH}$) and the generation of electron-hole pairs (e^-/h^+) [47]. Lastly, neutral pH conditions are well-suited for degrading a wide range of organic pollutants, making them the preferred choice for photocatalytic applications due to the equilibrium they strike between material stability and effectiveness in degrading diverse pollutants.

Regarding the evolution of K values (Table 5), The K values for MB degradation exhibit notable variations at different pH levels. At pH 4, the observed K value of 0.0079 min^{-1} indicates a relatively slow degradation rate, pointing to reduced efficiency under acidic conditions. This could be attributed to the inhibitory effect of excess protons on the degradation process.

Conversely, at neutral pH, the substantial increase in the K value to 0.0278 min^{-1} signifies a significantly faster reaction rate. This suggests that neutral pH is optimal for methylene blue degradation, reflecting higher efficiency compared to acidic conditions.

Moving to pH 8, the K value of 0.0177 min^{-1} , while lower than at neutral pH, still indicates a reasonably efficient degradation process under slightly alkaline conditions. The moderate reaction rate at pH 8 suggests effective degradation, though not as rapid as observed at neutral pH.

At pH 10, the K value of 0.0223 min^{-1} falls between the rates observed at neutral and pH 8. This indicates a moderate reaction rate and efficiency in the degradation process under more alkaline

conditions. Degradation at pH 10 occurs faster than under acidic conditions but not as rapid as at neutral pH.

The nuanced variations in K values across different pH levels underscore the sensitivity of methylene blue degradation kinetics to changes in acidity and alkalinity. The optimal efficiency observed at neutral pH highlights the importance of considering environmental conditions in understanding and optimizing the degradation process.

Table III.5. Rate constant K of degradation of MB with ZnO/rGO in different pH.

pH	4	neutral	8	10
K (min^{-1})	0.0079	0.0278	0.0177	0.0223
R^2	0.97781	0.99944	0.97807	0.9538

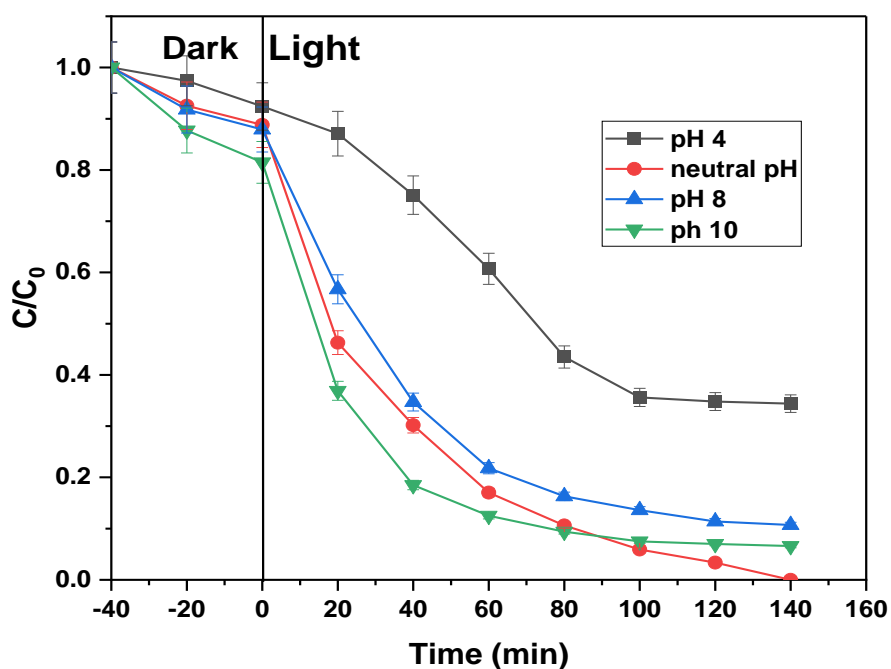


Figure III.12 Effect of reaction pH on photodegradation of MB by ZnO/rGO_{10%} (Catalyst 1 g/L, [MB] = 10 mg/L).

IV.1.2.5. Cycling test of the photocatalytic degradation of methylene blue under UV light

Photostability stands as a pivotal factor in determining the practical viability of a photocatalyst. In a bid to comprehensively evaluate the structural integrity and catalytic endurance of the ZnO/rGO_{10%} nanocomposite, a sequence of five successive tests centered around the photocatalytic degradation of MB was meticulously executed. The recycling protocol post-UV light-assisted MB degradation encompasses several crucial steps.

Initiating the process, the composite is meticulously recovered through a precision-centric centrifugation process following each photocatalytic test. Subsequently, a thorough four-cycle washing procedure is set in motion, employing a thoughtfully concocted mixture of distilled water and ethanol, culminating in the final cycle using double-distilled water. The material undergoes a five-hour UV light treatment in double-distilled water, ensuring the comprehensive elimination of any lingering MB residues post-photocatalytic decomposition. Post-UV treatment, the ZnO/rGO material is delicately recovered and subjected to a drying regimen at 60 °C for 24 hours, a crucial step ensuring its preservation for subsequent cycles. This meticulous and comprehensive approach serves as a robust framework for assessing the longevity and reusability of the ZnO/rGO composite within the realm of photocatalytic applications. Figure III.13 visually encapsulates the outcomes of five consecutive cycles of MB photodecomposition, revealing a steadfast maintenance of photocatalytic efficiency. This noteworthy finding underscores the inherent stability of the ZnO/rGO nanocomposite, emphasizing its resilience and reliability over successive photocatalytic test cycles.

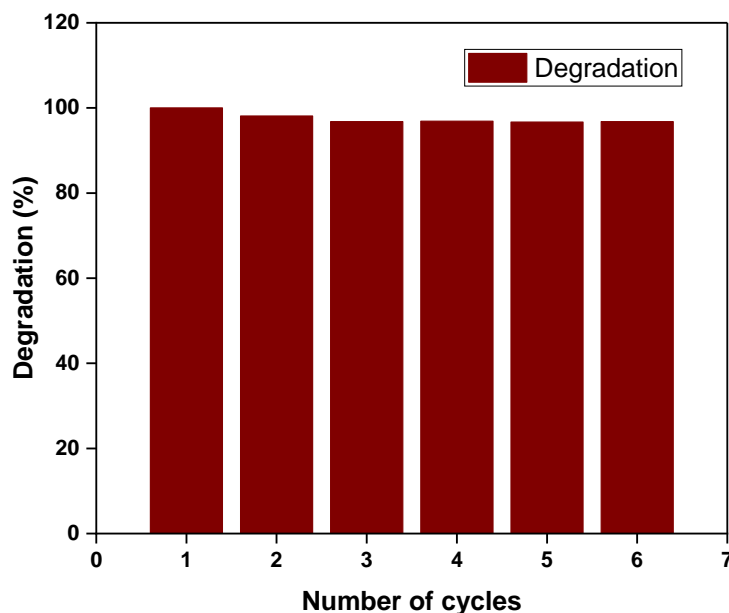


Figure III.13 Comparative performance of reused ZnO/rGO photocatalyst.

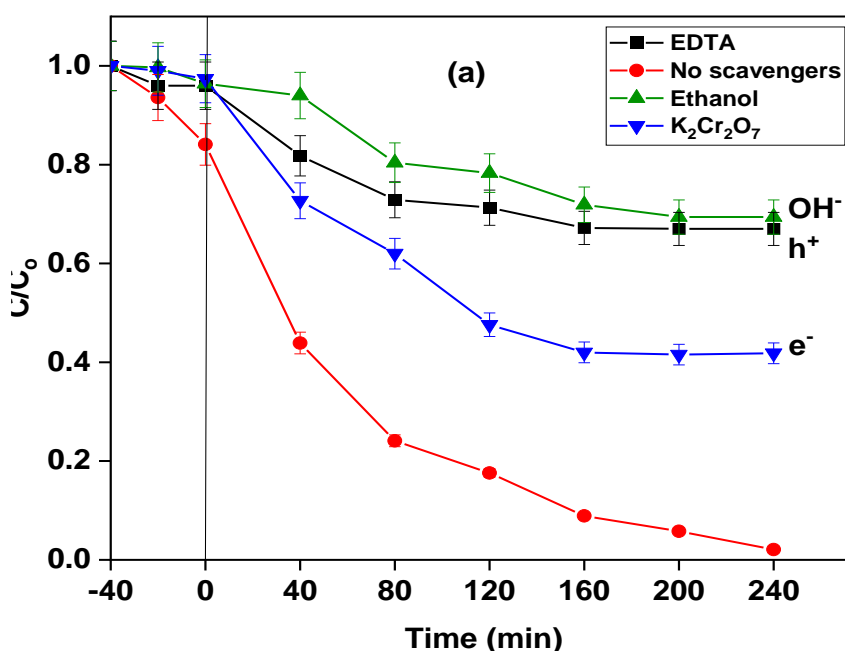
IV.1.2.6. Effect of Scavengers

The resulting impact of these scavengers on the photodegradation of MB using ZnO and ZnO/rGO catalysts is visually presented in Figure III.14. Using ethanol as a scavenger to sequester $\bullet\text{OH}$ radicals give a degradation rate of 31% for ZnO and 31.4% for ZnO/rGO. These degradation rates are less than the 100% degradation rate observed in the absence of scavengers as displayed in Figure 11. This experiment highlights the principal role of $\bullet\text{OH}$ radicals in the degradation of MB dye.

Moreover, the use of ethylenediaminetetraacetic acid (EDTA) as a scavenger for hydrogen ions (h^+) led to a degradation rate of 33% for ZnO and 38% for ZnO/ rGO, demonstrating the substantial contribution of h^+ ions in the MB photodegradation process. In addition, the use of $\text{K}_2\text{Cr}_2\text{O}_7$ as a scavenger gives a degradation rate of 59.2% for ZnO, suggesting a significant contribution of electron (e^-) species in the degradation mechanism. Moreover, it was observed that the degradation rate of ZnO/rGO was 11%, indicating that the participation of electrons is the primary factor in the degradation of MB when ZnO/rGO is involved in the process.

The significant difference in response in the presence of e-scavengers between the two systems is attributable to distinct degradation mechanisms between ZnO and the ZnO/rGO composite. ZnO, as an efficient photocatalyst exposed to UV light, generates electron-hole pairs, producing

reactive oxygen species such as hydroxyl radicals ($\bullet\text{OH}$) and superoxides ($\text{O}_2^{\bullet-}$). However, ZnO can also produce free electrons that react with oxygen species, generating reducing radicals that act as scavengers, neutralizing undesirable reactive species. In contrast, the ZnO/rGO composite integrates the photocatalytic properties of ZnO with the conductivity of reduced graphene oxide (rGO). The rGO acts as an electron acceptor, promoting the effective separation of electron-hole pairs generated during photocatalysis. In the presence of rGO, the recombination of electrons and holes is reduced, thereby enhancing the overall efficiency of the photocatalytic process.



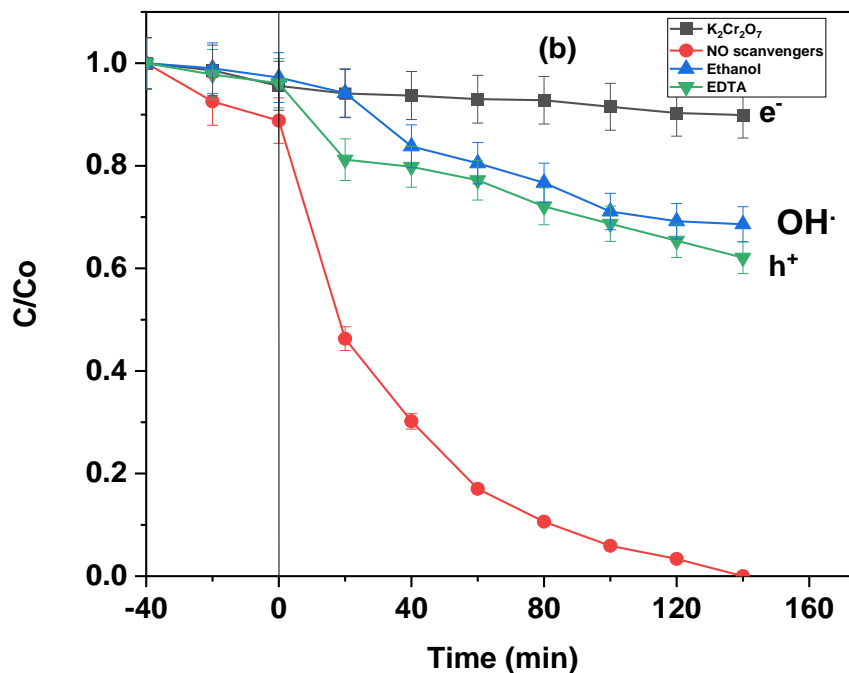


Figure III.14. Effect of scavengers on the photocatalytic activity of ZnO (a) and ZnO/rGO (b) (Neutral pH, catalyst 1g/L, [MB] = 10 mg/L).

IV.1.2.7. Degradation kinetic modeling

To investigate the kinetics of chemical pollutant degradation, it is essential to monitor how concentration changes over time in the outlet of a reactor. This involves conducting experiments with various initial concentrations of the pollutant. The apparent kinetic constants, denoted as k_{app} , are achieved by analyzing the plot depicting the natural logarithm of the ratio of the current concentration to the initial concentration ($\ln(C/C_0)$) as a function of time (figure III.15) [44].

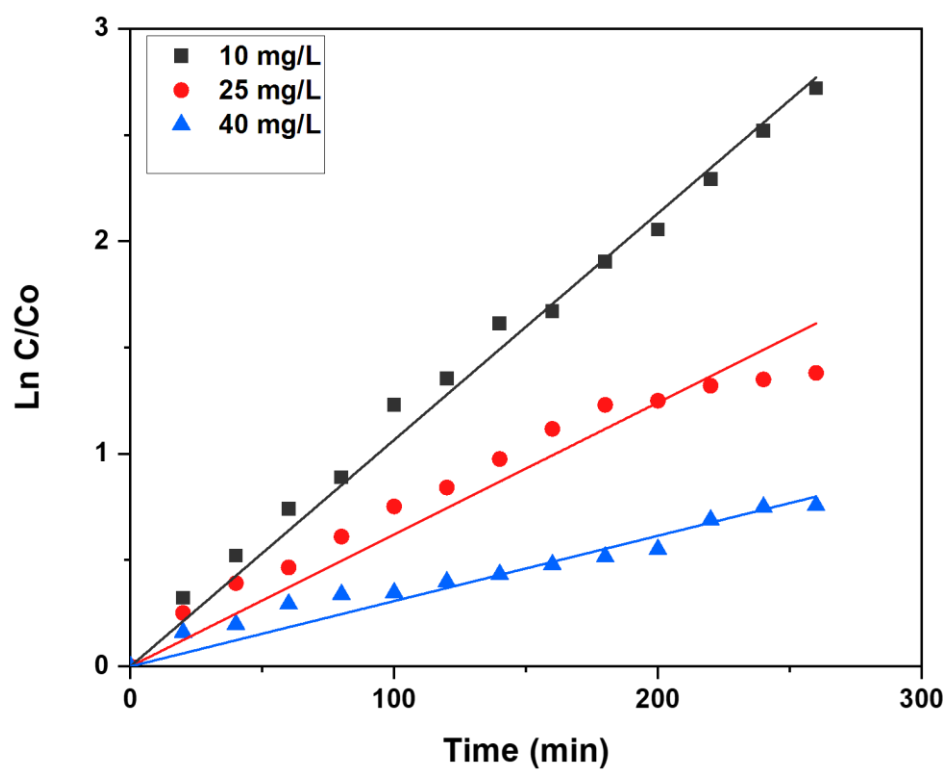


Figure III.15. Pseudo-first order apparent constant values for the different initial concentrations of MB.

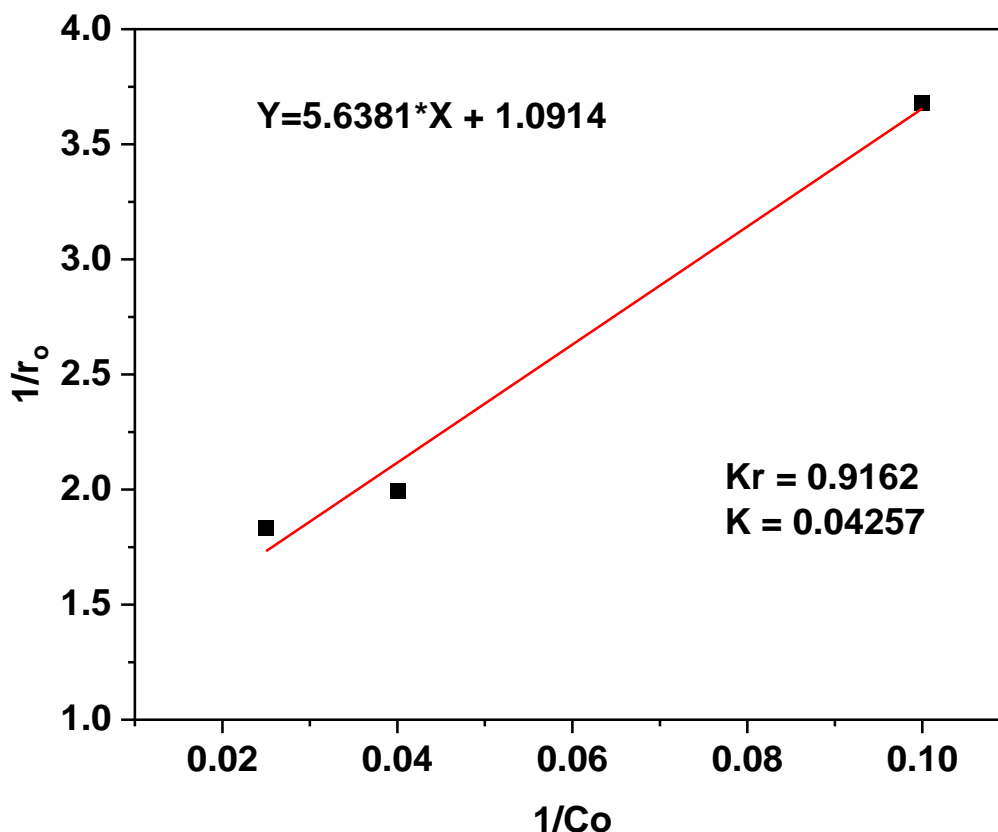
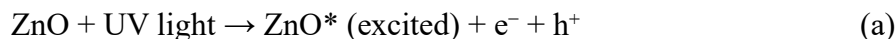


Figure III.16. Langmuir-Hinshelwood kinetic plot for the photocatalytic decolorization of methyl blue.

The calculated constants from the Langmuir Hinshelwood model are $k_r = 0.9162$ mg/L and $K = 0.04257$ L/mg. It is observed that k_r is greater than K indicating the differences between the photoabsorption and photodegradation reactions. According to the findings of the kinetic study, the Langmuir Hinshelwood model is confirmed in the MB photodegradation.

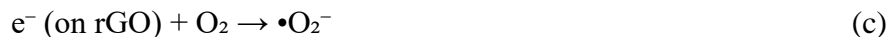
IV.1.2.8. Proposed photodegradation mechanism

The photodegradation mechanism of MB using a ZnO/rGO nanocomposite under UV light involves a series of intricate steps. When exposed to UV light, ZnO nanoparticles absorb photons, leading to the generation of electron-hole pairs (e^-h^+) due to bandgap excitation [45]. These excited electrons migrate to the nearby rGO sheets, preventing recombination with holes and enhancing their mobility. Simultaneously, MB ionic molecules in the solution are adsorbed onto the ZnO/rGO composite surface through electrostatic interactions [46].





The photocatalytic degradation process begins as the excited electrons on the rGO sheets participate in redox reactions with adsorbed oxygen species (O_2) or hydroxyl ions (OH^-) present in water, yielding superoxide radicals ($\bullet\text{O}_2^-$) and hydroxyl radicals ($\bullet\text{OH}$) [47]. These reactive radicals are highly oxidative and initiate attacks on the adsorbed MB molecules, breaking them down into smaller, less colored fragments.



As this degradation process continues, MB molecules are progressively transformed into non-toxic byproducts, such as carbon dioxide and water.

a) Oxidation by Superoxide Radicals: $\bullet\text{O}_2^-$ attacks MB, causing its breakdown:



b) Oxidation by Hydroxyl Radicals: $\bullet\text{OH}$ radicals also attack MB, further breaking it down: $\bullet\text{OH} + \text{MB (on ZnO/rGO)} \rightarrow \text{Degraded Products}$. (g)

Throughout this cycle, electrons back to the ZnO nanoparticles to fill the electron vacancies (holes) created during the initial excitation, facilitating the sustained photocatalytic activity of the composite [48].



This detailed mechanism underscores the synergistic actions of ZnO and rGO in harnessing UV light for the efficient degradation of MB, with ZnO serving as the photocatalyst and rGO enhancing electron transfer and minimizing electron-hole recombination, resulting in the effective removal of organic pollutants from the solution. Figure 14 summarizes the degradation mechanism.

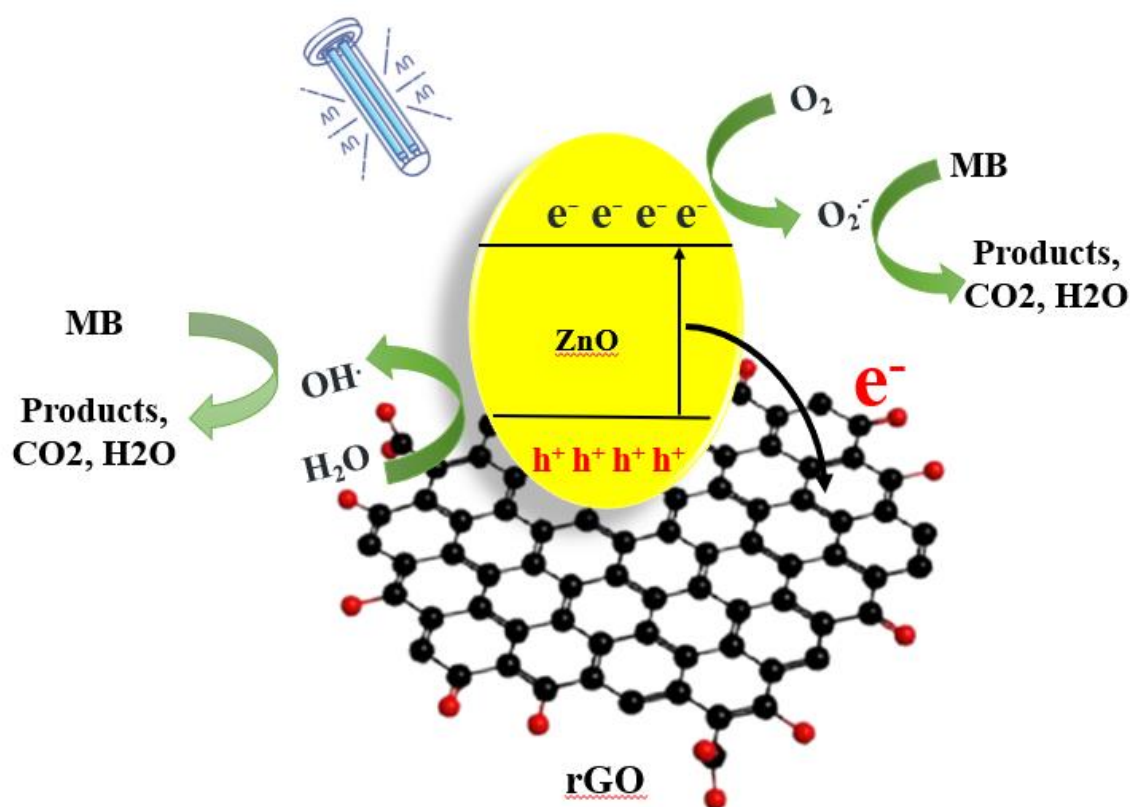


Figure III.17. The photodegradation mechanism of methylene blue.

IV.2. Comparison of the photocatalytic efficacy of commercial TiO₂ P25 and ZnO nanoparticles synthesized by different methods

A thorough comparative analysis was conducted to assess the photodegradation efficiency of ZnO-NPs) relative to TiO₂ P25. The detailed results, outlined in Table 6, cover a comprehensive examination of ZnO-NPs prepared through various alternative methods. Notably, previously documented ZnO-NP catalysts employed diverse synthesis approaches, with a particular focus on biological methods. The evaluation of their photocatalytic activity involved the use of MB as the selected dye, contributing a valuable dimension to the multifaceted exploration of catalyst performance.

Table III.6. Comparison of the photocatalytic efficacy of commercial TiO₂ P25 and ZnO nanoparticles

Catalyst	Preparation Method/ Plant	Dye	Irradiation	Particle Size (nm)	Irradiation Time/ min	Catalyst Dose/ g L ⁻¹	Dye Conc./ mg L ⁻¹	Degradation Efficiency/ %	Ref.
P25 Degussa		MB	UV lamp	<21	60	1	10	41	[49]
ZnO@OFE	Biosynthesis <i>O. europaea</i>	MB	Sunlight	24.3	180	1	10	75	[50]
ZnO	Sol gel	MB	UV (Hg lamp 365nm)	25	120	0.33	10	37	[51]
ZnO	Biosynthesis/ <i>Syzygium cumini</i>	MB	UV (365 nm)	25-30	60	2	1-2	84	[52]
ZnO-Bi₂O₃	Co-precipitation	RO16	UV lamp	29.6	100	0.2	100	28	[53]
ZnO	Biosynthesis/ Date Syrup	MB	UV lamp	14	140	1	10	86.6	present work
ZnO/rGO	Hydrothermal	MB	UV lamp	20	140	1	10	100	This work

Table 6 unfolds a comprehensive panorama of catalysts sourced from diverse studies, providing nuanced insights into their unique photodegradation efficiencies. Amidst this varied array, our ZnO nanoparticles, intricately synthesized through a distinctive biological process involving Date Syrup, emerge as beacons of excellence. Their extraordinary efficacy is accentuated when juxtaposed with other materials scrutinized in separate investigations.

A meticulous exploration of the entries reveals intriguing dynamics. For example, the initial catalyst, P25 Degussa, showcased a 41% degradation efficiency under UV lamp irradiation. In stark contrast, ZnO@OFE, synthesized via biosynthesis from *Olea europaea*, demonstrated a significantly higher efficiency of 75% under sunlight exposure, underscoring the inherent advantages of employing biologically synthesized ZnO nanoparticles, especially in harnessing solar energy for effective photocatalysis.

Delving deeper into the entries, which include ZnO synthesized through sol-gel and various biosynthetic methods, such as those incorporating *Syzygium cumini* and Date Syrup, reveals a captivating spectrum of particle sizes, irradiation times, and degradation efficiencies. For instance, ZnO synthesized through sol-gel methods showcased a degradation efficiency of 37%, employing UV (Hg lamp 365nm) irradiation. Additionally, ZnO synthesized via biosynthesis from *Syzygium cumini* exhibited a particle size range of 25-30 nm, an irradiation time of 60 minutes, and achieved a degradation efficiency of 84% (The initial concentration of MB is 2 mg/L) under UV (365 nm) irradiation. Furthermore, the table includes entries like ZnO-Bi₂O₃, synthesized through co-precipitation using RO16 as the dye, with a particle size of 29.6 nm, an irradiation time of 100 minutes, and a remarkable degradation efficiency of 28%. It is essential to note that despite ZnO-Bi₂O₃ degrading 28 mg/L of RO16, this does not necessarily imply superiority to our material. This is because MB is often considered relatively stable and persistent, potentially making its degradation more challenging compared to RO16.

The standout contribution of our study becomes evident when scrutinizing the ZnO nanoparticles synthesized with Date Syrup. Boasting an impressive degradation efficiency of 86.6% under UV lamp irradiation for 140 minutes, our catalyst surpasses its ZnO counterparts in the table. Furthermore, the hydrothermally synthesized ZnO/rGO composite in our study emerges as a pinnacle of photocatalytic capability, achieving a complete degradation efficiency of 100%.

In essence, our comparative analysis not only underscores the superior photodegradation efficiency of our ZnO nanoparticles, particularly those synthesized with Date Syrup, but also positions them as promising candidates for diverse applications in photocatalysis. Beyond the numerical outcomes, the richness of this exploration lies in the diverse synthesis methods employed, offering broader implications for the potential utilization of ZnO nanoparticles in various environmental and industrial contexts.

References

- [1] Z. Kuspanov, B. Bakbolat, A. Baimenov, A. Issadykov, M. Yeleuov, C. Daulbayev, Photocatalysts for a sustainable future: Innovations in large-scale environmental and energy applications, *Science of the Total Environment* 885 (2023). <https://doi.org/10.1016/j.scitotenv.2023.163914>.
- [2] M.K. Guediri, D. Chebli, A. Bouguettoucha, R. Bourzami, A. Amrane, Interfacial coupling effects on adsorptive and photocatalytic performances for photoresponsive graphene-wrapped SrTiO₃@Ag under UV–visible light: experimental and DFT approach, *Environmental Science and Pollution Research* (2022) 1–17.
- [3] I. Khan, K. Saeed, I. Khan, Nanoparticles: Properties, applications and toxicities, *Arabian Journal of Chemistry* 12 (2019) 908–931. <https://doi.org/10.1016/j.arabjc.2017.05.011>.
- [4] M.B. Tahir, M. Sohaib, M. Sagir, M. Rafique, Role of Nanotechnology in Photocatalysis, in: *Encyclopedia of Smart Materials*, Elsevier, 2021: pp. 578–589. <https://doi.org/10.1016/B978-0-12-815732-9.00006-1>.
- [5] G. Pal, P. Rai, A. Pandey, Green synthesis of nanoparticles: A greener approach for a cleaner future, in: *Green Synthesis, Characterization and Applications of Nanoparticles*, Elsevier, 2019: pp. 1–26.
- [6] N.S. Alsaiari, F.M. Alzahrani, A. Amari, H. Osman, H.N. Harharah, N. Elboughdiri, M.A. Tahooun, Plant and Microbial Approaches as Green Methods for the Synthesis of Nanomaterials: Synthesis, Applications, and Future Perspectives, *Molecules* 28 (2023) 463.
- [7] N. Baig, I. Kammakakam, W. Falath, I. Kammakakam, Nanomaterials: A review of synthesis methods, properties, recent progress, and challenges, *Mater Adv* 2 (2021) 1821–1871. <https://doi.org/10.1039/d0ma00807a>.
- [8] A. Klinbumrung, R. Panya, A. Pung-Ngama, P. Nasomjai, J. Saowalakmekha, R. Sirirak, Green synthesis of ZnO nanoparticles by pineapple peel extract from various alkali sources, *Journal of Asian Ceramic Societies* 10 (2022) 755–765.
- [9] M.N. Javed, S.A.K. Bangash, M. Abbas, S. Ahmed, A. Kaplan, S. Iqbal, M.N. Khan, M. Adnan, A. Ali, F. Zaman, Potential and Challenges in Green Synthesis of Nanoparticles: A Review, (n.d.).
- [10] D. Kulkarni, R. Sherkar, C. Shirsathe, R. Sonwane, N. Varpe, S. Shelke, M.P. More, S.R. Pardeshi, G. Dhaneshwar, V. Junnuthula, S. Dyawanapelly, Biofabrication of nanoparticles: sources,

- synthesis, and biomedical applications, *Front Bioeng Biotechnol* 11 (2023). <https://doi.org/10.3389/fbioe.2023.1159193>.
- [11] A. Balkrishna, A. Kumar, V. Arya, A. Rohela, R. Verma, E. Nepovimova, O. Krejcar, D. Kumar, N. Thakur, K. Kuca, Phytoantioxidant Functionalized Nanoparticles: A Green Approach to Combat Nanoparticle-Induced Oxidative Stress, *Oxid Med Cell Longev* 2021 (2021). <https://doi.org/10.1155/2021/3155962>.
- [12] H. Kumar, K. Bhardwaj, K. Kuča, A. Kalia, E. Nepovimova, R. Verma, D. Kumar, Flower-based green synthesis of metallic nanoparticles: Applications beyond fragrance, *Nanomaterials* 10 (2020). <https://doi.org/10.3390/nano10040766>.
- [13] S.M.A. Alhuzali, N.M.H. Jibrin, R.J.A. Aljaber, A.O.M. ALbisher, Dates palm (*Phoenix dactylifera* L.) Fruits: Nutritional Properties and Potential Applications, *المجلة العربية للعلوم الزراعية* 6 160–137 (2023). <https://doi.org/10.21608/asajs.2023.279329>.
- [14] K. Rambabu, G. Bharath, F. Banat, P.L. Show, Green synthesis of zinc oxide nanoparticles using *Phoenix dactylifera* waste as bioreductant for effective dye degradation and antibacterial performance in wastewater treatment, *J Hazard Mater* 402 (2021) 123560.
- [15] M.A. Subhan, N. Neogi, K.P. Choudhury, Industrial Manufacturing Applications of Zinc Oxide Nanomaterials: A Comprehensive Study, *Nanomanufacturing* 2 (2022) 265–291. <https://doi.org/10.3390/nanomanufacturing2040016>.
- [16] K. Thakur, B. Kandasubramanian, Graphene and Graphene Oxide-Based Composites for Removal of Organic Pollutants: A Review, *J Chem Eng Data* 64 (2019) 833–867. <https://doi.org/10.1021/acs.jced.8b01057>.
- [17] A. Hamad Al-Marri, F. Janene INRAP, T. Sidi-Thabet Ali Moulahi, A.T. Mogharbel, E.S. Al-Farraj, A.M. Al-Mohaimeed, I. Mjejri, Enhanced Photocatalytic Properties Of The Nb₂O₅@rGO For The Degradation Of Methylene Blue, (2023). <https://doi.org/10.21203/rs.3.rs-3084238/v1>.
- [18] Y.C. Pu, H.Y. Chou, W.S. Kuo, K.H. Wei, Y.J. Hsu, Interfacial charge carrier dynamics of cuprous oxide-reduced graphene oxide (Cu₂O-rGO) nanoheterostructures and their related visible-light-driven photocatalysis, *Appl Catal B* 204 (2017) 21–32. <https://doi.org/10.1016/j.apcatb.2016.11.012>.

- [19] S. Bagheri, A. Esrafil, M. Kermani, J. Mehralipour, M. Gholami, Performance evaluation of a novel rGO-Fe₀/Fe₃O₄-PEI nanocomposite for lead and cadmium removal from aqueous solutions, *J Mol Liq* 320 (2020). <https://doi.org/10.1016/j.molliq.2020.114422>.
- [20] M.Y.S. Wen, A.H. Abdullah, L.H. Ngee, Sintesis nanohibrid ZnO/rGO untuk mempertingkatkan aktiviti fotopemangkinan, *Malaysian Journal of Analytical Sciences* 21 (2017) 889–900. <https://doi.org/10.17576/mjas-2017-2104-15>.
- [21] M. Karpuraranjith, Y. Chen, R. Manigandan, K. Srinivas, S. Rajaboopathi, Hierarchical Ultrathin Layered GO-ZnO@CeO₂ Nanohybrids for Highly Efficient Methylene Blue Dye Degradation, *Molecules* 27 (2022). <https://doi.org/10.3390/molecules27248788>.
- [22] D. Li, J. Lu, X. Zhang, D. Jin, H. Jin, Engineering of ZnO/rGO towards NO₂ Gas Detection: Ratio Modulated Sensing Type and Heterojunction Determined Response, *Nanomaterials* 13 (2023). <https://doi.org/10.3390/nano13050917>.
- [23] A.B.D. Nandiyanto, R. Zaen, R. Oktiani, Correlation between crystallite size and photocatalytic performance of micrometer-sized monoclinic WO₃ particles, *Arabian Journal of Chemistry* 13 (2020) 1283–1296. <https://doi.org/10.1016/j.arabjc.2017.10.010>.
- [24] M.A. AbuDalo, I.R. Al-Mheidat, A.W. Al-Shurafat, C. Grinham, V. Oyanedel-Craver, Synthesis of silver nanoparticles using a modified Tollens' method in conjunction with phytochemicals and assessment of their antimicrobial activity, *PeerJ* 2019 (2019). <https://doi.org/10.7717/peerj.6413>.
- [25] H.A. Matar, M.A. Ibrahim, M. El-Hagary, Simple and cost-effective route for PANI-ZnO-rGO nanocomposite as a biosensor for L-arginine detection, *Diam Relat Mater* 133 (2023). <https://doi.org/10.1016/j.diamond.2023.109703>.
- [26] M. Sour, N. Ghaemi, A. Shakeri, V. Hoseinpour, Optimization of green synthesis of ZnO nanoparticles by *Dittrichia graveolens* (L.) aqueous extract, *Health Biotechnology and Biopharma* 1 (2017) 39–49. <https://doi.org/10.22034/HBB.2017.10>.
- [27] E.A. Alzahrani, A. Nabi, M.R. Kamli, S.M. Albukhari, S.A. Althabaiti, S.A. Al-Harbi, I. Khan, M.A. Malik, Facile Green Synthesis of ZnO NPs and Plasmonic Ag-Supported ZnO Nanocomposite for Photocatalytic Degradation of Methylene Blue, *Water (Switzerland)* 15 (2023). <https://doi.org/10.3390/w15030384>.
- [28] M.L. de Peres, R. de A. Delucis, S.C. Amico, D.A. Gatto, Zinc oxide nanoparticles from microwave-assisted solvothermal process: Photocatalytic performance and use for wood protection

- against xylophagous fungus, *Nanomaterials and Nanotechnology* 9 (2019). <https://doi.org/10.1177/1847980419876201>.
- [29] G.J. Christobel, Vibrational Spectroscopy of ZnO-ZnS Nanoparticles, *International Journal of Science and Research (IJSR) ISSN 5* (2013). <https://doi.org/10.21275/v5i6.NOV164755>.
- [30] S. Heena Khan, S. R. B. Pathak, M.H. Fulekar, Photocatalytic degradation of organophosphate pesticides (Chlorpyrifos) using synthesized zinc oxide nanoparticle by membrane filtration reactor under UV irradiation, *Frontiers in Nanoscience and Nanotechnology* 1 (2015) 23–27. <https://doi.org/10.15761/fnn.1000105>.
- [31] C.A. Jaramillo-Páez, J.A. Navío, M.C. Hidalgo, M. Macías, ZnO and Pt-ZnO photocatalysts: Characterization and photocatalytic activity assessing by means of three substrates, *Catal Today* 313 (2018) 12–19. <https://doi.org/10.1016/j.cattod.2017.12.009>.
- [32] K.P. Misra, A. Kumawat, P. Kumari, S. Samanta, N. Halder, S. Chattopadhyay, Band Gap Reduction and Petal-like Nanostructure Formation in Heavily Ce-doped ZnO Nanopowders, *Journal of Nano- and Electronic Physics* 13 (2021) 1–5. [https://doi.org/10.21272/jnep.13\(2\).02008](https://doi.org/10.21272/jnep.13(2).02008).
- [33] E. Üstün, S.C. Önbay, S.K. Çelik, M.Ç. Ayvaz, N. Şahin, Green synthesis of iron oxide nanoparticles by using ficus carica leaf extract and its antioxidant activity, *Biointerface Res Appl Chem* 12 (2022) 2108–2116. <https://doi.org/10.33263/BRIAC122.21082116>.
- [34] K.G. Chandrappa, T. V. Venkatesha, Electrochemical synthesis and photocatalytic property of zinc oxide nanoparticles, *Nanomicro Lett* 4 (2012) 14–24. <https://doi.org/10.3786/nml.v4i1.p14-24>.
- [35] V. Sharma, J.K. Sharma, V. Kansay, V.D. Sharma, A. Sharma, S. Kumar, A.K. Sharma, M.K. Bera, The effect of calcination temperatures on the structural and optical properties of zinc oxide nanoparticles and their influence on the photocatalytic degradation of leather dye, *Chemical Physics Impact* 6 (2023). <https://doi.org/10.1016/j.chphi.2023.100196>.
- [36] H.N. Tien, V.H. Luan, L.T. Hoa, N.T. Khoa, S.H. Hahn, J.S. Chung, E.W. Shin, S.H. Hur, One-pot synthesis of a reduced graphene oxide-zinc oxide sphere composite and its use as a visible light photocatalyst, *Chemical Engineering Journal* 229 (2013) 126–133. <https://doi.org/10.1016/j.cej.2013.05.110>.
- [37] S. Xu, L. Fu, T.S.H. Pham, A. Yu, F. Han, L. Chen, Preparation of ZnO flower/reduced graphene oxide composite with enhanced photocatalytic performance under sunlight, *Ceram Int* 41 (2015) 4007–4013. <https://doi.org/10.1016/j.ceramint.2014.11.086>.

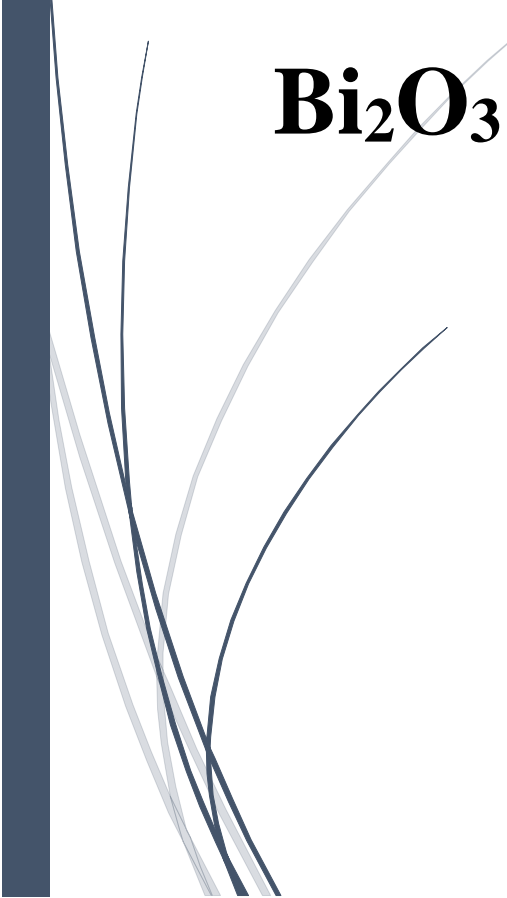
- [38] H.R. Liu, G.X. Shao, J.F. Zhao, Z.X. Zhang, Y. Zhang, J. Liang, X.G. Liu, H.S. Jia, B.S. Xu, Worm-like Ag/ZnO core-shell heterostructural composites: Fabrication, characterization, and photocatalysis, *Journal of Physical Chemistry C* 116 (2012) 16182–16190. <https://doi.org/10.1021/jp2115143>.
- [39] J. Fang, H. Fan, G. Dong, A facile way to synthesize cost-effective ZnO nanorods with enhanced photocatalytic activity, *Mater Lett* 120 (2014) 147–150. <https://doi.org/10.1016/j.matlet.2014.01.043>.
- [40] M.K. Guediri, D. Chebli, A. Bouguettoucha, R. Bourzami, A. Amrane, Novel Fe₂TiO₅/reduced graphene oxide heterojunction photocatalyst with improved adsorption capacity and visible light photoactivity: experimental and DFT approach, *Environmental Science and Pollution Research* 28 (2021) 8507–8519. <https://doi.org/10.1007/s11356-020-11221-0>.
- [41] N.H.M. Kaus, A.F. Rithwan, R. Adnan, M.L. Ibrahim, S. Thongmee, S.F.M. Yusoff, Effective strategies, mechanisms, and photocatalytic efficiency of semiconductor nanomaterials incorporating rgo for environmental contaminant degradation, *Catalysts* 11 (2021) 1–27. <https://doi.org/10.3390/catal11030302>.
- [42] R. Garg, R. Gupta, N. Singh, A. Bansal, Characterization and performance evaluation of synthesized ZnO nanoflowers, nanorods, and their hybrid nanocomposites with graphene oxide for degradation of Orange G, *Environmental Science and Pollution Research* 28 (2021) 57009–57029. <https://doi.org/10.1007/s11356-021-14511-3>.
- [43] F. Zhou, C. Yan, T. Liang, Q. Sun, H. Wang, Photocatalytic degradation of Orange G using sepiolite-TiO₂ nanocomposites: Optimization of physicochemical parameters and kinetics studies, *Chem Eng Sci* 183 (2018) 231–239. <https://doi.org/10.1016/j.ces.2018.03.016>.
- [44] R. Ahmad, P.K. Mondal, Adsorption and Photodegradation of Methylene Blue by Using PANi/TiO₂ Nanocomposite, *J Dispers Sci Technol* 33 (2012) 380–386. <https://doi.org/10.1080/01932691.2011.567172>.
- [45] M.S. Raghu, L. Parashuram, M.K. Prashanth, K.Y. Kumar, C.B.P. Kumar, H. Alrobei, Simple in-situ functionalization of polyaniline with boroncarbonitride as potential multipurpose photocatalyst: Generation of hydrogen, organic and inorganic pollutant detoxification, *Nano-Structures and Nano-Objects* 25 (2021). <https://doi.org/10.1016/j.nanoso.2021.100667>.

- [46] R. Sánchez-Albores, F.J. Cano, P.J. Sebastian, O. Reyes-Vallejo, Microwave-assisted biosynthesis of ZnO-GO particles using orange peel extract for photocatalytic degradation of methylene blue, *J Environ Chem Eng* 10 (2022). <https://doi.org/10.1016/j.jece.2022.108924>.
- [47] R.H. Waghchaure, V.A. Adole, B.S. Jagdale, Photocatalytic degradation of methylene blue, rhodamine B, methyl orange and Eriochrome black T dyes by modified ZnO nanocatalysts: A concise review, *Inorg Chem Commun* 143 (2022). <https://doi.org/10.1016/j.inoche.2022.109764>.
- [48] S. Ma, Y. Huang, R. Hong, X. Lu, J. Li, Y. Zheng, Enhancing photocatalytic activity of zno nanoparticles in a circulating fluidized bed with plasma jets, *Catalysts* 11 (2021) 1–15. <https://doi.org/10.3390/catal11010077>.
- [49] B. Rodríguez-Cabo, I. Rodríguez-Palmeiro, R. Corchero, R. Rodil, E. Rodil, A. Arce, A. Soto, Photocatalytic degradation of methyl orange, methylene blue and rhodamine B with AgCl nanocatalyst synthesised from its bulk material in the ionic liquid [P6 6 6 14]Cl, *Water Science and Technology* 75 (2017) 128–140. <https://doi.org/10.2166/wst.2016.499>.
- [50] S. Ghaffar, A. Abbas, M. Naeem-ul-Hassan, N. Assad, M. Sher, S. Ullah, H.A. Alhazmi, A. Najmi, K. Zoghebi, M. Al Bratty, A. Hanbashi, H.A. Makeen, H.M.A. Amin, Improved Photocatalytic and Antioxidant Activity of Olive Fruit Extract-Mediated ZnO Nanoparticles, *Antioxidants* 12 (2023). <https://doi.org/10.3390/antiox12061201>.
- [51] M. Azarang, A. Shuhaimi, R. Yousefi, S.P. Jahromi, One-pot sol–gel synthesis of reduced graphene oxide uniformly decorated zinc oxide nanoparticles in starch environment for highly efficient photodegradation of Methylene Blue, *RSC Adv.* 5 (2015) 21888–21896. <https://doi.org/10.1039/C4RA16767H>.
- [52] V. V Gawade, S.R. Sabale, R.S. Dhabbe, S. V Kite, K.M. Garadkar, Bio-mediated synthesis of ZnO nanostructures for efficient photodegradation of methyl orange and methylene blue, *Journal of Materials Science: Materials in Electronics* 32 (2021) 28573–28586. <https://doi.org/10.1007/s10854-021-07235-0>.
- [53] R. Shahzad, M. Muneer, R. Khalid, H.M.A. Amin, ZnO-Bi₂O₃ Heterostructured Composite for the Photocatalytic Degradation of Orange 16 Reactive Dye: Synergistic Effect of UV Irradiation and Hydrogen Peroxide, *Catalysts* 13 (2023). <https://doi.org/10.3390/catal13101328>.



Chapter IV

First-Time Green Synthesis, Characterization, and Photocatalytic Activity of $\text{Bi}_{12}\text{ZnO}_{20}$, Bi_2O_3 and $\text{Bi}_{12}\text{ZnO}_{20}/\text{Bi}_2\text{O}_3$



Chapter IV. First-Time Green Synthesis, Characterization, and Photocatalytic Activity of $\text{Bi}_{12}\text{ZnO}_{20}$, Bi_2O_3 and $\text{Bi}_{12}\text{ZnO}_{20}/\text{Bi}_2\text{O}_3$

IV.1. Introduction

Photocatalysis has emerged as a highly effective technology for the degradation of organic pollutants, providing sustainable solutions for water purification and wastewater treatment [1]. By harnessing light energy to produce reactive radicals capable of decomposing contaminants, this approach demonstrates significant environmental potential [2]. However, current photocatalysts face limitations, particularly low efficiency under visible light and rapid charge carrier recombination, which hinder their performance [3]. Therefore, ongoing research is essential to address these challenges. The development of new advanced semiconductors with enhanced light absorption properties and improved charge separation kinetics is crucial to optimizing photocatalytic efficiency and enabling widespread industrial application.

Bismuth oxide (Bi_2O_3) is a material of considerable versatility, existing in several distinct polymorphic forms, each exhibiting unique characteristics [4]. At lower temperatures, Bi_2O_3 adopts a monoclinic phase ($\alpha\text{-Bi}_2\text{O}_3$) [5]. As the temperature increases to 730 °C, $\alpha\text{-Bi}_2\text{O}_3$ transitions to a cubic phase ($\delta\text{-Bi}_2\text{O}_3$) [6], which remains stable up to its melting point at 825 °C. Upon cooling, $\delta\text{-Bi}_2\text{O}_3$ can transform into two metastable phases: the tetrahedral phase ($\beta\text{-Bi}_2\text{O}_3$) or the face-centered cubic phase ($\gamma\text{-Bi}_2\text{O}_3$) [7]. The $\gamma\text{-Bi}_2\text{O}_3$ phase, also known as sillenite, is stabilized by a small amount of various impurities and forms a compound with a structure of the type $\text{Bi}_{12}\text{MxO}_{20\pm d}$ [8], where M represents elements from groups II–V of the periodic table (e.g., Zn, Pb, Al, Si, Ge) [9]. The oxidation states of the cation M range from +2 to +5, and the sillenite structure maintains charge balance through local distortions within the bismuth-oxygen framework [10].

These bismuth sillenites, especially $\text{Bi}_{12}\text{ZnO}_{20}$, are highly valued for their diverse optical properties, including photorefractive, electro-optical, photochromic, and photocatalytic characteristics [11]. Their efficacy as photocatalysts under visible light is particularly noteworthy, making them significant for environmental applications aimed at pollutant degradation [12]. Bismuth oxide's advantageous optical and electronic properties, such as its ability to absorb visible light and generate free radicals, are crucial for effective photocatalysis.

The growing interest in nanomaterials further amplifies the potential of bismuth oxide in enhancing photocatalytic processes [13].

Recent advancements in semiconductor coupling technology have proven to be a highly effective approach for improving the separation of photo-generated electron-hole pairs, thereby enhancing photocatalytic performance [14]. This strategy has been shown to significantly boost the efficiency of photocatalysts by facilitating better charge carrier separation, which is crucial for achieving higher photocatalytic activity [15]. By integrating different semiconductor materials, it is possible to exploit synergies between their distinct properties, leading to superior photocatalytic capabilities compared to individual semiconductors [16].

The synthesis of Bi_2O_3 and $\text{Bi}_{12}\text{ZnO}_{20}$ nanoparticles has been extensively explored through a variety of methods, including sol-gel combustion, co-precipitation, combustion, solvothermal, thermal decomposition, seed growth, hydrothermal techniques. With increasing environmental concerns, there is a rising interest in eco-friendly synthesis approaches for inorganic materials. These green synthesis methods typically involve using natural extracts as stabilizing agents and water as a solvent, offering a more sustainable and environmentally conscious alternative to traditional preparation techniques.

This chapter presents an innovative study on the green synthesis of $\text{Bi}_{12}\text{ZnO}_{20}$ -type selenite, with in-depth characterization by XRD, FTIR, SEM, and energy gap analysis. The initial results obtained revealed promising photocatalytic activity in the degradation of the Beibrich Scarlet dye. To optimize the catalytic efficiency of $\text{Bi}_{12}\text{ZnO}_{20}$, the addition of Bi_2O_3 was carried out, maintaining the same synthesis method and varying the percentages of Bi_2O_3 . This approach achieved complete degradation of BS in 80 minutes, demonstrating a significant improvement in photocatalytic performance.

IV.2. Experiment

IV.2.1. Prickly pear peel extract preparation

The preparation of the prickly pear peel extract was carried out through the following steps: Initially, the peel was thoroughly washed three times with distilled water. The washed peel was then air-dried until completely dehydrated. Once fully dried, it was subjected to double grinding to obtain a very fine powder. A quantity of 10 g of this powder was dispersed in 200 mL of

distilled water, followed by stirring for 10 minutes. The mixture was then exposed to ultrasonic treatment for 15 minutes at 40°C. After sonication, the solution was filtered and subsequently centrifuged for 10 minutes at a speed of 10,000 rpm. A portion of 20 mL of the supernatant was used for material synthesis, while the remainder was dried in an oven at 40°C to produce a paste for further characterization of the extract.

IV.2.2. Synthesis of $\text{Bi}_{12}\text{ZnO}_{20}$ and Bi_2O_3

The synthesis of $\text{Bi}_{12}\text{ZnO}_{20}$ begins with the dissolution of 0.12 mol of bismuth nitrate in 50 mL of a 5% nitric acid solution. Simultaneously, 0.01 mol of zinc acetate is dissolved in 30 mL of distilled water. After complete dissolution of both salts, the zinc solution is added dropwise to the bismuth solution under continuous stirring. Following this, the previously prepared prickly pear peel extract is also added dropwise to the mixture, while maintaining strong agitation and heating at 50°C for 60 minutes. The mixture is then left under stirring at room temperature for 12 hours, during which a white precipitate forms. The precipitate is transferred to a 100 mL autoclave and heated in an oven at 120°C for 12 hours to promote the formation of the sillenite phase with enhanced crystallinity. After the thermal treatment, the material is washed three times with a 50/50 water-ethanol mixture, followed by a fourth wash using distilled water alone. The product is then dried in an oven at 60°C for 24 hours. The first calcination is carried out at 200°C in 12 hours. Subsequently, the material is divided into three portions, each subjected to a second calcination at 400, 500, and 600°C, respectively, in order to investigate the influence of temperature on the material's final properties.

The synthesis of bismuth oxide Bi_2O_3 follows the same steps as for $\text{Bi}_{12}\text{ZnO}_{20}$, except that zinc acetate is omitted. After drying, the material undergoes a single calcination step at 600°C.

The $\text{Bi}_{12}\text{ZnO}_{20}/\text{Bi}_2\text{O}_3$ composite was prepared by mechanical mixing of $\text{Bi}_{12}\text{ZnO}_{20}$ and Bi_2O_3 in different weight proportions to optimize photocatalytic performance. Four distinct compositions were formulated, namely 95% $\text{Bi}_{12}\text{ZnO}_{20}$ /5% Bi_2O_3 , 90% $\text{Bi}_{12}\text{ZnO}_{20}$ /10% Bi_2O_3 , 85% $\text{Bi}_{12}\text{ZnO}_{20}$ /15% Bi_2O_3 , and 80% $\text{Bi}_{12}\text{ZnO}_{20}$ /20% Bi_2O_3 . The two components were precisely weighed according to the desired proportions, then mixed using a mortar. This grinding allows for a homogeneous dispersion of Bi_2O_3 particles in the $\text{Bi}_{12}\text{ZnO}_{20}$ matrix, promoting optimal interaction between the phases to enhance the photocatalytic reactivity of the final composite.

IV.3. Characterization Results

IV.3.1. FTIR

The FTIR results reveal distinct features for each compound studied. For Bi₂O₃, the peak observed at 678.24 cm⁻¹ corresponds to the typical Bi-O bond vibrations which are commonly found in the 400-800 cm⁻¹ range in infrared spectroscopy [17]. This sharp band suggests a well-defined crystalline structure with uniform Bi-O bonds, indicative of a stable and ordered arrangement [18]. In the case of Bi₁₂ZnO₂₀, a broad peak at 725.85 cm⁻¹ is attributed to both Zn-O and Bi-O bond vibrations, typically located between 400-700 cm⁻¹ and 400-800 cm⁻¹, respectively. This suggests a more complex crystalline structure, possibly reflecting the interaction between these two types of bonds [19]. Additionally, the peak at 1089.46 cm⁻¹ could be associated with phonon vibrations, secondary vibrational modes, or specific structural defects within the Bi₁₂ZnO₂₀ compound, hinting at deviations from perfect crystallinity [20].

In the mixed compound Bi₁₂ZnO₂₀/Bi₂O₃, the peak at 706.97 cm⁻¹ likely represents hybrid vibrational modes arising from the interaction between Bi₁₂ZnO₂₀ and Bi₂O₃. This suggests that the coupling of these two compounds leads to new vibrational characteristics that differ from those of the individual components. The small peak observed at 1079 cm⁻¹, while similar to the peak in Bi₁₂ZnO₂₀, indicates subtle changes in the vibrational modes of Bi₁₂ZnO₂₀ due to its interaction with Bi₂O₃. These findings highlight the complex interactions between the compounds and suggest possible structural modifications resulting from these interactions, contributing to the unique properties of the composite material.

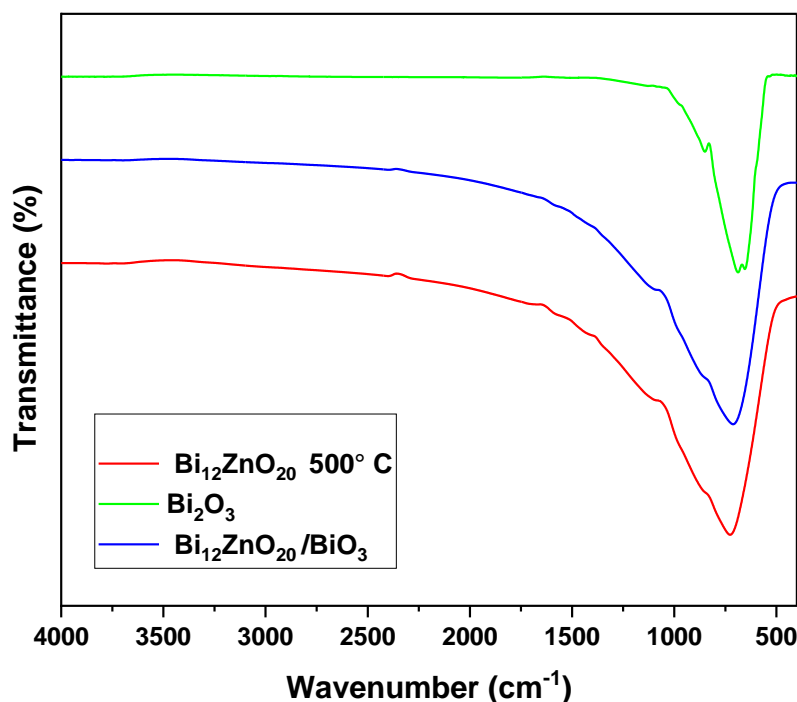


Figure IV.1. FTIR spectra of $\text{Bi}_{12}\text{ZnO}_{20}$, Bi_2O_3 and $\text{Bi}_{12}\text{ZnO}_{20}/\text{Bi}_2\text{O}_3$.

IV.3.2. The X-ray diffraction XRD

The XRD data for Bi_2O_3 reveal a series of well-defined peaks, primarily observed at 2θ angles of 26° , 27° , 27.5° , 27.7° , 28.1° , 33.3° , 35.2° , 37.66° , 46.5° , 48.7° , 52.6° , 58° , and 94.5° , with the most intense peak occurring at 27.5° . These diffraction peaks are characteristic of the α - Bi_2O_3 phase [6], a monoclinic structure that is commonly stable at room temperature. The sharpness and distinct nature of the peaks suggest a high degree of crystallinity in the sample, with the α phase being the predominant form under the experimental conditions [21]. Although other polymorphs of Bi_2O_3 , such as β (tetragonal), γ (cubic), and δ (cubic), may exhibit similar diffraction patterns, the dominance of the α -phase is strongly supported by the matching peak intensities and positions [22].

In the case of $\text{Bi}_{12}\text{ZnO}_{20}$, the XRD pattern reveals characteristic diffraction peaks at 2θ angles of 27.7° , 26° , 27° , 27.5° , 28.1° , 29.3° , and 30.6° , along with additional peaks at 33.3° , 35.2° , 37.66° , 46.5° , 48.7° , 52.6° , 58° , and 94.5° . These peaks align closely with standard diffraction data for $\text{Bi}_{12}\text{ZnO}_{20}$, confirming the presence of a well-ordered crystalline phase [23]. The slightly

broadener peak profiles in comparison to Bi_2O_3 may indicate the presence of structural complexity or slight variations in the lattice due to the incorporation of zinc atoms, which can modify the bond lengths and lattice parameters in the crystal structure [24].

When the two materials, $\text{Bi}_{12}\text{ZnO}_{20}$ and Bi_2O_3 , are combined, the resulting XRD pattern closely resembles that of $\text{Bi}_{12}\text{ZnO}_{20}$ alone, with diffraction peaks appearing at nearly identical 2θ positions. The peaks corresponding to the mixed sample primarily reflect the crystalline structure of $\text{Bi}_{12}\text{ZnO}_{20}$, which constitutes 90% of the mixture. The minor presence of Bi_2O_3 (10%) does not significantly alter the dominant crystalline phase, as evidenced by the persistence of $\text{Bi}_{12}\text{ZnO}_{20}$'s characteristic peaks. The lack of significant shifts or additional peaks suggests that the Bi_2O_3 phase remains relatively amorphous or poorly crystalline in the mixture, while $\text{Bi}_{12}\text{ZnO}_{20}$ retains its structural integrity as the primary component. This finding underscores the dominant role of $\text{Bi}_{12}\text{ZnO}_{20}$ in the mixed sample, with minimal disruption from the small proportion of Bi_2O_3 . These observations confirm the high degree of crystallinity and stability of $\text{Bi}_{12}\text{ZnO}_{20}$ in the mixture, while the presence of Bi_2O_3 , though detectable, does not substantially impact the overall diffraction pattern or the structural characteristics of the composite.

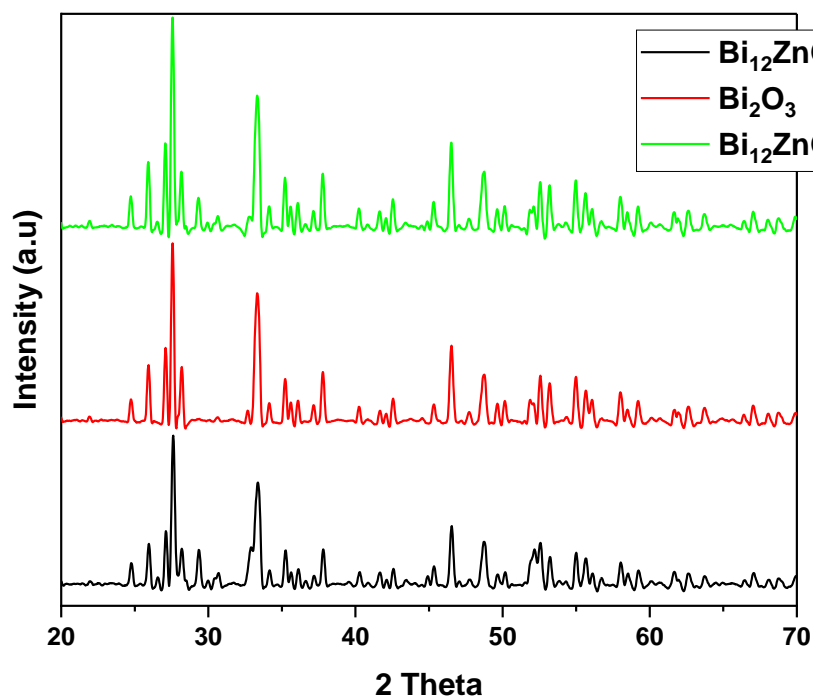


Figure IV.2. XRD patterns of $\text{Bi}_{12}\text{ZnO}_{20}$, Bi_2O_3 , and the composite $\text{Bi}_{12}\text{ZnO}_{20}/\text{Bi}_2\text{O}_3$.

Table IV.1. The average crystallize size and lattice parameter of $\text{Bi}_{12}\text{ZnO}_{20}$, Bi_2O_3 and $\text{Bi}_{12}\text{ZnO}_{20}/\text{Bi}_2\text{O}_3$.

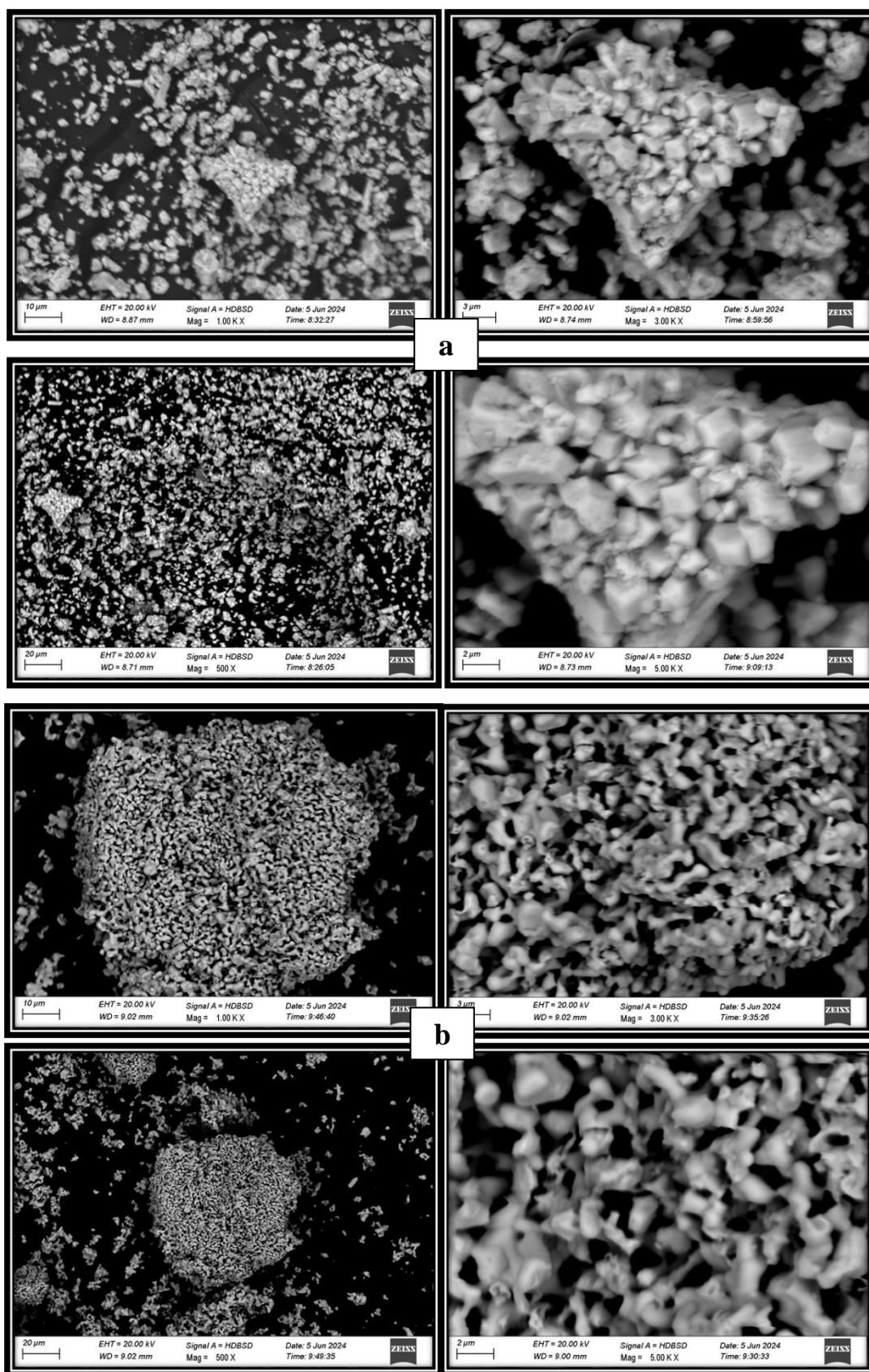
2 Theta	intesty	FWHM	d (hkl)	a	c	D	D moy (nm)
27.61745	22.84437	0.3083	0.322732	0.372658		26.53496	
33.30744	19.5979	0.50571	0.268784		0.537568	16.39696	17.6638755
52.32021	14.03597	0.87984	0.174718			10.0597	
27.54745	19.04628	0.27414	0.323536	0.373587		29.83695	
33.3144	22.5479	0.36205	0.26873		0.537459	22.90363	19.7672036
52.60021	11.83597	1.35064	0.173854			6.561031	
27.56971	23.22683	0.27456	0.32328	0.373291		29.79273	
33.31119	22.64648	0.35425	0.268755		0.53751	23.40773	25.8696506
46.50773	10.09773	0.35425	0.195109			24.40849	

The crystallite sizes for $\text{Bi}_{12}\text{ZnO}_{20}$ (17.66 nm), Bi_2O_3 (19.77 nm), and their physical mixture (25.86 nm) are presented in Table IV.1. In a physical mixture, the crystallites of both compounds can interact in a complex manner, especially when the materials are well-dispersed and mixed at the nanometric scale. The crystallite size in the mixture may increase compared to the individual components due to partial agglomeration or particle reorganization, driven by the interaction between the two phases. Additionally, contact zones between crystallites may form through mixing, resulting in stronger interactions that can alter the overall morphology and the observed particle size.

IV.3.3. Scanning electron microscopy images (SEM)

SEM images presented in Figures a, b, and c illustrate the surface morphology of the samples $\text{Bi}_{12}\text{ZnO}_{20}$, Bi_2O_3 , and the composite $\text{Bi}_{12}\text{ZnO}_{20}/\text{Bi}_2\text{O}_3$, respectively, with magnifications of 20, 10, 3, and 2 micrometers. The image of $\text{Bi}_{12}\text{ZnO}_{20}$ highlights well-defined cubic crystals characteristic of the sillenite phase, confirming the expected crystalline structure for this compound. These cubic crystals exhibit clear and regular features, typical of sillenite, reflecting the high quality of crystallization.

In contrast, the image of Bi_2O_3 reveals a heterogeneous morphology with structures resembling worm-like formations, indicative of a semi-amorphous structure. For the $\text{Bi}_{12}\text{ZnO}_{20}/\text{Bi}_2\text{O}_3$ composite, the cubic shape of $\text{Bi}_{12}\text{ZnO}_{20}$ is maintained, with visible surface irregularities suggesting that Bi_2O_3 is deposited on the surface of the $\text{Bi}_{12}\text{ZnO}_{20}$ crystals. This observation confirms the formation of the composite and the interaction between the two distinct phases.



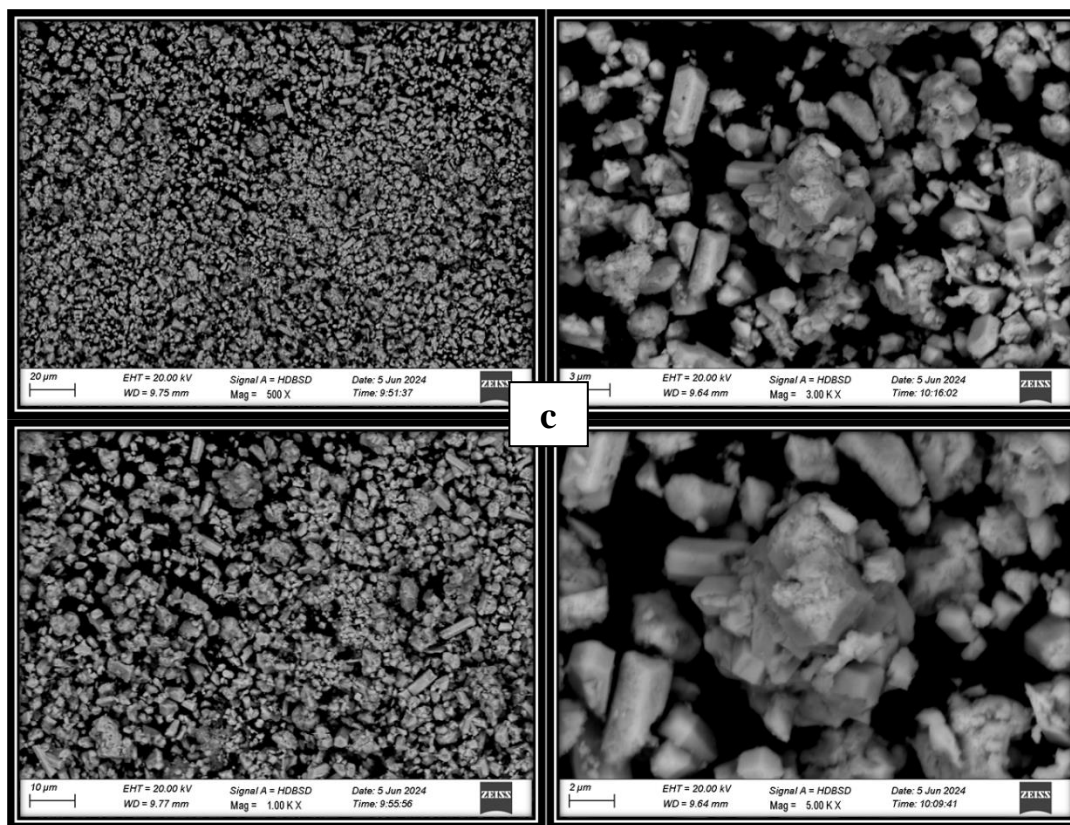


Figure IV.3. MEB image of (a) $\text{Bi}_{12}\text{ZnO}_{20}$, (b) Bi_2O_3 and (c) $\text{Bi}_{12}\text{ZnO}_{20}/\text{Bi}_2\text{O}_3$.

IV.3.4. The bandgap energies

The bandgap energies obtained for Bi_2O_3 (2.95 eV), $\text{Bi}_{12}\text{ZnO}_{20}$ (3.06 eV), and the $\text{Bi}_{12}\text{ZnO}_{20}/\text{Bi}_2\text{O}_3$ composite (3.01 eV) indicate that these materials absorb light in different regions of the spectrum. The composite's intermediate bandgap value of 3.01 eV confirms the successful formation of the composite material. Bi_2O_3 , with a bandgap of 2.95 eV, is primarily activated by visible light, while $\text{Bi}_{12}\text{ZnO}_{20}$ (3.06 eV) is more suitable for UV irradiation.

These results align with the literature, where Bi_2O_3 is often recognized for its performance under visible light, and $\text{Bi}_{12}\text{ZnO}_{20}$, with its slightly higher bandgap, is typically used under UV light. The composite combines the advantages of both materials, enhancing its efficiency across a broader spectrum, making it a promising candidate for photocatalytic applications under UV-visible irradiation.

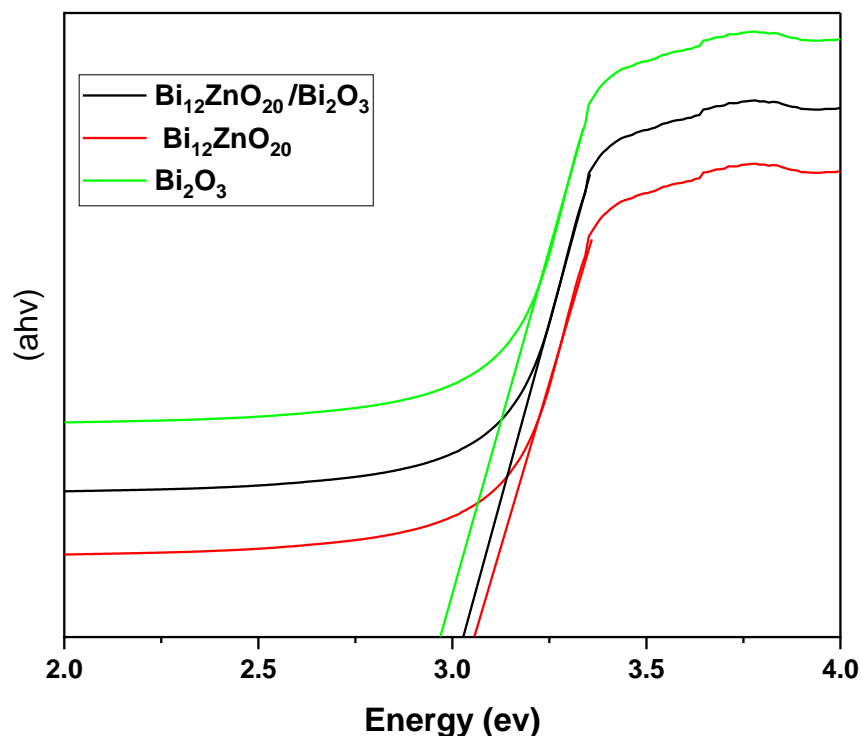


Figure IV.4. Band Gap Energy for Various Samples.

IV.4. Photocatalytic results

IV.4.1. Effect of calcination temperature on the photocatalytic activity of $\text{Bi}_{12}\text{ZnO}_{20}$

The results indicate that the calcination temperature significantly impacts the photocatalytic activity of $\text{Bi}_{12}\text{ZnO}_{20}$. After an initial calcination at 200 °C, a second calcination was performed at three different temperatures: 400 °C, 500 °C, and 600 °C. The observed photocatalytic degradation rates under UV irradiation were 70% ($k = 0.0297 \text{ min}^{-1}$) at 400 °C, 84% ($k = 0.0337 \text{ min}^{-1}$) at 500 °C, and 79% ($k = 0.0299 \text{ min}^{-1}$) at 600 °C after 100 minutes. At 400 °C, the degradation rate is 70%, suggesting that the sillenite phase is not fully developed at this temperature [25], limiting the photocatalytic efficiency. At 500 °C, the degradation rate improves to 84%, indicating that the formation of the sillenite phase is optimized at this temperature [23]. This temperature allows for more complete crystallization of the material, thereby significantly enhancing its photocatalytic performance [26].

However, at 600 °C, the photocatalytic degradation decreases slightly to 79%. Although this temperature promotes further crystallization, excessive heating may cause crystal agglomeration or structural modifications that could reduce the available active surface area for photocatalysis [27]. In summary, a calcination temperature of 500 °C appears to be most favorable for maximizing photocatalytic activity due to optimal sillenite phase formation and increased active surface area. Higher temperatures, while enhancing crystallization, may lead to negative effects on photocatalytic efficiency.

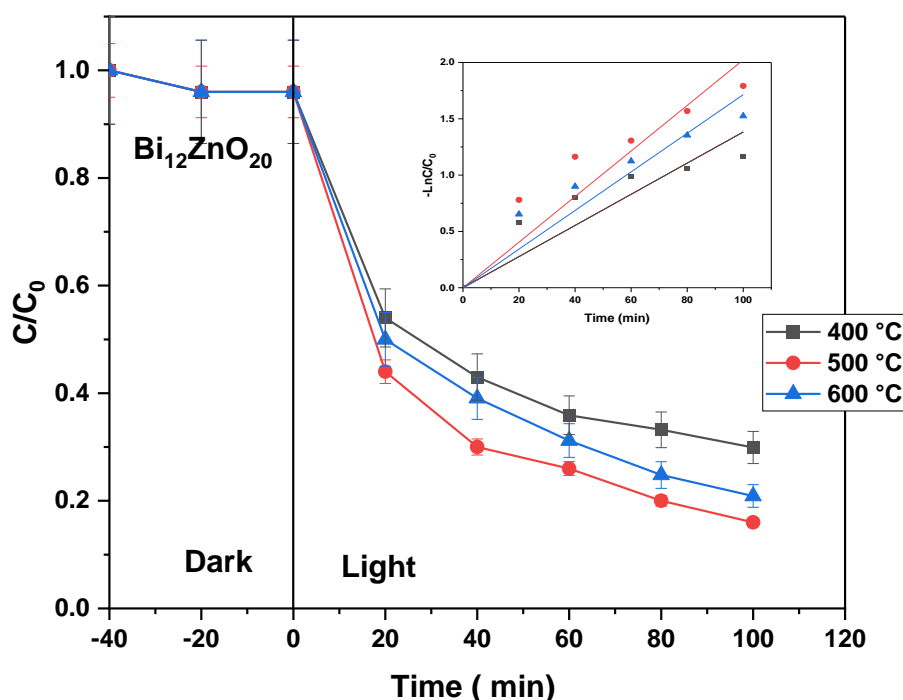


Figure IV.5. Influence of Calcination Temperature on $\text{Bi}_{12}\text{ZnO}_{20}$'s Photocatalytic Efficiency for BS Degradation under Neutral pH Conditions (1 g/L Catalyst, 20 mg/L MB).

IV.4.2. Photocatalytic activity of $\text{Bi}_{12}\text{ZnO}_{20}/\text{Bi}_2\text{O}_3$ (X/Y)

The experimental results of the photocatalytic degradation of Beibrich Scarlet (BS) using various photocatalysts revealed distinct performances for the materials studied. Bi_2O_3 alone demonstrated a degradation efficiency of 66% ($k = 0.02262 \text{ min}^{-1}$) for BS in 100 minutes, suggesting moderate photocatalytic activity, potentially limited by the high recombination rate of photogenerated charge carriers [28]. In contrast, $\text{Bi}_{12}\text{ZnO}_{20}$ alone exhibited better performance

with an 84% ($k = 0.0337 \text{ min}^{-1}$) degradation in 100 minutes, indicating an enhanced ability to separate and transfer charges, thus reducing carrier recombination.

For the composites, the Bi₁₂ZnO₂₀/Bi₂O₃ mixture with a 95% Bi₁₂ZnO₂₀ and 5% Bi₂O₃ ratio achieved a degradation of 93% in 100 minutes. This result illustrates that even a small concentration of Bi₂O₃ improves the photocatalytic activity of Bi₁₂ZnO₂₀, possibly by reducing recombination sites or increasing adsorption. The optimal ratio of 90% Bi₁₂ZnO₂₀ and 10% Bi₂O₃ enabled a complete 100% (0.6314 min^{-1}) degradation of BS in just 80 minutes. This finding demonstrates that 10% Bi₂O₃ maximizes photocatalytic efficiency by minimizing carrier recombination while maintaining the high performance [15] of Bi₁₂ZnO₂₀.

In comparison, the Bi₁₂ZnO₂₀/Bi₂O₃ ratio of 85%/15% resulted in an 89% degradation in 100 minutes, showing a slight decrease in efficiency relative to the optimal ratio, possibly due to the introduction of additional recombination centers or unfavorable interactions between the components. Similarly, the ratio of 80% Bi₁₂ZnO₂₀ and 20% Bi₁₂ZnO₂₀/Bi₂O₃ produced an 86% degradation in 100 minutes, indicating that higher proportions of Bi₂O₃ may reduce efficiency, probably by increasing recombination centers or disrupting component interactions.

Regarding the physical mixing technology, the use of Bi₁₂ZnO₂₀ and Bi₂O₃ in a physical blend achieved complete 100% degradation of BS in 80 minutes. This result suggests that the physical combination of the two photocatalysts is effective, likely due to a synergistic interaction that optimizes charge separation. However, physical mixing technology may not guarantee optimal interfacial contact, which could limit efficiency in some cases [29]. Nonetheless, in this context, the physical mixture demonstrated remarkable performance.

The addition of Bi₂O₃ to Bi₁₂ZnO₂₀ significantly enhances photocatalytic activity compared to individual photocatalysts. The 90% Bi₁₂ZnO₂₀ and 10% Bi₂O₃ ratio is identified as optimal, providing complete degradation of BS in 80 minutes, underscoring the importance of balancing components to maximize photocatalytic efficiency.

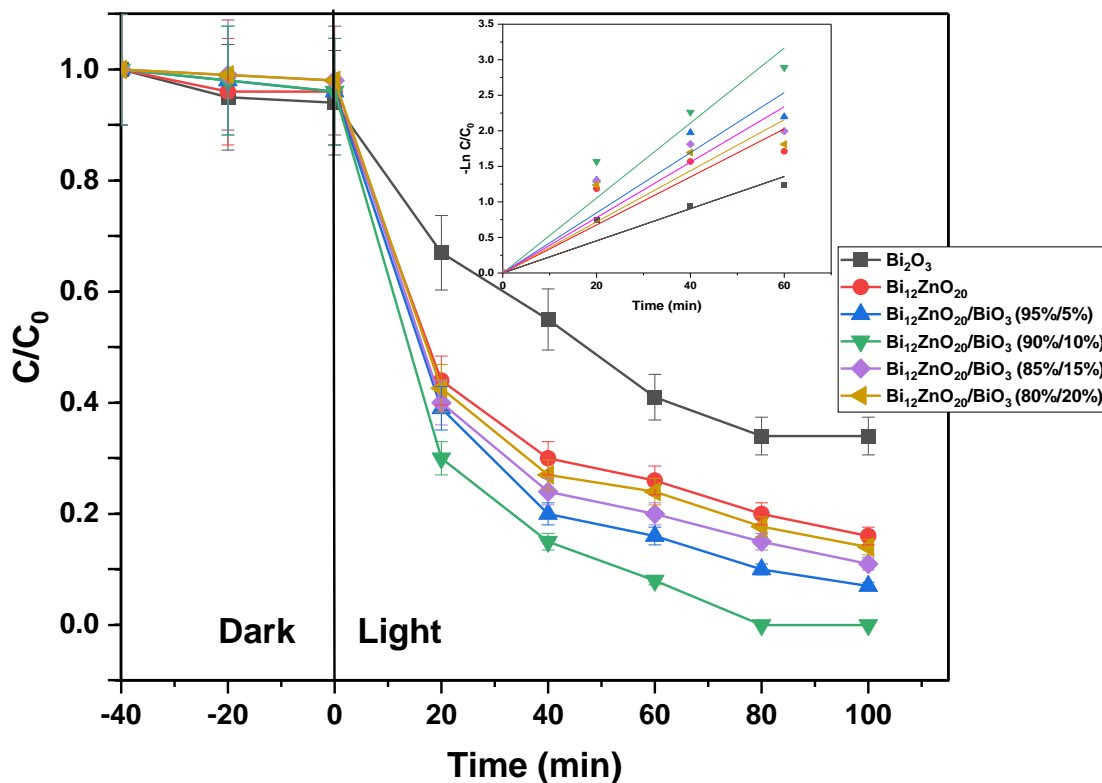


Figure IV.6. Photocatalytic degradation of BS dye by $\text{Bi}_{12}\text{ZnO}_{20}/\text{Bi}_2\text{O}_3$ (X/Y) (neutral pH, [BS] = 20mg/L, catalyst dose = 1g/L).

IV.4.3. Catalyst dosage effect

The study of the effect of catalyst dosage of $\text{Bi}_{12}\text{ZnO}_{20}/\text{Bi}_2\text{O}_3$ (90/10) on the degradation of BS reveals a direct relationship between catalyst concentration and photocatalytic efficiency. For a dose of 0.5 g/L, a degradation of 77.5% (0.03654 min^{-1}) of BS is observed after 100 minutes of UV irradiation. Increasing the dose to 1 g/L results in 100% (0.06314 min^{-1}) degradation within 80 minutes. A further increase in the dose to 1.5 g/L and 2 g/L reduces the degradation time to 60 and 40 minutes with constant rate 0.08509 min^{-1} and 0.14785 min^{-1} , respectively, while maintaining a complete degradation rate. This improvement with increasing catalyst dose is attributed to a greater availability of active sites on the catalyst surface, which promotes the increased generation of hydroxyl radicals ($\bullet\text{OH}$) and superoxide radicals ($\bullet\text{O}_2^-$) [30]. These radicals are essential for attacking BS molecules, accelerating their degradation. However, it is

important to note that the reduction in degradation time becomes less significant beyond a certain concentration. For instance, between 1.5 g/L and 2 g/L, the gain in efficiency is only 20 minutes, compared to the 20 minutes gained between 1 g/L and 1.5 g/L. For economic and practical reasons, a dose of 1 g/L has been chosen for further experiments. This concentration achieves complete degradation of BS while minimizing the required amount of catalyst. Increasing the dose beyond this value does not provide a sufficiently significant advantage to justify the additional use of photocatalytic material, especially since higher doses may lead to saturation of active sites, thereby limiting overall efficiency. At higher concentrations, catalyst agglomeration can reduce the specific surface area, thus diminishing photo-absorption efficiency and increasing treatment costs. Therefore, a dose of 1 g/L represents an optimal compromise between photocatalytic performance and economic feasibility.

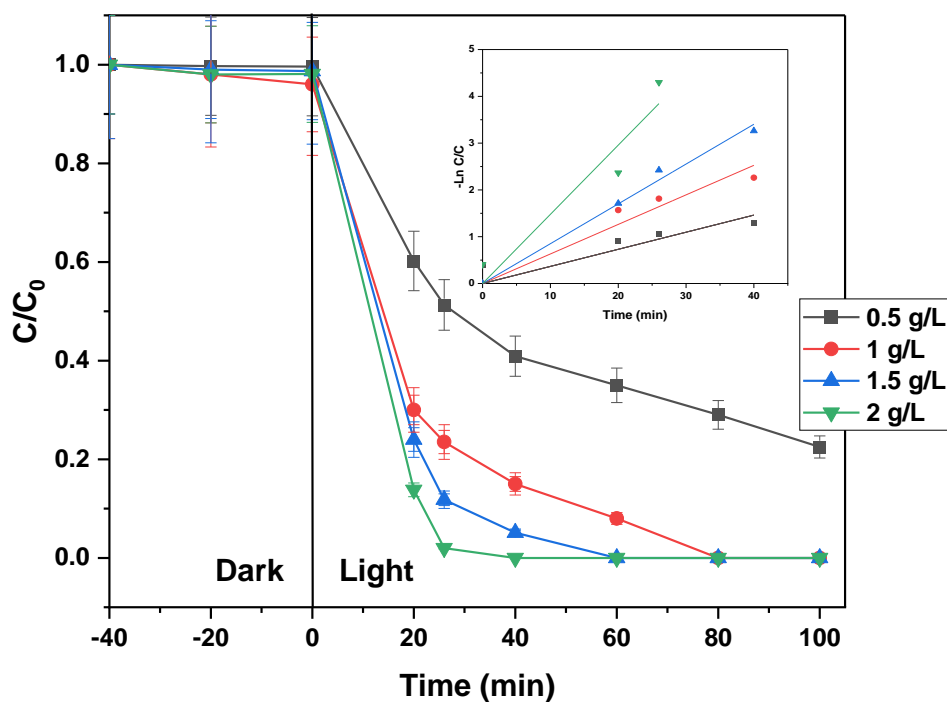


Figure IV.7. Catalyst dose effect on the degradation of BS (neutral pH, [BS] = 20mg/L , catalyst dose = 1 g/L).

IV.4.3.1. pH effect

The effect of pH on the photodegradation of BS by the Bi₁₂ZnO₂₀/Bi₂O₃ (90/10) composite shows significant variations in efficiency depending on the medium conditions. At neutral pH (pH 7), degradation reaches 100% in 80 minutes, indicating that this pH is optimal for photocatalytic degradation. This suggests that the surface of the composite is in an ideal state for interaction with BS [31], and the production of hydroxyl radicals ($\cdot\text{OH}$) is favorable [32]. In basic conditions (pH 10), the photodegradation efficiency decreases, with only 74.1% degradation after 100 minutes ($k = 0.03377 \text{ min}^{-1}$). This reduction can be attributed to a decrease in the formation of hydroxyl radicals, which are essential for the photocatalytic reaction, and to a negatively charged photocatalyst surface that may limit interaction with BS molecules [33]. At pH 8, 83.2% ($k = 0.04497 \text{ min}^{-1}$) degradation is observed after 100 minutes, reflecting better efficiency compared to pH 10, but still lower than at neutral pH. In acidic conditions (pH 4), significant initial adsorption of 51.3% is observed, followed by complete photodegradation ($k = 0.08898 \text{ min}^{-1}$) in just 40 minutes. This high adsorption in an acidic medium can be explained by a more positively charged surface of the photocatalyst, facilitating interaction with negatively charged BS molecules. Additionally, the high concentration of H^+ ions favor the formation of $\cdot\text{OH}$ radicals, accelerating the degradation of the dye [34]. In conclusion, neutral pH appears to be optimal for BS photodegradation, but acidic conditions allow for faster degradation due to prior adsorption. On the other hand, basic conditions, especially at pH 10, reduce photocatalytic efficiency.

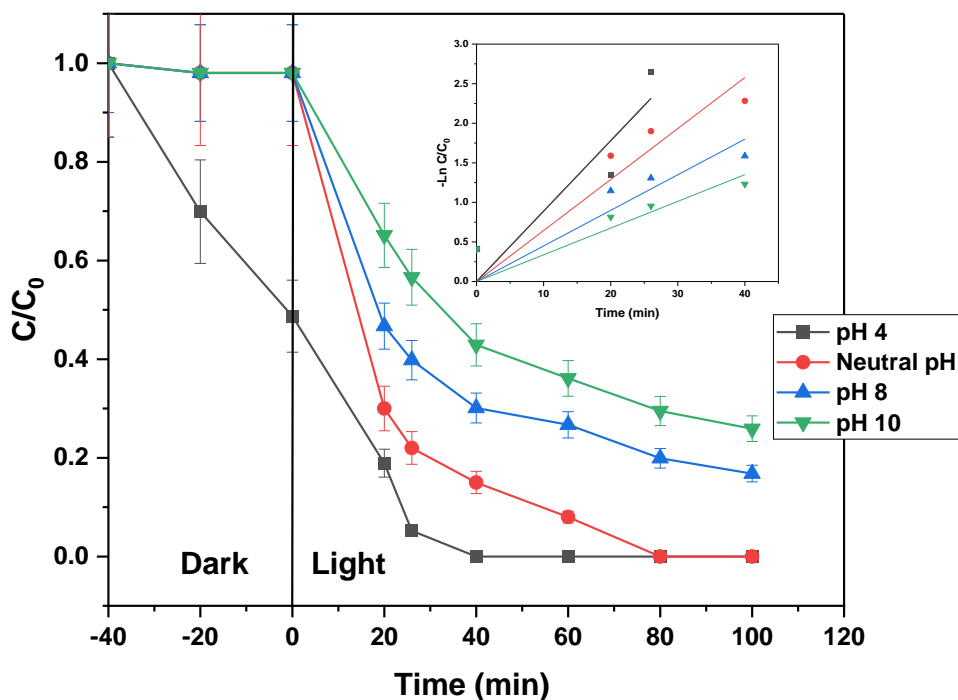


Figure IV.8. Effect of reaction pH on BS degradation (Catalyst dose = 1 g/L, [BS] = 20 mg/L).

IV.4.4. Initial concentration effect

The effect of the initial concentration of BS on its photodegradation by the $\text{Bi}_{12}\text{ZnO}_{20}/\text{Bi}_2\text{O}_3$ (90/10) composite shows that as the concentration of BS increases, the degradation efficiency decreases. At a concentration of 10 mg/L, the degradation is complete (100%) within 40 minutes, as the lower amount of BS molecules allows for optimal interaction with the available active sites on the photocatalyst. When the concentration increases to 20 mg/L, the degradation still reaches 100%, but the time required doubles to 80 minutes, indicating increased competition among BS molecules for the photocatalyst's active sites. At 30 mg/L, the degradation rate slightly drops to 96% in 100 minutes, showing that the system is nearing its capacity, with the active sites becoming saturated and the generation of $\cdot\text{OH}$ radicals no longer sufficient to degrade all the BS molecules in the given time. At 40 mg/L, the degradation efficiency decreases further to 87% in 100 minutes, likely due not only to catalyst saturation but also to reduced UV light penetration into the solution, limiting excitation of the photocatalyst and the generation of reactive species needed for degradation. In summary, higher initial concentrations of BS

negatively impact the photocatalytic performance, slowing down the reaction and reducing the overall degradation rate.

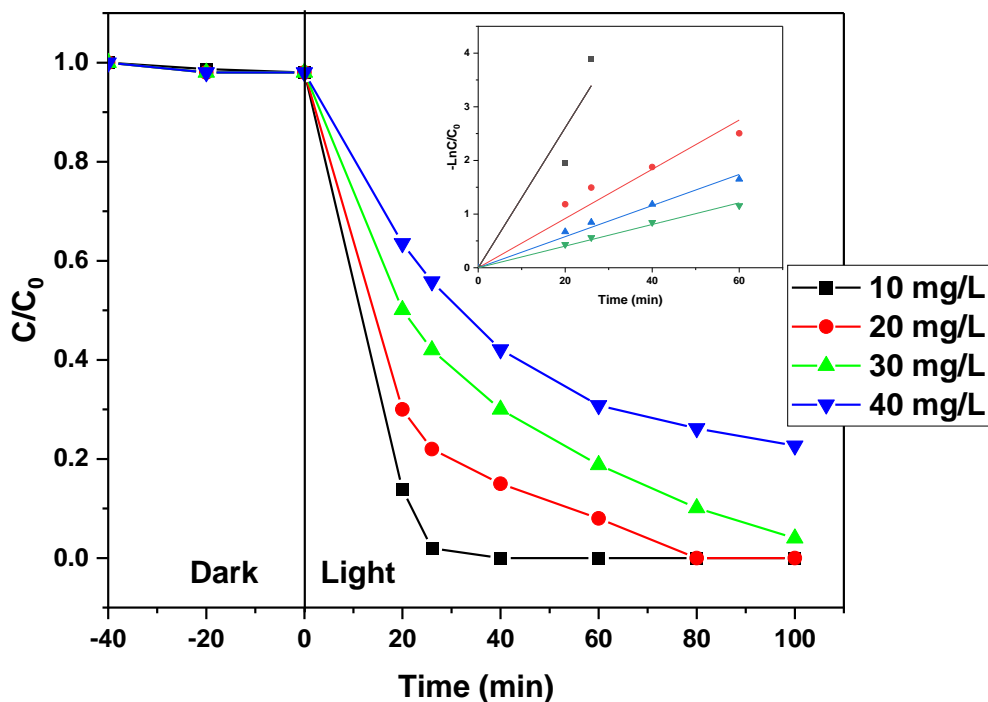


Figure IV.9. Influence of the initial concentration of BS dye on photodegradation reaction (neutral pH, catalyst dose = 1g/L).

IV.4.5. Recycling test of $\text{Bi}_{12}\text{ZnO}_{20}/\text{Bi}_2\text{O}_3$ for BS degradation

After the completion of the dye degradation reaction, the colloidal suspension containing the catalyst was recovered by centrifugation. The solid catalyst was then carefully washed several times with a mixture of distilled water and ethanol (in equal proportions) to remove any residual impurities. The washed catalyst was subsequently exposed to UV irradiation for 2 hours to ensure the complete removal of any remaining organic residues. Following this purification step, the catalyst was dehydrated by drying it at 80°C for 12 hours in an oven. Once dried, the catalyst was reused in a new dye degradation reaction, following the same experimental procedure. The process of recovery, purification, and reuse of the catalyst was repeated for a total of six successive photodegradation cycles, while maintaining the same experimental conditions. At

each cycle, the photocatalytic efficiency of the material was evaluated to assess its stability and ability to sustain good performance over repeated uses.

The results show that the $\text{Bi}_{12}\text{ZnO}_{20}/\text{Bi}_2\text{O}_3$ material maintains excellent photocatalytic stability after six successive degradation cycles. As illustrated in the figure IV.10, the dye degradation rate slightly decreases, from 100% in the first cycle to 97.7% after the sixth cycle. This minor decrease in efficiency, by only 2.3%, indicates that the material experiences very little loss of activity during repeated photodegradation cycles. These findings confirm the robustness and stability of the $\text{Bi}_{12}\text{ZnO}_{20}/\text{Bi}_2\text{O}_3$ catalyst, even after multiple uses, which is crucial for long-term practical applications. The slight reduction in efficiency can be attributed to factors such as the accumulation of by-products or the gradual loss of active sites on the catalyst surface. However, this reduction remains negligible, demonstrating that the material retains its capacity to effectively degrade the dye over time.

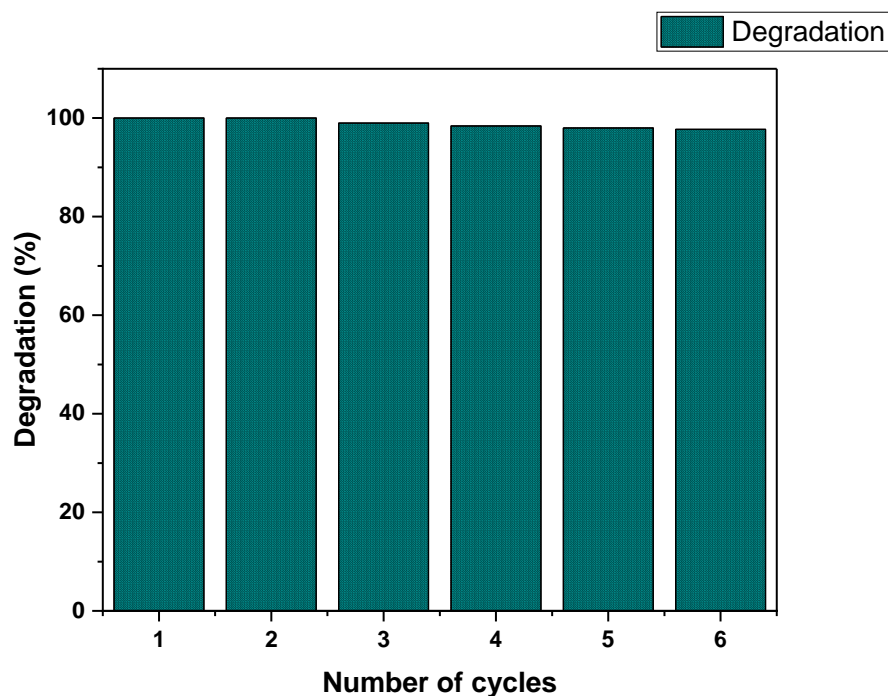


Figure IV.10. Six recycling runs of photocatalytic degradation of BS with $\text{Bi}_{12}\text{ZnO}_{20}/\text{Bi}_2\text{O}_3$ (Neutral pH, 1 g/L Catalyst, and 20 mg/L MB).

IV.4.6. Scavengers effect

The results (figure IV.11) of the analysis of the effects of scavengers on the photocatalytic degradation of BS in the presence of the Bi₁₂ZnO₂₀/Bi₂O₃ composite highlights that holes (h⁺) are the main reactive species involved in the process. Indeed, the addition of Na₂-EDTA, a specific hole scavenger, reduces the degradation efficiency to 12%, indicating that charge transfer via holes represents a dominant mechanism in photocatalytic degradation. The use of ethanol, a hydroxyl radical (•OH) trap, leads to a decrease in degradation efficiency to 44%, highlighting the secondary but significant contribution of •OH in the reaction. Furthermore, the addition of (K₂Cr₂O₇), which traps electrons (e⁻), reduces the degradation rate to 31%, showing that electrons also participate in the mechanism, albeit to a lesser extent. In conclusion, photocatalysis by Bi₁₂ZnO₂₀/Bi₂O₃ is predominantly governed by holes (h⁺), with a complementary contribution from hydroxyl radicals and electrons in the overall dye degradation process.

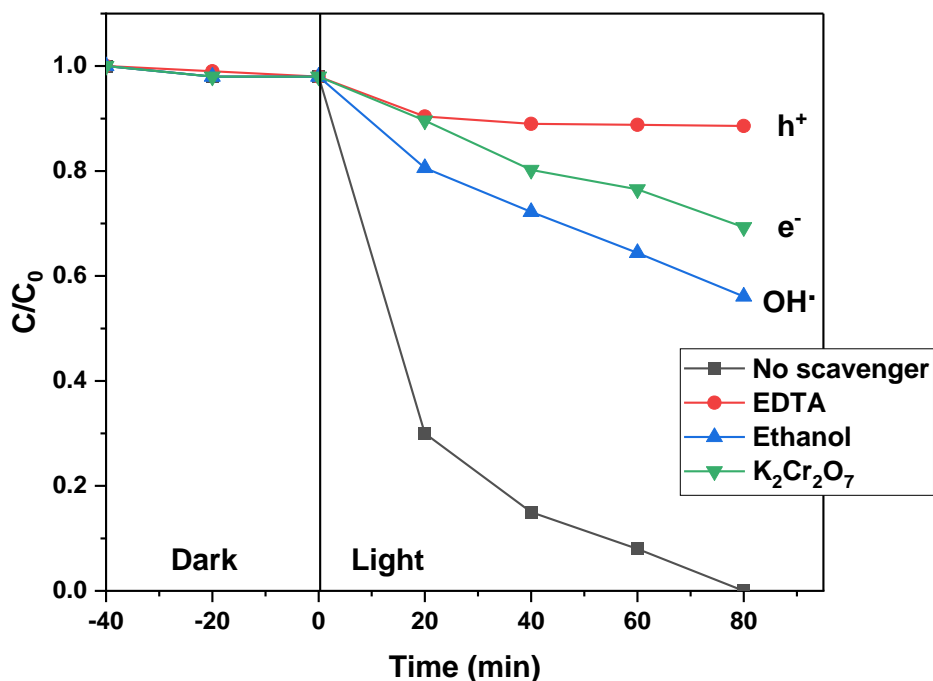


Figure IV.11. Effects of different scavengers on BS degradation with Bi₁₂ZnO₂₀/Bi₂O₃.

IV.4.7. Degradation kinetic modeling

The fitting of the Langmuir-Hinshelwood (L-H) model to the photocatalytic degradation of the BS dye by the Bi₁₂ZnO₂₀/Bi₂O₃ composite reveals crucial aspects of the reaction kinetics and adsorption mechanisms. The reaction rate ($k_r = 1.4142 \text{ mg. L}^{-1}$) indicates a rapid degradation of BS on the surface of the photocatalyst, highlighting the effectiveness of the composite in accelerating this decomposition under light irradiation. Simultaneously, the adsorption constant ($K = 0.1396 \text{ L.mg}^{-1}$) indicates a moderate affinity of the dye for the surface of the photocatalyst. This value suggests an optimal balance between adsorption and degradation, allowing the pollutant to be effectively adsorbed before being degraded, which is essential in photocatalytic processes. Moreover, the coefficient of determination ($R^2 = 0.94$) demonstrates an excellent match between the L-H model and the experimental data, confirming that the degradation of BS indeed follows Langmuir-Hinshelwood type kinetics. This highlights the importance of the adsorption step in the overall photocatalytic efficiency. In summary, these results highlight the remarkable performance of the Bi₁₂ZnO₂₀/Bi₂O₃ composite for photocatalysis, with promising potential for various applications in the degradation of organic pollutants under light irradiation.

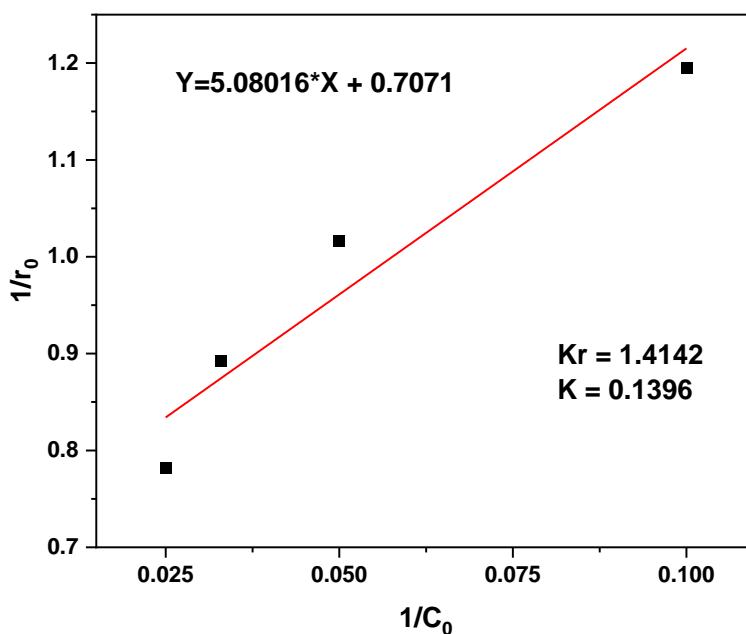


Figure IV.12. representation of Langmuir-Hinshelwood equation for photocatalytic removal of BS by Bi₁₂ZnO₂₀/Bi₂O₃.

IV.4.8. Proposed photodegradation mechanism

Based on the previous analysis, a potential degradation mechanism is proposed. As illustrated in Figure IV.13, when the photocatalyst $\text{Bi}_{12}\text{ZnO}_{20}/\text{Bi}_2\text{O}_3$ is illuminated by UV light, the photogenerated electrons (e^-) are activated and transferred from the conduction band (CB) of $\text{Bi}_{12}\text{ZnO}_{20}$ to the CB of Bi_2O_3 via the interface of the $\text{Bi}_{12}\text{ZnO}_{20}/\text{Bi}_2\text{O}_3$ composite. Meanwhile, the holes (h^+) are transferred from the valence band (VB) of Bi_2O_3 to the VB of $\text{Bi}_{12}\text{ZnO}_{20}$. Thus, the photogenerated holes accumulate at the heterojunction interface, which promotes the separation of the photogenerated electrons and holes. The photogenerated electrons and holes can then react as follows:

On one hand, the electrons react with dissolved oxygen (O_2) in the solution to produce superoxide anions ($\text{O}_2^{\cdot-}$). On the other hand, the holes (h^+) present in the valence band of $\text{Bi}_{12}\text{ZnO}_{20}$ oxidize water (H_2O) or hydroxide ions (OH^-) to form hydroxyl radicals (OH^\cdot) that participate in the degradation of the BS dye. Thus, the $\text{Bi}_{12}\text{ZnO}_{20}/\text{Bi}_2\text{O}_3$ composite exhibits high photocatalytic activity, thanks to the efficient separation of photogenerated charges and the production of reactive radicals responsible for the degradation of the dye.

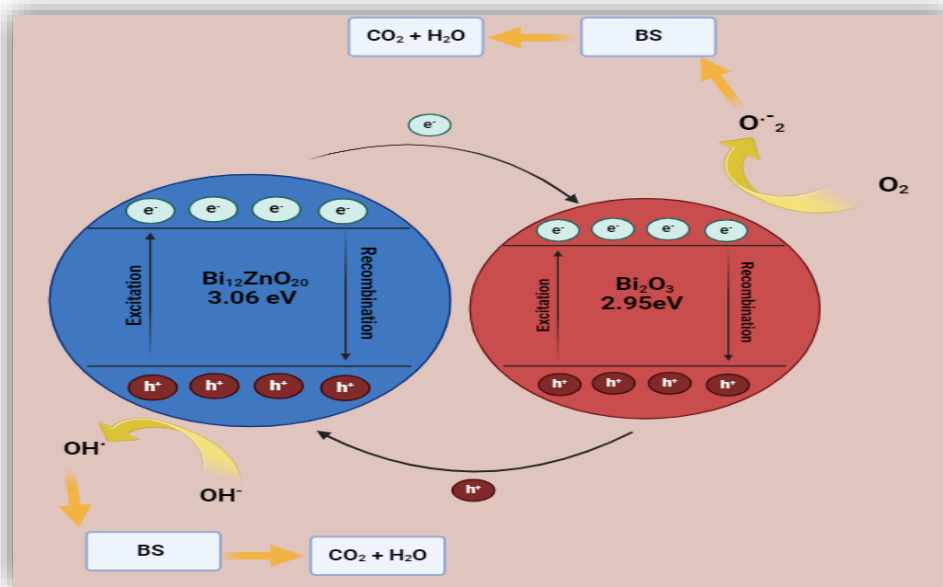


Figure IV.13. Photocatalytic degradation mechanism of BS over $\text{Bi}_{12}\text{ZnO}_{20}/\text{Bi}_2\text{O}_3$.

IV.5. Comparative Performance of Bi₁₂ZnO₂₀-Based Photocatalysts for Pollutant photocatalytic Degradation

Table IV.2. Photocatalytic performances of various Bi₁₂ZnO₂₀ based materials in the degradation of different pollutants.

Photocatalyst	pollutant	Initial Concentration	Light	Degradation rate	Ref
Bi ₁₂ ZnO ₂₀	RhB	5 mg/L	Visible 300 w	98.5 % 70 min	[23]
Bi ₁₂ ZnO ₂₀ /Bi ₂ WO ₆	RhB	10 mg/L	Visible 240 w	91 % 90 min	[26]
Bi ₁₂ ZnO ₂₀	CFRM	5 mg/L	UV 24 W	80 % 240 min	[24]
Bi ₁₂ ZnO ₂₀ /Bi ₂ O ₃	BS	20 mg/L	UV 24 w	100 % 80 min	This work

Table IV.2 compares the performance of different photocatalysts based on Bi₁₂ZnO₂₀ for the degradation of various pollutants. Pure Bi₁₂ZnO₂₀ proves effective for moderate concentrations of RhB (5 mg/L), with a rapid degradation time of 70 minutes. However, for the CFRM, it only reaches 80% degradation in 240 minutes under low UV light. The composite Bi₁₂ZnO₂₀/Bi₂WO₆ shows good performance for higher concentrations of RhB (10 mg/L), although the degradation time increases to 90 minutes. This reflects its ability to adapt to more rigorous conditions, such as increased concentrations, while using slightly lower light power. The composite Bi₁₂ZnO₂₀/Bi₂O₃ is the most efficient among the materials studied, completely degrading the BS pollutant (20 mg/L) in just 80 minutes under low UV light. This photocatalyst outperforms the others in terms of efficiency, particularly for high concentrations and under moderate light conditions. To effectively address high initial concentrations of pollutants, Bi₁₂ZnO₂₀/Bi₂O₃ emerges as the most efficient photocatalyst.

References

- [1] S.I. Sinar Mashuri, M.L. Ibrahim, M.F. Kasim, M.S. Mastuli, U. Rashid, A.H. Abdullah, A. Islam, N. Asikin Mijan, Y.H. Tan, N. Mansir, Photocatalysis for organic wastewater treatment: From the basis to current challenges for society, *Catalysts* 10 (2020) 1260.
- [2] W.Y. Teoh, J.A. Scott, R. Amal, Progress in Heterogeneous Photocatalysis: From Classical Radical Chemistry to Engineering Nanomaterials and Solar Reactors, *J. Phys. Chem. Lett.* 3 (2012) 629–639. <https://doi.org/10.1021/jz3000646>.
- [3] A.B. Djurišić, Y. He, A. Ng, Visible-light photocatalysts: Prospects and challenges, *Apl Materials* 8 (2020). <https://pubs.aip.org/aip/apm/article/8/3/030903/594645> (accessed September 29, 2024).
- [4] V. Mane, D. Dake, N. Raskar, R. Sonpir, E. Stathatos, B. Dole, A review on Bi₂O₃ nanomaterial for photocatalytic and antibacterial applications, *Chemical Physics Impact* (2024) 100517.
- [5] T.U. Abbasi, M. Ahmad, A.A. Alsahli, M. Asma, C.U. Mussagy, T.M. Abdellatief, C. Pastore, A. Mustafa, Eco-friendly production of biodiesel from *Carthamus tinctorius* L. seeds using bismuth oxide nanocatalysts derived from *Cannabis sativa* L. Leaf extract, *Process Safety and Environmental Protection* (2024). <https://www.sciencedirect.com/science/article/pii/S0957582024010826> (accessed September 29, 2024).
- [6] M.A. Wahba, S.M. Yakout, Y.K. Abdel-Monem, A.A.A. Hammood, Boosted visible light dye-decontamination and colossal dielectric constant features of Bi₂O₃: Role of In, Cu and Li-dopants, *Journal of Physics and Chemistry of Solids* 187 (2024) 111864.
- [7] A. Jaison, H.U. Lee, J. Hur, A. Mohan, Y.-C. Lee, Facile synthesis of Ni-doped tetrahedral γ -Bi₂O₃ and selective photocatalytic degradation of Congo red under simulated sunlight, *Journal of Alloys and Compounds* 1004 (2024) 175727.
- [8] M. Weber, R.D. Rodriguez, D.R. Zahn, M. Mehring, γ -Bi₂O₃—to Be or not to Be? Comparison of the sillenite γ -Bi₂O₃ and isomorphous sillenite-type Bi₁₂SiO₂₀, *Inorganic Chemistry* 57 (2018) 8540–8549.
- [9] A.F. de Lima, S.A. de S. Farias, M.V. Lalic, Structural, electronic, optical, and magneto-optical properties of Bi₁₂MO₂₀ (M= Ti, Ge, Si) sillenite crystals from first principles calculations, *Journal of Applied Physics* 110 (2011). <https://pubs.aip.org/aip/jap/article/110/8/083705/955352> (accessed October 1, 2024).
- [10] Y. Hu, Structure-composition-property relationships of stoichiometric and non-stoichiometric "Bi₁₂MO₂₀" sillenites, PhD Thesis, University of Sheffield, 2013. <https://etheses.whiterose.ac.uk/4489/> (accessed October 1, 2024).

- [11] O. Baaloudj, H. Kenfoud, A.K. Badawi, A.A. Assadi, A. El Jery, A.A. Assadi, A. Amrane, Bismuth sillenite crystals as recent photocatalysts for water treatment and energy generation: A critical review, *Catalysts* 12 (2022) 500.
- [12] A. Chauhan, R. Kumar, P. Raizada, A.A.P. Khan, T. Ahamad, Q. Van Le, V.-H. Nguyen, S. Thakur, P. Singh, A. Sudhaik, Advances in bismuth titanate (Bi₁₂TiO₂₀)-based photocatalysts for environmental remediation: Fundamentals and practical applications, *Journal of Water Process Engineering* 59 (2024) 104974.
- [13] Y. Liu, B. Yang, H. He, S. Yang, X. Duan, S. Wang, Bismuth-based complex oxides for photocatalytic applications in environmental remediation and water splitting: A review, *Science of The Total Environment* 804 (2022) 150215.
- [14] M. Tahir, S. Tasleem, B. Tahir, Recent development in band engineering of binary semiconductor materials for solar driven photocatalytic hydrogen production, *International Journal of Hydrogen Energy* 45 (2020) 15985–16038.
- [15] I. Ahmad, Y. Zou, J. Yan, Y. Liu, S. Shukrullah, M.Y. Naz, H. Hussain, W.Q. Khan, N.R. Khalid, Semiconductor photocatalysts: A critical review highlighting the various strategies to boost the photocatalytic performances for diverse applications, *Advances in Colloid and Interface Science* 311 (2023) 102830.
- [16] F. Fresno, R. Portela, S. Suárez, J.M. Coronado, Photocatalytic materials: recent achievements and near future trends, *Journal of Materials Chemistry A* 2 (2014) 2863–2884.
- [17] U.M. Nayef, R.I. Kamel, Enhancement the electrical properties of porous silicon for photo-detectors applications by depositing Bi₂O₃ nanoparticles, *Optik* 207 (2020) 163847.
- [18] L. Li, L. Meng, F. Wang, Y. Wang, Synthesis and optical characterization of In³⁺-stabilized γ -Bi₂O₃ sillenite semiconductor with cation deficiency, *Materials Science in Semiconductor Processing* 68 (2017) 48–52.
- [19] C. Zaldo, C. Coya, J.L.G. Fierro, K. Polgár, L. Kovács, Z. Szaller, X-Ray photoelectron spectroscopy and optical studies of Bi₁₂(GaxBi_{1-x})O_{20- δ} and Bi₁₂(ZnxBi_{1-x})O_{20- δ} single crystals, *Journal of Physics and Chemistry of Solids* 57 (1996) 1667–1672.
- [20] H. Sekhar, D. Narayana Rao, Preparation, structural and linear optical properties of zinc sillenite (Bi_{12.66}Zn_{0.33}O_{19.33}) nanocrystals, *J Mater Sci: Mater Electron* 24 (2013) 1569–1574. <https://doi.org/10.1007/s10854-012-0977-1>.
- [21] A. Deb, Photocatalytic degradation of Benzophenone 3 in aqueous media under UV light irradiation, (2018). <https://lutpub.lut.fi/handle/10024/158395> (accessed October 3, 2024).
- [22] S. Bandyopadhyay, S. Dutta, A. Dutta, S.K. Pradhan, Mechano-synthesis of Nanocrystalline Fully Stabilized bcc γ -phase of Bi₂O₃ without Any Additive: Manifestation of Ferroelasticity in

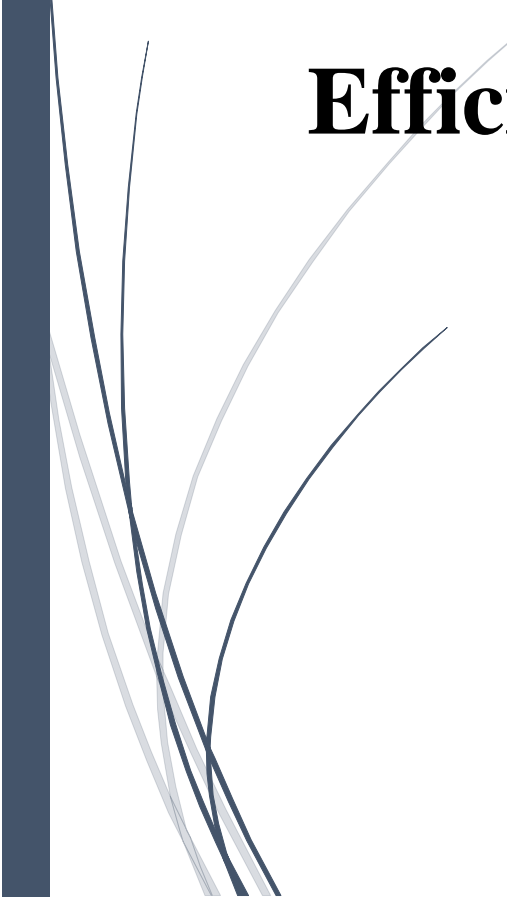
- Microstructure, Optical, and Transport Properties, *Crystal Growth & Design* 18 (2018) 6564–6572. <https://doi.org/10.1021/acs.cgd.8b00768>.
- [23] X.-L. Wang, Y. Xiao, Z.-J. Lv, H. Yu, Y. Yang, X.-T. Dong, A novel 2D nanosheets self-assembly camellia-like ordered mesoporous Bi₁₂ZnO₂₀ catalyst with excellent photocatalytic property, *Journal of Alloys and Compounds* 835 (2020) 155409.
- [24] O. Baaloudj, N. Nasrallah, H. Kenfoud, F. Algethami, A. Modwi, A. Guesmi, A.A. Assadi, L. Khezami, Application of Bi₁₂ZnO₂₀ sillenite as an efficient photocatalyst for wastewater treatment: removal of both organic and inorganic compounds, *Materials* 14 (2021) 5409.
- [25] T.I. Mel'nikova, G.M. Kuz'micheva, N.B. Bolotina, V.B. Rybakov, Ya.V. Zubavichus, N.V. Sadovskaya, E.A. Mar'ina, Structural features of compounds of the sillenite family, *Crystallogr. Rep.* 59 (2014) 353–361. <https://doi.org/10.1134/S1063774514030134>.
- [26] L. Zhang, X. Zhang, Y.-Q. Huang, C.-L. Pan, J.-S. Hu, C.-M. Hou, Novel Bi₁₂ZnO₂₀–Bi₂WO₆ heterostructures: facile synthesis and excellent visible-light-driven photocatalytic activities, *Rsc Advances* 5 (2015) 30239–30247.
- [27] C. Kang, L. Jing, T. Guo, H. Cui, J. Zhou, H. Fu, Mesoporous SiO₂-Modified Nanocrystalline TiO₂ with High Anatase Thermal Stability and Large Surface Area as Efficient Photocatalyst, *J. Phys. Chem. C* 113 (2009) 1006–1013. <https://doi.org/10.1021/jp807552u>.
- [28] Y. Huang, W. Wang, Q. Zhang, J. Cao, R. Huang, W. Ho, S.C. Lee, In situ fabrication of α -Bi₂O₃/(BiO)₂CO₃ nanoplate heterojunctions with tunable optical property and photocatalytic activity, *Scientific Reports* 6 (2016) 23435.
- [29] Q. Song, J. Zhou, G. Chen, Significant reduction in semiconductor interface resistance via interfacial atomic mixing, *Phys. Rev. B* 105 (2022) 195306. <https://doi.org/10.1103/PhysRevB.105.195306>.
- [30] S. Bagheri, N. Muhd Julkapli, S. Bee Abd Hamid, Titanium Dioxide as a Catalyst Support in Heterogeneous Catalysis, *The Scientific World Journal* 2014 (2014) 1–21. <https://doi.org/10.1155/2014/727496>.
- [31] S. Wang, H. Sun, H.-M. Ang, M.O. Tadé, Adsorptive remediation of environmental pollutants using novel graphene-based nanomaterials, *Chemical Engineering Journal* 226 (2013) 336–347.
- [32] J.-H. Shen, T.-H. Chiang, C.-K. Tsai, Z.-W. Jiang, J.-J. Horng, Mechanistic insights into hydroxyl radical formation of Cu-doped ZnO/g-C₃N₄ composite photocatalysis for enhanced degradation of ciprofloxacin under visible light: Efficiency, kinetics, products identification and toxicity evaluation, *Journal of Environmental Chemical Engineering* 10 (2022) 107352.

- [33] I. Kazeminezhad, A. Sadollahkhani, Influence of pH on the photocatalytic activity of ZnO nanoparticles, *J Mater Sci: Mater Electron* 27 (2016) 4206–4215. <https://doi.org/10.1007/s10854-016-4284-0>.
- [34] F.Z. Meghlaoui, S. Merouani, O. Hamdaoui, M. Bouhelassa, M. Ashokkumar, Rapid catalytic degradation of refractory textile dyes in Fe (II)/chlorine system at near neutral pH: radical mechanism involving chlorine radical anion (Cl_2^-)-mediated transformation pathways and impact of environmental matrices, *Separation and Purification Technology* 227 (2019) 115685.



Chapter V

Streamlined Synthesis of P-g-C₃N₄@Ti-g-C₃N₄ Composite: A Simple Approach to High- Efficiency Photocatalysts



Chapter V. Streamlined Synthesis of P-g-C₃N₄@Ti-g-C₃N₄ Composite: A Simple Approach to High-Efficiency Photocatalysts

V.1. Introduction

With the progression of socio-economic development, the escalating predicament of environmental pollution, particularly attributed to organic wastewater pollutants, has garnered heightened attention. The presence of these organic contaminants not only compromises the integrity of aquatic ecosystems but also engenders substantial risks to human health [1]. In wastewater treatment, various methodologies are employed broadly categorized into physical, chemical, and biological techniques. Physical treatment encompasses procedures such as membrane separation, sedimentation, and adsorption, each serving to address specific aspects of pollutant removal [2]. Removing organics from water through conventional physical treatment methods poses challenges [3], these challenges can be overcome through the implementation of biological treatment approaches. Among these, activated sludge and biofilm methods stand out as widely utilized solutions [4].

While the biological treatment process grapples with challenges like steep investment and operational expenses, vulnerability to sludge swelling, and protracted pre-preparation periods[5], chemical techniques emerge as a potent solution. Chemical methods exhibit the ability to swiftly oxidize and thoroughly degrade organic pollutants, presenting an efficient avenue for water treatment [6]. Among these methods, advanced oxidation processes (AOPs) stand out as the premier choice for addressing organic wastewater. AOPs offer notable advantages including superior mineralization efficiency, rapid rates of oxidation reactions, and the absence of secondary pollution [2]. Advanced oxidation processes (AOPs), such as Fenton reactions, photocatalytic oxidation, electrochemical oxidation reactions and sonochemical oxidation, have the capability to completely degrade organic pollutants by generating highly reactive radicals [7].

In recent years, there has been a surge in the popularity of photodegradation as a method for pollutant remediation [8]. This process involves heterogeneous catalysis, where a semiconductor photocatalyst utilizes light energy to break down various environmental contaminants, including organic pollutants present in water and air [9]. Photodegradation offers distinct advantages over

traditional wastewater treatment techniques. For instance, active photocatalysts can completely degrade organic pollutants within a short timeframe, typically a few hours, and at ambient temperature [10]. Moreover, unlike conventional methods, photodegradation does not lead to the formation of secondary toxic byproducts, as organic pollutants are mineralized into harmless substances such as water and CO₂ [11]. To enhance the efficiency of photodegradation, nanomaterials are often surface functionalized for improved degradation of hazardous pollutants [12].

During the past forty years, a diverse range of semiconductor materials, such as TiO₂, ZnO, SrTiO₃, CdS, BiVO₄, Ta₃N₅, TaON, g-C₃N₄, Ag₃PO₄, and their nanostructured counterparts, have been widely employed as photocatalysts to harness solar energy for different redox reactions [13]. Developing a novel photocatalytic material that combines efficiency, abundance, stability, and ease of synthesis poses a significant challenge. Recently, considerable attention has been directed towards utilizing certain 2D materials with exceptional properties for various applications, spanning energy storage and generation [14], chemical sensing, electronics, optics, and environmental cleanup. Among these materials, graphitic carbon nitride (g-C₃N₄) has garnered significant interest due to its remarkable photocatalytic capabilities as a metal-free polymer [15].

The heptazine ring structure and high degree of condensation grant metal-free g-C₃N₄ several benefits, including excellent physicochemical stability and an attractive electronic structure with a moderate band gap. (2.7 eV) [15]. These distinctive properties position g-C₃N₄ as a highly promising material for photocatalytic applications under visible and UV-visible light. [16]. Moreover, g-C₃N₄ is readily available and can be easily synthesized through a one-step polymerization process using inexpensive precursors such as dicyanamide, cyanamide, melamine, and urea. [17].

The inherent properties of pure g-C₃N₄ lead to a rapid recombination of photogenerated electron-hole pairs, which significantly restricts their overall photocatalytic efficiency. To address this limitation and enhance photocatalytic activity, various strategies have been explored. Metal doping [18], including transition metals (Fe, Cu, Ti, and W) and alkali metals (K, Li, Na), has been shown to introduce favorable functionalities to g-C₃N₄, such as narrowing the band gap, enhancing light

absorption, and improving catalytic performance [19]. Typically, metal incorporation involves mixing a soluble metal salt solution with the precursor followed by heat treatment to embed the metal within g-C₃N₄ structure [20]. Nonmetal doping, on the other hand, represents another avenue to enhance the performance of g-C₃N₄. As a n-type nonmetal semiconductor, doping with nonmetal elements maintains the metal-free nature of g-C₃N₄ while introducing beneficial effects [21]. Nonmetals, characterized by high ionization energies and electronegativities, readily form covalent bonds with other compounds by gaining electrons during reaction processes [22]. Introduction of nonmetal dopants, such as oxygen, phosphorus, sulfur, carbon, halogen, nitrogen, and boron, disrupts the symmetry of g-C₃N₄ and promotes faster separation of electron-hole pairs, thereby enhancing photocatalytic efficiency [23]. Additional strategies, including doping, protonation, preparation of mesoporous structures, and design of heterojunction composites, have also been proposed to further improve the performance of g-C₃N₄-based photocatalysts [24].

This chapter explores the design and optimization of photocatalytic materials based on the organic semiconductor g-C₃N₄. In particular, he is interested in the incorporation of dopants, phosphorus and titanium, into the structure of g-C₃N₄ in order to improve its photocatalytic efficiency. Preliminary studies show that the individual doping of these elements significantly increases the photocatalytic activity of g-C₃N₄, raising interest in combining these two elements to create a high-performance composite. Thus, this chapter details the preparation methods of the composite P- g-C₃N₄@Ti- g-C₃N₄, as well as the characterization techniques used to verify the structure and optical properties of the material, with the ultimate goal of optimizing the degradation of organic pollutants under visible light.

V.2. Experiment

V.2.1. Preparation of P-g-C₃N₄@Ti-g-C₃N₄

V.2.1.1. g-C₃N₄ preparation

The fabrication of g-C₃N₄ powder involved the following detailed procedure: Firstly, virgin g-C₃N₄ powders were synthesized through direct thermal treatment of melamine in a muffle furnace. During a standard synthesis procedure, an alumina crucible containing 5 grams of melamine was heated to 550°C for 4 hours with a heating rate of 10°C/min in the muffle furnace. After cooling to

room temperature, the resulting yellow product was ground to obtain a fine g-C₃N₄ powder. This process ensured the formation of g-C₃N₄ powder through controlled thermal decomposition of melamine, yielding a high-quality product suitable for further characterization and application purposes.

V.2.1.2. Phosphorus-Doped g-C₃N₄ synthesis

The phosphorus-doped g-C₃N₄ was synthesized using a two-step treatment method. Initially, 5 grams of melamine were dissolved in 50 mL of deionized water with agitation, followed by the gradual addition of a phosphoric acid (H₃PO₄) solution to reach concentrations equivalent to 0.5%, 1%, 2%, and 3%. The reaction was allowed to proceed for 12 hours under agitation to ensure homogeneous distribution of phosphorus within the g-C₃N₄ matrix. Subsequently, the resulting solution was heated to 100°C until complete evaporation of the liquids, promoting the formation of a solid precipitate. In the second step, the precipitate was recovered and ground to obtain a fine powder. This powder was then placed in a crucible and subjected to thermal treatment at 500°C for 4 hours in a high-temperature furnace under controlled atmosphere. This annealing process facilitated the polymerization reaction of g-C₃N₄ and the incorporation of the phosphorus dopant.

V.2.1.3. Titanium-doped g-C₃N₄ synthesis

The Ti-doped C₃N₄ materials were synthesized as follows: Initially, a specified quantity of titanium butoxide was dissolved in 50 mL of ethanol. Subsequently, 5 grams of melamine were dispersed in this solution and stirred together for 12 hours to achieve homogeneous dispersion. Following this, the mixture was heated until the complete evaporation of the ethanol. After this step, the resulting powders were collected and placed in an alumina crucible with a lid. This crucible was then heated to 500°C for 4 hours in a muffle furnace under controlled atmosphere conditions. Finally, the obtained product was ground into powder and labeled as xTi/g-C₃N₄, where x represents the percentage of titanium dopant, ranging from 0.5% to 3%. This synthesis method facilitated the incorporation of titanium into the g-C₃N₄ matrix.

V.2.1.4. The P-g-C₃N₄@Ti-g-C₃N₄ preparation

The P- g-C₃N₄@Ti-g-C₃N₄ composites were prepared by mechanical mixing of different quantities of P- g-C₃N₄@Ti-g-C₃N₄ in ratios of 75%/25%, 50%/50%, and 25%/75% (figure 2). Initially, precise amounts of Ti-g-C₃N₄ and P-g-C₃N₄ were weighed according to the targeted composition ratios. Subsequently, the components were homogenized using a mortar until a uniform mixture

was achieved. This method offers the advantage of simplicity and ease of implementation, as it does not require stringent reaction conditions such as high temperatures or specific pressures, making it an economical and accessible approach. Additionally, mechanical mixing typically promotes homogeneous dispersion of the constituents, potentially leading to enhanced properties of the final composite material.

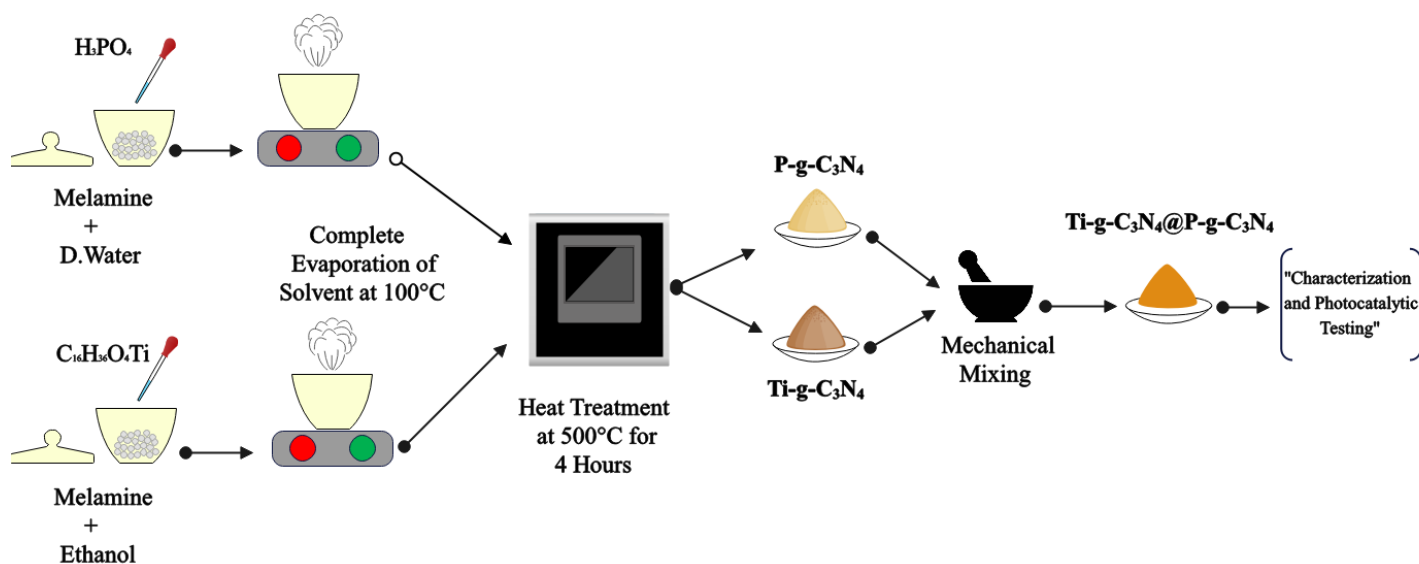


Figure V.1. Synthesis Scheme of P-g-C₃N₄, Ti- g-C₃N₄, and Ti- g-C₃N₄@P- g-C₃N₄.

V.3. Results

V.3.1. Characterization

V.3.1.1. The Fourier transform infrared (FTIR)

FTIR spectra of different samples are shown in figure 4, the prominent absorption peak at 782 cm⁻¹ observed in g-C₃N₄ corresponds to the bending vibration of the tri-s-triazine units, indicating that triazine is the basic synthetic unit of g-C₃N₄ [25]. This observation suggests that the fundamental structure of g-C₃N₄ relies on these tri-s-triazine units, playing a crucial role in its physicochemical properties [26]. Furthermore, the series of characteristic absorption peaks in the range of 1200–1650 cm⁻¹ corresponds to the stretching vibrations of the C–N bonds within the heterocycles, highlighting the presence and distribution of carbon-nitrogen bonds in the structure of g-C₃N₄ [27]. These vibrations provide insights into the molecular configuration and connectivity within the material. Additionally, the broad band observed in the range of 3000–3300 cm⁻¹ is attributed to the stretching vibrations of the N–H bonds in the aromatic ring cycles of the layered structure of g-

C₃N₄ [28]. This observation underscores the presence of specific functional groups, contributing to the stabilization of the material's three-dimensional structure as well as its potential interactions with other molecular entities. The characteristic absorption peak observed in the Ti-g-C₃N₄ spectrum is largely similar to that of g-C₃N₄, suggesting the preservation of the original graphitic structure of the C-N network. However, the absorption peak attributed to the titanium bond is not discernible, likely due to the low concentration of titanium doping or overlapping with characteristic absorption peaks of C-N heterocycles in the spectrum. In the absorption spectra of P- g-C₃N₄ and the composite P- g-C₃N₄@Ti- g-C₃N₄, no significant changes are observed compared to the characteristic peaks of g-C₃N₄. However, a relatively weak intensity peak at 453 cm⁻¹ is detected, typically attributed to the symmetric bending vibration of the P-N group [29].

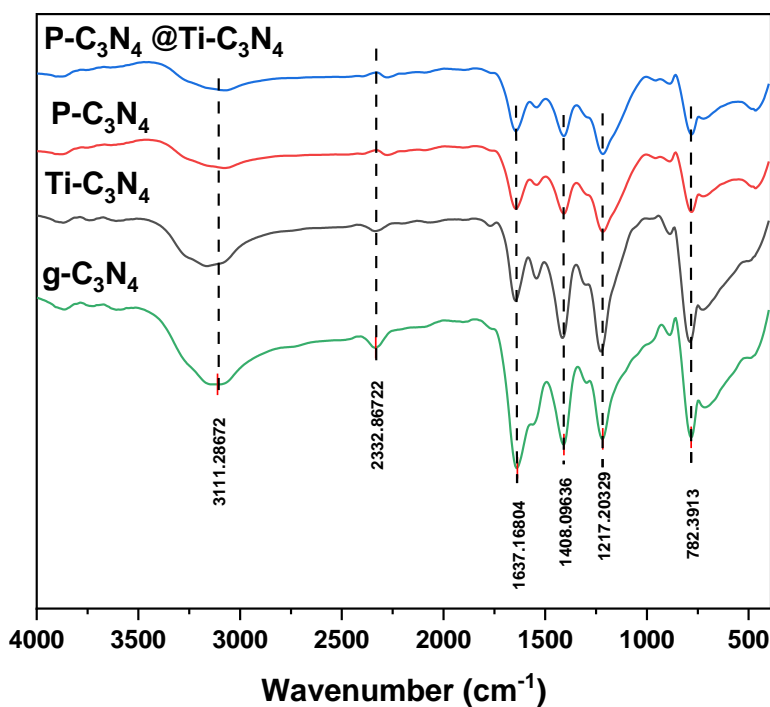


Figure V.2. FTIR spectra of g-C₃N₄, P- g-C₃N₄, Ti- g-C₃N₄, and the P-g-C₃N₄@ Ti-g-C₃N₄.

V.3.1.2. X ray Diffraction

Figure V.4 exhibited the XRD analysis pattern of g-C₃N₄, P- g-C₃N₄, Ti- g-C₃N₄, and the P-g-C₃N₄@ Ti-g-C₃N₄ mixture. XRD shows two characteristic peaks at $2\theta = 27.5^\circ$ and $2\theta = 13.1^\circ$.

These peaks correspond to the typical crystalline structures of graphitic carbon nitride (g-C₃N₄) [30], as referenced in the Joint Committee on Powder Diffraction Standards (JCPDS) files. The peak at $2\theta = 27.5^\circ$ is generally attributed to the diffraction from the (002) planes of g-C₃N₄, indicating the stacking of graphitic layers in the material's structure [31]. The peak at $2\theta = 13.1^\circ$ is attributed to the diffraction from the (100) planes of g-C₃N₄, representing the in-plane organization of tri-s-triazine motifs [32]. For pure g-C₃N₄, the peaks at 27.5° and 13.1° are intense and sharp, indicating good crystallinity of the base material. When doped with phosphorus (P-g-C₃N₄ at 3% P), the peaks at 27.5° and 13.1° are still present but with slightly reduced intensity compared to undoped g-C₃N₄. This suggests that phosphorus partially substitutes nitrogen sites in the g-C₃N₄ structure, creating defects or distortions in the crystal lattice, thus reducing the overall crystallinity and peak intensity [33]. In contrast, doping with titanium (Ti-g-C₃N₄ at 1% Ti) leads to a more significant reduction in peak intensity compared to both undoped g-C₃N₄ and P-g-C₃N₄. Titanium, being a larger element and significantly different in terms of valence and electronic structure, causes more disruptions in the crystal lattice, thereby further reducing the crystallinity and XRD peak intensity [5]. For the P-g-C₃N₄ (75%) @ Ti-g-C₃N₄ (25%) mixture, the peaks at 27.5° and 13.1° show intermediate intensity between those of P-g-C₃N₄ and Ti-g-C₃N₄. This indicates that the crystalline perturbation is a combination of the effects of both dopants. The majority presence of P-g-C₃N₄ (75%) moderates the stronger perturbative effect of Ti-g-C₃N₄ (25%), resulting in intermediate peak intensity.

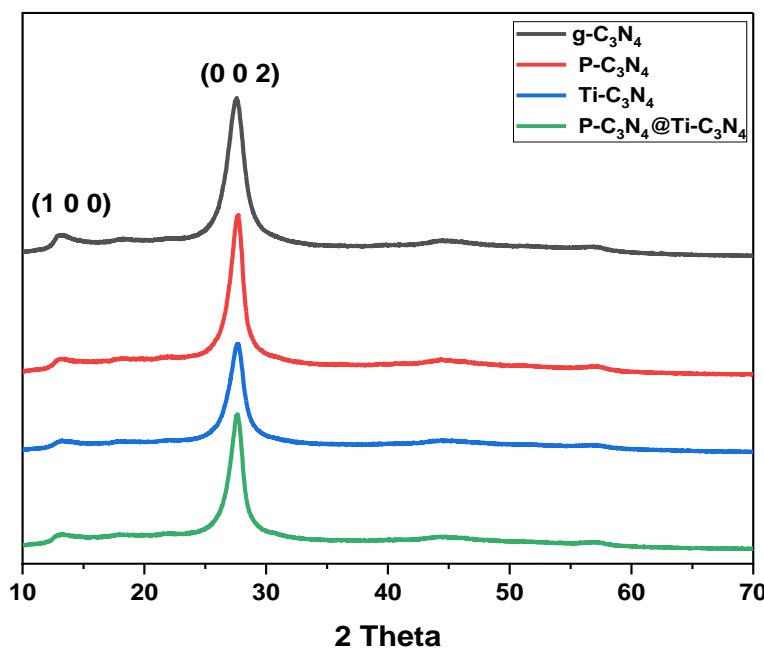


Figure V.3. XRD patterns of pure g-C₃N₄, P- g-C₃N₄, Ti- g-C₃N₄, and the P-g-C₃N₄@ Ti-g-C₃N₄.

V.3.1.3. SEM, Elemental mapping, and EDX spectroscopy

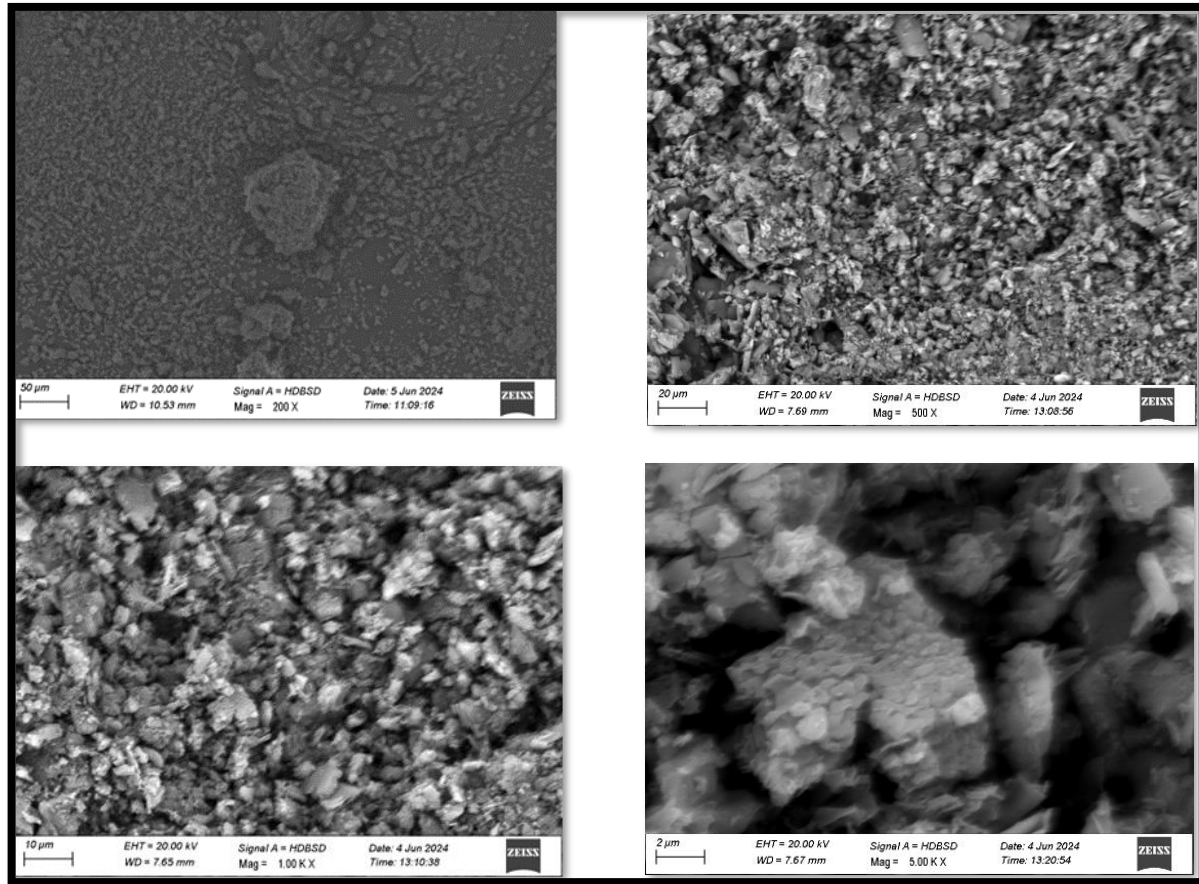
The Scanning electron microscopy (SEM), elemental mapping, and Energy-dispersive X-ray (EDX) spectroscopy analyses of the P-g-C₃N₄, Ti-g- C₃N₄, and P-g- C₃N₄@Ti-g- C₃N₄ samples provide crucial details about their morphology, structure, and elemental chemical composition, the obtained results are illustrated in Figures 5 (a, b,c and d). The SEM images depicted that the morphology of pure g-C₃N₄ (fig 5.a) primarily consists of large, irregular block structures, likely resulting from the thermal polymerization of melamine and consisting of sheet-like layered structures [34]. For the P-g- C₃N₄ sample, well-defined circular particles are observed on the surface of the g- C₃N₄ blocks, indicating the presence of phosphorus. Elemental mapping confirms a homogeneous phosphorus distribution, their association with EDX yields an elemental chemical composition of 36.38 wt% carbon, 42.55 wt% nitrogen, 14.01 wt% oxygen, and 1.65 wt% phosphorus (fig 5.b).

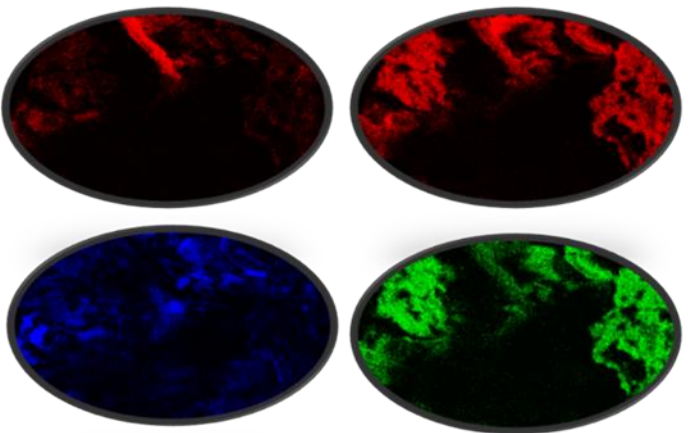
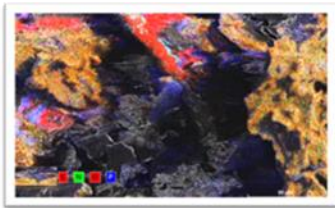
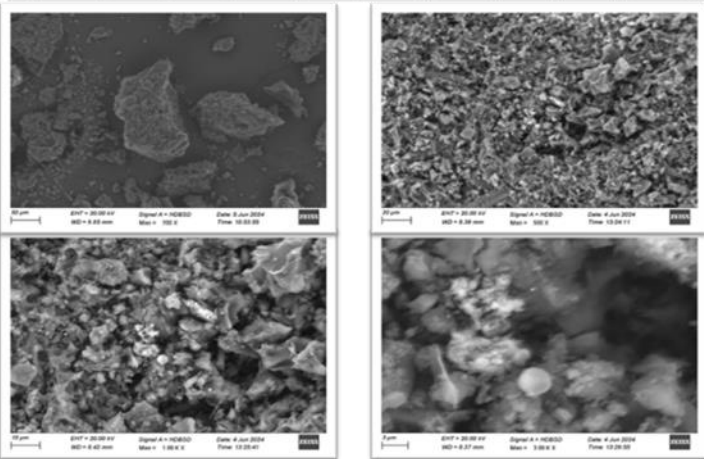
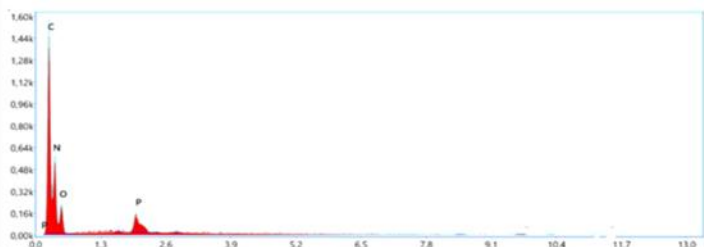
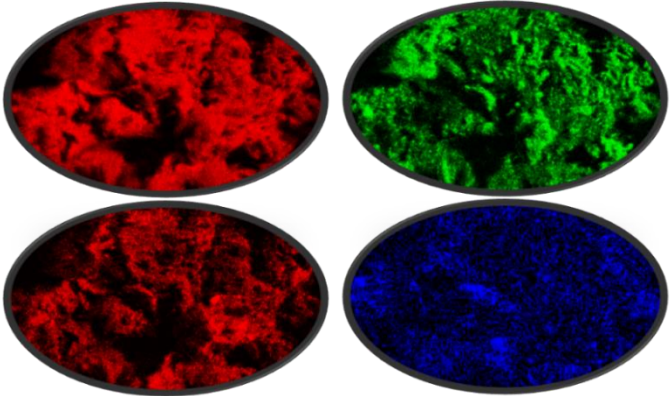
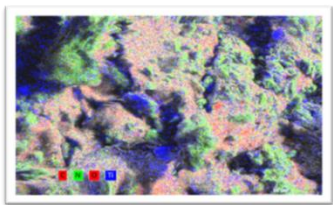
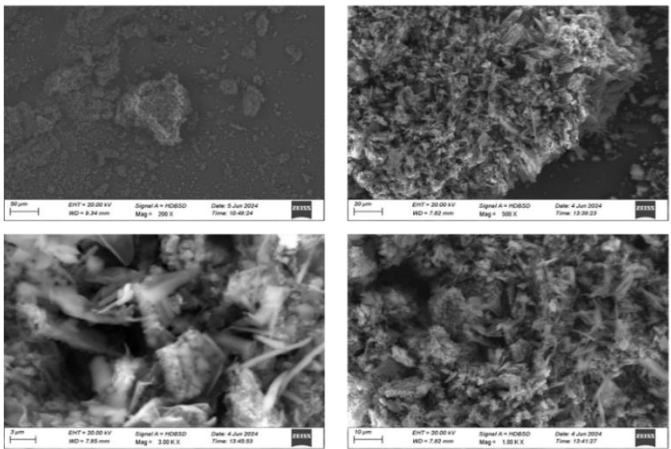
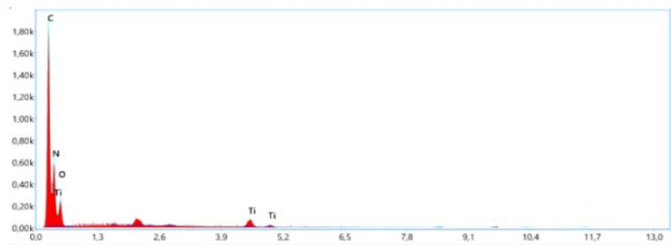
The SEM images of Ti-g-C₃N₄ (fig5.c) show varied morphologies of g-C₃N₄ blocks and plate-like crystals associated with titanium. Elemental mapping displayed the presence and the homogeneous dispersion of titanium atoms within the g- C₃N₄ matrix, thus, the EDX microanalysis revealed a

composition of 36.27 wt% carbon, 40.94 wt% nitrogen, 14.57 wt% oxygen, and 1.84 wt% titanium. Therefore, this uniform titanium incorporation is crucial for optimizing the photocatalytic properties of the material.

The SEM images of the P-g- C₃N₄ @Ti-g-C₃N₄ sample (fig 5.d) show block structures, crystals, and circular particles, characteristic of the incorporated elements. Elemental mapping reveals the homogeneous presence of carbon, nitrogen, oxygen, phosphorus, and titanium within the composite matrix. The EDX analysis of this sample provides an elemental composition of 37.65 wt% carbon, 39.83 wt% nitrogen, 12.94 wt% oxygen, 1.66 wt% phosphorus, and 0.62 wt% titanium. It was observed that the C/N atomic ratio close to 1 in all samples confirms that the basic structure of g-C₃N₄ is preserved after the addition of phosphorus and titanium. However, the notable presence of oxygen can be attributed to air adsorption or partial oxidation of the material. At the same time, the quantities of phosphorus and titanium indicate successful incorporation, sufficient to positively modify the photocatalytic properties without excessively altering the basic structure of g-C₃N₄.

Additionally, the incorporation of phosphorus and titanium in g-C₃N₄ modifies the morphology and enhances the material's photocatalytic properties, which makes it promising for achieving advanced applications due to its optimized structural and photocatalytic properties to overcome wastewater treatment.





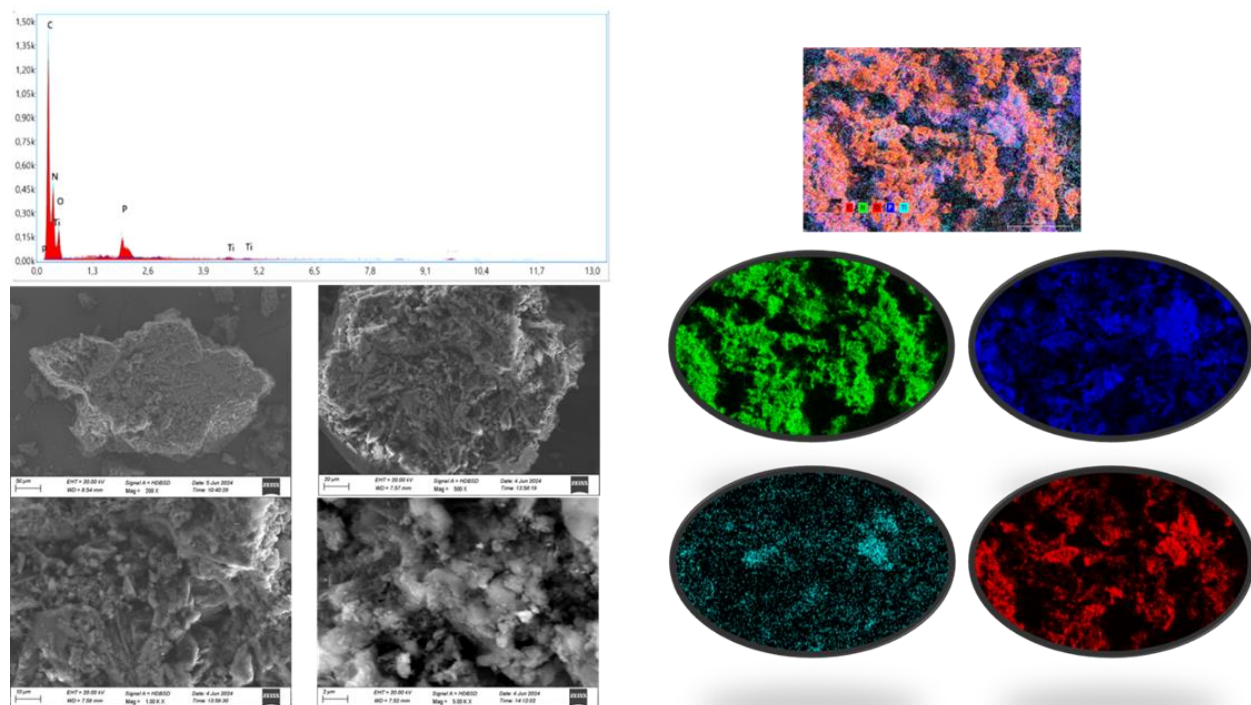


Figure V.4. The Scanning electron microscopy (SEM), elemental mapping, and Energy-dispersive X-ray (EDX) spectroscopy analyses of the (a) g-C₃N₄, (b) P-g-C₃N₄, (c) Ti-g-C₃N₄, and (d) P-g-C₃N₄@Ti-g-C₃N₄.

V.3.1.4. Transmission Electron Microscopy (TEM)

from 13.44 to 6.52 nm. The increase in particle size compared to pure g-C₃N₄ may be due to the introduction of phosphorus, which modifies the structure and may promote particle aggregation or growth. In addition, the wrinkled and rough surfaces further increase the specific surface area, which can improve the adsorption of reactive molecules, guarantee efficient charge carrier transfer and thus enhance photocatalytic efficiency. Finally, in the case of the g-C₃N₄ sample TEM images also show wrinkled nanosheets, with spots corresponding to areas containing titanium. The particle sizes range from 10.46 to 5.87 nm. Moreover, the presence of titanium seems to slightly affect morphology and reduce the particle size compared to phosphorus doping, which can be attributed to a more uniform and well distribution, and better incorporation of titanium into the g-C₃N₄ matrix. In this configuration, the wrinkled nanosheets with homogeneous titanium distribution can improve the photocatalytic properties by facilitating the overall charge separation and increasing light absorption efficiency. The TEM analysis indicates a strong binding between P, Ti, and g-C₃N₄. This

experiment showcases a productive and strong interaction between titanium, phosphorus, and g-C₃N₄, validating the successful creation of a hetero-system material.

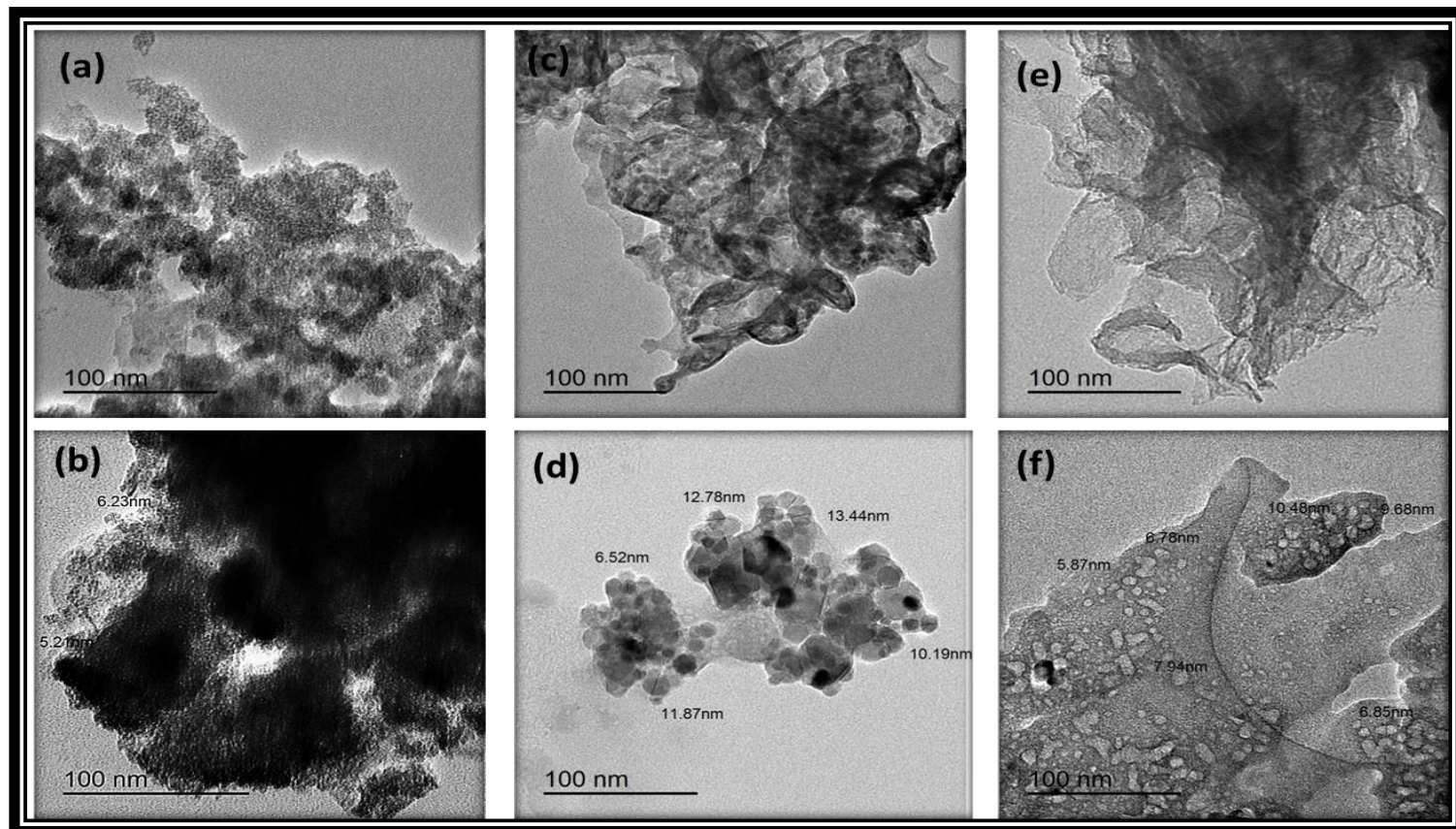


Figure V.5. TEM images of different samples g-C₃N₄ (a) and (b), P- g-C₃N₄ (c) and (d), Ti- g-C₃N₄ (e) and (f).

V.3.1.5. UV-Visible Diffuse Reflectance Spectroscopy (UV-DRS)

UV-Visible Diffuse Reflectance Spectroscopy (UV-DRS) is a crucial technique for studying the absorption properties of materials, particularly in the UV and visible regions. UV-DRS spectra measure absorption at different wavelengths, providing critical information about electronic transitions in materials. The position of absorption bands obtained from UV-DRS spectra can be used to calculate the material's band gap energy. To determine the band gap energy (E_g), the Tauc method is commonly employed. This method involves converting diffuse reflectance data as a function of the square root of the photon energy for direct band gap materials or the square root of the photon energy for indirect band gap materials.

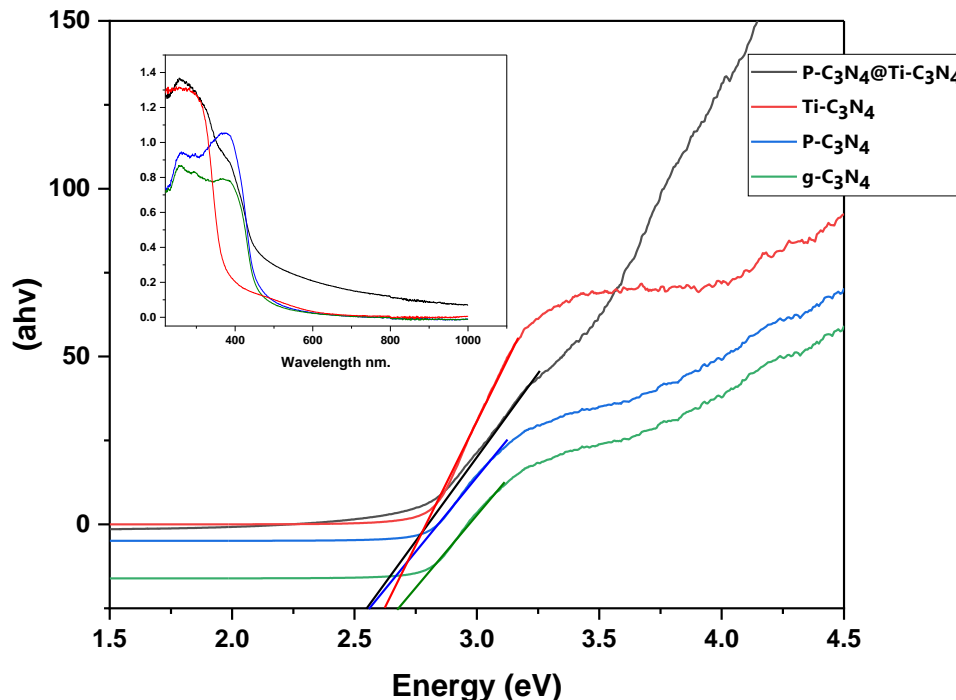


Figure V.6. Band gap energies and UV-vis diffuse reflectance spectra of pure g-C₃N₄, P- g-C₃N₄, Ti- g-C₃N₄, and the P-g-C₃N₄@ Ti-g-C₃N₄.

The results regarding the absorption bands and bandgap energies for the different dopings of graphitic carbon nitride (g-C₃N₄) and the P- g-C₃N₄@Ti- g-C₃N₄ composite reveal presented in figure 8 significant effects of doping on the optical and electronic properties of the material.

For undoped g-C₃N₄, the absorption band at 371.88 nm corresponds to a bandgap energy of 2.68 eV. This value aligns with the literature, which generally reports bandgap energies around 2.7 eV for pure g-C₃N₄. This indicates that pure g-C₃N₄ has a relatively large bandgap, making it suitable for UV light absorption but limiting its photocatalytic efficiency under visible light [35].

Doping g-C₃N₄ with titanium (Ti) shifts the absorption band to 374.49 nm and reduces the bandgap energy to 2.61 eV. This reduction in bandgap energy allows for better absorption of visible light. Titanium introduces new electronic states within the bandgap of g-C₃N₄, facilitating electron excitation under lower energy (closer to visible light) [36].

Doping g-C₃N₄ with phosphorus (P) shifts the absorption band to 261.76 nm and reduces the bandgap energy to 2.51 eV. Phosphorus has an even more pronounced effect on reducing the bandgap energy, suggesting the introduction of lower energy levels within the bandgap of g-C₃N₄. However, the absorption band at 261.76 nm is in the UV range, which might indicate electronic transitions specific to the dopant states introduced by phosphorus [37].

The P-g-C₃N₄@Ti-g-C₃N₄ composite exhibits an absorption band at 271.13 nm and a bandgap energy of 2.56 eV. This absorption band results from the interaction between the doping effects of phosphorus and titanium. The shift of the absorption band to shorter wavelengths can be attributed to synergies between the two dopants, while the reduced bandgap energy of 2.56 eV suggests improved visible light absorption compared to pure g-C₃N₄. The composite thus optimizes the beneficial effects of both dopants, potentially enhancing photocatalytic performance under visible light. Doping g-C₃N₄ with titanium and phosphorus significantly alters the optical and electronic properties of the material. Both Ti and P introduce new states within the bandgap, reducing the bandgap energy and improving visible light absorption. The P-g-C₃N₄@Ti-g-C₃N₄ composite combines the advantages of both dopants, optimizing properties for photocatalytic applications.

V.3.1.6. Fluorescence spectra (PL)

The photoluminescence (PL) results for pure g-C₃N₄, phosphorus-doped P-g-C₃N₄, titanium-doped Ti-g-C₃N₄ and their composite (P-g-C₃N₄@Ti-g-C₃N₄) (figure 9) reveal significant differences in the intensity of the peak around 460 nm, providing key insights into charge separation efficiency and photocatalysis. For pure g-C₃N₄, the intense PL peak at 460 nm indicates a high recombination rate of electron-hole pairs [38], which may limit photocatalytic efficiency by reducing the availability of charge carriers for dye degradation reactions [39]. In contrast, Ti-g-C₃N₄ exhibits a notable decrease in PL intensity, suggesting improved charge separation. The titanium doping appears to enhance charge carrier separation, thereby reducing recombination and potentially increasing photocatalytic efficiency. P-g-C₃N₄ also shows a reduction in PL intensity compared to the pure material, indicating improved charge separation. However, this improvement is more pronounced than that observed with titanium doping. Finally, the P-g-C₃N₄@Ti-g-C₃N₄ composite demonstrates an even lower PL intensity, suggesting optimal charge separation due to the

synergistic effects of both phosphorus and titanium doping. This indicates that the composite may offer the best photocatalytic performance for dye degradation by minimizing charge recombination.

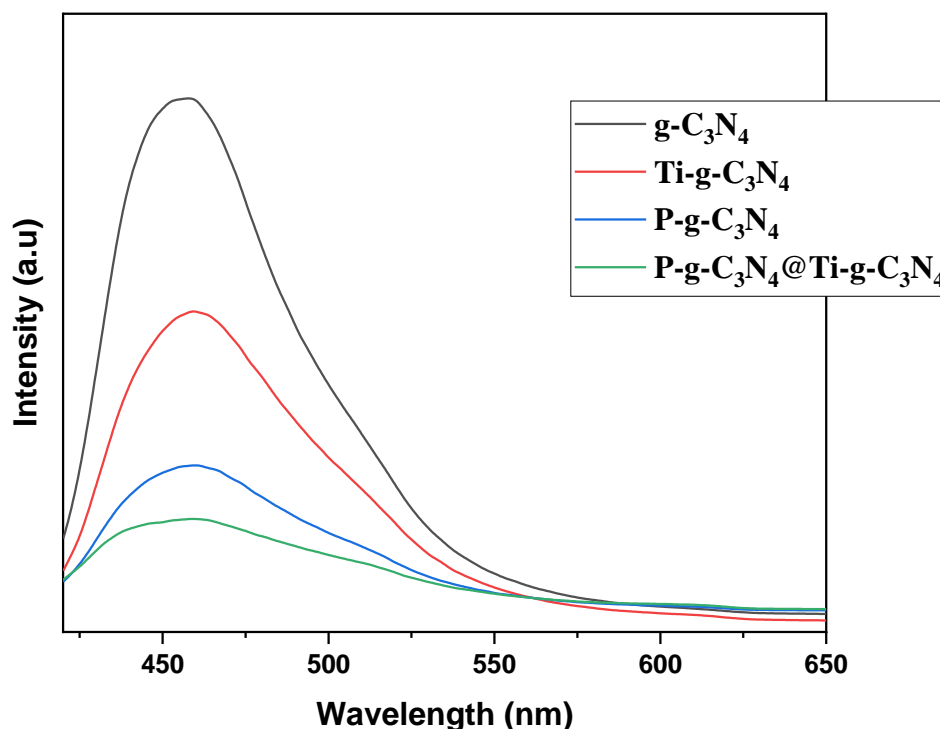


Figure V.7. Photoluminescence spectra pure g-C₃N₄, P- g-C₃N₄, Ti- g-C₃N₄, and the P-g-C₃N₄@Ti-g-C₃N₄.

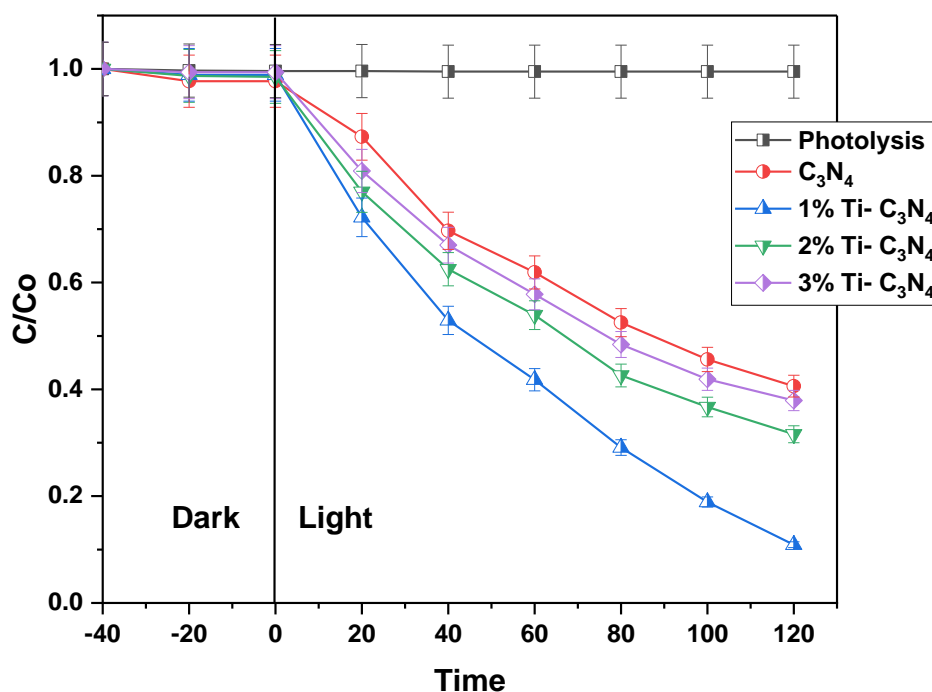
V.3.2. Photocatalytic results

V.3.2.1. Titanium- g-C₃N₄ doped

The results of our current study demonstrate that the introduction of titanium (Ti) atoms into the structure of g-C₃N₄ leads to a reduction in the band gap width and a decrease in the recombination rate of photo-induced charge carriers, resulting in an enhancement of photocatalytic performance. To validate this hypothesis, we evaluated the photocatalytic activities of pure and Ti-doped g-C₃N₄ samples for the degradation of (BS) under light, monitoring the variation of the C/C_0 ratio and observing the characteristic emission intensity of BS. To minimize errors attributed to physical adsorption during photocatalytic processes, we established the absorption-desorption equilibrium

behavior of the catalyst in darkness for 40 minutes prior to light irradiation. Our observations clearly demonstrate that approximately 54.4% of BS was degraded on the undoped g-C₃N₄, while nearly 89% of the dye (BS) was degraded on the Ti- g-C₃N₄ after 120 minutes of irradiation, confirming a significant enhancement in photocatalytic capacity following Ti doping. Among the different doped compounds, g-C₃N₄ doped with 1% Ti exhibited the best performance during the photocatalytic process, with a degradation of 89.1% of BS, compared to degradation rates of 68.4% and 62.1% for samples doped with 2% and 3% Ti, respectively.

The photocatalytic degradation rate constants (K) further support this trend. Without the catalyst, the rate constant was measured as $2.15 \times 10^{-5} \text{ min}^{-1}$. The undoped g-C₃N₄ displayed a rate constant of 0.00754 min^{-1} , whereas the Ti-doped g-C₃N₄ samples showed the following values: 0.01679 min^{-1} for 1% Ti, 0.00993 min^{-1} for 2% Ti, and 0.00857 min^{-1} for 3% Ti. These results highlight that the 1% Ti-doped g-C₃N₄ sample exhibited the highest rate constant, further underscoring the efficacy of low-level Ti doping in improving the photocatalytic performance of g-C₃N₄. This improvement is attributed to the efficient reduction of charge carrier recombination and enhanced light sensitivity induced by doping [40].



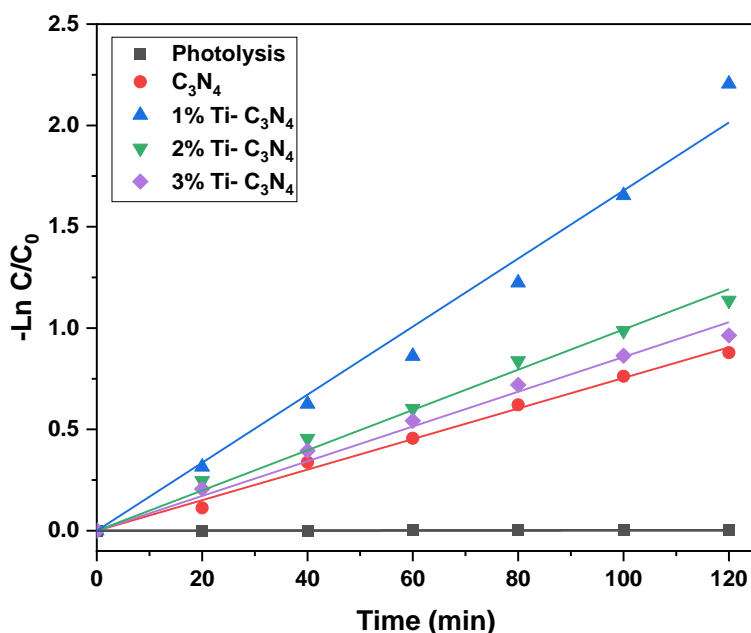
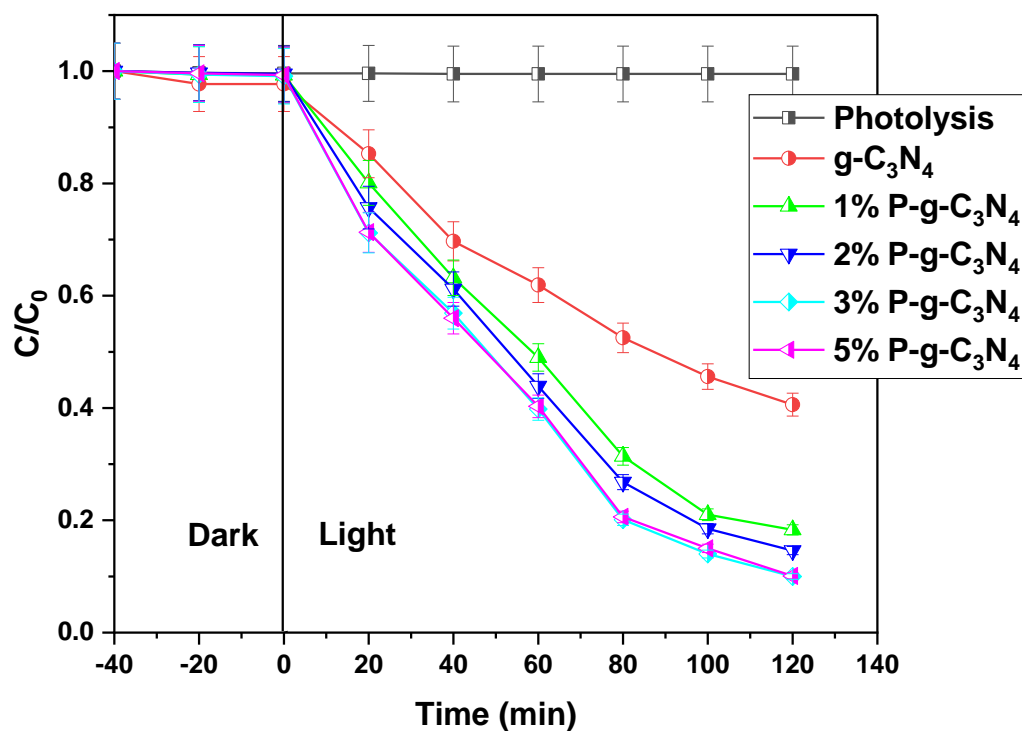


Figure V.8. Photodegradation behaviors of BS on pure and Ti-doped g-C₃N₄ under visible light irradiation. (neutral pH, catalyst 1 g/L, [BS] = 30 mg/L).

V.3.2.2. Phosphorus-g-C₃N₄ doped

The photocatalytic activities of the prepared samples were studied for the decomposition of (BS) under simulated light. The concentration ratio C/C_0 , depicted in the figure, reflects the concentration of BS at a certain reaction time using g-C₃N₄ and P-g-C₃N₄ photocatalysts. When phosphorus doping is performed, the photocatalytic activity of g-C₃N₄ is enhanced to some extent. Specifically, the results show that the degradation percentages of (BS) for samples doped with 1% P- g-C₃N₄, 2% P- g-C₃N₄, 3% P- g-C₃N₄, and 5% P- g-C₃N₄ were 81.7%, 85.4%, 90%, and 90%, respectively. These degradation percentages were significantly higher compared to undoped g-C₃N₄, which exhibited a degradation of 54.4%. The enhancement in photocatalytic activity with increasing phosphorus doping levels indicates that the introduction of phosphorus into the g-C₃N₄ structure plays a crucial role in enhancing its photocatalytic performance. The observed increase in degradation percentages attributed to various factors, including the modification of electronic properties [41], changes in surface morphology, adjustment of the band gap width, and the creation of active sites for photocatalytic reactions [42]. The photocatalytic degradation rate constants (K) reveal a similar pattern. The undoped g-C₃N₄ had a rate constant of 0.00754 min⁻¹, while P-doped

samples exhibited higher values: 0.01415 min⁻¹ for 1% P, 0.01586 min⁻¹ for 2% P, 0.01877 min⁻¹ for 3% P, and 0.01848 min⁻¹ for 5% P. Although 5% phosphorus doping also achieved a 90% degradation rate, the 3% P-doped g-C₃N₄ was chosen due to its comparable performance and better cost-efficiency, making it the optimal choice in terms of both efficiency and economic viability.



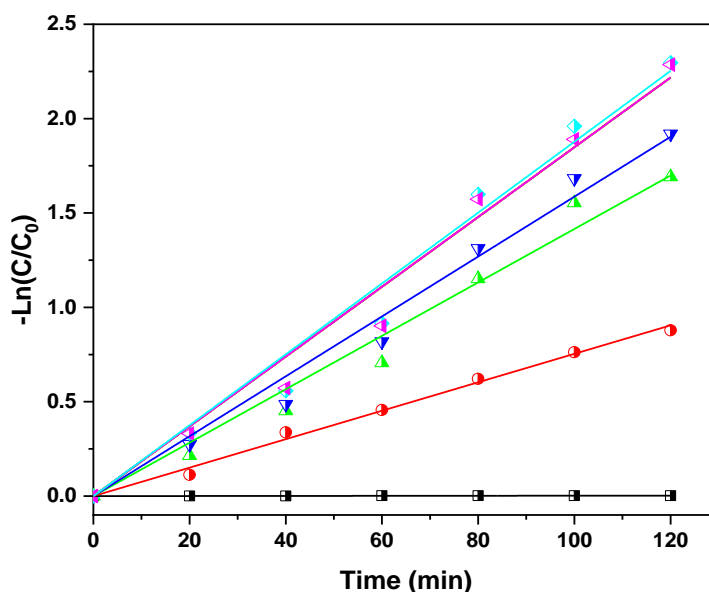


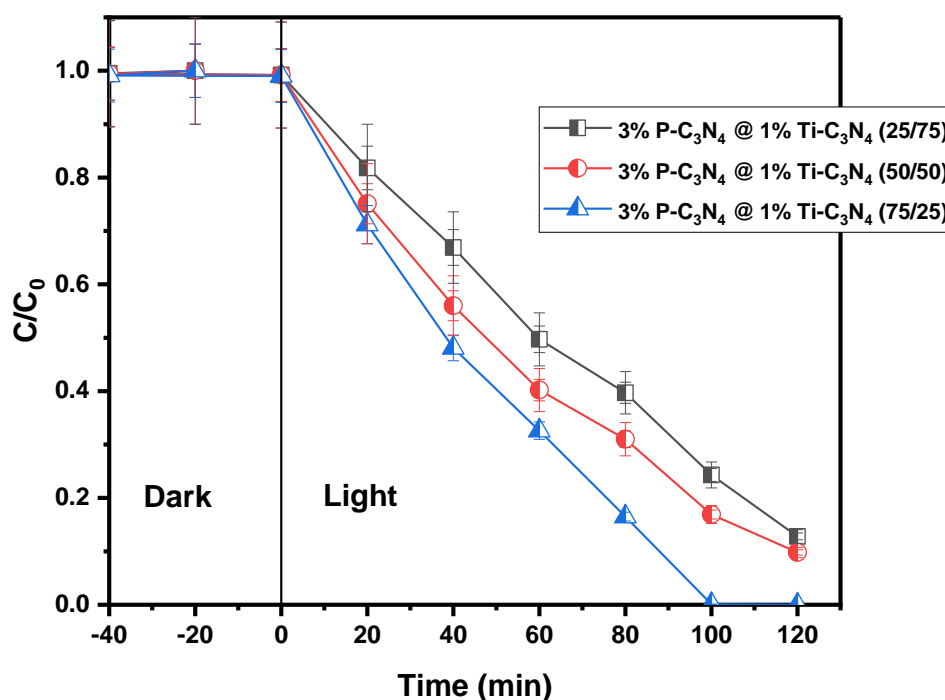
Figure V.9. Photodegradation behaviors of BS on pure and P-doped g-C₃N₄ under visible light irradiation. (neutral pH, catalyst 1 g/L, [BS] = 30 mg/L).

V.3.2.3. P-C₃N₄ @ Ti-C₃N₄ (x/y) Composite

The results obtained from the photocatalytic degradation of (BS) using phosphorus carbon nitride (P-g-C₃N₄) and titanium carbon nitride (Ti-g-C₃N₄) compounds have been promising. Following these encouraging observations, a strategy of physically mixing these two materials was pursued in different proportions, namely (25%/75%), (50%/50%), and (75%/25%) for P- g- C₃N₄ and Ti-g-C₃N₄, respectively. The photocatalytic results of these composites were evaluated and presented graphically. Significantly, the composite containing 75% P- g-C₃N₄ and 25% Ti- g-C₃N₄ demonstrated the best performance, achieving a 100% degradation efficiency of BS over a 100-minute period. This observation starkly contrasts with the performances of the other composites, which contained different proportions of P-g-C₃N₄ and Ti- g-C₃N₄. The enhanced photocatalytic performance in this case can be attributed to increased synergy between the two compounds, thereby more effectively harnessing pollutant degradation mechanisms. Furthermore, this study revealed that the composite resulting from the mixture of the two materials surpassed the degradation performances observed for each of the materials used individually. Indeed, compared to the use of P-g-C₃N₄ or Ti-g-C₃N₄ alone, the total degradation time was reduced by approximately

40 minutes. This result underscores the importance of the composite design approach for enhancing photocatalytic performances, thus offering promising prospects for the development of more efficient and sustainable wastewater treatment technologies.

The photocatalytic degradation rate constants (K) offer additional insight into the performance of the composites. The mixture containing 25% P-g-C₃N₄ and 75% Ti-g-C₃N₄ showed a rate constant of 0.0112 min⁻¹, while the 50%/50% blend exhibited a slightly higher rate constant of 0.01464 min⁻¹. The most effective composite, consisting of 75% P-g-C₃N₄ and 25% Ti-g-C₃N₄, achieved a significantly higher rate constant of 0.02045 min⁻¹, highlighting its superior efficiency in degrading the pollutant.



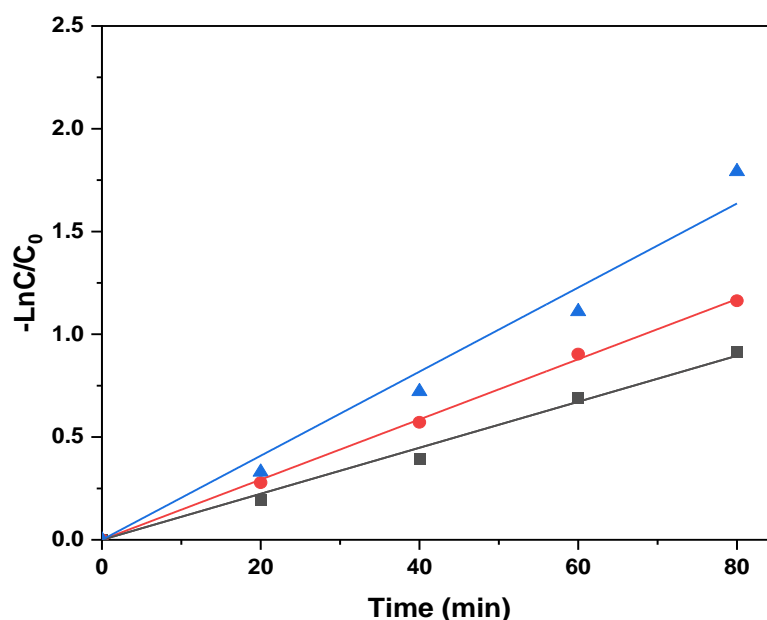
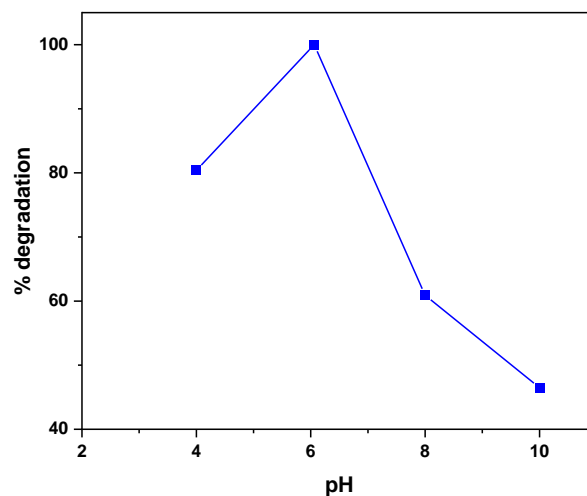
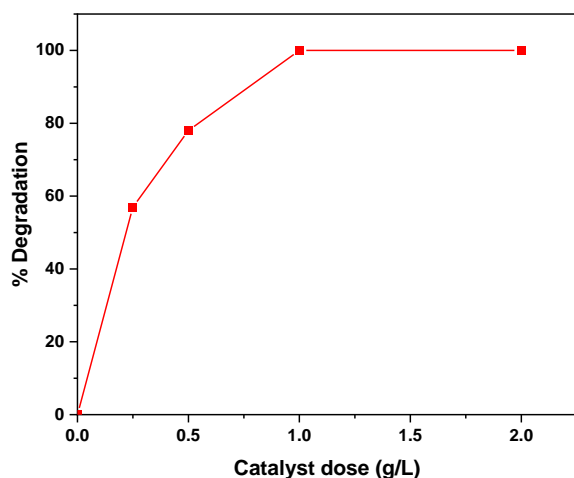


Figure V.10. Photodegradation of BS dye P-C₃N₄ @ Ti-C₃N₄ (x/y) (x = 25, 50 and 75%) (y = 75, 50 and 25%) (neutral pH, catalyst 1 g/L, [BS] = 30 mg/L).

V.3.2.4. The effects of operational parameters on photocatalytic degradation of bieberich scarlet

The investigation of operational parameters for the photodegradation of the dye Beibrich Scarlet using the P- g-C₃N₄ 4@Ti- g-C₃N₄ composite was conducted to optimize pH, catalyst dosage, and initial dye concentration. The results are presented in the figure. The photocatalytic tests of the P- g-C₃N₄ 4@Ti- g-C₃N₄ composite revealed a significant response to different pH values and various catalyst doses. At pH 6, the composite demonstrated its best performance, achieving a degradation rate of 100%. At pH 4, although slightly less effective, a respectable degradation rate of 80.4% was recorded. However, at higher pH levels of 8 and 10, the performances decreased, with degradation rates of 60.9% and 46.5%, respectively. This decrease in efficiency in alkaline environments could be attributed to potential catalyst deactivation or secondary reactions limiting the effectiveness of the photocatalytic process at higher pH levels [43]. Regarding catalyst doses, progressive improvements in efficiency were observed with increasing concentration. At a concentration of 0.25 g/L, the degradation rate was 57%, increasing to 78% at 0.5 g/L. A dose of 1 g/L resulted in a maximum efficiency of 100%, as did a dose of 2 g/L. This suggests that the process efficiency is directly proportional to the catalyst dose up to a saturation threshold of 1 g/L. These results indicate

that the composite exhibits photocatalytic activity over a range of pH values from slightly acidic to neutral, with an optimal pH of 6. However, lower performance is observed in more acidic or alkaline environments. Finally the influence of the initial concentration of the BS dye on photocatalysis was investigated, yielding remarkable results. At an initial concentration of 10 mg/L, complete degradation of the dye was achieved in just 20 minutes, indicating a rapid and efficient photocatalytic process, with a kinetic constant (k) of 0.05229 min^{-1} . When the initial concentration was increased to 20 mg/L, complete degradation still occurred, albeit in a longer period of 80 minutes, with a kinetic constant of 0.0188 min^{-1} . This suggests that although the photocatalyst remains effective, higher dye concentrations require more time for complete degradation. Similarly, at an initial concentration of 30 mg/L, complete degradation was achieved in 100 minutes, with a kinetic constant of 0.01269 min^{-1} . However, at an initial concentration of 40 mg/L, although the degradation rate was high, complete degradation was not achieved within the same timeframe. The corresponding kinetic constant was 0.00588 min^{-1} . These results indicate that the photocatalyst is capable of efficiently treating higher dye concentrations, although slightly longer reaction times are necessary.



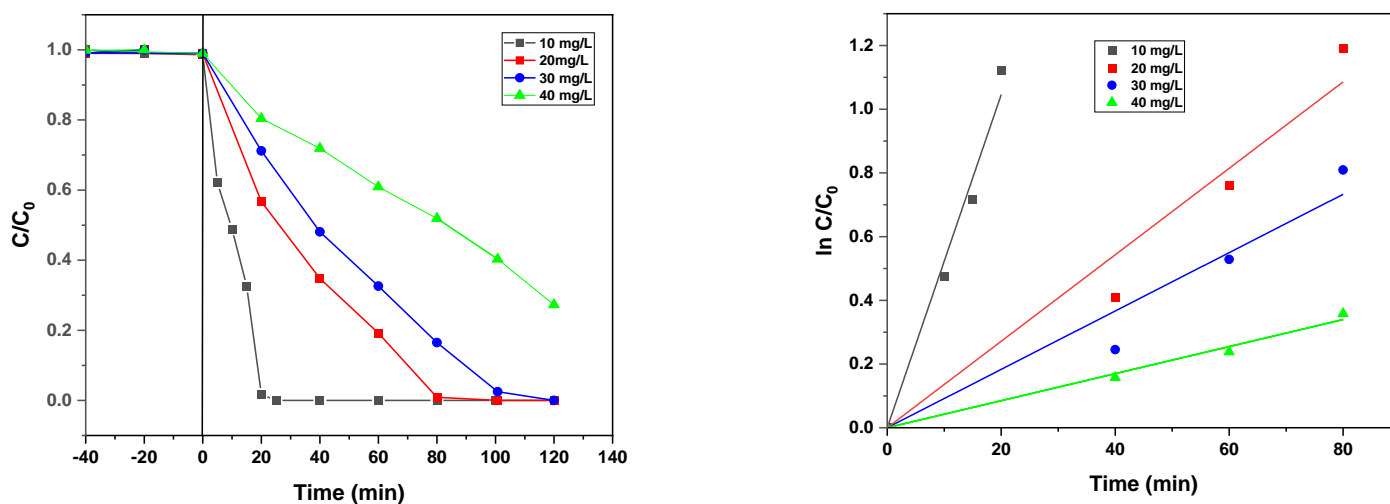


Figure V.11. The effects of operational parameters on photocatalytic degradation of BS Where (a) dose effect, (b) pH effect, (c) initial concentration effect.

V.3.2.5. Normalized intensities of absorption bands

Figure 14 shows the normalized intensities of the absorption bands for BS at 228 nm (benzene ring) [Ilán et al., 1976], 325 nm (naphthalene ring) [44], and 506 nm (azo bond) [45], plotted as a function of irradiation time and represented as the ratio of absorbance at a given time to its initial value.

For Ti-C₃N₄, it is observed that the intensity of the band corresponding to the azo bond (visible light chromophore) decreases over time, while the intensities of the bands due to the benzene and naphthalene rings increase. This increase in intensities can be explained by the formation of by-products containing benzene and naphthalene structures resulting from ring opening. In other words, the azo bond breaks earlier and more rapidly, releasing aromatic fragments. For P-C₃N₄, the intensity of the band due to the azo linkage (visible light chromophore) decreases more rapidly than that of the benzene and naphthalene ring chromophores. This suggests a faster degradation of the azo bond compared to the aromatic structures, indicating different rupture kinetics. Finally, for P-g-C₃N₄@Ti-g-C₃N₄, the intensity of all bands decreases at almost the same rate, with the azo bond decreasing slightly faster. This indicates that the issue of marked by-products during degradation by Ti-C₃N₄ is mitigated by the mixture. In other words, the mixture P-g-C₃N₄@Ti-g-C₃N₄ is able to degrade both the BS molecule and its degradation by-products simultaneously within the same irradiation time. This interaction between the two materials not only reduces the degradation time of BS but also ensures a complete degradation of the by-products. This suggests

a synergy between P-g-C₃N₄ and Ti-g-C₃N₄ that optimizes the degradation process, making it more efficient and complete.

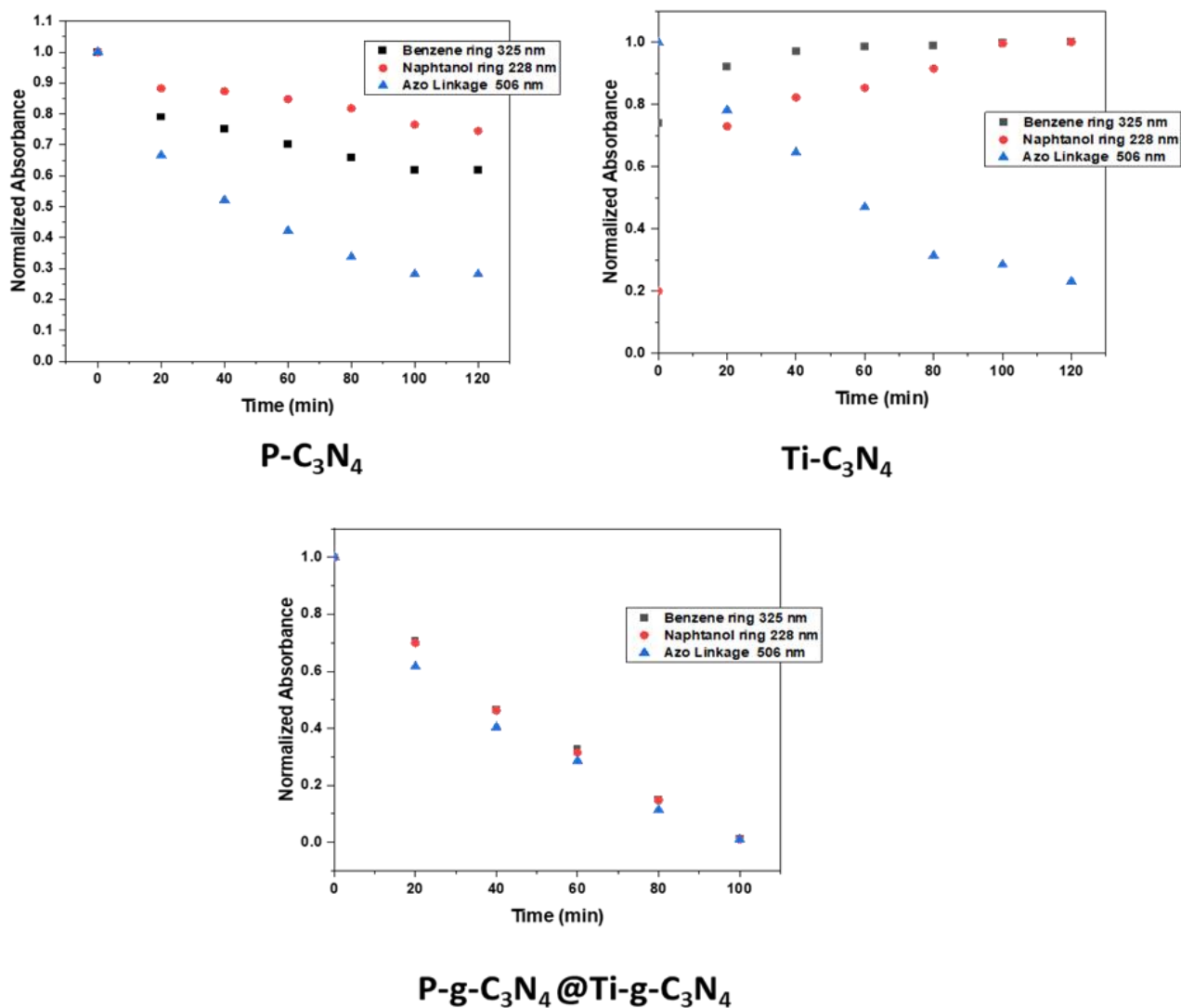


Figure V.12. The normalized intensities of the absorption bands for BS

V.3.2.6. Systematic Evaluation of Photostability and Reusability of P-g-C₃N₄@Ti-g-C₃N₄ Composite

Photostability is a crucial factor in determining the practical viability of a photocatalyst. To thoroughly evaluate the structural integrity and catalytic endurance of the P-g-C₃N₄@Ti-g-C₃N₄ composite, a series of four successive tests focused on the photocatalytic degradation of BS were conducted. The recycling process after each Visible-light-assisted BS degradation involved several critical steps. First, the composite was carefully recovered through precision centrifugation following each photocatalytic test. Then, it underwent a thorough washing protocol consisting of four cycles using a mixture of distilled water and ethanol, with the final cycle employing double-distilled water. After washing, the material was subjected to a five-hour UV light treatment in double-distilled water to ensure the complete removal of any residual BS from the photocatalytic process. Following the UV treatment, the P-g-C₃N₄@Ti-g-C₃N₄ composite was gently recovered and dried at 60 °C for 24 hours. This drying step was essential to preserve the material for subsequent cycles. This meticulous and comprehensive approach provides a robust framework for assessing the longevity and reusability of the P-g-C₃N₄@Ti-g-C₃N₄ composite in photocatalytic applications.

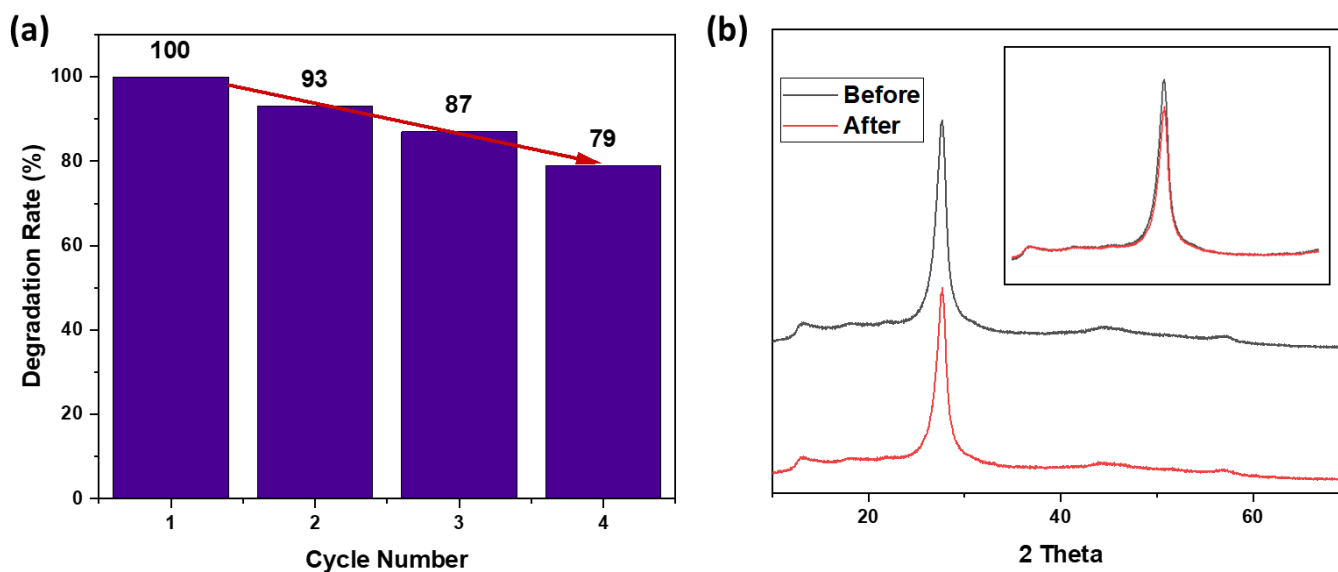


Figure V.13. The cycling degradation curves of BS using P-g-C₃N₄@Ti-g-C₃N₄ composite photocatalyst (a); XRD patterns of the fresh and the used catalysts after 4 recycling runs (b).

Figure V.15.a demonstrates the high initial efficiency and robust performance of the P-g-C₃N₄@Ti-g-C₃N₄ composite over multiple cycles. The composite achieves complete degradation in the first cycle and maintains significant degradation efficiencies of 93%, 87%, and 79% over the second, third, and fourth cycles, respectively. This highlights the composite's strong photocatalytic activity and durability, even after repeated use. The slight decrease in efficiency across the cycles is expected and underscores the material's resilience and capability to perform effectively over extended periods. The carefully designed washing and UV treatment protocols play a crucial role in maintaining the composite's performance, ensuring it remains a viable and efficient photocatalyst. Additionally, the XRD analysis of the materials before and after the degradation process (figure 15.b) shows no difference in the peaks, with only a very slight decrease in the intensity of the main peaks. Overall, these results showcase the P-g-C₃N₄@Ti-g-C₃N₄ composite as a promising and durable material for photocatalytic applications, with excellent potential for long-term use. The composite's ability to sustain high degradation rates over multiple cycles attests to its robustness and reliability, making it a valuable addition to the field of photocatalysis.

V.3.2.7. Scavengers effect

The scavenger test results present in figure V.15 revealed that different reactive species contribute variably to the degradation of the dye BS in the presence of the p-g-C₃N₄@Ti-g-C₃N₄ catalyst. The addition of ethanol, a scavenger for hydroxyl radicals (OH), led to a degradation rate of 21%, indicating that hydroxyl radicals are the most dominant reactive species in the degradation process. In contrast, the use of EDTA, a scavenger for holes (h⁺), reduced the degradation rate to 34%, suggesting that holes also play an important role, although less dominant than hydroxyl radicals. Finally, the addition of K₂Cr₂O₇, a scavenger for electrons (e⁻), decreased the degradation rate to 37%, indicating that electrons have a notable influence but are the least dominant among the three reactive species studied. In summary, these results show that hydroxyl radicals (•OH) are the most important reactive species in the degradation of the dye BS, followed by holes (h⁺) and electrons (e⁻), highlighting the significant role of hydroxyl radicals in the photocatalytic degradation mechanism.

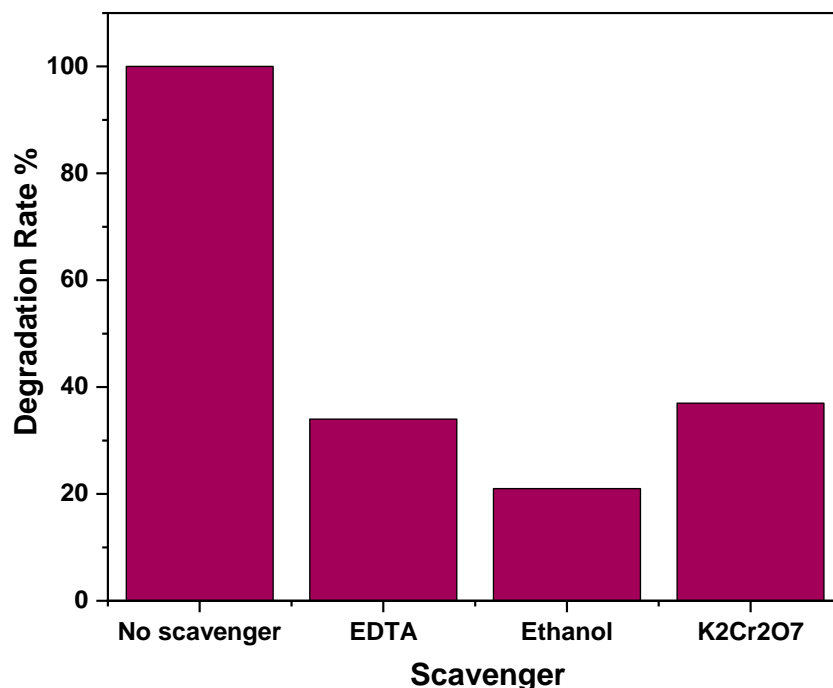


Figure V.14. The degradation rates of BS using P-g-C₃N₄@Ti-g-C₃N₄ photocatalyst when adding different scavengers.

V.3.3. The plausible photodegradation mechanism

The detailed mechanism of dye BS degradation by the p-g-C₃N₄@Ti-g-C₃N₄ composite presented in figure 17 begins with the excitation of the catalyst under visible light irradiation, generating electron-hole pairs (e^-/h^+) [46]. The combination of P-C₃N₄ and Ti-C₃N₄ forms a heterojunction that allows for better charge separation, with electrons generated in P-C₃N₄ migrating to Ti-C₃N₄, thereby reducing the recombination of electron-hole pairs. The holes (h^+) react with water adsorbed on the surface of the composite to form hydroxyl radicals ($\bullet OH$) [47], while the electrons (e^-) reduce dissolved oxygen to form superoxide anions ($O_2^{\bullet -}$) [48]. The dye BS is adsorbed onto the surface of the composite, which is essential for its interaction with the reactive species [49]. The hydroxyl radicals ($\bullet OH$) and superoxide anions ($O_2^{\bullet -}$) then attack the dye BS molecules, leading to their degradation into intermediates. These intermediates are subsequently mineralized into harmless final products such as water (H₂O) and carbon dioxide (CO₂). This process highlights the importance of the formation of hydroxyl radicals and superoxide anions, as well as the crucial role

of the heterojunction structure of the composite in achieving efficient charge separation and reducing recombination.

Here are the chemical reactions corresponding to the mechanism of BS dye degradation using the P-g-C₃N₄@Ti-g-C₃N₄ composite:

1. Excitation of the photocatalyst:



(Electron-hole pair generation under light irradiation)

2. Electron transfer between P-g- C₃N₄ and Ti-g- C₃N₄ (heterojunction formation):



(Electrons migrate from P-g- C₃N₄ to Ti-g- C₃N₄)

3. Hole transfer from Ti-g-C₃N₄ to P-g-C₃N₄:



(Holes migrate from Ti-g-C₃N₄ to P-g- C₃N₄)

4. Hydroxyl radical formation from surface water:



(Holes oxidize water on the P-g-C₃N₄ side to produce hydroxyl radicals)

5. Reduction of oxygen by electrons to form superoxide anions:



(Electrons reduce oxygen to form superoxide anions)

6. Dye degradation by reactive species:



(Hydroxyl radicals and superoxide anions attack the dye BS molecules)

7. Mineralization of intermediates:



Intermediates are mineralized into carbon dioxide and water

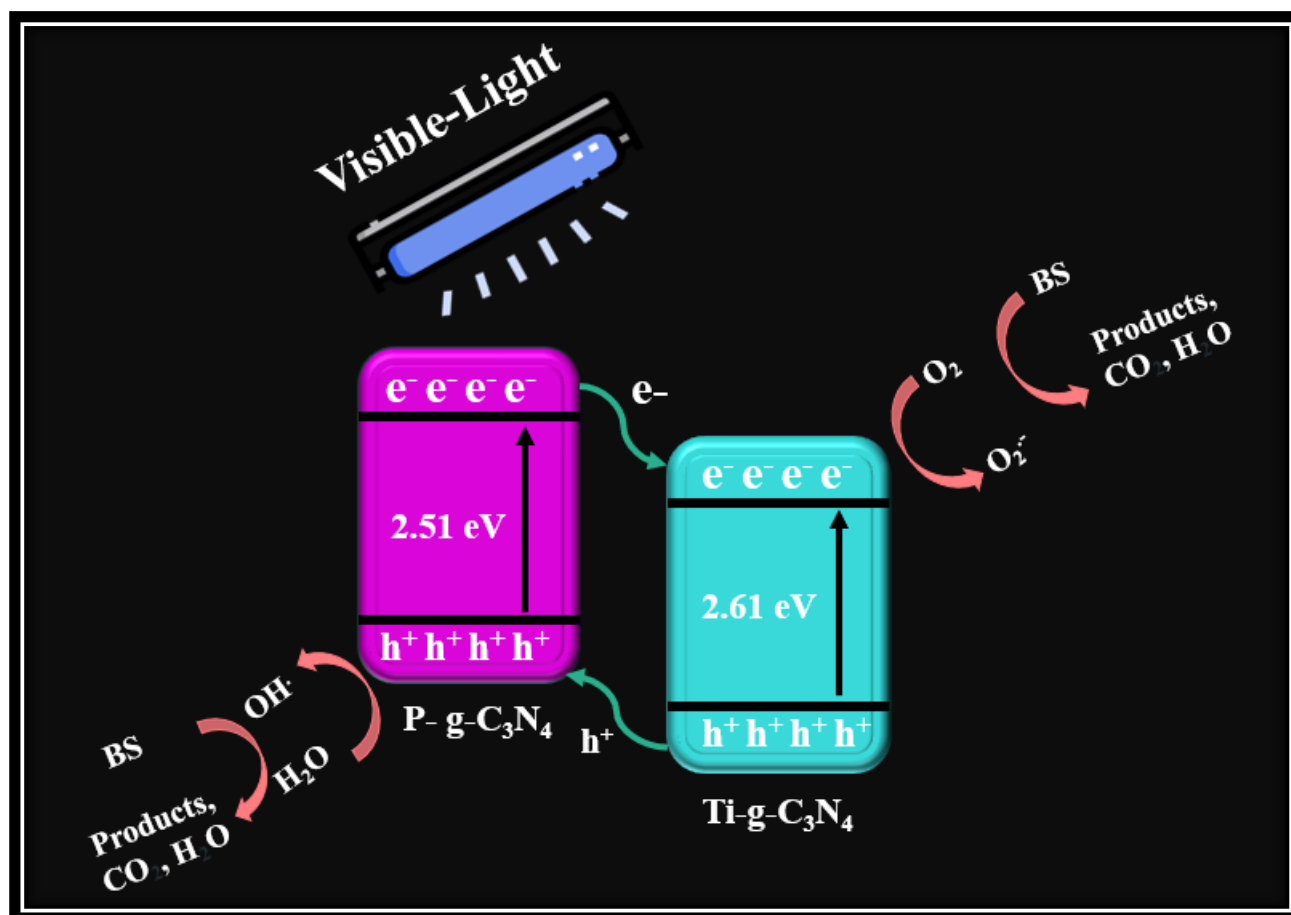


Figure V.15. The photodegradation mechanism of BS.

V.4. Comparison of the Photocatalytic Efficacy of various g- C₃N₄-based composites in degrading different organic dyes

Table V.1. Photocatalytic Efficiency of g-C₃N₄-Based Composites in the Degradation of Various Organic Dyes.

Catalyst	Dye	Concentration (mg/L)	Irradiation Time (min)	degradation Efficiency (%)	References
ZnO/g-C ₃ N ₄	MB	5	120	92	[50]
WO ₃ @g-gC ₃ N ₄	RhB	10	140	90	[51]
g-C ₃ N ₄ /V ₂ O ₅	RhB	10	100	100	[52]
ZnFe ₂ O ₄ /S-g-C ₃ N ₄	MB	10	120	92	[53]
P-g-c3n4@Ti-g-C ₃ N ₄	BS	30	100	100	Present work

Table V.1 compares the photocatalytic efficiency of various g- C₃N₄-based composites in degrading different organic dyes under light irradiation. A detailed comparative analysis highlights the superiority of the P-g-C₃N₄@Ti-g-C₃N₄ composite, which demonstrated complete degradation of BS at a concentration of 30 mg/L in 100 minutes. This performance is particularly noteworthy compared to the other materials tested, which required more time or were tested at lower dye concentrations.

For example, ZnO/ g-C₃N₄ degraded 92% of Methylene Blue (MB) in 120 minutes, but at a lower concentration of 5 mg/L. Similarly, the WO₃@g- g-C₃N₄ composite achieved 90% degradation of Rhodamine B (RhB) in 140 minutes with a dye concentration of 10 mg/L, indicating less effective photocatalytic activity compared to P- g-C₃N₄ @Ti- g-C₃N₄. The g- g-C₃N₄ /V₂O₅ composite also showed complete degradation of RhB but at a lower concentration of 10 mg/L in 100 minutes, which, although comparable in terms of time, is inferior in terms of the dye load treated.

Finally, ZnFe₂O₄/S-g-C₃N₄ achieved 92% degradation of MB at a concentration of 10 mg/L in 120 minutes, which is also less effective than P- g-C₃N₄ @Ti- g-C₃N₄. The ability of P- g-C₃N₄ @Ti-

g-C₃N₄ to maintain maximum degradation efficiency with a higher dye concentration and in a shorter time suggests that the structural modifications introduced by phosphorus and titanium doping significantly optimize the photocatalytic activity. In conclusion, P-g-C₃N₄@Ti-g-C₃N₄ emerges as the most promising candidate for photocatalytic degradation applications among the materials studied.

References

- [1] H.M. Abd El-Lateef, M.M. Khalaf, I.M. Mohamed, An efficient and non-precious anode electrocatalyst of NiO-modified carbon nanofibers towards electrochemical urea oxidation in alkaline media, *Ceramics International* 46 (2020) 20376–20384.
- [2] D. Ma, H. Yi, C. Lai, X. Liu, X. Huo, Z. An, L. Li, Y. Fu, B. Li, M. Zhang, Critical review of advanced oxidation processes in organic wastewater treatment, *Chemosphere* 275 (2021) 130104.
- [3] M.F. Hanafi, N. Sapawe, A review on the current techniques and technologies of organic pollutants removal from water/wastewater, *Materials Today: Proceedings* 31 (2020) A158–A165.
- [4] S. Murshid, A. Antonysamy, G. Dhakshinamoorthy, A. Jayaseelan, A. Pugazhendhi, A review on biofilm-based reactors for wastewater treatment: Recent advancements in biofilm carriers, kinetics, reactors, economics, and future perspectives, *Science of The Total Environment* 892 (2023) 164796.
- [5] X. Zhang, M. Zhang, H. Liu, J. Gu, Y. Liu, Environmental sustainability: a pressing challenge to biological sewage treatment processes, *Current Opinion in Environmental Science & Health* 12 (2019) 1–5.
- [6] P.O. Oladoye, M. Kadhom, I. Khan, K.H.H. Aziz, Y.A. Alli, Advancements in adsorption and photodegradation technologies for rhodamine B dye wastewater treatment: fundamentals, applications, and future directions, *Green Chemical Engineering* (2023). <https://www.sciencedirect.com/science/article/pii/S2666952823000729> (accessed August 1, 2024).
- [7] G.-I. Lupu, C. Orbeci, L. Bobirică, C. Bobirică, L.F. Pascu, Key principles of advanced oxidation processes: A systematic analysis of current and future perspectives of the removal of antibiotics from wastewater, *Catalysts* 13 (2023) 1280.
- [8] P. Singh, A. Ojha, A. Borthakur, R. Singh, D. Lahiry, D. Tiwary, P.K. Mishra, Emerging trends in photodegradation of petrochemical wastes: a review, *Environ Sci Pollut Res* 23 (2016) 22340–22364. <https://doi.org/10.1007/s11356-016-7373-y>.
- [9] H. Wu, L. Li, S. Wang, N. Zhu, Z. Li, L. Zhao, Y. Wang, Recent advances of semiconductor photocatalysis for water pollutant treatment: mechanisms, materials and applications, *Physical Chemistry Chemical Physics* 25 (2023) 25899–25924.
- [10] Y.Y. Lee, J.H. Moon, Y.S. Choi, G.O. Park, M. Jin, L.Y. Jin, D. Li, J.Y. Lee, S.U. Son, J.M. Kim, Visible-Light Driven Photocatalytic Degradation of Organic Dyes over Ordered Mesoporous Cd_xZn_{1-x}S Materials, *J. Phys. Chem. C* 121 (2017) 5137–5144. <https://doi.org/10.1021/acs.jpcc.7b00038>.
- [11] Z. Lin, J. Xu, H. Gu, J. Huang, J. Lin, J. Shao, D. Wang, H. Li, A review on research progress in photocatalytic degradation of organic pollutants by Bi₂MoO₆, *Journal of Environmental Chemical Engineering* (2023) 110911.

- [12] A. Rafiq, M. Ikram, S. Ali, F. Niaz, M. Khan, Q. Khan, M. Maqbool, Photocatalytic degradation of dyes using semiconductor photocatalysts to clean industrial water pollution, *Journal of Industrial and Engineering Chemistry* 97 (2021) 111–128.
- [13] K. Madi, D. Chebli, H. Ait Youcef, H. Tahraoui, A. Bouguettoucha, M. Kebir, J. Zhang, A. Amrane, Green Fabrication of ZnO Nanoparticles and ZnO/rGO Nanocomposites from Algerian Date Syrup Extract: Synthesis, Characterization, and Augmented Photocatalytic Efficiency in Methylene Blue Degradation, *Catalysts* 14 (2024) 62.
- [14] P.C. Kumar, S. Senapati, D. Pradhan, J. Kumar, R. Naik, A facile one-step microwave-assisted synthesis of bismuth oxytelluride nanosheets for optoelectronic and dielectric application: An experimental & computational approach, *Journal of Alloys and Compounds* 968 (2023) 172166.
- [15] Y. Ren, D. Zeng, W.-J. Ong, Interfacial engineering of graphitic carbon nitride (g-C₃N₄)-based metal sulfide heterojunction photocatalysts for energy conversion: a review, *Chinese Journal of Catalysis* 40 (2019) 289–319.
- [16] G. Mamba, A.K. Mishra, Graphitic carbon nitride (g-C₃N₄) nanocomposites: a new and exciting generation of visible light driven photocatalysts for environmental pollution remediation, *Applied Catalysis B: Environmental* 198 (2016) 347–377.
- [17] A. Hayat, M. Sohail, J. Ali Shah Syed, A.G. Al-Sehemi, M.H. Mohammed, A.A. Al-Ghamdi, T.A. Taha, H. Salem AlSalem, A.M. Alenad, M.A. Amin, A. Palamanit, C. Liu, W.I. Nawawi, M. Tariq Saeed Chani, M. Muzibur Rahman, Recent Advancement of the Current Aspects of g-C₃N₄ for its Photocatalytic Applications in Sustainable Energy System, *The Chemical Record* 22 (2022) e202100310. <https://doi.org/10.1002/tcr.202100310>.
- [18] L. Hammoud, C. Marchal, V. Caps, J. Toufaily, T. Hamieh, V. Keller, Influence of low level of non-metal doping on g-C₃N₄ performance for H₂ production from water under solar light irradiation, *International Journal of Hydrogen Energy* 51 (2024) 285–300.
- [19] F. Ling, W. Li, L. Ye, The synergistic effect of non-metal doping or defect engineering and interface coupling on the photocatalytic property of g-C₃N₄: First-principle investigations, *Applied Surface Science* 473 (2019) 386–392.
- [20] D. Masih, Y. Ma, S. Rohani, Graphitic C₃N₄ based noble-metal-free photocatalyst systems: a review, *Applied Catalysis B: Environmental* 206 (2017) 556–588.
- [21] L. Zhou, H. Zhang, H. Sun, S. Liu, M.O. Tade, S. Wang, W. Jin, Recent advances in non-metal modification of graphitic carbon nitride for photocatalysis: a historic review, *Catalysis Science & Technology* 6 (2016) 7002–7023.
- [22] P. Powell, *The Chemistry of the Non-metals*, Springer Science & Business Media, 2013. <https://books.google.com/books?hl=fr&lr=&id=4a->

- 3BgAAQBAJ&oi=fnd&pg=PA20&dq=Nonmetals,+characterized+by+high+ionization+energies+and+electronegativities,+readily+form+covalent+bonds+with+other+compounds+by+gaining+electrons+during+reaction+processes.+&ots=d2Q_NlvNIU&sig=zEFSWaCSs14_eT9tLjATPvHDdGI (accessed August 1, 2024).
- [23] S. Sahoo, P. Mahamallik, R. Das, S. Panigrahi, A Critical Review on Non-metal Doped g-C₃N₄ based Photocatalyst for Organic Pollutant Remediation with Sustainability Assessment by Life Cycle Analysis, *Environmental Research* (2024) 119390.
- [24] B. Zhu, B. Cheng, J. Fan, W. Ho, J. Yu, g-C₃N₄-Based 2D/2D Composite Heterojunction Photocatalyst, *Small Structures* 2 (2021) 2100086. <https://doi.org/10.1002/ssstr.202100086>.
- [25] M. Ghalkhani, M.H. Khaneghah, E. Sohouli, Graphitic carbon nitride: synthesis and characterization, in: *Handbook of Carbon-Based Nanomaterials*, Elsevier, 2021: pp. 573–590. <https://www.sciencedirect.com/science/article/pii/B9780128219966000142> (accessed August 1, 2024).
- [26] J. Dong, Y. Zhang, M.I. Hussain, W. Zhou, Y. Chen, L.-N. Wang, g-C₃N₄: properties, pore modifications, and photocatalytic applications, *Nanomaterials* 12 (2021) 121.
- [27] A.B. Hamou, M. Enneimy, S. Farsad, A. Amjlef, A. Chaoui, N. Nouj, A. Majdoub, A. Jada, M. Ezzahery, N. El Alem, Novel chemically reduced cobalt-doped gC₃N₄ (CoCN-x) as a highly heterogeneous catalyst for the super-degradation of organic dyes via peroxymonosulfate activation, *Materials Advances* 5 (2024) 1960–1976.
- [28] T. Yu, Z. Hu, H. Wang, X. Tan, Enhanced visible-light-driven hydrogen evolution of ultrathin narrow-band-gap g-C₃N₄ nanosheets, *J Mater Sci* 55 (2020) 2118–2128. <https://doi.org/10.1007/s10853-019-04082-7>.
- [29] E.M. Popov, M.I. Kabachnik, L. Mayants, Vibrational spectra of organophosphorus compounds, *Russian Chemical Reviews* 30 (1961) 362.
- [30] P. Sharma, P.P. Sarngan, A. Lakshmanan, D. Sarkar, One-step synthesis of highly reactive g-C₃N₄, *J Mater Sci: Mater Electron* 33 (2022) 9116–9125. <https://doi.org/10.1007/s10854-021-07142-4>.
- [31] Z. Yang, Z. Xing, Q. Feng, H. Jiang, J. Zhang, Y. Xiao, Z. Li, P. Chen, W. Zhou, Sandwich-like mesoporous graphite-like carbon nitride (Meso-g-C₃N₄)/WP/Meso-g-C₃N₄ laminated heterojunctions solar-driven photocatalysts, *Journal of Colloid and Interface Science* 568 (2020) 255–263.
- [32] M. Majdoub, Z. Anfar, A. Amedlous, Emerging Chemical Functionalization of g-C₃N₄: Covalent/Noncovalent Modifications and Applications, *ACS Nano* 14 (2020) 12390–12469. <https://doi.org/10.1021/acsnano.0c06116>.

- [33] S. Patnaik, S. Martha, K.M. Parida, An overview of the structural, textural and morphological modulations of gC₃N₄ towards photocatalytic hydrogen production, *Rsc Advances* 6 (2016) 46929–46951.
- [34] J. Rashid, N. Parveen, A. Iqbal, S.U. Awan, N. Iqbal, S.H. Talib, N. Hussain, B. Akram, A. Ulhaq, B. Ahmed, Facile synthesis of g-C₃N₄ (0.94)/CeO₂ (0.05)/Fe₃O₄ (0.01) nanosheets for DFT supported visible photocatalysis of 2-Chlorophenol, *Scientific Reports* 9 (2019) 10202.
- [35] Q. Tay, P. Kanhere, C.F. Ng, S. Chen, S. Chakraborty, A.C.H. Huan, T.C. Sum, R. Ahuja, Z. Chen, Defect Engineered g-C₃N₄ for Efficient Visible Light Photocatalytic Hydrogen Production, *Chem. Mater.* 27 (2015) 4930–4933. <https://doi.org/10.1021/acs.chemmater.5b02344>.
- [36] M.M. Khan, S.A. Ansari, D. Pradhan, M.O. Ansari, J. Lee, M.H. Cho, Band gap engineered TiO₂ nanoparticles for visible light induced photoelectrochemical and photocatalytic studies, *Journal of Materials Chemistry A* 2 (2014) 637–644.
- [37] R. Marschall, Semiconductor Composites: Strategies for Enhancing Charge Carrier Separation to Improve Photocatalytic Activity, *Adv Funct Materials* 24 (2014) 2421–2440. <https://doi.org/10.1002/adfm.201303214>.
- [38] L. Ge, C. Han, X. Xiao, L. Guo, Y. Li, Enhanced visible light photocatalytic hydrogen evolution of sulfur-doped polymeric g-C₃N₄ photocatalysts, *Materials Research Bulletin* 48 (2013) 3919–3925.
- [39] M. Sun, C. Zhu, S. Wei, L. Chen, H. Ji, T. Su, Z. Qin, Phosphorus-Doped Hollow Tubular g-C₃N₄ for Enhanced Photocatalytic CO₂ Reduction, *Materials* 16 (2023) 6665.
- [40] Y. Wang, Y. Wang, Y. Chen, C. Yin, Y. Zuo, L.-F. Cui, Synthesis of Ti-doped graphitic carbon nitride with improved photocatalytic activity under visible light, *Materials Letters* 139 (2015) 70–72.
- [41] S.M. Hosseini, I.A. Sarsari, P. Kameli, Hjj. Salamati, Effect of Ag doping on structural, optical, and photocatalytic properties of ZnO nanoparticles, *Journal of Alloys and Compounds* 640 (2015) 408–415.
- [42] C. Karthikeyan, P. Arunachalam, K. Ramachandran, A.M. Al-Mayouf, S. Karuppuchamy, Recent advances in semiconductor metal oxides with enhanced methods for solar photocatalytic applications, *Journal of Alloys and Compounds* 828 (2020) 154281.
- [43] X. Zhao, G. Zhang, Z. Zhang, TiO₂-based catalysts for photocatalytic reduction of aqueous oxyanions: State-of-the-art and future prospects, *Environment International* 136 (2020) 105453.
- [44] F. Márquez, C.M. Zicovich-Wilson, A. Corma, E. Palomares, H. García, Naphthalene Included within All-Silica Zeolites: Influence of the Host on the Naphthalene Photophysics, *J. Phys. Chem. B* 105 (2001) 9973–9979. <https://doi.org/10.1021/jp012095c>.

- [45] A.A.P. Khan, M. Nazim, A.M. Asiri, Efficient catalytic degradation of organic pollutants with cupric oxide nanomaterials in aqueous medium, *Journal of Environmental Chemical Engineering* 9 (2021) 106305.
- [46] M. Guo, Y. Ma, Z. Liu, D. Wang, Y. Yang, X. Li, E. Liu, Electron, hole and radical competition mechanism of layered porous g-C₃N₄ for hydrogen generation and organic pollutant degradation, *Journal of Catalysis* 430 (2024) 115332.
- [47] G. Xue, H. Liu, Q. Chen, C. Hills, M. Tyrer, F. Innocent, Synergy between surface adsorption and photocatalysis during degradation of humic acid on TiO₂/activated carbon composites, *Journal of Hazardous Materials* 186 (2011) 765–772.
- [48] D.L. Maricle, W.G. Hodgson, Reducion of Oxygen to Superoxide Anion in Aprotic Solvents., *Analytical Chemistry* 37 (1965) 1562–1565.
- [49] A. Haleem, A. Shafiq, S.-Q. Chen, M. Nazar, A comprehensive review on adsorption, photocatalytic and chemical degradation of dyes and nitro-compounds over different kinds of porous and composite materials, *Molecules* 28 (2023) 1081.
- [50] Y.R. Girish, N.M. Byrappa, G. Alnaggar, A. Hezam, G. Nagaraju, K. Pramoda, K. Byrappa, Rapid and facile synthesis of Z-scheme ZnO/g-C₃N₄ heterostructure as efficient visible light-driven photocatalysts for dye degradation and hydrogen evolution reaction, *Journal of Hazardous Materials Advances* 9 (2023) 100230.
- [51] P. Wang, N. Lu, Y. Su, N. Liu, H. Yu, J. Li, Y. Wu, Fabrication of WO₃@ g-C₃N₄ with core@ shell nanostructure for enhanced photocatalytic degradation activity under visible light, *Applied Surface Science* 423 (2017) 197–204.
- [52] Q. Liu, C. Fan, H. Tang, X. Sun, J. Yang, X. Cheng, One-pot synthesis of g-C₃N₄/V₂O₅ composites for visible light-driven photocatalytic activity, *Applied Surface Science* 358 (2015) 188–195.
- [53] M. Javed, W.B. Khalid, S. Iqbal, M.A. Qamar, H. Alrbyawi, N.S. Awwad, H.A. Ibrahim, M.M. Al-Anazy, E.B. Elkaeed, R.A. Pashameah, Integration of Mn-ZnFe₂O₄ with Sg-C₃N₄ for boosting spatial charge generation and separation as an efficient photocatalyst, *Molecules* 27 (2022) 6925.



Conclusions and Outlooks

General conclusions

This thesis focuses on the design and study of advanced hybrid composites applied to the treatment of urban and industrial wastewater. Titled “Synthesis of New Hybrid Materials Incorporated into Photocatalytic Semiconductors: Application in the Treatment of Urban and Industrial Wastewater”, this thesis is based on experimental work conducted at the Laboratory of Chemical Process Engineering (LGPC) of the University of Sétif 1. The main objective of this research was to design innovative hybrid materials capable of improving the efficiency of photocatalytic semiconductors in the degradation of organic pollutants present in effluents. By adopting green synthesis approaches, we have not only targeted photocatalytic performance but also sought to minimize the environmental impact of the manufacturing process of these materials.

In the first part of our research, we studied the biosynthesis and photocatalytic applications of zinc oxide nanoparticles. (ZnO-NPs).

- ✓ We successfully synthesized these nanoparticles from an aqueous extract of Algerian date syrup, followed by thorough characterization using various techniques, including SEM, UV DRS, FTIR, and XRD.
- ✓ The results obtained revealed that the ZnO/rGO nanocomposites exhibit remarkable photocatalytic efficiency, achieving a complete degradation of 100% of methylene blue (MB) in just 140 minutes under UV irradiation. The optimization of experimental conditions showed that the ZnO/rGO photocatalyst achieves its best performance at a neutral pH and a concentration of 1 g/L.
- ✓ Furthermore, we have demonstrated the recyclability of ZnO/rGO_{10%} over five degradation cycles, which attests to its stability and potential for practical applications. Finally, trapping experiments have identified hydroxyl radicals ($\bullet\text{OH}$) and electrons (e^-) as the main species involved in the photodegradation mechanism, highlighting the synergy between ZnO and rGO that helps reduce electron-hole recombination.

Secondly, we successfully synthesized bismuth oxide (Bi_2O_3) as well as the $\text{Bi}_{12}\text{ZnO}_{20}$ type selenite, both obtained through a green method.

- ✓ The selenite $\text{Bi}_{12}\text{ZnO}_{20}$ was produced for the first time using a natural extract derived from prickly pear skin waste as a reducing agent. The identification of the phases of the synthesized materials was confirmed by X-ray diffraction (XRD) and other characterization techniques, thus ensuring the integrity and purity of the compounds.
- ✓ We then evaluated the photocatalytic performance of the $\text{Bi}_{12}\text{ZnO}_{20}/\text{Bi}_2\text{O}_3$ composite by varying the proportions of the materials. The optimal ratio of 90% $\text{Bi}_{12}\text{ZnO}_{20}$ and 10% Bi_2O_3 achieved a 100% degradation rate of Beibrich scarlet in just 80 minutes, starting from an initial concentration of 20 mg/L.
- ✓ Moreover, the composite demonstrated excellent stability, maintaining a degradation rate of 97.7% after six cycles of use. These results highlight the promising potential of synthesized materials for practical applications in wastewater treatment.

At the end of our studies, we synthesized hybrid compounds based on an organic semiconductor, g- C_3N_4 , by integrating two elements into its structure, phosphorus and titanium. The individual doping of these elements revealed a significant improvement in the photocatalytic activity of g- C_3N_4 . Encouraged by these promising results, we have chosen to combine the properties of titanium and phosphorus in order to modify the material's characteristics and optimize its photocatalytic performance. This strategy has led to achieving remarkable degradation rates, exceeding our initial expectations. The obtained results validate the effectiveness of this combination in enhancing the photocatalytic activity of g- C_3N_4 .

We can summarize our results as follows:

- ✓ The success of the preparation of the composite P-g- $\text{C}_3\text{N}_4@\text{Ti-g-C}_3\text{N}_4$ was validated by various characterization methods, including EDX and mapping, which provide an accurate analysis of the composition of our material.
- ✓ The improvement in the optical properties of g- C_3N_4 was corroborated by the UV DRS results, showing a decrease in the band gap energy, as well as by photoluminescence analyses, suggesting an efficient charge separation due to the synergistic effects of phosphorus and titanium doping.

- ✓ A degradation rate of 100% of Beibrich Scarlet (BS) was achieved in 100 minutes with an initial concentration of 30 mg/L under visible light, demonstrating the success of our work in creating a composite with exceptional photocatalytic performance.

Outlooks

- Test the composites on a wide range of pollutants to evaluate their effectiveness under various conditions.
- Adapting photocatalysts to sunlight for a more ecological and economical application. Exploring other natural extracts such as precursors or reducing agents could lead to more sustainable synthesis methods.
- Introduce artificial intelligence to optimize synthesis and reaction parameters, thereby enabling continuous improvement of photocatalytic efficiency and precise prediction of performance under various processing conditions.
- Study, using COD and TOC, the mineralization of pollutants as well as the by-products generated during the reactions to better understand the degradation pathways and ensure the safety and efficiency of the photocatalytic process in contaminant reduction.
- Study the feasibility of scaling up the synthesis of hybrid composites to an industrial level, by evaluating their economic viability for wastewater treatment applications.

Abstract

The preservation of the environment and the resolution of ecological problems are essential for sustainably improving the quality of life and promoting sustainable development. Photocatalysis assisted by semiconductors is garnering increasing interest due to its immense potential to address global energy and environmental challenges. This thesis explores the design and evaluation of advanced hybrid nanomaterials for the photocatalytic degradation of organic pollutants in wastewater, specifically targeting recalcitrant dyes such as methylene blue and Biebrich scarlet. The main objective is to develop innovative photocatalysts based on zinc, bismuth, and graphitic carbon nitride (g-C₃N₄), by integrating green synthesis methods to minimize the environmental impact of manufacturing processes. The results demonstrate a notable photocatalytic efficiency of ZnO/rGO nanocomposites, ensuring complete degradation of methylene blue in 140 minutes under UV irradiation. Moreover, the Bi₁₂ZnO₂₀/Bi₂O₃ composite demonstrated exceptional performance in the degradation of Biebrich scarlet, achieving a degradation rate of 100% in just 80 minutes. Moreover, doping g-C₃N₄ with phosphorus and titanium has significantly improved its photocatalytic activity under visible light, allowing for the complete degradation of Biebrich scarlet in 100 minutes. These studies highlight the potential of hybrid materials developed for practical applications in wastewater treatment, while emphasizing the importance of eco-friendly synthesis strategies for sustainable water resource management.

Keywords: Photocatalysis, hybrid materials, green synthesis, degradation of organic dyes, ZnO/rGO, Bi₁₂ZnO₂₀/Bi₂O₃, P-g-C₃N₄@Ti-g-C₃N₄.

Résumé

La préservation de l'environnement et la résolution des problèmes écologiques sont essentielles pour améliorer durablement la qualité de vie et promouvoir un développement durable. La photocatalyse assistée par des semi-conducteurs suscite un intérêt croissant en raison de son potentiel immense pour répondre aux défis énergétiques et environnementaux mondiaux. Cette thèse, explore la conception et l'évaluation de nanomatériaux hybrides avancés pour la dégradation photocatalytique de polluants organiques dans les eaux usées, ciblant spécifiquement les colorants récalcitrants, tels que le bleu de méthylène et le Biebrich scarlet. L'objectif principal est de développer des photocatalyseurs innovants à base de zinc, de bismuth et de graphitic carbon nitride (g-C₃N₄), en intégrant des méthodes de synthèse verte afin de minimiser l'impact environnemental des procédés de fabrication. Les résultats démontrent une efficacité photocatalytique notable des nanocomposites ZnO/rGO, assurant une dégradation complète du bleu de méthylène en 140 minutes sous irradiation UV. Par ailleurs, le composite Bi₁₂ZnO₂₀/Bi₂O₃ a montré des performances exceptionnelles dans la dégradation du Biebrich scarlet, atteignant un taux de dégradation de 100 % en seulement 80 minutes. De plus, le dopage du g-C₃N₄ avec du phosphore et du titane a significativement amélioré son activité photocatalytique sous lumière visible, permettant une dégradation totale du Biebrich scarlet en 100 minutes. Ces travaux mettent en évidence le potentiel des matériaux hybrides développés pour des applications concrètes dans le traitement des eaux usées, tout en soulignant l'importance de stratégies de synthèse écologiques pour une gestion durable des ressources hydriques.

Mots clés : Photocatalyse, matériaux hybrides, Synthèse verte, Dégradation des colorants organiques, ZnO/rGO, Bi₁₂ZnO₂₀/Bi₂O₃, P-g-C₃N₄@Ti-g-C₃N₄.

الملخص

تُعد حماية البيئة وحلّ المشاكل البيئية من الضرورات الأساسية لتحسين جودة الحياة بشكل مستدام وتعزيز التنمية المستدامة. تحظى تقنية التحفيز الضوئي بمساعدة أشباه الموصلات باهتمام متزايد نظرًا لإمكاناتها الهائلة في مواجهة التحديات العالمية المرتبطة بالطاقة والبيئة. تستكشف هذه الأطروحة تصميم وتقييم مواد نانوية هجينة متقدمة لتحفيز التحلل الضوئي للملوثات العضوية في مياه الصرف، مع التركيز بشكل خاص على الأصباغ المستعصية مثل الميثيلين الأزرق وبييرتش سكارليت. ، (g-C₃N₄) الهدف الرئيسي يتمثل في تطوير محفزات ضوئية مبتكرة تعتمد على الزنك والبيزموت و نترات الكربون الغرافيتي مع اعتماد طرق تخليق خضراء لتقليل الأثر البيئي لعمليات التحضير. وقد أظهرت النتائج فعالية ملحوظة للمواد النانوية في التحلل الكامل للميثيلين الأزرق خلال 140 دقيقة تحت إشعاع فوق بنفسجي. من جهة أخرى، أظهر المركب ZnO/rGO أداءً استثنائيًا في تفكيك صبغة بييرتش سكارليت، حيث بلغ معدل التحلل 100% في غضون 80 دقيقة Bi₁₂ZnO₂₀/Bi₂O₃ بالفوسفور والتيتانيوم في تعزيز نشاطه التحفيزي الضوئي تحت الضوء المرئي، g-C₃N₄ فقط. علاوة على ذلك، ساهم تطعيم مما مكن من تحلل كامل لبييرتش سكارليت خلال 100 دقيقة. تُبرز هذه الأعمال الإمكانيات الكبيرة للمواد الهجينة المطورة في التطبيقات العملية لمعالجة مياه الصرف، كما تؤكد على أهمية اعتماد استراتيجيات تخليق صديقة للبيئة من أجل إدارة مستدامة للموارد المائية.

الكلمات المفتاحية

ZnO/rGO ،Bi₁₂ZnO₂₀/Bi₂O₃ ،P-g-C₃N₄@Ti-g-C₃N₄ التحفيز الضوئي، المواد الهجينة، التخليق الأخضر، تحلل الأصباغ العضوي